



**FACULTY
OF MATHEMATICS
AND PHYSICS**
Charles University

DOCTORAL THESIS

RNDr. Jana Hudecová

Theory and application of optical spectroscopic methods for structural molecular studies

Institute of Organic Chemistry and Biochemistry
Academy of Sciences of the Czech Republic

Supervisor of the doctoral thesis: Prof. RNDr. Petr Bouř, DSc.

Consultant: Prof. RNDr. Vladimír Baumruk, DrSc.,

Institute of Physics of Charles University

Study programme: Physics

Study branch: Biophysics, Chemical and Macromolecular Physics

Prague 2018

I declare that I carried out this doctoral thesis independently, and only with the cited sources, literature and other professional sources.

I understand that my work relates to the rights and obligations under the Act No. 121/2000 Coll., the Copyright Act, as amended, in particular the fact that the Charles University has the right to conclude a license agreement on the use of this work as a school work pursuant to Section 60 paragraph 1 of the Copyright Act.

In Prague 15th June 2018

Acknowledgements

First and foremost, I would like to thank my supervisor, Prof. Petr Bouř for his guidance throughout the whole work - for his time, patience, constant support, endless effort, valuable advices and for providing me with a lot of programs, which made the work easier. I am grateful for his support that allowed me to continue in my research after each of my two maternity leaves. I would also like to thank to all former and current members of Molecular Spectroscopy group at the Institute of Organic Chemistry and Biochemistry, who I had an opportunity to meet from 2008 for a friendly environment, fruitful discussions and beneficial collaboration with many of them.

I would also like to thank my consultant Prof. Vladimír Baumruk who introduced me to the realm of Raman optical activity. My great appreciation goes to my collaborators from the Institute of Physics, Faculty of Mathematics and Physics at Charles University in Prague (Dr. Václav Profant), Institute of Chemical Technology in Prague (Prof. Marie Urbanová and Dr. Pavlína Novotná), University of Tromsø, Norway (Prof. Kenneth Ruud, Dr. Kathrin Helen Hopmann, Dr. Xiaojun Li) and University of Illinois in Chicago, USA (Prof. Timothy A. Keiderling, Dr. Ge Zhang).

I gratefully acknowledge financial support from the Grant Agency of the Charles University in Prague (the project no. 126310) and the Czech Science Foundation, where I was a team member in a number of projects (P208-11-0105, 16-05935S, 16-08764Y and 18-05770S).

Last but not least, my personal thanks belong to my family for their endless support throughout my studies. A special thank belongs to my husband Honza for his patience, encouragement and being here for me and our sons Adam and David all the time.

Title: Theory and application of optical spectroscopic methods for structural molecular studies

Author: RNDr. Jana Hudecová

Department / Institute: Institute of Organic Chemistry and Biochemistry,
Academy of Sciences of the Czech Republic

Supervisor of the doctoral thesis: Prof. RNDr. Petr Bouř, DSc.

Abstract:

In the thesis, methods of the chiroptical spectroscopy (Raman optical activity, electronic and vibrational circular dichroism, circularly polarized luminescence) were utilized to obtain information on structure of chiral molecules. In four main projects, we focused on improving accuracy of quantum-chemical computations used for interpretation of experimental spectra by including anharmonic effects, solvent, molecular flexibility and dynamics. In the first project, the normal mode geometry optimization method was investigated and a suitable frequency limit providing realistic vibrational band broadening was found. Then the ability of harmonic and anharmonic computational approaches to describe the C-H stretching vibrations was explored for three terpene molecules and four spectroscopic methods. In the third project, we estimated the role of dispersion forces and different organic solvents for conformer equilibria and dynamics of cyclic dipeptides containing tryptophan. In the last project, circularly polarized luminescence spectra, which were sensitive to the position of histidine in the peptide chain, could be rationalized by free energies obtained from molecular dynamics simulations.

Keywords: chiroptical spectroscopy, Raman optical activity, quantum-chemical calculations, conformational flexibility, anharmonic corrections

Contents

Preface.....	3
1. Spectroscopic studies of chiral molecules	5
1.1. Chirality.....	5
1.2. Chiroptical spectroscopy	6
1.2.1. Raman optical activity	9
1.2.2. Circular dichroism	11
1.2.3. Circularly polarized luminescence.....	13
1.3. Applications of chiroptical spectroscopies.....	15
1.3.1. Determination of the absolute configuration	16
1.3.2. Structural studies of the biologically significant molecules	17
1.4. Interpretation of chiroptical spectra	19
2. Molecular spectroscopic properties.....	20
2.1. Methods for simulations of the spectra	20
2.1.1. Basics of quantum chemistry	20
2.1.2. <i>Ab-initio</i> methods.....	21
2.1.3. Density functional theory.....	25
2.1.4. Harmonic approximation and anharmonic corrections.....	27
2.2. Computational implementation	30
2.2.1. Conformational search	31
2.2.2. Solvent models.....	35
2.2.3. Raman optical activity – theoretical aspects	36
2.2.4. Circular dichroism – theoretical aspects	41
2.2.5. Comparison of calculated and experimental spectra	43
3. Objectives of the thesis	46
4. Computational and experimental methods.....	48
4.1. Computational methods.....	48
4.1.1. Normal mode geometry optimization method	48
4.1.2. Harmonic and anharmonic calculations for terpenes.....	50

4.1.3.	Cyclic dipeptides with tryptophan	53
4.1.4.	Interaction of the $[\text{Eu}(\text{DPA})_3]^{-3}$ complex with histidine-peptides	55
4.2.	Studied compounds	56
4.3.	Experimental methods.....	57
4.3.1.	ROA experiment	57
4.3.2.	VCD experiment	59
4.3.3.	ECD experiment.....	60
5.	Results and discussion	61
5.1.	Normal mode geometry optimization and vibrational broadening	61
5.2.	VOA spectra in the C-H stretching region	65
5.3.	Tryptophan optical activity	73
5.4.	Circularly polarized luminiscence of the europium (III) complex.....	83
	Conclusions.....	89
	Bibliography	91
	List of figures.....	108
	List of tables.....	110
	List of abbreviations	111
	List of publications.....	114
A.	Attachments.....	117
A1.	Publication [I]: Hudecová et al. <i>J. Phys. Chem. B</i> (2012).....	117
A2.	Publication [II]: Hudecová et al. <i>J. Chem. Theory Comput.</i> (2013)	125
A3.	Publication [III]: Hudecová et al. <i>ChemPhysChem</i> (2012).....	150
A4.	Publication [IV]: Brichtová et al. <i>Chem. Eur. J.</i> (2018)	169

Preface

Optical spectroscopic methods are based on interactions of molecules with electromagnetic radiation. Many different types of spectroscopic techniques have been developed and found numerous applications in biochemical and structural studies of peptides, proteins, nucleic acids and other natural compound. The determination of structure of biomolecules and consecutive clarification of the relation between their structure and functionality is one of the main tasks of biophysics.

As many of biomolecules are chiral, chiroptical spectroscopic methods are being widely used for determining the structure (i.e., absolute configuration and preferred conformation in solution). Chiroptical spectroscopy explores the interaction of polarized light with a chiral sample. Differences in absorption, scattering, or dispersion of left- and right-circularly polarized light on molecules can be utilized.

Two methods of vibrational optical activity, Raman optical activity (ROA) and vibrational circular dichroism (VCD), are used in this thesis. They combine the sensitivity of chiroptical methods to spatial arrangement of atoms in molecules with the richness of vibrational spectra. Vibrational spectroscopy can also be used to study dynamic structural changes. The time scale of vibrational transitions is shorter than for conformational changes and the vibrational spectrum represents a sum of the conformer spectra. We also used the electronic circular dichroism (ECD), circularly polarized luminescence (CPL) and chirality-insensitive nuclear magnetic resonance (NMR). A brief overview of the methods is in Chapter 1.

It is important to understand the origin of measured spectra and physical principles behind them. Computational chemistry can help us with it. Quantum-chemical computations on real systems require many approximations. New algorithms were developed in the last decade, for example an analytical derivative procedure for ROA tensors implemented into Gaussian09 enabled to efficiently compute ROA intensities. Especially accurate simulations, taking into account the solvent and many conformations of flexible molecules, are needed for chiroptical spectra. The methods, which we used, are summarized in Chapter 2.

The objectives of the thesis are formulated in Chapter 3. Chapter 4 contains descriptions of the computational and experimental details. Achieved results, related to four publications that can be found as Attachments, are discussed in Chapter 5.

Averaging of many conformers and solvent configurations is necessary for flexible molecules to represent the investigated system more realistically. However, cluster geometries obtained directly from molecular dynamics often provide unrealistic vibrational band broadening. The normal mode optimization method was used to reduce this broadening in publication [I] (Chapter 5.1).

Publication [II] (Chapter 5.2) represents another methodological study. The ability of several harmonic and anharmonic computational approaches to describe vibrations in the C-H stretching region ($\sim 3000\text{ cm}^{-1}$) is explored for three terpene molecules. Four spectroscopic methods (IR, VCD, Raman, ROA) are examined together in order to better assess the reliability of the simulations.

The role of dispersion forces and influence of different organic solvents on conformer equilibria is examined for cyclic dipeptides with tryptophan by ECD, VCD, ROA and NMR spectroscopy in publication [III] (Chapter 5.3).

The last project deals with lanthanide complexes that are used as convenient spectroscopic probes for many biomolecules. The lanthanide-peptide interaction and its effect on lanthanide spectroscopic properties was investigated systematically in a series of histidine-containing peptides and complexes of europium as described in publication [IV] (Chapter 5.4). CPL spectra sensitively reacted on the histidine position in the peptide chain, peptide length and pH. These findings were rationalized by molecular dynamics simulations.

Common attributes of all papers included in this thesis are the technique of the Raman optical activity and interest in details that can affect the computed spectra.

1. Spectroscopic studies of chiral molecules

1.1. Chirality

Chirality is one of the fundamental principles in nature and describes the ability of an object to exist in two forms called enantiomers. They are “mirror images” to each other and cannot be superimposed (**Fig. 1.1**).^{1,2} Such objects do not have a plane or a centre of symmetry. The word chirality is derived from the Greek word “kheir” meaning hand. This term was suggested by Lord Kelvin in 1904. Human hands are perhaps the most universally recognized example of chirality. For molecules, many chemical and physical properties (molecular formula, bonding arrangement, melting point, boiling point, density) are identical for both enantiomers.

Enantiomers may interact in different ways with other chiral molecules and they can also be resolved by interaction with polarized light. As a linearly polarized light passes through an optical active system (a solution of chiral molecules), the plane of polarization, when viewed along the axis toward the source, may be rotated in a clockwise (to the right) or anticlockwise (to the left) direction. In 1848, Louis Pasteur discovered that mirror-image enantiomers generate equal but opposite optical-rotation angles. Observation of this phenomenon^{3,4,5} started the chirality research. A right handed rotation is called dextrorotary (D-), a left handed rotation is levorotary (L-), according to the Fischer system.⁶ The Cahn-Ingold-Prelog system⁷ represents another way how to distinguish between two enantiomers. It deals with a chiral center, which is the simplest molecular element that leads to chirality. Usually, it is a carbon with sp^3 orbital hybridization forming four different bonds arranged in a tetrahedron. The configuration of the chiral center is specified by the letters R- for rectus (right) and S- for sinister (left) orientation. Apart from the chiral center, the chirality can be based on a helix, chiral axis, etc.

Chirality is a crucial concept in chemistry of living organisms because many biologically important molecules are chiral. These molecules are often naturally present in one enantiomeric form only. D-saccharides are typically preferred in nucleic acids and L-amino acids are present in proteins. Chirality of biomolecules is related to biologically important processes. For example, proteins are often highly stereoselective towards their binding partners. For a molecule with n chiral centers, the maximum number of possible stereoisomers is 2^n . Quite often, only one of the possible forms is biologically active.⁸ The enzymes are the most conspicuous examples of

chirality among biomolecules. All of them have many stereocenters (well-known example is a proteolytic enzyme chymotrypsin containing 251 stereocenters)⁹ but usually only one of these stereoisomers is produced and utilized in a given organism.

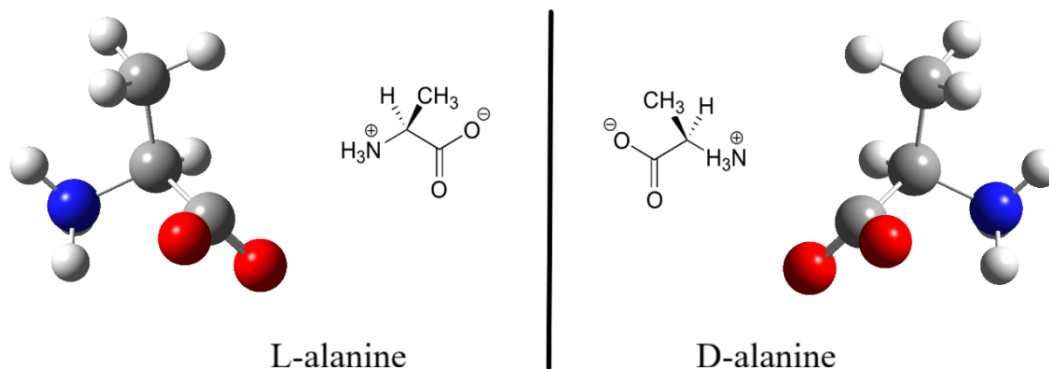


Fig. 1.1: Two enantiomers of the simplest chiral aminoacid – alanine.

1.2. Chiroptical spectroscopy

Chiroptical spectroscopy probes interaction of polarized light with a chiral sample. It can explore differences in absorption, scattering, or dispersion of left- (LCP) and right- (RCP) circularly polarized light on molecules.¹⁰ The circularly polarized light, being intrinsically chiral itself, acts as a chiral probe.

Historically, the first observation of molecular chirality was rotation of the plane of linearly polarized light, referred to as optical rotation (OR). OR or optical rotatory dispersion (ORD), which is OR as a function of wavelength, have been routinely used by synthetic chemists for compound characterization for more than 100 years.^{11,12,13} Later, the absorption difference of LCP and RCP light, electronic circular dichroism (ECD), was observed as well. Both techniques typically use ultraviolet or visible light and explore the electronic transitions in molecules. The ECD and ORD spectra are related through the Kramers–Kronig transform relations.¹⁴ As a result, an ECD spectrum can be converted into an ORD spectrum when a full ECD spectrum covering all electronic transitions is available and vice versa. Thus, ECD and ORD are not truly independent spectroscopic methods. Nevertheless, practical limitations (a full range ECD/ORD spectrum covering all electronic transitions is not measurable in practice) make these two methods complementary.¹⁵ ECD, however, is easier to interpret.

Another technique related to ECD, is the circularly polarized luminescence (CPL), that measures differences in emission of the LCP and RCP light, i.e. transitions from the excited states are detected.^{16,17}

The introduction of commercial instrumentation for measuring ORD in the 1950s and ECD in the 1960s led to a rapid expansion of applications of chiroptical spectroscopy in organic and inorganic chemistry and biochemistry and, more recently, in supramolecular chemistry and chiral nanoscience.^{18,19} ECD is currently the most common chiroptical method. It is routinely used as a probe of the stereochemistry and behavior of chiral molecules in solutions, especially for proteins.

In mid-1970's it was shown that the enantiomer selectivity can be incorporated into the vibrational spectroscopy, which led to the development of the new field of the vibrational optical activity (VOA). Similarly as the vibrational spectroscopy consists of two complementary techniques: Raman and infrared (IR) spectroscopy, VOA consists of their chiral variants: Raman optical activity (ROA) and vibrational circular dichroism (VCD). Many resolved vibrational bands ($3N-6$ vibrational modes for N -atomic molecule) can be distinguished in VOA spectra compared to few bands usually observable for electronic transitions. VOA is therefore more sensitive to structural details. ROA explores the same vibrational transitions as VCD, but the technique is more complex.

The first ROA spectrum was reported in 1973 by Prof. Barron et al.²⁰ measured for both enantiomers of 1-phenylethanol and 1-phenylethylamin from 300 to 400 cm^{-1} . The reliability of the measured signal was confirmed by Prof. Hug.²¹ The first VCD spectra were measured in 1974 by Holzwarth et al.²² for C-H (2920 cm^{-1}) and C-D (2204 cm^{-1}) stretching modes of both enantiomers of 2,2,2,-trifluoro-1-phenylethanol. Thanks to the availability of commercial instruments (first VCD in 1997²³ and ROA in 2003²⁴), VOA is now more accessible to the wider scientific community. VOA was applied for many types of biomolecules:²⁵ peptides,²⁶ nucleic acids,²⁷ sugars,²⁸ and viruses.²⁹

Also the level of analysis of chiroptical spectra is improving rapidly thanks to advances in computational chemistry,³⁰ which has improved our understanding of the underlying principles behind these chiroptical techniques. The availability of fast computers with large memory allowed quantum-chemical calculations for larger molecules of synthetic, pharmaceutical and biological importance. Nowadays

calculations of chiroptical spectra are implemented into free and commercial computer programs (Gaussian,³¹ Dalton,³² ADF,³³ CADPAC,³⁴ etc.).

A comparison of the chiroptical methods used in this thesis is in **Table 1.1**. Commercially available ECD spectrometers cover a broad range of wavelengths (~180–800 nm). This range may be severely restricted by the solvent transmission, material of the sample cell, etc. Below 180 nm, special vacuum techniques and synchrotron radiation can be used as the source of light.³⁵ Low-lying electronic transitions, for example in lanthanide complexes, can be seen by extending the wavelength range to the near-infrared region (800–1100 nm). Many organic solvents enabling ECD measurement in a large part of the 180–800 nm intervals are available, the concentration can be lower and accumulation times shorter than for VOA. The electronic spectra, however, provide a limited number of features, not necessarily associated with local geometry. VOA spectroscopies are generally more sensitive to the local structure. Signals corresponding to distinct parts of the molecule are usually well separated in VOA spectra.

Table 1.1: Comparison of chiroptical techniques. Modified from³⁶

Method	CPL	ECD	VCD	ROA
Cost	0.3	0.1	0.1	0.2
Usual detection range	180-800 nm	180-800 nm	800-4000 cm ⁻¹	100-2400 cm ⁻¹ **
Peak resolution	Few bands	Few bands	Many transitions	Many transitions
Solid state measurement	Possible	Possible	Possible	Not known
Typical concentration	0.1 mg/ml	0.1 mg/ml	10 mg/ml	30 mg/ml *
Water as a solvent	OK	OK	Problematic	Ideal
Organic solvents	OK	OK	Acceptable	Problematic
Theoretical prediction (DFT/TD-DFT)	Difficult	Usually reliable	Very reliable	Very reliable

* for many compounds the recommended concentration for ROA is not possible due to a limited solubility

** shift from the laser radiation

Other advantages of VOA (ROA and VCD) are inherited from the parent Raman and IR spectroscopies. The usual spectral range for VCD is from 800 to 4 000 cm⁻¹ but it is extensible up to 14 000 cm⁻¹, where overtones and combination bands occur. ROA is usually measured from 200 to 2400 cm⁻¹ (rarely 4000 cm⁻¹).³⁷

The low-frequency vibrational modes (amide modes IV–VII in proteins, helix breathing, torsions and skeletal deformations)³⁸ accessible by ROA may be particularly sensitive to the conformation and dynamics of molecules. The ROA measurement requires even higher sample concentration than VCD. The most commonly used solvents represent another difference between ROA and VCD spectroscopy. Water has a weak Raman scattering, whereas a scattering from organic solvents often masks the ROA signal from the sample. Therefore, ROA spectroscopy is particularly well-suited for biomolecular applications like investigations of the secondary structures of peptides in the natural aqueous environment. Purification of samples in order to minimize the fluorescence from impurities is often required for ROA spectroscopy. Water and other polar solvents have broad and intense absorption bands, so less polar solvents are preferred in the VCD spectroscopy. The ROA and VCD spectroscopies have different selection rules, consequently, they have different sensitivities towards distinct parts of biomolecules.

A brief overview of common principles of ROA, VCD, ECD and CPL is presented in the following chapters. The quantum-chemical methods used for calculations of the spectra are introduced in Chapter 2 and discussed with the focus on computational aspects and investigation of flexibility of chiral molecules in solution. Other information can be found in books of Barron,² Nafie,³⁹ and Polavarapu.⁴⁰

1.2.1. Raman optical activity

Raman optical activity measures a small difference in Raman scattering of RCP and LCP light, either in the incident or scattered beams, or even in both²

$$I^{ROA} = I(R) - I(L). \quad (1.1)$$

A normalized circular intensity difference (CID) can be defined as⁴¹

$$\Delta = \frac{I^{ROA}}{I^{RAM}} = \frac{I(R) - I(L)}{I(R) + I(L)}. \quad (1.2)$$

ROA is a weak effect, $\Delta \sim 10^{-3}$ – 10^{-5} , and the parent Raman scattering is already a relatively weak phenomenon – only about one from 10^6 photons is scattered inelastically. A high experimental sensitivity is therefore required for ROA measurements and the technique is susceptible to artifacts. If both enantiomers are

measured, the mirror imaged signals should be obtained.⁴² These signals can be used to check the experimental reliability.

There are several experimental configurations. First selectable parameter is the scattering angle between directions of the incident and scattered light. Three basic geometries are: the forward (0°), right-angle (90°) and backward (180°) scattering. The backscattering geometry is currently considered to be the best experimental strategy. Its main advantage is a high signal intensity and lower artifacts level.⁴³

Another parameter is the polarization of incident and scattered light. There are three basic circular polarization schemes:

1. The incident circular polarisation (ICP),²⁰
where the incident laser beam is periodically switched between RCP and LCP states, and the detected scattered light is linearly polarized or unpolarized.
2. The scattered circular polarisation (SCP),²¹
where the incident light is linear or unpolarized and the difference in RCP and LCP Raman scattered light is detected.
3. The combination of ICP and SCP called dual circular polarisation (DCP),⁴⁴
where both the incident and scattered light are circularly polarized, either in-phase (DCP_I) or out-of-phase (DCP_{II}) as summarized in **Fig. 1.2**.

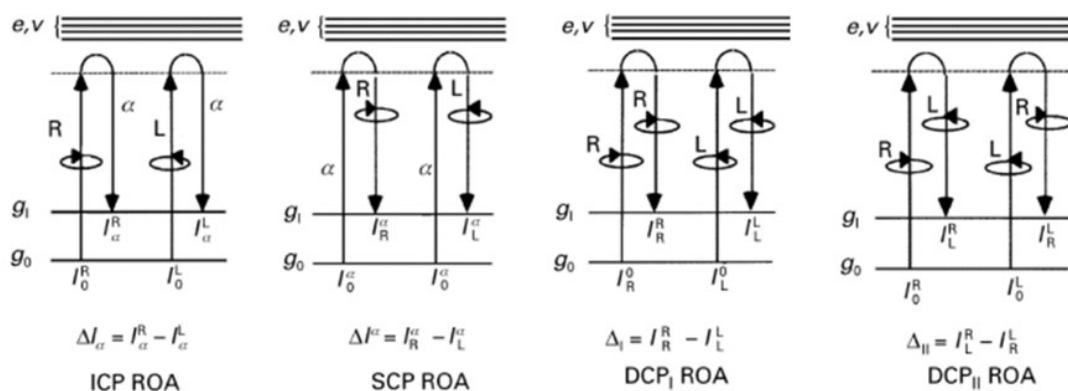


Fig. 1.2: Diagram of energetic levels of a molecule showing polarization states of the incident and scattered light for four experimental forms of ROA. Adapted from ⁴⁵.

First ROA instruments of Prof. Barron in Glasgow laboratory were based on the ICP scheme and used the right-angle⁴⁶ and backscattering geometry.⁴⁷ The only one commercial ROA instrument so far was introduced by BioTools, Inc., USA in 2003.²⁴ This spectrometer is based on the design of Hug and Hangartner. It uses the SCP scheme and the backscattering geometry. Relatively easy ROA measurements with artifact reduction were enabled by two novel features:

1. the RCP and LCP scattered radiation separated by a polarization beam splitter is measured simultaneously on the upper and lower halves of a multichannel charge-coupled device (CCD) detector. The ROA spectrum is obtained by subtracting the LCP intensity from the RCP intensity.
2. the use of electronically controlled half-wave led to optical generation of virtual enantiomers and thus to elimination of the artifacts resulting from residual linear polarization components in RCP and LCP scattered light.⁴⁸

The simultaneous measurement of both states of circular polarization enabled elimination of the “flicker noise” (a random noise, which might be caused by fluctuations in the laser power, sample density, dust particles in the optical path or heat fluctuations of the detector) and speeded up the experiment. Theoretical aspects of ROA will be discussed in Chapter 2.2.3.

1.2.2. Circular dichroism

The circular dichroism (CD) intensity is defined as the difference in the absorbance for LCP and RCP (**Fig. 1.3**)³⁹

$$\Delta A(\nu) = A_L(\nu) - A_R(\nu) \quad (1.3)$$

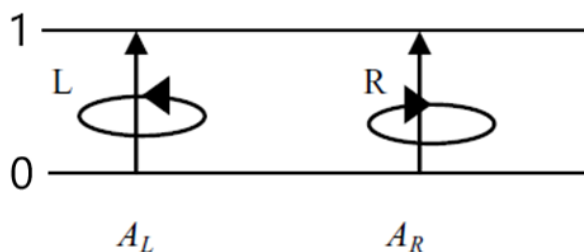


Fig. 1.3: Energy-level polarization diagram illustrating the photon transitions associated with CD. For VCD energetic levels 0 and 1 correspond to the zeroth and the first vibrational levels of the ground electronic state. For ECD energetic levels 0 and 1 refer to the ground and the excited electronic state. Adapted from ⁴⁵.

The corresponding absorption spectrum can be defined as the average

$$A(\nu) = \frac{1}{2}[A_R(\nu) + A_L(\nu)]. \quad (1.4)$$

The differential molar absorption coefficient defined by the Beer-Lambert law can be also used

$$\Delta\varepsilon(\nu) = \varepsilon_L(\nu) - \varepsilon_R(\nu) = \frac{\Delta A}{cl}, \quad (1.5)$$

where c is the molar concentration in mol.L⁻¹ and l is the pathlength in cm. This definition of CD does not depend on the choice of sampling variables such as pathlength and concentration. Therefore it is useful for comparison of experimental and calculated CD spectra.

Two spectral regions are the most frequent: ultraviolet-visible (UV/vis) and infrared (IR). CD measured in the UV/vis region is called electronic CD, because electronic transitions are involved. CD measured in the IR region is called vibrational CD as it mostly samples vibrational transitions. While ECD is more sensitive to molecular environment, VCD spectra provide more local information about the structure. The theoretical aspects will be discussed in Chapter 2.2.4.

A dimensionless anisotropy ratio can be defined as⁴¹

$$g = \frac{\Delta A}{A} = \frac{2[A_L - A_R]}{A_R + A_L}, \quad (1.6)$$

in analogy to Δ (1.2) in ROA. g is typically $\sim 10^{-3}$ for ECD and 10^{-4} for VCD.⁴⁹ A high stability of spectrometers is therefore required.

Commercial instrumentation is available for both ECD and VCD. Two types of VCD spectrometers exist: dispersive and Fourier-transform (FT). The dispersive instruments⁵⁰ use a grating monochromator to scan through the wavelength region of interest, recording the spectrum sequentially. The FT-CD instruments use the Michelson interferometer and collect all wavenumbers simultaneously. The first FT-VCD spectrometer was constructed in 1979⁵¹ and the first commercial instrument was offered in 1997 by BioTools.²³ Shortly after, Bruker, Jasco and Thermo-Fisher also introduced the VCD accessories into their FT-IR spectrometers. Despite the different designs of VCD spectrometers, all of them use the photoelastic modulator (PEM) placed in front of the sample to modulate the IR beam.

The FT technique dominates the commercial market. It can produce high-quality spectra over the entire mid-IR, typically from ~ 600 to ~ 2000 cm^{-1} with a good resolution (typically 4 cm^{-1}) and in a reasonable time. The dispersive VCD instruments are still used for measuring isolated bands, e.g., for biopolymers in aqueous solution in the midIR region, taking advantage of a stronger source and a narrower spectral region.^{26,52}

Samples suitable for VCD measurement should exhibit absorbance in a relatively narrow range of 0.1–1.0; the most desirable value is around 0.5. Too high absorption means the lack of incident light on the detector and sizable artifacts. For small absorptions, the noise level is increasing and birefringence in the optical material of optical lenses, filters, cells and other windows, and reflections may cause artifacts. The absorbance can be optimized by a combination of sample concentration, optical pathlength and choice of the solvent. Water and other polar solvents have broad and intense absorption bands, so less polar solvents are preferred. Deuterated organic solvents are frequently employed to reduce the absorbance within the spectroscopic window.

1.2.3. Circularly polarized luminescence

Circularly polarized luminescence can be viewed as the emission analogue of ECD, i.e. the light is emitted by an excited state and we measure the differences in emissions of the LCP and RCP light (**Fig. 1.4**).¹⁶ Another form of fluorescence optical activity, for which the total fluorescence is measured for absorption of LCP and RCP light, is called fluorescence detected circular dichroism (FD CD).

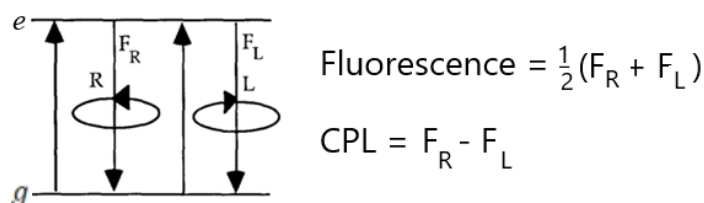


Fig. 1.4: Energy-level polarization diagram illustrating definition of CPL. Adapted from ⁴⁵. g is the ground state, e is the excited electronic state.

A normalized dissymmetry factor can be defined in analogy to Δ (eq. 1.2) in ROA and g (eq. 1.6) in VCD as

$$g = \frac{2[F(R) - F(L)]}{F(R) + F(L)}, \quad (1.7)$$

For isolated organic molecules $g \sim 10^{-3} - 10^{-2}$.

Custom-built instruments for measurement of CPL were designed, developed and improved by a limited number of research groups.¹⁷ CPL instruments contain a quarter-wave modulating circular polarization analyzer that converts alternately LCP and RCP light in a luminescence beam into a linear polarization. Nowadays, also commercial instruments are available. The first commercial CPL spectrometer from JASCO (CPL-200) consists of two CD spectrometers, with the second one used as the emission spectrometer.

CPL spectroscopy has been useful for some organic molecules, liquid crystals and polymers. In the last 20 years, applications involving luminescent lanthanide (III) ions, particularly Eu(III) and Tb(III) also appeared. The Eu fluorescence bands are as narrow as the vibrational ones, and occur within the operational range of the SCP-ROA spectrometers, so CPL can be measured using this technique.^{53,54} Similarly, the ICP-ROA instrument can measure FDCCD. In addition, the strong laser radiation source makes it possible to observe quite weak signals, undetectable on conventional CPL spectrometers.^{36,55} For example, the strongest Eu(III) signal, which can be measured on the SCP ROA spectrometer, belongs to the ${}^5D_0 \rightarrow {}^7F_1$ transitions^{56,57} and appears as (“false”) Raman bands shifted by $\sim 1700 - 2100 \text{ cm}^{-1}$ from the 532 nm laser excitation. A weaker signal around 850 cm^{-1} belongs to the ${}^5D_1 \rightarrow {}^7F_2$ transitions⁵⁸ and is visible in the differential (CPL) spectrum only. The luminescence can be distinguished from the “true” Raman scattering.⁵⁹

Many of the applications of lanthanides (III) involve selective and sensitive probes of biomolecules,⁶⁰ such as amino acids, peptides^{61,[IV]} and sugars.⁶² However, modelling of the lanthanide complexes is not directly approachable by current computational tools as it often involves energy transfer between many molecular energy levels and excited state optimization, i.e. it is quite more complex than for ECD. The theoretical understanding of lanthanides and the fluorescence enhancement effects is rather poor as discussed in Chapter 5.4 (publication [IV]).

1.3. Applications of chiroptical spectroscopies

Chiroptical spectroscopies are being used for determining the molecular structure (i.e., absolute configurations and conformations) in solution.⁴² They do not provide an atomic resolution, unlike the X-ray crystallography⁶³ and nuclear magnetic resonance spectroscopy (NMR).⁶⁴ These higher-resolution techniques dominate in structural biology, but methods of chiroptical spectroscopy are more convenient sometimes.

For X-ray crystallography and similar diffraction techniques⁶⁵ it is necessary to obtain a crystal structure of a studied system, which can change its native structure in some cases. The absolute configuration determination is possible only in the case of monocrystalline samples. The crystallization process may be rather problematic for some proteins (especially for short peptides or membrane proteins). Another limitation is that larger molecules must contain “heavy” atoms.

The NMR spectroscopy measurements is limited by molecular size (molecular weight can not be usually larger than a few hundreds of kDa)^{66,67} and absolute configuration can be obtained from NMR only through an interaction with another system (solvent or reagent) of known chirality.⁶⁸ NMR is able to probe the molecular motion over a wide range of timescales, ranging from picoseconds to tens of seconds.⁶⁹ Nevertheless, faster conformational changes are not detectable and only an average signal of conformer populations is obtained. For optical spectroscopies, a very fast optical response (absorption/emission of a photon $\sim 3 \cdot 10^{-14}$ s) enables to discriminate these conformers and the measured spectrum is an algebraic sum of the subspectra.

Chiroptical spectroscopies are not only suitable for measurements in solutions, but they easily enable to study molecules under different experimental conditions including pH, temperature, concentration and/or chemical environment. It is therefore possible to study structural changes in various biomolecular processes including protein folding^{70,71} denaturation⁷² or interaction with ligands. Of all available chiroptical spectroscopic methods, VOA is by far the richest in the ability to reflect structural details. The main applications of VOA methods are described in the following chapters.

1.3.1. Determination of the absolute configuration

This is a fundamental problem in stereochemistry encountered during organic synthesis, analysis, drug screening and natural product isolation, especially in the pharmaceutical industry.⁷³ As the human body is amazingly chiral-selective, single-enantiomer drugs are more efficient in binding to biological targets and have fewer side effects than the equivalent racemic drugs (which contain an equal mixture of the enantiomers). Nearly 50% of drugs are chiral; the pharmacological activity resides with the eutomer (pharmacologically active enantiomer) whereas the distomer (inactive or less potent or equally potent or different pharmacological activity or toxic enantiomer) metabolizes by a different pathway and can create unnecessary burden on the body. A notorious example is thalidomide that was used in 1960s to alleviate morning sickness in pregnant women and caused that between 5,000 and 7,000 infants were born with phocomelia (malformation of the limbs).⁷⁴

Every chiral drug substance approved for sale by the US Food and Drug Administration (FDA) must have a known absolute configuration. The use of stereochemically pure drugs with specified level of the enantiomeric excess (EE), usually greater than 99%, was recommended in 1992. Recently, both ROA and VCD methods were approved as suitable quantitative tools for chiral active pharmaceutical ingredient tests as an alternative, or supplement, to the X-ray crystallography and NMR method. Structures of over 7000 molecules have been determined with VCD and over 150 patents for new drug applications have been filed, where the absolute configuration is proven with VCD.

Currently, VCD is used more routinely than ROA. In some cases however, for example the (*R*)-[²H₁, ²H₂, ²H₃]-neopentane,^{75,76} or bromochlorofluoromethane,⁷⁷ ROA represents the only technique how to determine the absolute configuration. The focus is on simultaneous use of multiple methods.⁷⁸ A combination of VCD and ROA methods with theoretical calculations (sometimes accompanied by ECD and NMR) was found to be the most useful for determination of the absolute configuration for molecules with two or three chiral centres.^{79,[III],[IV]}

Many applications involve the measurement of the enantiomeric excess, which is the excess of one enantiomer over the other in the sample. In favorable circumstances, EE may be determined to an accuracy of ~0.1%.⁸⁰ It is predominantly handled by VCD,^{81,82} but also ROA can be useful.^{83,84}

1.3.2. Structural studies of the biologically significant molecules

Chiroptical methods, especially ROA spectroscopy measured in aqueous solution, are useful probes of the structure and behaviour of many biomolecules.^{43,85} As for the small molecules, ROA spectra provides valuable information on proteins,⁸⁶ carbohydrates,^{28,87} polypeptide and carbohydrate components of intact glycoproteins,⁸⁸ and nucleic acids.^{27,89} The systems of biological interest are often large and complicated and their investigation represents a challenge at both experimental and theoretical levels. In biopolymers (peptides/proteins, nucleic acids), however, the more or less regular repetition of the chiral subunits provides intense and unique spectral patterns.⁹⁰

ECD was the first method that enabled determination of the secondary structure content in proteins.^{91,92,93} ECD is well-suited for the investigation of light-absorbing molecular subunits.⁹⁴ The amides groups are the most active chromophores of protein backbone. Their different arrangement leads to characteristic ECD spectra of different secondary structures.^{95,96} Characteristic ECD bands can be found in the spectral region of amide group absorption (far-UV CD, below 250 nm). A typical protein spectrum contains $n-\pi^*$ transitions (~ 220 nm) and $\pi-\pi^*$ transitions (~ 190 nm and ~ 140 nm). α -helices have intense ECD signals and are easily detectable. ECD spectra of β -sheet or β -turn structures are not so characteristic. Signals from aromatic residues (phenylalanine, tyrosine and tryptophan) can be found in the spectral range of 250–290 nm, which can contribute to the tertiary structure assessment.

The most intense bands in ROA spectra of proteins are assigned to vibrations of the protein backbone. They are found in three main spectral regions:

1. the backbone skeletal stretch region (~ 870 – 1150 cm^{-1}), which is assigned mostly to $C_\alpha-C$, $C_\alpha-C_\beta$ and C-N stretching vibrations,
2. the extended amide III region (~ 1230 – 1350 cm^{-1}) corresponding to the in-phase combination of the in-plane N-H deformation with the C-N stretch together with $C_\alpha-H$ deformations,
3. the amide I region (1600 – 1700 cm^{-1}), where C=O stretching bands can be found. The amide III region is supposed to be the most characteristic for the peptide backbone conformation, due to the coupling between N-H and $C_\alpha-H$ deformations.⁴³

α -helices are characterized by a positive band at ~ 1340 - 1345 cm^{-1} , a negative/positive couplet at ~ 1640 and 1660 cm^{-1} and a positive signal within ~ 870 - 950 cm^{-1} . β -sheets have a negative band at $\sim 1245\text{ cm}^{-1}$ and a negative/positive couplet at ~ 1650 and 1680 cm^{-1} .⁹⁷ The signal corresponding to β -turns also involves a positive band at $\sim 1295\text{ cm}^{-1}$ and a negative band at ~ 1345 and 1375 cm^{-1} .

Side chain vibrations generate many characteristic Raman bands, but they are often less prominent in ROA spectra due to conformational freedom, which can suppress the ROA intensities. Only a few side chain vibrations generate strong ROA signals^{98,99} such as tryptophan (~ 1545 - 1560 cm^{-1} and ~ 1400 - 1480 cm^{-1}), or phenylalanine and tyrosine (~ 1545 - 1560 cm^{-1}).¹⁰⁰ The tryptophan band ~ 1545 - 1560 cm^{-1} which is assigned to the W3 vibration of the indole ring in tryptophan, can be used to determine the conformation of the tryptophan side chain. The wavenumber of this W3 vibration correlates with the magnitude of the χ_2 torsion angle. While a positive W3 ROA signal corresponds to the positive χ_2 torsion angle, a negative signal corresponds to the negative one.^{101,102,[III]}

For VCD spectroscopy, the secondary structure can be derived from the patterns of the amide I and amide II regions.^{103,26,104} The following pattern is characteristic for α -helical structure: a negative/positive couplet at ~ 1660 and 1640 cm^{-1} and a negative band at $\sim 1515\text{ cm}^{-1}$. Random coil proteins provide a positive/negative couplet at ~ 1660 and 1640 cm^{-1} in amide I region together with a negative VCD band in the amide II region. The β -sheet structures often have a characteristic negative band in the amide I and a positive/negative couplet in the amide II region.¹⁰⁵ VCD is also sensitive to aggregated supramolecular structures, such as protein fibrils.¹⁰⁶ The VCD intensity is enhanced and characteristic spectral amide I patterns - either $(+,+,-,+,+)$, or $(-,-,+,-,-)$, correspond to the left- or right-handed supramolecular chirality.^{107,108}

1.4. Interpretation of chiroptical spectra

Reliable interpretation of the experimental data is essential for many applications. A few rules for the empirical correlation of VOA intensities and molecular structure are known today.¹⁰² Spectroscopic signatures of main structural motives (α -helix and β -sheet for proteins) as mentioned in the previous chapter have been revealed by the analysis of known structures.¹⁰⁹

A more general procedure is to analyze the experimental data using quantum-chemical predictions introduced in Chapter 2.^{110,111,112} Those are able to assign signals to appropriate vibrations and provide other stereochemical information. The absolute configuration or conformation is established by comparison of signs and relative intensities of bands in the measured and calculated VOA spectrum.¹¹³

Simulations of vibrational spectra are generally more reliable than those for electronic ones, because the calculations involve molecules in their ground electronic states. However, interpretation of VOA spectra of even small molecules by computations can be still complicated. The molecules are often very flexible (not stabilized by intramolecular non-covalent bonding) and their interaction with the solvent has a profound effect on the vibrational modes. Molecular flexibility can modify Raman/ROA and IR/VCD spectral intensities, band positions and, in an extreme case, the signs of ROA/VCD bands. In general, flexibility makes the VOA signal weaker and causes a large inhomogeneous broadening of the spectral bands. It has been shown that ROA spectra of rigid molecules show sharper bands and more ROA features than of flexible molecules.¹¹⁴

2. Molecular spectroscopic properties

Calculations have become an indispensable part of spectroscopic research. Simulated spectra can be used to confirm structural parameters, understand the vibrational nature of observed bands and give precious information on conformational dynamics. Methods of quantum chemistry are used in this thesis as well as molecular dynamics simulations with empirical force fields.

2.1. Methods for simulations of the spectra

2.1.1. Basics of quantum chemistry

Molecular systems are described by the Schrödinger equation (SE)¹¹⁵

$$i\hbar \frac{\partial \psi}{\partial t} = \hat{H}\psi, \quad (2.1)$$

where \hbar is the reduced Planck constant, $\psi = \psi(\mathbf{r}, \mathbf{R}, t)$ is the wave function for electrons and nuclei dependent on their positions \mathbf{r}, \mathbf{R} and time t , \hat{H} is molecular Hamiltonian. For the time-independent Hamiltonian, SE can be transformed to

$$\hat{H}\psi = E\psi, \quad (2.2)$$

where E is the energy. The Hamiltonian

$$\hat{H} = \hat{T}_n + \hat{T}_e + \hat{V}(\mathbf{r}, \mathbf{R}), \quad (2.3)$$

consists of the nuclear kinetic energy operator

$$\hat{T}_n = - \sum_A \frac{\hbar^2}{2M_A} \sum_A \nabla_A^2, \quad (2.4)$$

the electronic kinetic energy operator

$$\hat{T}_e = - \frac{\hbar^2}{2m_e} \sum_i \nabla_i^2, \quad (2.5)$$

and the potential

$$\hat{V}(\mathbf{r}, \mathbf{R}) = \frac{e^2}{4\pi\epsilon_0} \sum_A \sum_{B>A} \frac{Z_A Z_B}{R_{AB}} - \frac{e^2}{4\pi\epsilon_0} \sum_A \sum_i \frac{Z_A}{r_{Ai}} + \frac{e^2}{4\pi\epsilon_0} \sum_i \sum_{i>j} \frac{1}{r_{ij}}, \quad (2.6)$$

which is determined by the nucleus-nucleus (distances R_{AB}) and the electron-electron (distances r_{ij}) repulsion terms and the electrostatic attraction between electrons and nuclei (distances r_{Ai}). Indexes A, B indicate nuclei and i, j specify electrons, M_A and Z_A are nuclear masses and atomic numbers, m_e is the electron mass and e is the electron charge, ϵ_0 is the permittivity of the vacuum. The nuclear repulsion term, the first one in eq. 2.6, can be calculated most easily because it does not depend on coordinates of electrons.

The Born-Oppenheimer approximation (B–O) is considered necessary in quantum chemistry in order to practically solve the SE for a molecule. The B–O wave function is assumed as a product of the electronic and nuclear parts

$$\psi(\mathbf{r}, \mathbf{R}) = \psi_e(\mathbf{r}, \mathbf{R})\Phi_n(\mathbf{R}). \quad (2.7)$$

The electronic wave function ψ_e implicitly depends not only on the positions of electrons \mathbf{r} , but also on the positions of nuclei \mathbf{R} . The B–O approximation is based on the fact that atomic nuclei are much heavier (>1800 times) than electrons. Therefore, the electrons are moving faster in the field of “fixed” nuclei. SE can be separated into two:

one for electrons:

$$\hat{H}_e\psi_e(\mathbf{r}, \mathbf{R}) = [\hat{T}_e + \hat{V}(\mathbf{r}, \mathbf{R})]\psi_e(\mathbf{r}, \mathbf{R}) = \varepsilon(\mathbf{R})\psi_e(\mathbf{r}, \mathbf{R}) \quad (2.8)$$

and one for nuclei:

$$\left(\hat{T}_n + \varepsilon(\mathbf{R})\right)\Phi_n(\mathbf{R}) = E\Phi_n(\mathbf{R}). \quad (2.9)$$

Thus in the B–O approximation, the nuclei move on the multidimensional “potential energy surface” (PES) $\varepsilon(\mathbf{R})$ that is parametrically dependent on the coordinates of atomic nuclei \mathbf{R} . In the SE for nuclei (eq. 2.9), $\varepsilon(\mathbf{R})$ obtained by solving the electronic problem (eq. 2.8) serves as an effective potential. Many special mathematical routines and approximations are needed to solve the SE equation.

2.1.2. *Ab-initio* methods

The SE for electrons (eq. 2.8) can not be solved analytically for most multi-electron systems. Approximate solutions were proposed.¹¹⁶ The Hartree-Fock (HF) method is the simplest reasonable approach that enables to calculate the molecular energy as a function of nuclear positions. The N -electron wave function $\psi(\mathbf{r}, \mathbf{R})$ is assumed

in the form of antisymmetrized product of orthonormal one-electron spin orbitals, called the Slater determinant

$$\psi_e(\{x_i\}) = \frac{1}{\sqrt{N!}} \begin{vmatrix} \chi_1(\mathbf{x}_1) & \cdots & \chi_N(\mathbf{x}_1) \\ \vdots & \ddots & \vdots \\ \chi_1(\mathbf{x}_N) & \cdots & \chi_N(\mathbf{x}_N) \end{vmatrix}, \quad (2.10)$$

where $\chi(\mathbf{x}_i)$ is the spin-orbital of i -th electron defined as a product of a molecular orbital $\psi(\mathbf{r}_i)$ (MO) and a spin function $\sigma(s_i)$; \mathbf{x}_i is a generalized coordinate which includes a spatial (\mathbf{r}_i) and spin (s_i) coordinate.

Spin orbitals of the electronic ground state are found by applying the variational principle to minimize the energy $E[\psi_e^{HF}] = \langle \psi_e^{HF} | \hat{H} | \psi_e^{HF} \rangle$ and the condition of orthonormality of spin orbitals $\langle \psi_e^{HF} | \psi_e^{HF} \rangle = 1$. The HF approach leads to the set of N equations for N electrons. Simpler one-particle HF spin-orbitals ψ_i^{HF} are found together with orbital energies ε_i^{HF}

$$\hat{f}^{HF} \psi_i^{HF} = \left[-\frac{\hbar^2}{2m_e} \nabla^2 - \frac{e^2}{4\pi\epsilon_0} \sum_A \frac{Z_A}{r_{Ai}} + \sum_{j=1}^N (\hat{J}_j - \hat{K}_j) \right] \psi_i^{HF} = \varepsilon_i^{HF} \psi_i^{HF}, \quad (2.11)$$

where the Fock operator \hat{f}^{HF} consists of the electron kinetic energy term, the one-electron nuclear potential and two-electron Coulomb and exchange operators \hat{J}_j and \hat{K}_j .

The HF method can be characterized as a one-electron approximation for solving the general SE (eq. 2.8), since each electron is subjected to the mean field created by all other electrons. These equations are solved numerically by an expansion of the MOs into a set of k atomic orbitals ϕ_μ (AO) centered on atoms,

$$\psi(\mathbf{r}_i) = \sum_{\mu=1}^K C_{i\mu} \phi_\mu \quad i = 1, \dots, N, \quad N \leq K, \quad (2.12)$$

where $C_{\mu i}$ are expansion coefficients. This leads to the Roothan equations¹¹⁷

$$\sum_{\mu=1}^k F_{\nu\mu} C_{i\mu} = \varepsilon_i \sum_{\mu=1}^K S_{\nu\mu} C_{i\mu} \quad i = 1, \dots, N, \quad \nu = 1, \dots, K, \quad (2.13)$$

where $F_{\nu\mu} = \langle \phi_\nu | \hat{f} | \phi_\mu \rangle$ is the Fock matrix and $S_{\nu\mu} = \langle \phi_\nu | \phi_\mu \rangle$ is the overlap matrix. The HF solution is obtained iteratively using the self-consistent field (SCF) approach.

The usual form of AOs is based on real combinations of electron orbitals derived for hydrogen-like atoms, which are characterized by three quantum numbers n , l , m and formed by a product of angular part (spherical harmonic Y_{lm}) and radial part $R_{nl}(\mathbf{r}) = P_{nl}(\mathbf{r}) \exp(-\alpha_n r)$, where $P_{nl}(\mathbf{r})$ is the Laguerre polynomial and the exponential function describes Slater-type atomic orbitals (STOs). However, most quantum chemistry packages exploit Gaussian-type orbitals (GTOs) given by a linear combination of several Gaussian functions $\sum_v c_v \exp(-\alpha_v r^2)$ instead of STOs. The accuracy of the expansion in eq. 2.12 and consequently the HF method can be systematically improved by increasing the size and quality of the used basis set.

The Pople basis set 6-31G is assumed as a starting point. Each electron in the first shell is described by a contraction of 6 primitive Gaussian functions and each valence shell is split into the inner and outer part, expanded into three and one primitive Gaussian function, respectively. We usually used the 6-311++G** basis set¹¹⁸ with one more primitive Gaussian function for valence orbitals and extended by the polarization and diffuse functions as the most advanced and still computationally feasible basis set. Polarization functions (marked by *) give electrons the ability to respond to an electric field. The hydrogen and helium basis sets are enhanced by p basis functions and basis sets of first row atoms by d basis functions. The diffuse functions are important for anions and weakly bound complexes involving hydrogen bonding or cation-molecule interactions. A basis set with diffuse functions on heavy atoms and hydrogens is indicated by ++.

The applicability of the HF approach for quantitative predictions is limited due to the lack of the correlation energy

$$E^{corr} = E - E^{HF}, \quad (2.14)$$

where E is the exact Schrödinger ground-state energy and the HF ground-state energy E^{HF} is obtained as

$$E^{HF} = \sum_{i=1}^N \varepsilon_i^{HF} + \frac{1}{2} \sum_{i=1}^N \sum_{j=1}^N \langle \psi_i^{HF} | \hat{J}_j - \hat{K}_j | \psi_i^{HF} \rangle. \quad (2.15)$$

The HF approach serves as a starting point for more sophisticated correlated *ab-initio* methods such as Møller-Plesset perturbation theory (MP),¹¹⁹ configurational interaction (CI) and coupled clusters theory (CC).^{116,120}

In the MP approach, the system Hamiltonian is splitted into a part $\hat{H}^{(0)}$ of known exact solution (the HF reference) and a small perturbation $\lambda\hat{W}$

$$\hat{H} = \hat{H}^{(0)} + \lambda\hat{W}. \quad (2.16)$$

We suppose that the energy and wave functions depend on the parameter λ as

$$E = E^{(0)} + \lambda E^{(1)} + \lambda^2 E^{(2)} + \dots \quad (2.17)$$

$$|\psi\rangle = |\psi^{(0)}\rangle + \lambda|\psi^{(1)}\rangle + \lambda^2|\psi^{(2)}\rangle + \dots, \quad (2.18)$$

where $E^{(0)}$ is the energy of the unperturbed system and $\psi^{(0)}$ is its wave function. The higher energy terms that improve the HF energy are obtained from the time-independent SE (eq. 2.2), eq. 2.17 and eq. 2.18 as

$$E_n^{(1)} = \langle \psi_n^{(0)} | \hat{W} | \psi_n^{(0)} \rangle, \quad (2.19)$$

$$E_n^{(2)} = \sum_{n \neq m} \frac{|\langle \psi_n^{(0)} | \hat{W} | \psi_m^{(0)} \rangle|^2}{E_n^{(0)} - E_m^{(0)}}. \quad (2.20)$$

Depending on the order of the correction, the MP methods are named as MPx. Usually, the MP2 method represents an efficient tool for obtaining correlation energy, geometry or molecular properties.

The CI method uses for the wave function more variously configured Slater determinants. A limited number of occupied spin orbitals χ_i is replaced by virtual orbitals χ^a to form single, double, etc., excited determinants $\chi_{ijk\dots}^{abc\dots}$. The full CI includes infinite expansion and infinite basis set. Usually, the limited CI is used.

The coupled clusters method, especially its variant assuming only single, double and partially triple excitations of the reference wave function, CCSD(T), is considered as a computational method providing almost experimental accuracy for molecular properties.

While the time needed to calculate HF energies is $O(N^4)$, the computational requirements grow rapidly with the increasing level of approximation. The MP2 scales as $O(N^5)$ and often gives results similar to the CCSD scaling as $O(N^6)$. The full CI even exhibits an exponential scaling $O(e^N)$. The correlated *ab-initio* methods are therefore not often applicable to larger molecules.

2.1.3. Density functional theory

The density functional theory (DFT)^{121,122} represents an alternative to wave function-based *ab-initio* methods. DFT is currently the dominant quantum-chemical approach for spectroscopy of large molecules as it provides reasonably accurate calculations of geometry, force fields and intensities. The computational costs is usually comparable to the HF method ($O(N^3)$ - $O(N^4)$). However, the quality of results achieved by DFT is often much better than HF and corresponds to about MP2.

The idea of describing many-electron systems with one electron density

$$\rho(\mathbf{r}) = N \int \dots \int |\psi(\mathbf{r}_1, \mathbf{r}_2 \dots \mathbf{r}_N)|^2 d\mathbf{r}_2 \dots d\mathbf{r}_N \quad (2.21)$$

depending only on three spatial coordinates instead of electronic wave function $\psi_e(\mathbf{r}, \mathbf{R})$, originates in the works of Thomas,¹²³ Fermi,¹²⁴ and Dirac¹²⁵ from late 1920s. The electron density satisfies following conditions:

$$\int \rho(\mathbf{r}) d\mathbf{r} = N, \text{ where } N \text{ is the number of electrons,}$$

$$\rho(\mathbf{r}) \geq 0.$$

$$\text{In molecules } \rho(\mathbf{r}) \text{ exponentially decays for } \mathbf{r} \rightarrow \infty. \quad (2.22)$$

The accurate DFT theory applicable to molecular systems was developed in 1960s by Hohenberg, Kohn and Sham.^{126,127} The electron density $\rho(\mathbf{r})$ is according to the Hohenberg–Kohn theorem uniquely related to the one-electron potential $v(\mathbf{r})$. It can be determined according to the second Hohenberg–Kohn theorem by the variation of energy in the ground state

$$\frac{\delta E_g(\rho)}{\delta \rho} = 0. \quad (2.23)$$

The exact form of the ground state energy $E_g(\rho(\mathbf{r}))$ is unknown. Kohn and Sham proposed a reference system of non-interacting electrons, which generates the same density as the system of interacting particles, and formulated Kohn–Sham equations in a similar way as HF equations (eq. 2.11)

$$\hat{f}^{KS} \psi_i^{KS} = \left[-\frac{\hbar^2}{2m_e} \nabla^2 + v_{eff}(\mathbf{r}) \right] \psi_i^{KS} = \epsilon_i^{HF} \psi_i^{KS}. \quad (2.24)$$

Kohn–Sham equations correspond to a system of electrons moving in an effective potential

$$v_{eff}(\mathbf{r}) = \frac{1}{4\pi\epsilon_0} \int \frac{\rho(\mathbf{r}')}{|\mathbf{r} - \mathbf{r}'|} d\mathbf{r}' + v(\mathbf{r}) + v_{xc}(\mathbf{r}), \quad (2.25)$$

where the exchange-correlation functional is obtained as

$$v_{xc}(\mathbf{r}) = \frac{\delta E_{xc}}{\delta \rho}. \quad (2.26)$$

As the v_{eff} depends on the orbitals through the density, these equations need to be solved by the SCF approach. A large number of empirically developed DFT functionals have been proposed.⁴⁹ In the simplest case, the E_{xc} is a function of $\rho(\mathbf{r})$ (local spin density approximation),¹²⁷ or eventually of density derivatives (e.g. $\nabla\rho(\mathbf{r})$; generalized gradient approximation, GGA). A commonly used GGA functional is BPW91, which combines the exchange energy functional of Becke¹²⁸ and the correlation energy functional of Perdew and Wang.¹²⁹

The performance of GGA functionals may be improved by including the HF exchange into E_{xc} . Such hybrid functionals are B3PW91 and B3LYP.¹³⁰ The B3LYP functional contains three empirical parameters and consists of the HF exchange energy, the Becke exchange contribution¹²⁸ and the LYP correlation named after its authors, Lee, Yang and Parr.¹³¹ It is uniquely universal and it has been applied probably in all major fields of computational chemistry, providing acceptable results in most of the cases.

The construction of the DFT functionals is not straightforward and there is no systematic way how to improve them. They are usually “benchmarked” on a set of molecules to optimize selected parameters, e.g., the total electronic energy, thermodynamic quantities, electric dipole polarizability or NMR shielding. Therefore, DFT functionals need to be carefully tested.

Older semi-local or hybrid functionals are not able to describe long-range dispersion interactions.¹³² Their inclusion is extremely important for a correct description of many biomolecular systems. Grimme therefore proposed an empirical correction to DFT functionals¹³³

$$E_{disp}^{DFT-D} = -\frac{1}{2} \sum_{A \neq B} \sum_{n=6,8..} s_n \frac{C_n^{AB}}{R_{AB}^n} f_{damp}(R_{AB}), \quad (2.27)$$

where C_n^{AB} denote the averaged (isotropic) n -order dispersion coefficient for the atom pair AB in the R_{AB} distance. Global (functional dependent) scaling factors s_n are used for particular functional.¹³⁴ The damping function f_{damp} determines the short-range behavior of the dispersion correction and several expressions have been suggested.^{135,136} Such an approach with $n = 6$ and 8 is referred to as DFT-D3 in Gaussian09, rev.D¹³⁷ and Gaussian16.³¹ The addition of the dispersion forces to common DFT functionals significantly enhances their performance for systems with larger aromatic residues¹³⁸ in particular and also for cyclic dipeptides with tryptophan or tyrosin (publications [IV] , [III'] and [IV']) as it provides a better description of weak interactions.

In addition to DFT, there also exists its time-dependent variant, TD-DFT.^{139,140} It enables calculations of excited electronic states and can be used for modeling of UV and ECD spectra. The system is described by modified Kohn-Sham equations. The time dependence of electronic density is considered, i.e. electron density $\rho(\mathbf{r}, t)$ is a function of three space coordinates and time.

2.1.4. Harmonic approximation and anharmonic corrections

2.1.4.1 Nuclear motion and definition of normal modes

The starting point for prediction of molecular vibrational properties is usually the harmonic approximation. It enables to split the multidimensional SE for nuclei (eq. 2.9) into a set of independent one-dimensional problems with an analytic solution. A molecule with N nuclei (with $3N$ nuclear coordinates) in the lowest point on the potential energy surface (ground state, $\varepsilon_g(\mathbf{R})$) is considered. The Taylor expansion of $\varepsilon_g(\mathbf{R})$ around the equilibrium nuclear positions \mathbf{R}^0 is

$$\begin{aligned} \varepsilon_g(\mathbf{R}) = & \varepsilon_g(\mathbf{R}^0) + \sum_{J=1}^N \sum_{\alpha} \left. \frac{\partial \varepsilon_g(\mathbf{R})}{\partial \Delta R_{J,\alpha}} \right|_{\mathbf{R}=\mathbf{R}^0} \Delta R_{J,\alpha} \\ & + \frac{1}{2} \sum_{J,K=1}^N \sum_{\alpha} \sum_{\beta} \left. \frac{\partial^2 \varepsilon_g(\mathbf{R})}{\partial \Delta R_{J,\alpha} \partial \Delta R_{K,\beta}} \right|_{\mathbf{R}=\mathbf{R}^0} \Delta R_{J,\alpha} \Delta R_{K,\beta} + \dots, \end{aligned} \quad (2.28)$$

where the first term is a constant and can be eliminated by the appropriate choice of the zero energy level. Since \mathbf{R}^0 is at the minimum of the PES, the first derivatives in

the second term are equal to zero as well. The second derivatives in the third term are non-zero. They are also called the force field or force constants (Hessian matrix, FF)

$$F_{J,\alpha,K,\beta} = \frac{\partial^2 \varepsilon_g(\mathbf{R})}{\partial \Delta R_{J,\alpha} \partial \Delta R_{K,\beta}} \quad (2.29)$$

and define the harmonic nuclear motion. With $X_i = R_{J,\alpha}$, where α marks three Cartesian coordinates of every \mathbf{R} , the SE for nuclei (eq. 2.9) can be rewritten as

$$\hat{H}_{vib} \Phi_g(\mathbf{R}) = \sum_{j,k=1}^{3N} \frac{1}{2} \left[F_{jk} \Delta X_j \Delta X_k - \frac{\hbar^2}{M_j} \frac{\partial^2}{\partial \Delta X_j^2} \right] \Phi_g(\mathbf{R}) = E_g \Phi_g(\mathbf{R}). \quad (2.30)$$

This equation can be solved by a linear transformation of the Cartesian displacement coordinates into normal mode coordinates Q_i given by

$$Q_i = \sum_{j=1}^{3N} s_{ij}^{-1} \Delta X_j \sqrt{M_j} = \sum_{j=1}^{3N} S_{ij}^{-1} \Delta X_j, \quad (2.31)$$

where S_{ij} is called S-matrix. It satisfies the condition $\mathbf{S}^t \mathbf{S} = \mathbf{1}$ (the unit matrix). The transformed force field is diagonalized $\mathbf{S}^t \mathbf{F} \mathbf{S} = \mathbf{\Lambda}$, where $\mathbf{\Lambda}$ is a diagonal matrix containing squares of the normal mode frequencies ω_i ($\Lambda_{ij} = \omega_i^2 \delta_{ij}$). Then the resultant vibrational Hamiltonian does not contain any coupling between the normal mode coordinates. The splitting of the $3N$ -dimensional SE for nuclei leads to one-dimensional SEs

$$\left[-\frac{\hbar^2}{2} \frac{\partial^2}{\partial Q_i^2} + \frac{1}{2} \omega_i^2 Q_i^2 \right] \Phi_g(Q_i) = E \Phi_g(Q_i) \quad (2.32)$$

where $i = 1 \dots 3N$. The vibrational wave function is a product of $3N$ individual wave functions

$$\Phi_g(\mathbf{R}) = \prod_{i=1}^{3N} \Phi_g(Q_i) \quad (2.33)$$

In fact, for nonlinear molecules, six from the total of $3N$ eigenvalues ω_i are equal to zero, or, due to errors in electronic calculations, close to zero. These modes correspond to translational and rotational motions.

The solution of eq. 2.32 is equal to that of the linear harmonic oscillator (HO)

$$E_{i,n} = \left(\frac{1}{2} + n_i\right) \hbar\omega_i \quad (2.34)$$

$$\Phi_{n_i}(\xi) = A_{n_i} H_{n_i}(\xi) e^{-\frac{\xi^2}{2}}, \quad (2.35)$$

where $n_i = 0, 1 \dots$ is the quantum number of the normal mode coordinate Q_i , $\xi = \sqrt{\omega/\hbar}Q_i$, A_{n_i} is a normalization constant and H_{n_i} are normalized Hermite polynomials.¹⁴¹ The accuracy of vibrational frequencies and normal modes within the harmonic approximation is determined by the accuracy of computations of the FF.

2.1.4.2 Anharmonic corrections

The harmonic approximation is useful but often overestimates the frequencies (especially the hydrogen stretching vibrations). The harmonic oscillator potential with a parabolic shape of the potential well differs from the real one (**Fig. 2.1**).¹⁴² While the energy levels of the harmonic oscillator potential are evenly spaced by $\hbar\omega$, the real spacing decreases as the energy approaches to the dissociation limit. To get a more correct potential, higher-order terms of the Taylor expansion (eq. 2.28) may be included. The vibrational SE (eq. 2.9) is not separable then and evaluation of anharmonic energies is computationally very demanding.

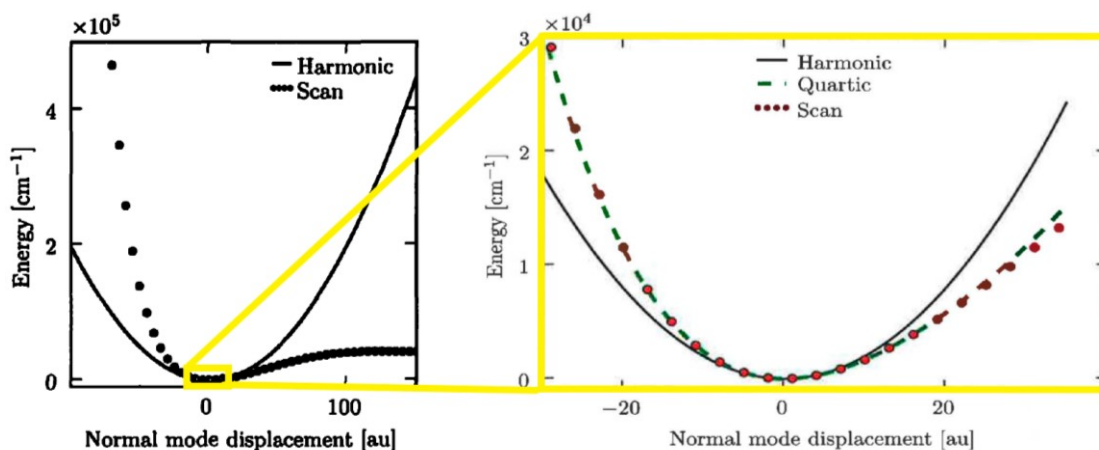


Fig. 2. 1: Left: comparison of the harmonic and exact (CCSD/cc-pVTZ scan) potential of the symmetric C-H stretching vibration of formaldehyde. Right: semidiagonal quartic terms V_{ijk}^{143} are added in the detail of the energy minimum. Redrawn from ¹⁴¹.

Various computational schemes,¹⁴¹ including vibrational self-consistent field (VSCF),^{144,145,146} vibrational configuration interaction (VCI),^{147,148,149} many-body perturbation theory (PT),^{150,151} contact transformation,¹⁵² and vibrational coupled cluster method,¹⁵³ can be used. Some of them are analogical to the electronic approaches discussed in Chapter 2.1.2. Two of these procedures (PT and limited VCI) implemented within the S4 program¹⁵⁴ were used in project [II] (Chapter 5.2). The anharmonic analysis via the PT and limited resonance approach is from 2017 available within the Gaussian16³¹ program for IR, Raman, VCD and ROA spectra.¹⁵⁵

2.2. Computational implementation

Calculations of spectra consist of several steps (**Fig. 2.2**). Firstly, a suitable geometry and the right absolute configuration are chosen (usually the X-ray or NMR structure). Molecular flexibility should be taken into account and many conformers averaged. The searching over the conformational space can be done in several ways, described in Chapter 2.2.1. The proper involvement of the solvent (especially strongly polar solvents generating hydrogen bonds, e.g. water) into calculations is discussed in Chapter 2.2.2.

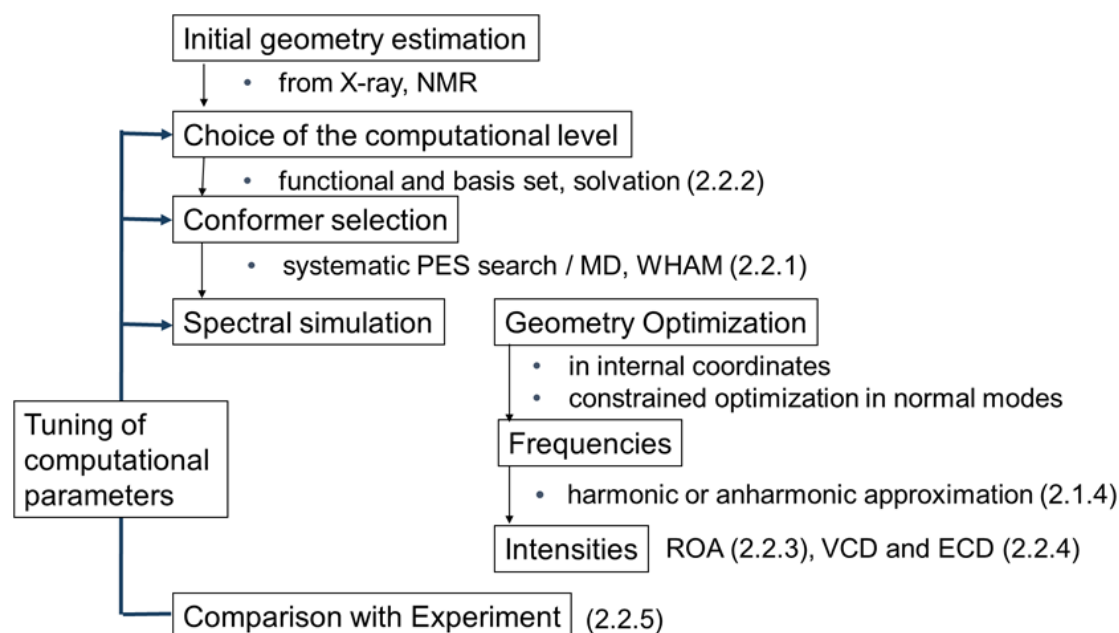


Fig. 2. 2: Typical steps required for calculations of chiroptical spectra.

The calculations of chiroptical spectra are implemented into many computer programs (e.g. Gaussian,^{31,156} Dalton,³² ADF³³ and CADPAC³⁴). In equilibrium, the gradient $\partial \varepsilon_g(\mathbf{R})/\partial \Delta R_{j,\alpha}$ is zero and the Hessian (eq. 2.29) has all eigenvalues positive. Vibrational simulations are done for the optimized molecular geometry and involve calculations of vibrational frequencies and spectral intensities. The frequency estimation is very computer memory and time consuming.

Derivatives of the energy needed for spectroscopic properties can be obtained by numerical differentiation, but an analytical scheme is usually preferred since it provides reliable results with a well-defined accuracy.¹⁵⁷ Theoretical aspects of calculations of ROA, VCD and ECD spectra are mentioned in Chapters 2.2.3 and 2.2.4. The choice of a functional and basis set is also discussed. The transfer of molecular properties tensors (CCTN)^{158,159} from smaller model molecules can be applied for larger molecules.^{160,161,162} Finally, the calculated spectra are compared with the measured ones and analyzed (Chapter 2.2.5).

2.2.1. Conformational search

Finding suitable geometry is always the first step in calculations of any molecular property. Most molecules are flexible and can exist in several conformations, which can have very different chiroptical properties. The total ROA spectrum is a weighted sum over individual conformers.¹¹⁴

2.2.1.1. Potential energy surface searching

The most energetically favored conformers can be identified by the PES scan, which is constructed in relevant molecular coordinates, such as dihedral angles. The “scanned” coordinates (usually in equidistant increments) are held constant during the molecular optimization at each PES point, while others can relax. The PES scan is a powerful tool especially for studies of small molecules with only a few relevant coordinates (used in publication [III], Chapter 5.3).

Contributions of individual conformers to the final spectrum are obtained using their Boltzmann weights, e.g. based on sum of the electronic and zero point energy.

Spectral curve S_j for j -th conformer with relative energy ΔE_j is multiplied by the Boltzmann factor

$$B_j = \frac{e^{-\frac{\Delta E_j}{kT}}}{\sum_j e^{-\frac{\Delta E_j}{kT}}}, \quad (2.36)$$

where k is the Boltzmann constant and T is temperature.

Nowadays plenty of programs exist (Spartan,¹⁶³ Conflex,¹⁶⁴ Hyperchem¹⁶⁵) that generate possible conformations via automated rotation of the atoms/groups around single bonds and optimize their energies using molecular mechanics force fields. For molecules containing rings, the conformational flexibility arises not only from rotation around single bonds but also from puckering of rings. The number of possible conformations grows rapidly for larger molecules and molecular dynamics simulations (MD) represent an efficient way of identifying the relevant conformations.

2.2.1.2. Molecular dynamics simulations

The MD method can be used not only to explore the molecular conformations,¹⁶⁶ but it can provide many solute-solvent configurations (snapshots). The simple averaging of 'snapshots' spectra is usually applied as the energy of conformers is reflected in their relative fractions. The molecule is allowed to explore all energetically favorable conformations in a sufficiently long MD simulation.

In MD simulations,¹⁶⁷ the system evolves in time according to the Newton equations of motions

$$\ddot{\mathbf{r}}_i = \frac{\mathbf{f}_i}{m_i}, i = 1..N, \quad (2.37)$$

where the forces \mathbf{f}_i acting on the atoms can be derived from an empirical potential $U(\mathbf{r})$ (**Fig. 2.3**)

$$\mathbf{f}_i = -\frac{\partial U(\mathbf{r})}{\partial \mathbf{r}_i}, \quad (2.38)$$

$$U = E^{intra} + E^{inter}. \quad (2.39)$$

The intramolecular (bonding) terms are the harmonic bond potential (the equilibrium distance is d_{0l}), harmonic bond angle potential around the equilibrium angle α_{0l} , out of plane deviations and torsion angles contributions

$$E^{intra} = \sum_{bonds,l} k_l (d_l - d_{0l})^2 + \sum_{angles,l} k_{\alpha l} (\alpha_l - \alpha_{0l})^2 + \sum_{oop,l} k_{oopl} s_l^2 + \sum_{torsions,l} [A_{1l} \cos(\tau_1) + A_{2l} \cos(2\tau_1) + A_{3l} \cos(3\tau_1)]. \quad (2.40)$$

The intermolecular (non-bonding) interactions include electrostatic, dispersion and repulsion terms (e.g., Lennard-Jones potential)

$$E^{inter} = \sum_{i,j=1,i<j}^N \frac{1}{4\pi\epsilon} \frac{q_i q_j}{r_{ij}} + \sum_{i,j=1,i<j}^N 4\epsilon_{ij} \left[\left(\frac{\sigma_{ij}}{r_{ij}} \right)^{12} - \left(\frac{\sigma_{ij}}{r_{ij}} \right)^6 \right]. \quad (2.41)$$

The parameters ($k_l, k_{\alpha l}, k_{oopl}, A_l, \epsilon_{ij}, \sigma_{ij}$) are optimized to reproduce target properties such as the enthalpy of solvation, the enthalpy of vaporization, dipole moment, spectroscopic data or electronic structure calculations. The set of these constants is also called the force field, similarly as the Hessian.

The equations of motion (eq. 2.37) can be solved numerically. The most common integration algorithm is the Verlet method.¹⁶⁸ The initial velocities and accelerations are set randomly according to the Maxwell-Boltzmann statistics for desired temperature.

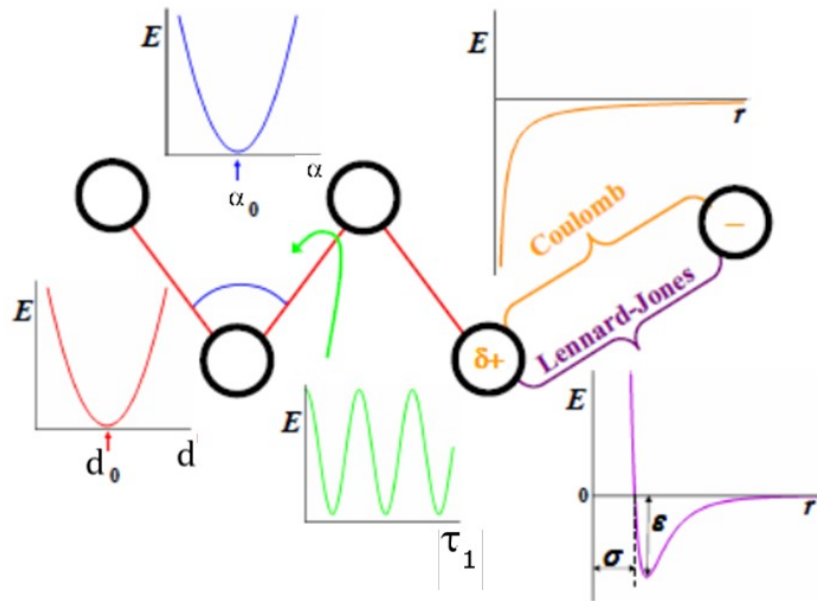


Figure 2.3: Intramolecular and intermolecular energy contributions described by molecular mechanics. Adapted from ¹⁶⁹.

Classical MD simulations may be employed to study systems containing thousands of atoms in times up to hundreds of nanoseconds, while computationally more demanding *ab-initio* MD is limited to much smaller systems and shorter times. Periodic boundary conditions (PBC) are applied in order to remove surface effects for a description of a condensed phase. The systems are usually studied at constant temperature and volume or pressure constrained by additional algorithms, i.e. using the NVT or NpT ensembles.

When converged results cannot be obtained in a limited simulation time, so called free energy methods can be applied. They enable better sampling of the molecular PES. The umbrella sampling method, in which the reaction coordinate is restrained with a biasing potential $V_i(\xi)$, usually in the harmonic form, was used in publication [IV] (Chapter 5.4) to obtain the profile of free energy along the reaction coordinate ξ

$$F(\xi) = -k_B T \ln P^b(\xi) - V(\xi) + A, \quad (2.42)$$

where k_B is the Boltzmann constant, T is temperature and $P^b(\xi)$ are the biased probability distributions, A is a constant.

The protocol consists of a series of simulations sampling different areas of the reaction coordinate or PES. From each simulation window, biased probability distributions are obtained as

$$P_i^b(\xi) = \frac{\int \delta[\xi'(R) - \xi] e^{-\beta[\varepsilon(R) + V_i(\xi(R))]} dR}{\int e^{-\beta[\varepsilon(R) + V_i(\xi(R))]} dR}, \quad (2.43)$$

where $\varepsilon(R)$ is the energy of the system. The weighted histogram analysis method (WHAM)^{170,171} is used to calculate the unbiased probability distribution $P^\mu(\xi)$ from a weighted average of unbiased probability distributions $P_i^\mu(\xi)$ over all windows

$$P^\mu(\xi) = \sum_{i=1}^n p_i(\xi) P_i^\mu(\xi), \quad \sum_{i=1}^n p_i(\xi) = 1. \quad (2.44)$$

The weights $p_i(\xi)$ are determined in order to minimize a statistical error made on the unbiased distribution as

$$p_i(\xi) = \frac{N_i e^{-\beta[V_i(\xi) - A_i]}}{\sum_{j=1}^n N_j e^{-\beta[V_j(\xi) - A_j]}}, \quad (2.45)$$

where A_i corresponds to an additional free energy coming from the bias potential $V_i(\xi)$ and satisfies the relation

$$e^{-\beta A_i} = \int P^\mu(\xi) e^{-\beta V_i(\xi)}, \quad (2.46)$$

The equations 2.44 - 2.46 are solved in an iterative way. An overlap between the neighboring biased probability distributions is required for the determination of these weights.

2.2.2. Solvent models

Chiroptical spectra reflect not only the molecular structure and conformation but also the dynamics and interactions with the solvent.¹⁷² An incomplete account of the solvent effects can cause large errors in simulated spectra and in the subsequent analysis of the experiment.^{173,42} When experimental data are obtained for samples in solution, the influence of the solvent on chiroptical properties can originate from different solvent-mediated processes, including dielectric effect, hydrogen bonding and aggregation of the solute molecules (e.g. dimer formation). The solvent can be implicitly treated in quantum-chemical computations as a continuous medium, or some solvent molecules can be added into computations “explicitly”.

Models of implicit solvation are usually successful in case of weakly interacting solute-solvent systems, such as carbon tetrachloride (CCl_4) or dichloromethane solutions. The conductor-like screening model (COSMO)¹⁷⁴ is based on the assumption that the solvent may be represented by a conductor. The polarizable continuum model (PCM)¹⁷⁵ represents the solvent by a polarizable medium characterized mainly by its dielectric constant. The cavity for the solute is formed by spheres centered on each atom and the surface of the cavity is divided into small regions (called tesserae) on which charges induced by the solute are evaluated. The conductor-like PCM (CPCM),^{176,177} an implementation of COSMO in the PCM framework, is used in all projects discussed in this thesis.

Polar solvents, such as DMSO or water, generate hydrogen bonds and strongly interact with the amide groups or polar side chains, which affects the solute's conformation, charge distribution and vibrational modes. Additionally, for some low-frequency modes, it is difficult to separate the solvent and solute spectral signal.¹⁷⁸

The use of a hybrid model (explicit solvent molecules for the first solvation shell and polarizable continuum model for the remaining part of the solvent) seems to be the best approach to simulate the solvent effects on the VOA spectrum.^{179,180,181} Electronic spectra are even more problematic since solvent orbitals may participate in solute electronic transitions.¹⁸² Such methods are computationally more demanding as many clusters need to be considered.

The clusters can be obtained ad hoc or generated from MD simulations (Chapter 2.2.1.2).¹⁸³ As they can be far from energy minima on the PES, their direct use for simulations of vibrational spectra would lead to a very large number of imaginary frequencies and unphysical artifacts in the simulated spectra. Therefore, the geometry optimization should be carried out prior to calculation of vibrational frequencies. The clusters can be treated in the layered quantum mechanics/molecular mechanics (QM/MM)^{184,185} approach, where the solute molecule is described by QM, explicit solvent molecules create the MM part, and the whole system can be enclosed in a CPCM cavity.

Another possibility is the normal mode optimization (NMO) technique, which was introduced to vibrational spectroscopy by Bouř and Keiderling in 2002.^{186,187} The NMO provides better numerical stability than the optimization in conventional redundant internal coordinates,¹⁸⁸ especially for weakly bonded molecular complexes with noncovalent interactions such as solvent–solute clusters. Spectroscopically important coordinates (stretching and bending) are allowed to relax without unnecessary geometry deformation, while low-frequency modes (mostly torsional and solvent molecules movement) are constrained. The dynamical information obtained for the clusters from MD is not lost (publication [I]).

2.2.3. Raman optical activity – theoretical aspects

Molecular theory of ROA was introduced by Prof. Barron with Prof. Atkins (University of Oxford, UK)¹⁸⁹ and further developed with Prof. Buckingham (University of Cambridge, UK).⁴¹ The following text represents just a short summary. Throughout this chapter Greek indices label Cartesian coordinates, Latin indices are used to number particles (nuclei, electrons), the Einstein summation convention is assumed for the Greek indices, $\delta_{\alpha\beta}$ is the Kronecker delta, and $\varepsilon_{\alpha\beta\gamma}$ is the Levi-Civita symbol.

In a “semiclassical” approach, the electromagnetic radiation is described classically, while molecules interacting with this radiation are described quantum mechanically. The oscillating electromagnetic field of the incident laser beam induces oscillating electric and magnetic multipoles in the molecules that are sources of the scattered light. Whereas the induced electric dipole is sufficient for the description of the Raman scattering, for ROA it is necessary to go beyond the dipole approximation and include also the magnetic dipole and electric quadrupole. These induced moments are defined as

electric dipole

$$\mu_{\alpha} = \alpha_{\alpha\beta} E_{\beta} + \frac{1}{\omega} G'_{\alpha\beta} \frac{\partial B_{\beta}}{\partial t} + \frac{1}{3} A_{\alpha,\beta\gamma} \nabla_{\beta} E_{\gamma} + \dots, \quad (2.47)$$

magnetic dipole

$$m_{\beta} = -\frac{1}{\omega} G'_{\alpha\beta} \dot{E}_{\alpha} + \dots, \quad (2.48)$$

electric quadrupole

$$\theta_{\beta\gamma} = A_{\alpha,\beta\gamma} E_{\alpha}, \quad (2.49)$$

where $\alpha_{\alpha\beta}$ is the electric-dipole–electric-dipole polarizability, $G'_{\alpha\beta}$ is the electric-dipole–magnetic-dipole polarizability, $A_{\alpha,\beta\gamma}$ is the electric-dipole–electric-quadrupole polarizability, and ω is the angular frequency of the incident laser beam.

Quantum-mechanical expressions for these three polarizability tensors can be found from the time-dependent perturbation theory of the second order in the far-from-resonance approximation,³⁹ assuming that the photon energy of the incident laser beam is far from any molecular transition energy. Then the transition polarizability tensors needed for computations of Raman/ROA spectra are⁴³

$$\alpha_{\alpha\beta} = \frac{2}{\hbar} \sum_{j \neq n} \frac{\omega_{jn}}{\omega_{jn}^2 - \omega^2} \text{Re}(\langle n | \hat{\mu}_{\alpha} | j \rangle \langle j | \hat{\mu}_{\beta} | n \rangle), \quad (2.50)$$

$$G'_{\alpha\beta} = -\frac{2}{\hbar} \sum_{j \neq n} \frac{\omega}{\omega_{jn}^2 - \omega^2} \text{Im}(\langle n | \hat{\mu}_{\alpha} | j \rangle \langle j | \hat{m}_{\beta} | n \rangle), \quad (2.51)$$

$$A_{\alpha,\beta\gamma} = \frac{2}{\hbar} \sum_{j \neq n} \frac{\omega_{jn}}{\omega_{jn}^2 - \omega^2} \text{Re}(\langle n | \hat{\mu}_{\alpha} | j \rangle \langle j | \hat{Q}_{\beta\gamma} | n \rangle), \quad (2.52)$$

where n , j and n' denote initial, excited and terminal state of a molecule, $\omega_{jn} = \omega_j - \omega_n$ is the angular frequency difference, $\hat{\mu}_\alpha$, \hat{m}_α and $\hat{Q}_{\alpha\beta}$ are operators of electric dipole, magnetic dipole and electric quadrupole moments defined as

$$\hat{\mu}_\alpha = \sum_i e_i r_{i\alpha}, \quad (2.53)$$

$$\hat{m}_\alpha = \sum_i \frac{e_i}{2m_i} \epsilon_{\alpha\beta\gamma} r_{i\beta} p_{i\gamma}, \quad (2.54)$$

$$\hat{Q}_{\alpha\beta} = \frac{1}{2} \sum_i e_i (3r_{i\alpha} r_{i\beta} - r_i^2 \delta_{\alpha\beta}), \quad (2.55)$$

where a particle i has the position vector r_i , charge e_i , mass m_i and momentum p_i .

The Placzek's approximation¹⁹⁰ may be employed for the evaluation of the polarizability tensors α , G' and A for fundamental vibrational transitions (from the $|0\rangle$ to the first excited state of p -th normal mode $|1_p\rangle$). The nuclear displacements are expressed in the normal mode coordinates Q_i (eq. 2.31). The quantities necessary for the determination of Raman and ROA intensity are

$$\alpha_i^2 = \frac{1}{9} \left(\frac{\partial \alpha_{\alpha\alpha}}{\partial Q_i} \right) \Big|_0 \left(\frac{\partial \alpha_{\beta\beta}}{\partial Q_i} \right) \Big|_0, \quad (2.56)$$

$$\beta(\alpha_i)^2 = \frac{1}{2} \left[3 \left(\frac{\partial \alpha_{\alpha\beta}}{\partial Q_i} \right) \Big|_0 \left(\frac{\partial \alpha_{\alpha\beta}}{\partial Q_i} \right) \Big|_0 - \left(\frac{\partial \alpha_{\alpha\alpha}}{\partial Q_i} \right) \Big|_0 \left(\frac{\partial \alpha_{\beta\beta}}{\partial Q_i} \right) \Big|_0 \right], \quad (2.57)$$

$$\alpha G_i' = \frac{1}{9} \left(\frac{\partial \alpha_{\alpha\alpha}}{\partial Q_i} \right) \Big|_0 \left(\frac{\partial G'_{\beta\beta}}{\partial Q_i} \right) \Big|_0, \quad (2.58)$$

$$\beta(G_i')^2 = \frac{1}{2} \left[3 \left(\frac{\partial \alpha_{\alpha\beta}}{\partial Q_i} \right) \Big|_0 \left(\frac{\partial G'_{\alpha\beta}}{\partial Q_i} \right) \Big|_0 - \left(\frac{\partial \alpha_{\alpha\alpha}}{\partial Q_i} \right) \Big|_0 \left(\frac{\partial G'_{\beta\beta}}{\partial Q_i} \right) \Big|_0 \right], \quad (2.59)$$

$$\beta(A_i)^2 = \frac{\omega}{2} \left[\left(\frac{\partial \alpha_{\alpha\beta}}{\partial Q_i} \right) \Big|_0 \left(\frac{\epsilon_{\alpha\gamma\delta} \partial A_{\gamma,\delta\beta}}{\partial Q_i} \right) \Big|_0 \right], \quad (2.60)$$

where Q_i is the normal mode of the i -th vibration. All derivatives are taken at the molecular equilibrium position, indicated by the subscript 0.

The Raman and ROA intensity terms¹⁹¹ can be expressed from these invariants as

$$I^{RAM} = I(R) + I(L) = 4K[D_1\alpha^2 + D_2\beta(\alpha)^2], \quad (2.61)$$

$$I^{ROA} = I(R) - I(L) = \frac{8K}{c}[D_3\alpha G' + D_4\beta(G')^2 + D_5\beta(A)^2], \quad (2.62)$$

where the coefficients D_{1-5} depend on both the scattering geometry and used modulation scheme.^{192,193}

The same result is obtained for the ICP and SCP scheme in the backscattering geometry,

$$\Delta(180^\circ) = \frac{I^{ROA}}{I^{RAM}} = \frac{24[\beta(G')^2 + 1/3\beta(A)^2]}{c[45\alpha^2 + 7\beta(\alpha)^2]}, \quad (2.63)$$

so these measurements are equivalent.

Relative Raman and ROA spectral $S(\omega)$ profiles are obtained by convoluting the calculated intensities I^{RAM} (eq. 2.61) and I^{ROA} (eq. 2.62) with Lorentzian bands with the bandwidth Δ and multiplying by a temperature-correction factor for $T = 298$ K, so that the spectrum from each mode i can be represented as

$$S(\omega) = I \left[1 - \exp\left(-\frac{\omega_i}{kT}\right) \right]^{-1} \frac{1}{\omega_i} \left[4 \left(\frac{\omega - \omega_i}{\Delta} \right)^2 + 1 \right]^{-1}, \quad (2.64)$$

where k is the Boltzmann constant, ω is the frequency of the incident laser beam and ω_i is the vibrational frequency. Since absolute Raman and ROA intensities are usually not measured experimentally, the computed spectra are adjusted by one scaling factor.

Calculations of the $\alpha_{\alpha\beta}$, $G'_{\alpha\beta}$ and $A_{\alpha,\beta\gamma}$ tensor derivatives needed in eq. 2.56 - 2.60 are very demanding as these are third-order energy derivatives.¹⁹⁴ The first ROA spectrum calculated *ab-initio* (methylthiirane, HF, 6-31G* basis set) appeared in 1989^{195,196} in the static limit of the $\frac{1}{\omega}G'(\omega)$ tensor.¹⁹⁷ The implementation of ROA calculations within DFT via the response theory,¹⁹⁸ leading to a large improvement in accuracy, was done by Ruud in 2002¹⁹⁹ (methyloxirane, α -pinene and trans-pinane using the B3LYP functional with the 6-31G,²⁰⁰ 6-31G** and (aug)-cc-pVDZ^{201,202} basis sets).

Originally, the tensors derivatives were obtained by expensive numerical differentiation using Cartesian displacements of the nuclei, followed by transformation to the normal coordinates according to eq. 2.31.¹⁹⁵ Fully analytical implementation

appeared relatively recently. The early protocol, originated in 2007,²⁰³ used an analytical time-dependent HF algorithm for calculations of the derivatives of the $G'_{\alpha\beta}$ tensor. An analytical derivative “two-step” procedure ($n + 1$ algorithm) was described by Ruud and Thorvaldsen¹⁹⁴ and implemented into the Gaussian09 by Cheeseman and coworkers.²⁰⁴ Frequency dependent ROA and Raman tensors are computed using magnetic field dependent basis functions (gauge-including atomic orbitals GIAOs, also called London atomic orbitals).^{205,206} The GIAOs orbitals are obtained by multiplying each atomic basis function by a magnetic field-dependent phase factor

$$\phi_{\lambda}^{GIAO}(\mathbf{r}) = \exp\left[-i\frac{e}{\hbar}\mathbf{A}_{\lambda}\cdot\mathbf{r}\right]\phi_{\lambda}(\mathbf{r}), \quad (2.65)$$

where the vector potential $\mathbf{A}_{\lambda} = \mathbf{B} \times \mathbf{R}_{\lambda}/2$ is located at nucleus λ . The introduction of GIAOs solved the problem that theoretical calculations were origin dependent (because of the $G'_{\alpha\beta}$ tensor) in finite basis sets.²⁰⁷

Addition of diffuse functions into calculations of ROA spectra can significantly improve predicted spectra^{208,209} as the electrons far from nuclei considerably affect molecular vibrations. The Pople double- ζ basis set 6-311++G** can be considered as a convenient choice.¹¹⁸ More accurate results (at much higher cost) can be achieved with the aug-cc-pVTZ^{201,202} basis set. Minimalistic basis set rDPS²¹⁰ is the 3-21++G basis set with a semidiffuse p function (exponent 0.2) on hydrogen atoms. It provides ROA intensity differences close to those obtained using the larger diffuse augmented triple- ζ basis set aug-cc-pVDZ. It is recommended for calculations of larger molecules.²¹¹ In addition, the ROA tensor invariants can be computed in the “two-step” procedure at a different level of theory than the geometry optimization and force field calculations. The combination of aug(sp)-cc-pVDZ for the ROA tensor invariant and cc-pVTZ for the force field calculations was suggested for intermediate sized system and the rDPS//6-31G* combination for large systems.²¹²

The performance of DFT functionals was also tested.^{211,213} The B3LYP functional is widely used in recent computational ROA studies as it provides a well-balanced model between accuracy and cost. Also the B3PW91 functional performs well as shown by Daněček et al.²¹⁴ in a study where the alanine and proline Raman and ROA spectra simulated with 25 different DFT functionals are compared to the experiment, to explore limits of the harmonic approach.

2.2.4. Circular dichroism – theoretical aspects

Both electronic and vibrational circular dichroism spectroscopy (**Fig. 1.3**) obeys the same basic relations. The theoretical description of CD includes subtraction of the transitions probabilities induced by LCP and RCP radiation. The interaction Hamiltonian describes electromagnetic perturbation of a molecule exposed to uniform electric and magnetic fields (\mathbf{E} and \mathbf{B} , respectively)

$$\mathbf{H}^{int} = -\hat{\mu} \cdot \mathbf{E} - \hat{m} \cdot \mathbf{B} + \text{higher orders}, \quad (2.66)$$

where $\hat{\mu}$ and \hat{m} are operators of the electric and magnetic dipole moments of the molecule defined in eq. 2.53 and eq. 2.54, respectively.

The Rosenfeld relation²¹⁵ was derived in 1928 for isotropic samples. It determines the relation between the structure of a molecule and its interaction with CP radiation. The rotatory strength for a transition between molecular states n and j is defined as

$$R_{jn} = \text{Im}[\langle n | \hat{\mu} | j \rangle \cdot \langle j | \hat{m} | n \rangle], \quad (2.67)$$

where $\langle n | \hat{\mu} | j \rangle$ is the electric and $\langle j | \hat{m} | n \rangle$ is the magnetic dipole transition moment. The scalar product in eq. 2.67 can be either positive or negative, depending on the relative orientation of the transition moments. The rotatory strength R is related to the CD intensity $\Delta\varepsilon$ (eq. 1.5)

$$R = k_R \int_{CD\text{band}} \frac{\Delta\varepsilon(\lambda)}{\lambda} d\lambda, \quad (2.68)$$

where

$$k_R = \frac{3 \ln 10 c^2 \varepsilon_0 \hbar}{4\pi N_A} = 7.659 \times 10^{-54}$$

in SI units. c is the speed of light, ε_0 is the permittivity of vacuum, \hbar is the reduced Planck constant and N_A is Avogadro's number.¹⁸

The dipole strength of the $j \rightarrow n$ transition is defined as

$$D_{jn} = \text{Re}(\langle n | \hat{\mu} | j \rangle \cdot \langle j | \hat{\mu} | n \rangle), \quad (2.69)$$

and is always positive. It is related to the integral (area) of an absorption band

$$D = k_D \int_{ABS\text{band}} \frac{\varepsilon(\lambda)}{\lambda} d\lambda; \quad k_D = \frac{3 \ln 10 c \varepsilon_0 \hbar}{\pi N_A} = 1.022 \times 10^{-61}. \quad (2.70)$$

For VCD, which refers to molecules in their well-defined electronic ground states, the transition moments in eq. 2.67 and eq. 2.69 involve vibrational wave functions instead of electronic ones. The evaluation of the vibrational rotatory strength was found to be less straightforward than for the electronic rotatory strength, since the electronic contribution to the magnetic dipole moment vanishes for a vibrational transition in the B–O approximation. Rigorous theoretical calculations of the VCD spectra of chiral molecules become feasible after development of the magnetic field perturbation (MFP)²¹⁶ formalism by Prof. Stephens (University of Southern California, USA) and its first analytical implementation in CADPAC by Amos.²¹⁷ An alternate method is based on the vibronic coupling theory²¹⁸ and similarly as MFP describes perturbation of the ground electronic state wave function by a magnetic field. The electronic part of the magnetic moment is obtained as the first-order correction to the B–O wavefunction.

When the electronic part of the transition dipole moment is expressed in normal modes coordinates and expanded into Taylor series

$$\mu_e(Q_1 \dots Q_M) = \mu_e(0) + \sum_i \left(\frac{\partial \mu_e}{\partial Q_i} \right)_0 Q_i + \frac{1}{2} \sum_i \sum_j \left(\frac{\partial^2 \mu_e}{\partial Q_i \partial Q_j} \right)_0 Q_i Q_j + \dots, \quad (2.71)$$

the atomic polar tensor (APT) can be defined as

$$P_i^\lambda = \left(\frac{\partial \mu_e}{\partial Q_i} \right)_0, \quad (2.72)$$

where the partial derivative is taken in the equilibrium geometry 0.

The magnetic transition dipole moment can also be expanded in Taylor series with respect to nuclear momenta and the atomic axial tensor (AAT) is obtained as

$$M_i^\lambda = \left(\frac{\partial m_e}{\partial p_i} \right)_0, \quad (2.73)$$

where the partial derivative according to the momentum p_i instead of the normal mode coordinate Q_i is also taken in the equilibrium geometry 0 and zero velocity.

Then the vibrational rotatory strength (eq. 2.67) of a fundamental transition of the i -th normal mode can be obtained as

$$R_i = \hbar^2 \text{Im} [P_i \cdot M_i], \quad (2.74)$$

where $P_{i\beta} = \sum_{\lambda} \sum_{\alpha} P_{\alpha\beta}^{\lambda} S_{\lambda\alpha,i}$, $M_{i\beta} = \sum_{\lambda} \sum_{\alpha} M_{\alpha\beta}^{\lambda} S_{\lambda\alpha,i}$. The matrix $S_{\lambda\alpha,i}$ transforms normal mode coordinates Q_i into Cartesian coordinates, λ is the nucleus number, and α and β are Cartesian coordinates. The AAT tensor generally depends on the choice of coordinate system origin, which brings another difficulty to practical calculations of VCD intensities.²¹⁹ This has been solved by implementing the gauge-independent atomic orbitals (GIAOs, eq. 2.65).²²⁰ Current VCD calculations usually involve the MFP formalism, DFT with hybrid functionals like B3LYP or B3PW91 and a GIAO basis set at the minimal level of 6-31G*.

For ECD, the same relations for the rotatory strength and the dipole strength are obtained as for VCD (eq. 2.67 and eq. 2.69), but ECD requires rather extensive computations of excited electronic states. First calculations of rotatory strengths based on the general linear response formalism appeared in 1995.²²¹ TD-DFT implementations for ECD and also ORD have been presented by a number of groups,^{222,223,224,225} The TD-DFT equations lead to diagonalization of large matrices, usually solved by the Davidson iterative schemes. The B3LYP functional was found to be reliable also for ECD computations. Another option is CAM-B3LYP functional, adapted for asymptotic behavior of the wave function. Larger basis sets than for VCD are usually needed, e. g. 6-31++G** provides satisfactory results.

2.2.5. Comparison of calculated and experimental spectra

Visual comparison of the simulated and experimental spectra is by far the most frequent approach, especially for smaller molecules with spectra composed of a few well-resolved bands. However, for larger molecules with many conformers, or molecules with multiple stereocenters, accurate visual judgement of the agreement may be difficult. VCD and ROA and sometimes also ECD spectra contain several overlapping spectral bands. Therefore correlations between observed and simulated spectral bands can be biased by personal judgments.

Quite often, the band positions in the calculated and experimental spectra do not match. Errors appearing in the harmonic calculations are largely systematic. Different scaling factors for vibrational frequencies obtained at different quantum-chemical models have been proposed. The method may be remarkably successful.⁷⁶ The frequency scaling factors do not modify normal mode compositions or vibrational

intensities much. However, they enter in the thermodynamic quantities that depend on vibrational frequencies.

Sometimes, a linear transformation of the vibrational frequencies

$$\omega' = a\omega + b \quad (2.75)$$

is applied to maximize the normalized overlap S_{fg} ²²⁶ between calculated $f(\omega')$ and experimental spectra $g(\omega)$ ^{227,228}

$$S_{fg} = \frac{\int f(\omega')g(\omega)d\omega}{\sqrt{\int f^2(\omega')d\omega \int g^2(\omega)d\omega}}. \quad (2.76)$$

S_{fg} can be adapted as a measure of similarity of the experimental and computed spectra. For identical spectra, the spectral overlap integral is equal to 1. For spectra with positive values only (UV, IR, Raman), the overlap integral approaches 0 when the spectra are different. For spectra with positive and negative bands (ECD, VCD and ROA), the overlap can be either positive or negative (the overlap S_{fg} is equal to -1 , when the spectra are opposite). Overlaps over regions, in which the calculated and measured VOA spectra have the same sign, can be defined as

$$S_{fg}^{++} = \frac{\int_{f,g>0} f(\omega')g(\omega)d\omega}{\sqrt{\int_{f,g>0} f^2(\omega')d\omega \int_{f,g>0} g^2(\omega')d\omega}}$$

and

$$S_{fg}^{--} = \frac{\int_{f,g<0} f(\omega')g(\omega)d\omega}{\sqrt{\int_{f,g<0} f^2(\omega')d\omega \int_{f,g<0} g^2(\omega')d\omega}}. \quad (2.77)$$

The enantiomeric similarity index (ESI)²²⁹ provides a discrimination between a chiral molecule and its enantiomer and can be defined as

$$\Delta = |\Sigma_{fg} - \Sigma_{\bar{f}\bar{g}}|, \quad (2.78)$$

where $\Sigma_{fg} = \frac{\Phi^{++}S_{fg}^{++} + \Phi^{--}S_{fg}^{--}}{\Phi^{++} + \Phi^{--}}$ is a single similarity index

and $\Sigma_{\bar{f}g} = \frac{\Phi^{-+}S_{fg}^{-+} + \Phi^{+-}S_{fg}^{+-}}{\Phi^{-+} + \Phi^{+-}}$ is a single similarity index for the opposite enantiomer. The weight factors Φ^{++} , Φ^{--} , Φ^{-+} and Φ^{+-} are the sums of the measured and calculated VOA intensity of a given sign

$$\Phi^{+-} = \int_{f>0} f(\omega) d\omega + \left| \int_{g<0} g(\omega) d\omega \right|, \text{ etc.} \quad (2.79)$$

ESI is limited to the interval of 0 to 1 and a high ESI value indicates a better agreement with the experimentally measured spectrum. The dimensionless anisotropy ratio g (eq. 1.6) or CID (Δ , eq. 1.2) can be used with advantage for the similarity, instead of individually VCD and IR (or ROA and Raman) spectra.²³⁰

In IR and VCD spectra, integrated band areas determine the calculated dipole (eq. 2.70) and rotational strength (eq. 2.68), respectively.²²⁰ But the bands have to be resolved one by one. Overlapping bands can lead to uncertainties.

A decomposition of experimental into simulated spectra of individual conformers can provide conformer populations,^{231,232}

$$S_{exp}(\omega) = \sum_i c_i S_i(\omega), \quad (2.80)$$

where $c_i \geq 0$ and $\sum_i c_i = 1$. The coefficients c_i are obtained by minimizing of the difference function

$$\delta = \int_{\omega_{min}}^{\omega_{max}} d\omega [S_{exp}(\omega) - \sum_i c_i S_i(\omega)]^2, \quad (2.81)$$

e.g. by scanning the (c_1, c_2, \dots, c_n) coefficient space within the used spectral range $(\omega_{min}, \omega_{max})$. Unlike usual minimization methods (Lagrange multipliers, singular value decomposition), the direct scanning allows to satisfy the conditions imposed on c_i in eq. 2.80 without any additional penalty functions. The smoothness of the coefficient space and uniqueness of the solution can be estimated easily.²³³

3. Objectives of the thesis

Effects influencing the accuracy of VOA spectra computed by DFT were investigated in this work. We concentrated on small molecules enabling precise calculations in four separate projects:

I.

A combined explicit/implicit solvation model, in which a “cluster” (a few solvent molecules around the solute) is embedded in a polarizable continuum, appears indispensable for an adequate description of vibrational frequencies of molecules with polar groups. Raman and ROA spectra are often significantly improved.¹⁸³ We investigated the normal mode geometry optimization method¹⁸⁶ applicable for a partial optimization of such clusters. A suitable frequency limit providing realistic vibrational band broadening was found (Chapter 5.1).

II.

Most organic compounds provide vibrational spectra in the C-H stretching region ($\sim 2500\text{--}3400\text{ cm}^{-1}$), which is well-separated from other molecular vibrations. The C-H stretching vibrations are sensitive to molecular stereochemistry,^{75,234} and also to intermolecular interactions,²³⁵ because molecular surface is mostly formed by C-H groups. So far, the C-H stretching signal is only rarely used for structural studies due to multiple difficulties in experiment and modelling.^{151, 214, 236-238} ROA and VCD spectra are often weak and prone to artifacts in this region ($\Delta \sim 5 \times 10^{-5}$, i.e. close to the measurement limit). The extension of the ROA measurements up to 3500 cm^{-1} became possible due to rather recent innovation of the home-built ROA instrument at Institute of Physics of Charles University.³⁷

The interpretation of spectra is complicated by the anharmonicity of the potential energy surface of the C-H stretching motion and overlapping of many C-H vibrational bands due to similar strength of different C-H groups in a molecule. The error of the harmonic C-H stretching frequencies from experimental values can reach up to 150 cm^{-1} .^{239,237} Therefore, we explored how current computational methods are able to simulate the VOA spectra in the C-H stretching region and estimated the benefits of the anharmonic corrections for terpene molecules (Chapter 5.2).

III.

The tryptophan residue in chiral matrices often exhibits a large optical activity and provides valuable information about the peptide structure. We were interested in the interaction of the tryptophan residue with the backbone and other side chain parts of cyclic dipeptides, as such effects are crucial for developing of ROA and ECD spectroscopic responses. We wanted to demonstrate the role of the dispersion forces and different organic solvents for conformer equilibria and dynamics. The structural information could be obtained, when chiroptical spectroscopies were supported by the theoretical modelling (Chapter 5.3).

IV.

The lanthanide-tagged proteins and peptides are increasingly used for investigating structure, function and dynamics of proteins and other biomolecules.⁵⁶ However, the actual lanthanide-peptide interaction and its effect on lanthanide spectroscopic properties are not fully understood. The europium (Eu) binding to proteins is believed to be enhanced by the presence of histidine (His), but the strength of the interaction significantly varies across different systems (length of peptides, pH and position of His residue in a peptide sequence). Therefore we studied the $[\text{Eu}(\text{DPA})_3]^{-3}$ complex interacting with a series of histidine-containing peptides. CPL spectra were measured by a relatively new „ROA/CPL“ methodology.⁵⁷ We rationalized the data by calculations of the binding strength with the aid of MD simulations (Chapter 5.4).

4. Computational and experimental methods

This chapter provides detailed description of DFT and MD computations (Chapter 4.1), model systems (Chapter 4.2), used chiroptical instruments (ROA, VCD and ECD) and the measurements (Chapter 4.3).

4.1. Computational methods

The Gaussian09 program¹⁵⁶ was used for DFT calculations. The B3LYP¹³⁰ functional and 6-311++G** basis set was often employed as it was found to provide a reasonable agreement with experiment. Harmonic IR, VCD, Raman and ROA intensities were usually computed at the same level of theory as optimized structures. Excitation frequency of 532 nm was used for backscattered Raman and ROA dynamic polarizabilities. The effect of solvent was included in all calculations by the implicit solvation model CPCM. Final vibrational and electronic spectral profiles were simulated at 298 K using the Lorentzian bands with the bandwidth $\Delta \sim 10 \text{ cm}^{-1}$ (eq. 2.64) and Gaussian bands of 15 nm bandwidth (for ECD) as default. The dipole and rotational strengths for ECD spectra in publication [III] were calculated by the TD-DFT method. MD simulations in publications [III] and [IV] were performed by the Amber program package.^{240,241}

4.1.1. Normal mode geometry optimization method

The lactamide (**Fig. 4.1**) was chosen in project [I] as a small, flexible and strongly hydrated compound to investigate the role of the aqueous environment on the Raman and ROA spectra.

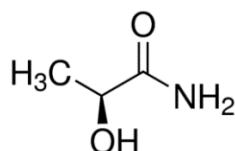


Fig. 4.1: (S)-lactamide studied in publication [I].

100 clusters containing (S)-lactamide and 3-9 hydrogen-bonded waters from the first hydration shell (closer than 3.6 Å to a lactamide atom) were selected as snapshots from a 48 ps Car-Parrinello MD (CPMD)²⁴² simulation that provided results superior to classical MD.¹⁸³ The NMO method introduced in Chapter 2.2.2 and implemented as the Fortran program QGRAD²⁴³ interfaced to Gaussian, was used for the partial optimization of these cluster geometries.

The NMO method is based on the harmonic approximation in the vicinity of an energy minimum (chapter 2.1.4.1). The normal modes coordinates Q_i are obtained from Cartesian displacement coordinations ΔX_j via a linear transformation determined by the **S**-matrix (eq. 2.31). The NMO algorithm consists of the following steps. Firstly, the initial force field $\mathbf{F}^{(i)}$ (eq. 2.29) is estimated and the **S**-matrix is obtained. Then the Cartesian gradient $\mathbf{g}_c^{(i)}$ is calculated. In the case that the previous step is available, Hessian **F** is updated using the Broyden-Fletcher-Goldfarb-Shann formula²⁴⁴⁻²⁴⁷

$$\mathbf{F}^{(i+1)} = \mathbf{F}^{(i)} - \left(\frac{\Delta \mathbf{g}^{(i)t} \Delta \mathbf{g}^{(i)}}{\mathbf{dX}^{(i)} \cdot \Delta \mathbf{g}^{(i)}} + \frac{(\mathbf{F}^{(i)} \cdot \mathbf{dX}^{(i)t}) \mathbf{dX}^{(i)} \cdot \mathbf{F}^{(i)}}{\mathbf{dX}^{(i)} \cdot \mathbf{F}^{(i)} \cdot \mathbf{dX}^{(i)}} \right), \quad (4.1)$$

where Cartesian displacements $\mathbf{dX}^{(i)} = \mathbf{X}^{(i)} - \mathbf{X}^{(i-1)}$ and the gradient differences $\Delta \mathbf{g}^{(i)} = \mathbf{g}_c^{(i)} - \mathbf{g}_c^{(i-1)}$. The actual optimization is performed in normal modes, using the rational function optimization updating.²⁴⁸⁻²⁵² New normal mode displacements are

$$\mathbf{dQ}^{(i+1)} = - \frac{2\mathbf{g}^{(i)}}{\Lambda_{ii} + \sqrt{\Lambda_{ii}^2 + 4(\mathbf{g}^{(i)})^2}}, \quad (4.2)$$

where Λ is a diagonal matrix ($\Lambda_{ij} = \omega_i^2 \delta_{ij}$) containing the second derivatives of energy at optimization point i . The updated Cartesian coordinates may be obtained as $\mathbf{X}^{(i+1)} = \mathbf{X}^{(i)} - \mathbf{SdQ}^{(i+1)}$. The new Cartesian gradient $\mathbf{g}_c^{(i+1)}$ is computed then and the optimization procedure is repeated until convergence.

This scheme enables a full optimization of the system. In the restricted NMO adapted in this work, modes with frequencies $\omega_i \in (\omega_{min}, \omega_{max})$ are kept constant ($\mathbf{dQ}_i = 0$). A lower limit $\omega_{min} = 300i \text{ cm}^{-1}$ (imaginary, often treated as negative in computer codes) was introduced to allow a relaxation of large imaginary frequencies occasionally exhibited by some CPMD geometries. Seven values of ω_{max} (10, 20, 50,

100, 200, 300 and 600 cm^{-1}) were applied. In addition, raw non-optimized CPMD snapshots corresponding to infinite ω_{max} were studied.

Raman and ROA spectra were calculated and the water signal (corresponding polarizability derivatives) was deleted for the $8 \times 100 = 800$ optimized and raw geometries. Smoother spectra were generated by summing the 100 cluster signals and performing a convolution (eq. 2.64) with Lorentzian bands 2 cm^{-1} wide, which were much narrower than the inhomogeneous broadening. All computations were performed at the B3LYP/6-311++G** level of theory, using the CPCM model to simulate the effect of the more distant waters, not explicitly included in the computations.

4.1.2. Harmonic and anharmonic calculations for terpenes

In publication [II], the Raman, ROA, IR and VCD spectra of α -pinene, fenchone and camphor (Fig. 4.2) were calculated within the harmonic approximation in order to investigate various factors that can influence the quality of the computed force fields. Various DFT functionals (B2PLYP, B3LYP,¹³⁰ BPW91, B3PW91,²⁵³ CAM-B3LYP,²⁵⁴ dispersion-corrected variants^{135, 255} B3LYP-D, B3PW91-D), HF, MP2¹¹⁹ and hybrid electronic approaches (mPW2PLYP²⁵⁵ and mPW2PLYP-D) were tested for (1R)-(-)-fenchone. Different basis sets (6-31G, D95, 6-31G*, TZV, 6-31+G*, 6-31G**, D95**, TZVP, 6-31++G**, D95+**, 6-311++G**, cc-pVTZ and aug-cc-pVTZ) were also tested.

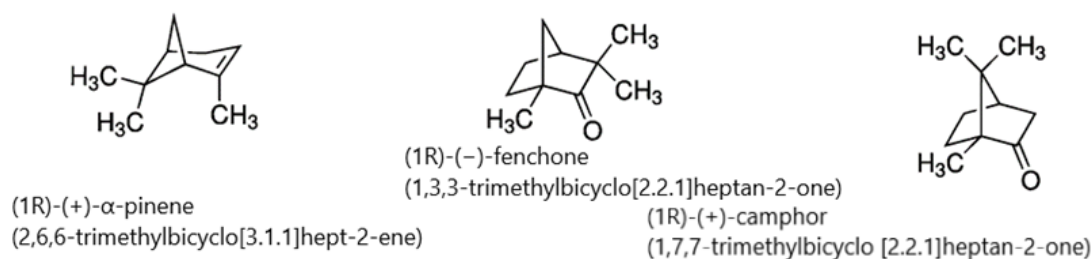


Fig. 4.2: Studied molecules of terpenes: (1R)-(+)- α -pinene, (1R)-(-)-fenchone and (1R)-(+)-camphor.

The solvent influence was estimated for (1R)-(+)-camphor at the B3LYP/6-311++G** level. Nine different solvents of a broad scale of relative dielectric constants ϵ_r were used in the CPCM dielectric model.²⁵⁶ The experimental

conditions were mimicked by $\epsilon_r = 2.23$ (camphor solution in CCl_4), $\epsilon_r = 2.69$ (neat α -pinene, using Gaussian parameters for pentanoic acid) and $\epsilon_r = 12.51$ (neat fenchone, using Gaussian parameters for 1-hexanol).

In order to add anharmonic corrections to vibrational energies and spectral intensities, a limited Taylor expansion (up to the fourth order) of the vibrational potential was used, where the anharmonic part was given as

$$W(Q_1 \dots Q_M) = \frac{1}{6} \sum_{i=1}^M \sum_{j=1}^M \sum_{k=1}^M c_{ijk} Q_i Q_j Q_k + \frac{1}{24} \sum_{i=1}^M \sum_{j=1}^M \sum_{k=1}^M \sum_{l=1}^M d_{ijkl} Q_i Q_j Q_k Q_l, \quad (4.3)$$

All cubic c_{ijk} and semidiagonal quartic constants d_{ijkl} were obtained by a two-step numerical differentiation of the second energy derivatives. The differentiation was performed in dimensionless²⁵⁷ normal mode coordinates q_i with a step of $\Delta q_i = \Delta Q_i \times 1000 / \omega_i$, where $\Delta Q_i = 0.05$ atomic units, and the harmonic frequency ω_i is in cm^{-1} . The variable step size prevents too small displacements for the lowest-frequency modes.²⁵⁸

The mPW2PLYP/CPCM/6-311++G** method was used for the force field, which allows for both the harmonic and anharmonic force field term calculations in a reasonable time in a consistent way. As computations of the ROA intensity tensors are not implemented within mPW2PLYP, they were calculated at the DFT B3LYP/6-311++G**/CPCM level. Previous experience suggests that the error associated with such simplification would be very small.^{194, 199, 210}

The second order vibrational perturbation theory (PT2) and limited vibrational configuration interaction (LVCI) schemes were used.¹⁵¹ The PT2 treats cubic and quartic terms in eq. 4.3 as a perturbation with respect to the harmonic solution (these terms are small in terms of their influence on the energies of interest). The harmonic vibrational energy for each state n , E_n , is corrected by adding a first-order term

$$E_n^{(1)} = W_{nn} \quad (4.4)$$

(cf. electronic variant in eq. 2.19) and by a second-order term, inspired by an electronic correction (eq. 2.20)

$$E_n^{(2)} = \sum_{m \neq n} A_{mn}, \quad (4.5)$$

$$\text{where } A_{mn} = \left(E_m - E_n \pm \sqrt{(E_m - E_n)^2 + 4W_{mn}^2} \right) / 2, \quad (4.6)$$

and the „+“ sign holds for $E_m > E_n$, the „-“ sign for $E_m < E_n$, and $W_{nm} = \langle n|W|m\rangle$.

This form was proposed to avoid numerical instability due to random degeneracies.²⁵⁹

Similarly, the PT2 wave function was considered as

$$\psi_n^{\hat{}} = \psi_n - \sum_{m \neq n} A_{mn} W_{mn}^{-1} \psi_m, \quad (4.7)$$

where ψ_n is the unperturbed state.

The spectral properties (electric dipole moment $\boldsymbol{\mu}$ for IR, and $\boldsymbol{\alpha}$, \mathbf{G} , \mathbf{A} tensors for Raman and ROA intensities) were also considered to be dependent on the coordinates to the second order (eq. 2.71). For VCD, the dependence of the magnetic dipole moment on the coordinates and momenta Π_i was also used

$$m = m_0 + \sum_i A_{1,i} \Pi_i + \frac{1}{2} \sum_{i,j} A_{2,ij} (\Pi_i Q_j + Q_j \Pi_i), \quad (4.8)$$

where $A_{1,i}$ is the axial tensor. The derivatives with respect to momenta, $A_{2,ij}$, could be treated within the MFP theory in the same way.

In the LVCI, the vibrational wave function was expressed as a linear combination of harmonic oscillator wave functions, $\Phi_\varepsilon = \sum_f C_f^\varepsilon \psi_f$. Several criteria were employed to limit the number of HO basis functions:^{151, 260}

1. the lowest-frequency normal modes (e.g. 1..36) were not excited,
2. only states (f) obliging $W_{fn} > c_1 |E_n - E_f|$ were included, where c_1 is an interaction parameter, and n is a ground or fundamental state,
3. a second set of HO basis functions (f') obliging $W_{f'f} > c_2 |E_{f'} - E_f|$ was added, interacting with the already chosen basis,
4. Hamiltonian elements with too energy-separated states $|H_{ij}| < 10^{-4} |E_i - E_j|$ were excluded as well.

The parameters were tested (**Fig. 5.9**) and set by default to 31 or 36 fixed modes, $c_1 = 0.002$, $c_2 = 0.1$, which led to a high, but still affordable calculation time ($\sim 10^3$ CPU hours). States with a maximum of five excitations were considered, because the FF was expanded up to the quartic terms. The coefficients C_f^ε and associated energies E_ε were obtained from the Hamiltonian matrix by the Mitin's version²⁶¹ of the Davidson²⁶² diagonalization procedure. Our implementation¹⁵¹ within

the S4 program¹⁵⁴ allowed a fast diagonalization of a very large vibrational Hamiltonian matrix ($\sim 10^6$ basis states) and a consistent spectra generation in a “double-anharmonic” approximation, where the energy and intensity tensor derivatives were evaluated up to the fourth and second order, respectively. Details about the diagonalization algorithm can be found in publication [II].

4.1.3. Cyclic dipeptides with tryptophan

In publication [III], the lowest-energy conformations of selected cyclic dipeptides with tryptophan (**Fig. 4.3**) were obtained by geometry optimization at the B3LYP/CPCM/6-311++G** level as default. For some tests, the aug-cc-pVTZ basis set and MP2,¹¹⁹ mPW2PLYP,²⁵⁵ B3PW91,²⁵³ and BPW91¹²⁸ methods were used. The CPCM solvent model¹⁷⁵ was used with acetonitrile (AcCN, $\epsilon_r = 36$), chloroform (CHCl_3 , $\epsilon_r = 4.7$), 2,2,2-trifluoroethanol (TFE, $\epsilon_r = 27$), methanol (CH_3OH , $\epsilon_r = 33$) and dimethylsulfoxid (DMSO, $\epsilon_r = 47$) parameters. The solvent variations, however, had only a minor effect on the resultant spectra and relative conformer energies (see Fig. S1 in publication [III]). Only the ϵ_r value for DMSO was used with both the normal B3LYP and dispersion-corrected B3LYP-D^{135,255,263} functional for calculations of other molecules.

A two-dimensional scan was performed for c-(L-Ala-L-Ala) to construct the PES of the inner ring. Torsion angles φ and ψ (**Fig. 4.3**) were scanned in range from -50° to 50° with a step of 5° . For the other dipeptides only a relaxed 1D scan along the φ -angle was performed because of the relatively simple „single-valley“ PES that resulted from the scan (**Fig. 5.10**).

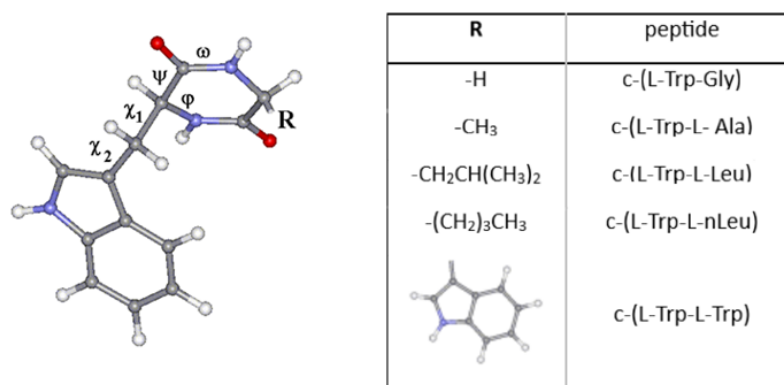


Figure 4.3: Cyclic dipeptides c-(L-Trp-X), where X=Gly, L-Ala, L-Leu, L-nLeu, L-Trp and L-Pro, with characteristic torsional angles. Adapted from publication [III].

The tryptophan side chain conformation was investigated for c-(L-Trp-L-Trp) by a scan along torsion angles χ_1 and χ_2 , from -180° to 165° with 15° increments, other coordinates were allowed to relax. This revealed four minima; the angle χ_1 favors values around -60° and 60° , and χ_2 prefers -90° and 90° (**Fig. 4.4**, left).

Based on these scans, c-(L-Trp-Gly), c-(L-Trp-L-Ala), c-(L-Trp-L-Trp), c-(L-Trp-L-Leu) and c-(L-Trp-L-Pro) dipeptide geometries were generated with starting values χ_1 of about -60° , 60° and 180° , $\chi_2 \sim -90^\circ$ and 90° (these conformations are depicted in **Fig. 4.4**) together with two possible ring conformations, $\varphi \sim -25^\circ$ and 25° . The conformation of the second side chain in c-(L-Trp-L-Trp), c-(L-Trp-L-Leu) and c-(L-Trp-L-Pro) was also investigated systematically: for Leu, the χ_1 ' and χ_2 ' torsion angles were set at -60° , 60° or 180° , similarly we used the S and N conformations^{178, 264-266} of the proline five-member ring.

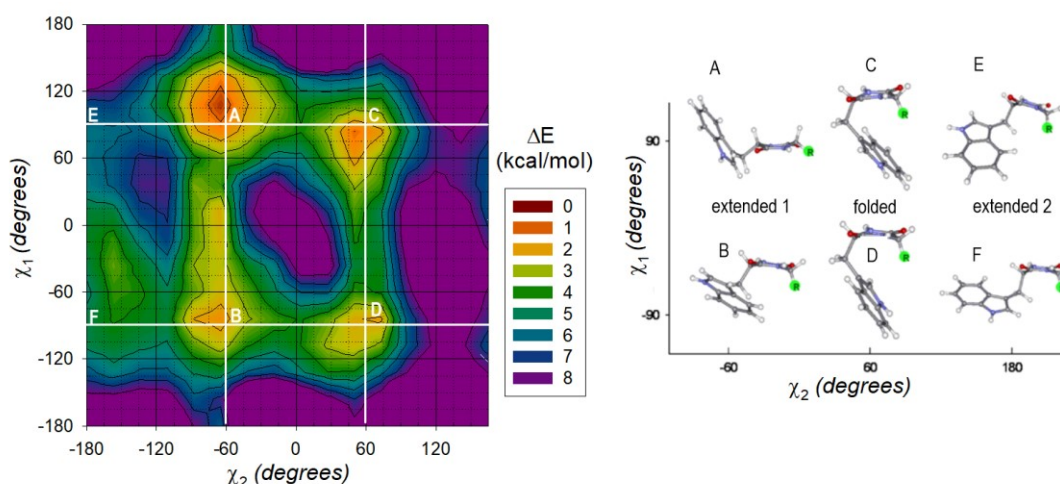


Figure 4.4: Left: 2D potential energy scan of c-(L-Trp-L-Trp) as a function of two torsion angles (χ_1 , χ_2 ; see **Fig. 4.3**), calculated at the B3LYP/CPCM/6-311G** level. Right: Conformational classes (A-F) of the tryptophan-containing dipeptides. The canonical angles (χ_1 , χ_2) are A (-60° , 90°), B (-60° , -90°), C (60° , 90°), D (60° , -90°), E (180° , 90°) and F (180° , -90°).

MD simulations with the Amber10 program package²⁴¹ using the Amber99 force field were done for c-(L-Trp-L-Trp) and c-(L-Trp-L-Pro) in water, CH_3OH , DMSO and CHCl_3 . Force fields for DMSO and CHCl_3 were obtained from the extended Amber database (<http://www.pharmacy.manchester.ac.uk/bryce/amber>). Missing force field parameters for the cyclic dipeptide ring were derived from

a HF/6-31G* calculation by the Gaussian09 program,¹⁵⁶ using the “POP=MK” keyword. The solute molecule was surrounded by solvent molecules up to the distance 8–14 Å. A four-step equilibration²⁶⁷ was carried out, followed by a 50 ns (100 ns for c-(L-Trp-L-Trp) in water) production run, using NpT ensembles and 1 fs integration time. Snapshots were taken each 5 ps and the relative conformer populations were found as dependent on the angles χ_1 and χ_2 . The population error was estimated as 20% from three independent MD runs for c-(L-Trp-L-Trp).

4.1.4. Interaction of the $[\text{Eu}(\text{DPA})_3]^{3-}$ complex with histidine-peptides

The interaction of seven histidine-containing peptides (**Fig. 4.5**) with the $[\text{Eu}(\text{DPA})_3]^{3-}$ complex in aqueous solutions was investigated using the Amber14²⁴⁰ program package. Initial $[\text{Eu}(\text{DPA})_3]^{3-}$ complex geometries were obtained using the Gaussian09 program¹⁵⁶ adapting the B3LYP/6-311++G**/CPCM (MWB28 pseudopotential and basis set for Eu).

To model mild acidic conditions (pH ~ 4, corresponding to most experiments), the histidine aromatic ring and the amine group were protonated ($-\text{NH}_3^+$), and the carboxyl group was deprotonated ($-\text{COO}^-$). For lower pH (< 2) the carboxyl group ($-\text{COOH}$) was protonated as well. For His-(Gly)₂ neutral and basic forms were investigated as zwitterionic and deprotonated peptides. For other peptides only structures corresponding to acidic conditions (pH < 2 and pH ~ 4, with peptide's charges of +2 and +1, respectively) were investigated.

The peptides were inserted into a cubic (30 Å)³ box containing 880 water molecules and one $[\text{Eu}(\text{DPA})_3]^{3-}$ ion in the Λ or Δ conformation, initially separated from the peptide by ~ 12 Å. MD simulations were run for NVT ensembles using 1 fs integration step, temperature of 300 K, GAFF²⁶⁸ (DPA ligands), Amber14SB²⁶⁹ (His and Gly) and TIP3P6²⁷⁰ (water) force fields. After an equilibration (1 ns), constrained MD simulations were run for 8 ns. A harmonic penalty function (restraint constant of 4 kcal·Å⁻²·mol⁻¹) was put on the distance r between Eu of the complex and C^α of His, which was changed from 12 to 9 Å in 1 Å increments and from 9 to 4 Å in 0.5 Å increments. The potential of the mean force $F(r)$ was calculated from individual distance distributions using the weighted histogram analysis method (WHAM)^{271,272} and the Amber14 scripts. The complex formation profiles thus could be correlated with the CPL intensity.

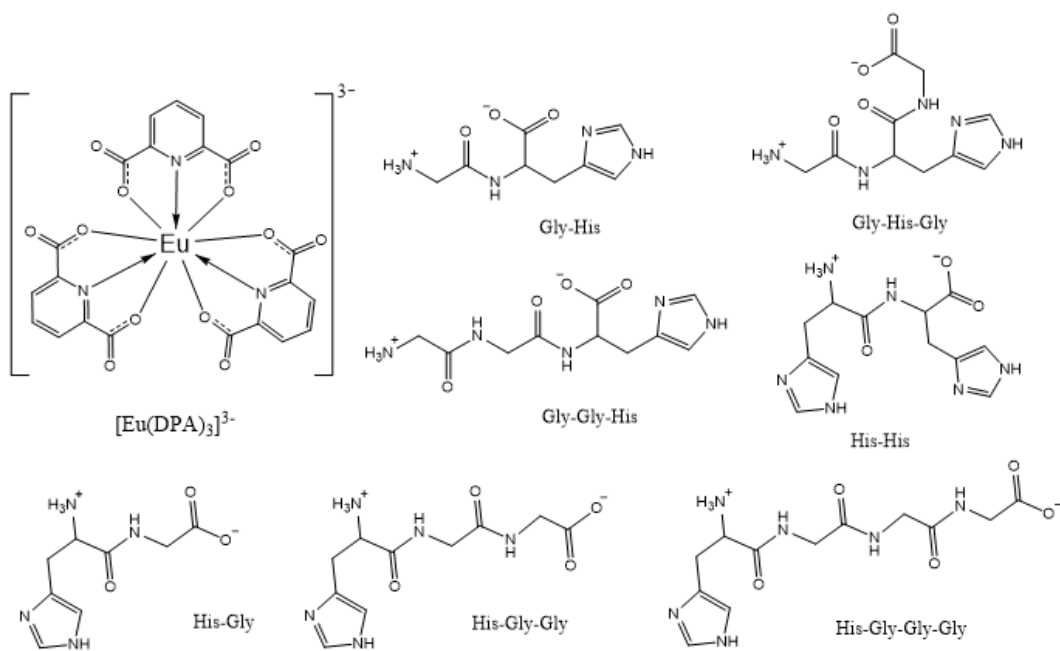


Figure 4.5: Structure of the $[\text{Eu}(\text{DPA})_3]^{3-}$ complex and investigated model peptides.

Effective relative binding strengths (s) were evaluated as equilibrium ratios of the numbers of bonded (N_B , $r < 10 \text{ \AA}$) and free (N_F , $r > 10 \text{ \AA}$) Eu complexes for each simulation as

$$s = \frac{N_B}{N_F} = \frac{\int_0^{10} \exp\left(-\frac{F}{kT}\right) r^2 dr}{\int_{10}^{12} \exp\left(-\frac{F}{kT}\right) r^2 dr}. \quad (4.9)$$

4.2. Studied compounds

The samples from publications [I] (**Fig. 4.1**) and [II] (**Fig. 4.2**) were purchased from Sigma-Aldrich. All commercial reagents were of high purity or analytical grade and were used without further refinement. Lactamide was dissolved in deionized water, α -pinene and fenchone were used neat and camphor was dissolved in CCl_4 solution to 0.2 M concentration.

The cyclic dipeptides with tryptophan for project [III] (**Fig. 4.3**) were synthesized at IOCB by dr. Jaroslav Šebestík and Martin Šafařík as described in publication [III]. A relatively wide range of solvents had to be used for the experimental ECD, VCD, ROA and NMR spectroscopy due to limited solubilities of the various cyclic dipeptides (**Table 1** in publication [III]).

Short peptides with histidine (His-Gly, His-Gly-Gly, His-Gly-Gly-Gly, Gly-His, Gly-His-Gly, His-His and Gly-Gly-His; **Fig. 4.5**), which were studied in publication [IV], were synthesized by the Fmoc/tBu strategy on 2-chlorotrityl resin at IOCB by Eva Brichtová, Nikola Vršková and dr. Jaroslav Šebestík. The $\text{Na}_3[\text{Eu}(\text{DPA})_3]$ (DPA = dipicolinate = 2,6-pyridinedicarboxylate) complex was obtained by a reaction of europium(III) carbonate and pyridine-2,6-dicarboxylic acid (1:3 molar ratio) in water.

4.3. Experimental methods

The measurements were performed at different locations on various instruments (two ROA, three VCD and one ECD) as described in following chapters.

4.3.1. ROA experiment

Measurements of Raman and ROA backscattering spectra for projects [I], [III] and [IV] were performed on a commercial ROA spectrometer Chiral*RAMAN-2X*TM (BioTools, Inc., USA),^{24,48} located at IOCB. It is based on the SCP backscattering scheme described in Chapter 1.2.1. It uses 2 W diode-pumped solid state laser operating at 532 nm (OPUS 532). It covers the spectral range of $-10 - 2430 \text{ cm}^{-1}$. The replacement of the originally implemented notch filter (SuperNotch-PlusTM, Kaiser Optical Systems, Inc.) to edge filter (532-nm RazorEdge, LP03-532RE-25, Semrock, Inc.) enabled blocking Rayleigh line more efficiently and allowed measurements down to $\sim 100 \text{ cm}^{-1}$. The spectral resolution of the spectrometer is $\sim 7 \text{ cm}^{-1}$. Raman spectra of toluene (eventually neon lamp) were used for wavenumber scale calibration.

Raman and ROA spectra of lactamide in aqueous solution for publication [I] were measured with the accumulation time 12 h, laser power at the laser head 360 mW and concentration 100 mg/ml.¹⁸³

Raman and ROA spectra of both enantiomers of c-(Trp-Trp) and c-(Trp-Gly) in DMSO (concentrations were 50-100 mg/ml) were analyzed in publication [III]. The total acquisition time was about 20 h for each sample. The laser power was set to 50-100 mW, and power at the sample was 30-60 mW. Higher powers would cause a faster degradation of the samples. Residual fluorescence was quenched by leaving the sample in the laser beam for a few hours. ROA spectra from two or three independent measurements were averaged.

In publication [IV], the SCP ROA spectrometer was used to detect the total luminescence (TL) and CPL spectra (Chapter 1.2.3). Raman and ROA spectra (dominated by Eu TL and CPL) were acquired by dr. Tao Wu and Eva Brichtová for complexes of $[\text{Eu}(\text{DPA})_3]^{3-}$ (concentration 4mM) with His-containing peptides (**Fig. 4.4**, concentrations 20 mM or 4–40 mM for titrations). The accumulation times were one (for solutions at pH = 4), eight (pH = 7) and twelve (pH=10) hours. The laser power at the sample was 150–400 mW. pH was adjusted by 0.1 M HCl or NaOH. In the presented spectra the intensities were normalized to the 1650 cm^{-1} band, and a broad fluorescence background coming from sample impurities was subtracted from the Raman signal.

ROA spectra of α -pinene, fenchone and 0.2 M camphor in CCl_4 solution covering the whole region of fundamental molecular vibrations ($\sim 100\text{--}3400\text{ cm}^{-1}$)³⁷ were measured by dr. Václav Profant on the home-built ROA instrument at Institute of Physics of Charles University in Prague^{273,192} for publication [II]. This instrument follows the original ICP backscattering concept of ROA instrumentation as it was suggested by Prof. Barron's group in Glasgow, UK.⁴⁷ Polarization of the incident beam is modulated between RCP and LCP states using electro-optic modulator consisting of a longitudinal Pockels cell with a potassium dideuterium phosphate crystal. The excitation source is an argon laser (Coherent, Innova 305, 514.5 nm). The elastic Rayleigh scattering is suppressed by high efficient notch filter. A fast stigmatic spectrograph HoloSpec HS-f/1.4 (Kaiser Optical Systems) is used.

The extension of spectral region to higher wavenumbers was allowed by a combination of three interchangeable holographic transmission gratings: HSG-514.5-LF ($-250\text{--}2370\text{ cm}^{-1}$), HSG-532-LF ($580\text{--}3070\text{ cm}^{-1}$) and HSG-514.5-HF ($2270\text{--}4510\text{ cm}^{-1}$) and an independent intensity correction using a fluorescence standard (National Institute of Standards and Technology, USA).³⁷ Spectral resolution of the spectrometer combining the gratings with the used CCD array (nitrogen-cooled CCD detector from Roper Scientific contains 1340×100 pixels) was nearly uniform ($\sim 7\text{ cm}^{-1}$). A neon-lamp standard was used for the calibration of wavenumber scale. The total acquisition time was about 20 h for each sample and grating, the laser power was set to 500 mW. Raw ROA spectra were processed by Fourier filtration to suppress quasiperiodic high-frequency CCD signal. The measurement of both enantiomers was particularly important for the C-H stretching signal, where the CID ratio $\Delta \sim 5 \times 10^{-5}$.

All measurements were performed in low-volume quartz cells with antireflectively coated windows (Starna Scientific Ltd; ~60 μl , 4×3 mm) at room temperature (293 K). For Raman spectra, the solvent signal was subtracted and the baseline was slightly straightened by a polynomial fit (using the sc95 program²⁷⁴). For ROA spectra, the noise level was reduced (by $\sqrt{2}$) by measuring and averaging both enantiomers [$\text{ROA}=(\text{L}-\text{D})/2$]. An occasional minor baseline arrangement was done. The experimental spectra were corrected for the instrument response, i.e. the relative intensity correction.³⁷

4.3.2. VCD experiment

VCD measurements of terpenes in publication [II] were performed by Prof. Marie Urbanová and Pavlína Novotná at the Institute of Chemical Technology in Prague with two FT spectrometers designed for different spectral regions.

Measurements in the mid-IR region ($800\text{-}1800\text{ cm}^{-1}$) were performed by a commercial FTIR IFS 66/S spectrometer equipped with a PMA 37 VCD/IRRAS module (Bruker, Germany). The setup included BaF_2 polarizer, ZnSe PEM (Hinds Instruments, Inc.), HgCdTe (MCT) detector (InfraRed Associates, Inc.) and a lock-in amplifier SR830 (Stanford Research Systems, Inc.). The measurement of C–H stretching vibrations ($2000\text{-}3800\text{ cm}^{-1}$) was provided by the Tensor 27 FTIR spectrometer equipped with VCD/IRRAS module PMA 50 (Bruker, Germany). The instrument is equipped with BaF_2 polarizer, ZnSe PEM (Hinds Instruments, Inc.), LN-InSb detector D4143/6 (InfraRed Associates, Inc.) and a lock-in amplifier SR830 (Stanford Research Systems, Inc.).

The samples were placed in a demountable cell (A145, Bruker, Germany) composed of KBr or CaF_2 windows separated by a 6, 50, or 100 mm Teflon spacer with a spectral resolution of 4 or 8 cm^{-1} , and averages of 6 - 16 blocks of 3686 scans were used. The experimental conditions for all compounds and spectral ranges are summarized in Table S1 in publication [II].

For project [III], VCD spectra of the D- and L- forms of c-(Trp-Gly), c-(Trp-Trp) and c-(Trp-Pro) in DMSO and eventually AcCN were measured at Department of Chemistry at University of Illinois at Chicago, USA. A homemade dispersive VCD instrument was used.^{275,276} It consists of a 0.3 m monochromator (Acton Research, SpectraPro 2300i), Carbon-Rod source (a high black-body temperature ~2500 K) and

a narrow band liquid-nitrogen-cooled MCT detector (Infrared Assoc.). The corresponding IR spectra were recorded on the same samples using a Vertex 80 FTIR (Bruker) spectrometer. Samples were prepared by dissolving the peptides in DMSO or AcCN to a concentration of about 10 mg/ml, and placing them into a cell composed of two CaF₂ windows separated by a 100 mm spacer. Spectra were obtained as averages of 6 scans.

In both publications, the VCD spectra are presented as the difference of enantiomers [(L-D)/2]. Similarly, IR spectra are presented as their sum [(L+D)/2] with the IR baseline corrected by subtraction of the solvent.

4.3.3. ECD experiment

ECD spectra of cyclic dipeptides for publication [III] were measured using a Jasco J-810 spectropolarimeter located at Department of Chemistry at University of Illinois at Chicago, USA. This spectropolarimeter, operating in the interval 163-900 nm, is a hybrid instrument consisting of a variable wavelength polarimeter and absorption spectrophotometer. Samples were measured in 0.1 cm path length quartz cells, using concentrations of about 0.2 M in AcCN or TFE. *c*-(Trp-Gly) was not sufficiently soluble under these conditions. Each spectrum was obtained as an average of 6 scans taken with a band pass of 1 nm and scanning speed of 50 nm·min⁻¹. The concentration was determined by the Trp UV absorption in order to express the experimental spectra in $\Delta\epsilon$ (L·mol⁻¹·cm⁻¹).

5. Results and discussion

5.1. Normal mode geometry optimization and vibrational broadening

Raw cluster geometries (based on MD simulations) provided too wide vibrational bands and unrealistic geometry dispersion of the higher-frequency motions.¹⁸³ This may be primarily caused by the coupling of vibrational modes and anharmonic force field terms as we have shown in publication [I] on a simplified two-dimensional model. However, the clusters could not be optimized completely, to avoid collapse to an energy minimum.

Therefore, the normal mode optimization method,¹⁸⁶ which is controlled by a sole parameter, the maximal harmonic normal mode frequency (ω_{max}), was used to obtain a more realistic vibrational band broadening for clusters of (*S*)-lactamide with a few water molecules. This parameter has been used on an empirical basis so far. In this work, the choice of ω_{max} was rationalized by its effect on resulting bandwidths.

Raman and ROA spectra simulated with different ω_{max} are compared in **Fig. 5.1**. Raw non-optimized clusters are unusable for a detailed assignment of the lactamide bands as they overestimate the broadening and provide quite unrealistic spectral shapes. The partial optimization of cluster geometries lead to a radical improvement. For $\omega_{max} = 600 \text{ cm}^{-1}$ the bands are still too broad, and no improvement is apparent in the region below 600 cm^{-1} . Most of the Raman and ROA intensity features are well developed for $\omega_{max} = 200 \text{ cm}^{-1}$, and the bandwidths are realistic within the entire wavenumber region. For $\omega_{max} = 20 \text{ cm}^{-1}$ individual bands can be recognized as well, but most bandwidths become too narrow if compared to the experiment.

The experimental bandwidths for three non-overlapping Raman bands with central frequencies at 528 , 813 and 920 cm^{-1} were compared to the theoretical bandwidths, which were obtained from the simulated spectra by fitting with Lorentzian bands (**Fig. 5.2**). An optimal ω_{max} can be estimated at least approximately from the crossing of the simulated bandwidth curve with the experimental line, ranging from $\omega_{max} \sim 200 \text{ cm}^{-1}$ (for the 528 cm^{-1} band) to $\sim 500 \text{ cm}^{-1}$ (813 cm^{-1} band).

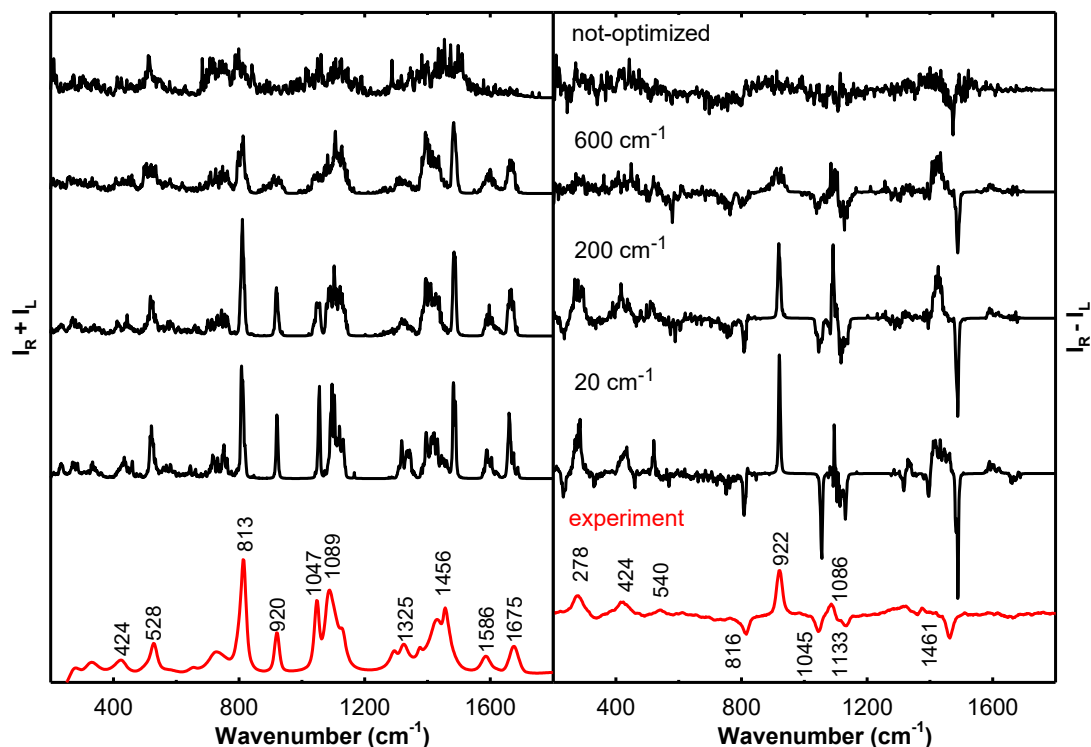


Figure 5.1: Comparison of backscattered Raman (left, $I_R + I_L$) and ROA (right, $I_R - I_L$) spectra of (*S*)-lactamide dissolved in water (bottom) with an average of 100 spectra calculated for CPMD clusters, which were partially optimized with different values of ω_{max} . Adapted from publication [1].

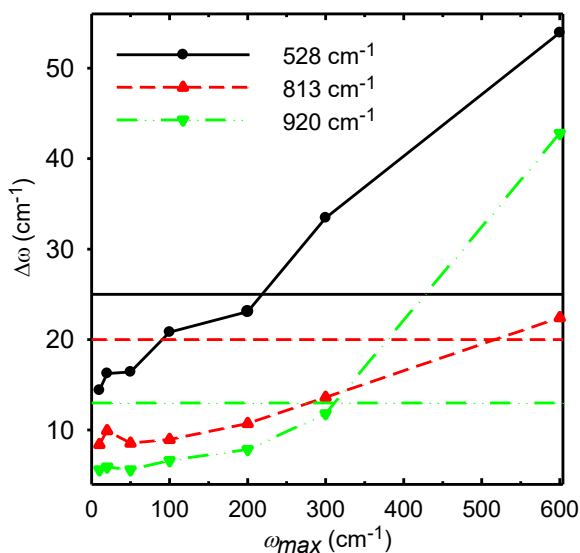


Figure 5.2: Simulated (*S*)-lactamide Raman bandwidths ($\Delta\omega$) as calculated for seven values of ω_{max} for the bending (528 cm^{-1}), NH_2 wagging (813 cm^{-1}) and C-C/C-O stretching (920 cm^{-1}) vibrational modes. Experimental bandwidths are indicated by the horizontal lines. Adapted from publication [1].

The changes of molecular coordinates occurring during the NMO with different values of ω_{max} were also monitored (**Fig. 5.3**). The OH rotation is associated with the shallowest potential, and thus remains fixed for most of ω_{max} . The rotation is released for $\omega_{max} < 100 \text{ cm}^{-1}$, when the change increases steeply. The ψ angle responds more gradually, but it is starting to change already for $\omega_{max} < 300 \text{ cm}^{-1}$. The CH_3 rotation exhibits the most developed sigmoidal "melting" pattern with a transition frequency at about 250 cm^{-1} .

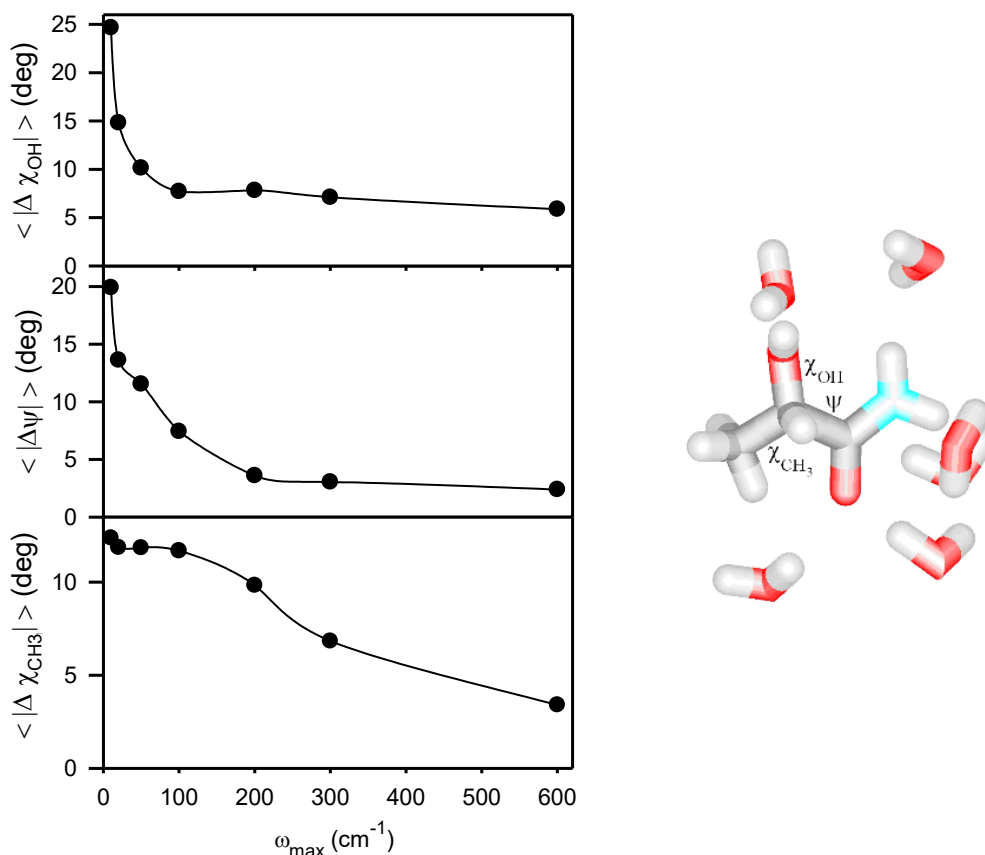


Figure 5.3: The average absolute changes of three (*S*)-lactamide torsional angles during the optimization, as obtained from 100 CPMD clusters for seven values of ω_{max} . The angles $\chi_{OH} = \angle(\text{C}=\text{O}\text{COH})$, $\psi = \angle(\text{NCCC})$ and $\chi_{CH_3} = \angle(\text{CCCH})$ are indicated in the randomly chosen snapshot. Adapted from publication [I].

We thus suggested that the empirical procedure of partial NMO provides an efficient means of modeling vibrational properties of molecules in solutions. An optimal ω_{max} value is within $200 \dots 300 \text{ cm}^{-1}$. The spectral profiles (**Fig. 5.1**) change very slowly with ω_{max} ; thus in a wide interval around the optimal value the spectra can be simulated realistically enough to allow for the normal mode

assignment and estimation of most of the solvent inhomogeneous normal mode broadening.

In order to average the signal however, a relatively large number of MD geometries needs to be considered. A parallel variable selection of MD clusters was proposed by Kessler et al. in 2013.²⁷⁷ The mass, charge, or atomic density MD distributions were used as a secondary variable to preselect the most probable cluster geometries used for averaging of solute spectral properties. About 10 times fewer clusters of (*S*)-lactamide with waters were needed to provide the same accuracy as the plain averaging. Since then, the partial NMO was applied in our group to clusters of aminoacids,²⁷⁸ Ala-Ala dimer²³³ and monosaccharides in water,⁸⁷ and also for clusters of benzene with methane.²⁷⁹ The threshold was set to the upper suggested limit ($\omega_{max} = 300 \text{ cm}^{-1}$), because the CPU time needed for the partial NMO increases with the lowering of ω_{max} .

5.2. VOA spectra in the C-H stretching region

In publication [II], the ability of several harmonic and anharmonic computational approaches to describe strongly anharmonic vibrations in the C-H stretching region ($2500\text{-}3400\text{ cm}^{-1}$) was studied for three terpene molecules (camphor, fenchone and α -pinene; **Fig. 4.1**). Four spectroscopic methods (Raman, ROA, IR and VCD) were examined to avoid accidental agreement/disagreement between measured and calculated spectra.

Firstly, we explored how the harmonic approximation is able to describe C-H stretching vibrations. The solvent dependence was tested for camphor (**Fig. 5.4**). Increasing the solvent polarity mostly causes downshift of the lower-frequency modes. Positions of the C-H bands change in both directions, occasionally also their ordering is changed. The spectral intensities are even more dependent on the solvent variations than frequencies, for all the Raman, ROA, IR and VCD spectral types.

The 6-311++G** basis set was chosen as default as it provided similar results as the more computationally demanding ones, e.g. aug-cc-pVTZ (for a detailed analysis made for fenchone see Fig. 5 in publication [II]).

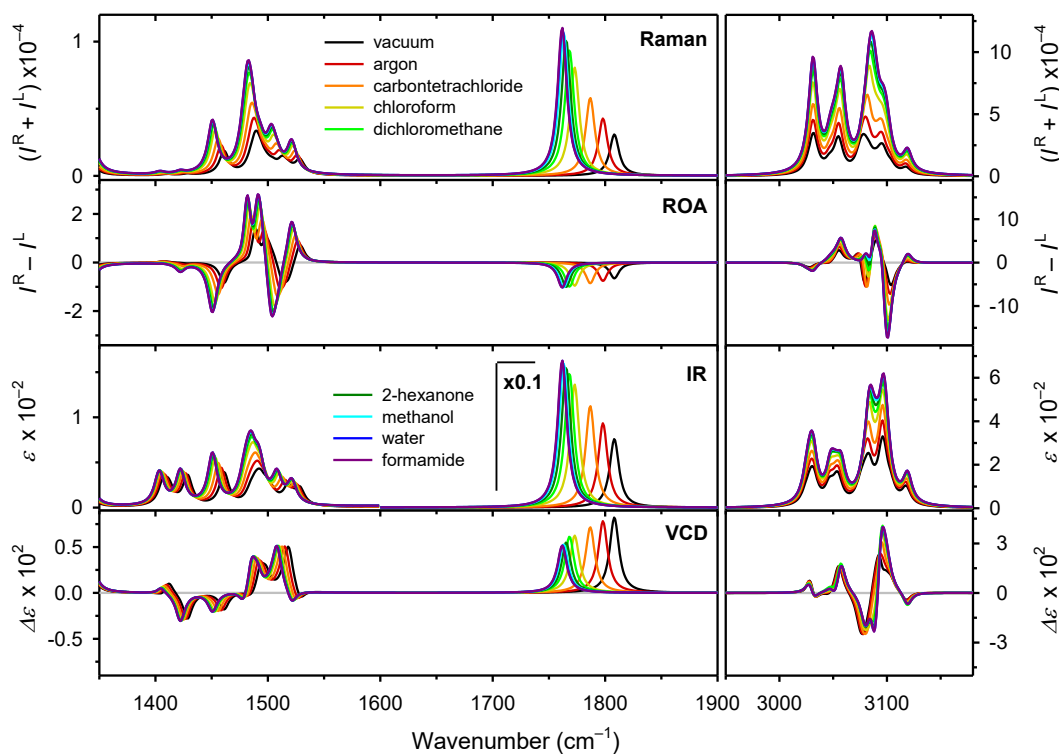


Figure 5.4: Solvent dependence of the calculated (B3LYP/6-311++G**/CPCM) (1R)-(+)-camphor Raman, ROA, IR and VCD spectra. Adapted from publication [II].

The computational reliability for frequencies was tested for fenchone. Errors of C-H stretching frequencies calculated at 14 electronic computational levels were compared to the experiment (**Fig. 5.5**). Although the harmonic approaches (1-12) approximately reproduce the experimental spectral patterns, they overestimate the C-H stretching frequencies.^{237, 239} The average frequency error ($\langle \nu \rangle - \langle \nu_{exp} \rangle$) is $\sim 260 \text{ cm}^{-1}$ for the HF method and $\sim 70\text{--}160 \text{ cm}^{-1}$ for different DFT functionals with a negligible influence of a dispersion correction. This large deviation from experiment could be improved only by the PT2 and LVCI anharmonic corrections (13-14, included at the mPW2PLYP level) giving the average errors 35 and 5 cm^{-1} , respectively. The remaining frequency error of the LVCI computation is most probably given by the limited Taylor expansion of the potential and errors of the electronic quantum-chemical and LVCI approaches.

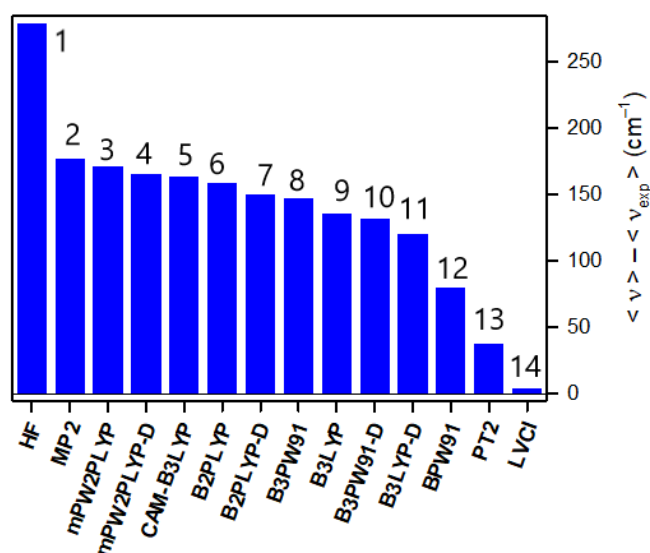


Figure 5.5: Average harmonic (HF...BPW91, 1-12) and anharmonic (PT2 and LVCI, for the mPW2PLYP force field, 13-14) frequency errors for fenchone compared to the experiment. Adapted from publication [II].

The behavior of the harmonic, PT2 and LVCI computational method is documented in **Fig. 5.6** for α -pinene, which is the smallest of the three studied molecules. The harmonic spectra are close to the experiment at the lower-frequency region ($1350\text{--}1770 \text{ cm}^{-1}$). This region comprising of mostly the C-H bending modes is traditionally considered as harmonic. Still, it significantly benefits from the anharmonic computations. For example, mode number 24 is shifted from the harmonic position at 1492 cm^{-1} to 1418 cm^{-1} , which is closer to the experiment (1434 cm^{-1}).

Only the C=C stretching band (mode number 17) is rather indifferent to anharmonicity corrections.

In the C-H stretching region, reasonable vibrational frequencies were obtained within PT2, but with significant errors in ROA and VCD intensities. It has been shown previously that the PT2 may not be sufficient to treat all anharmonicities, especially for the VOA, and should be replaced by the more universal VCI.²⁸⁰

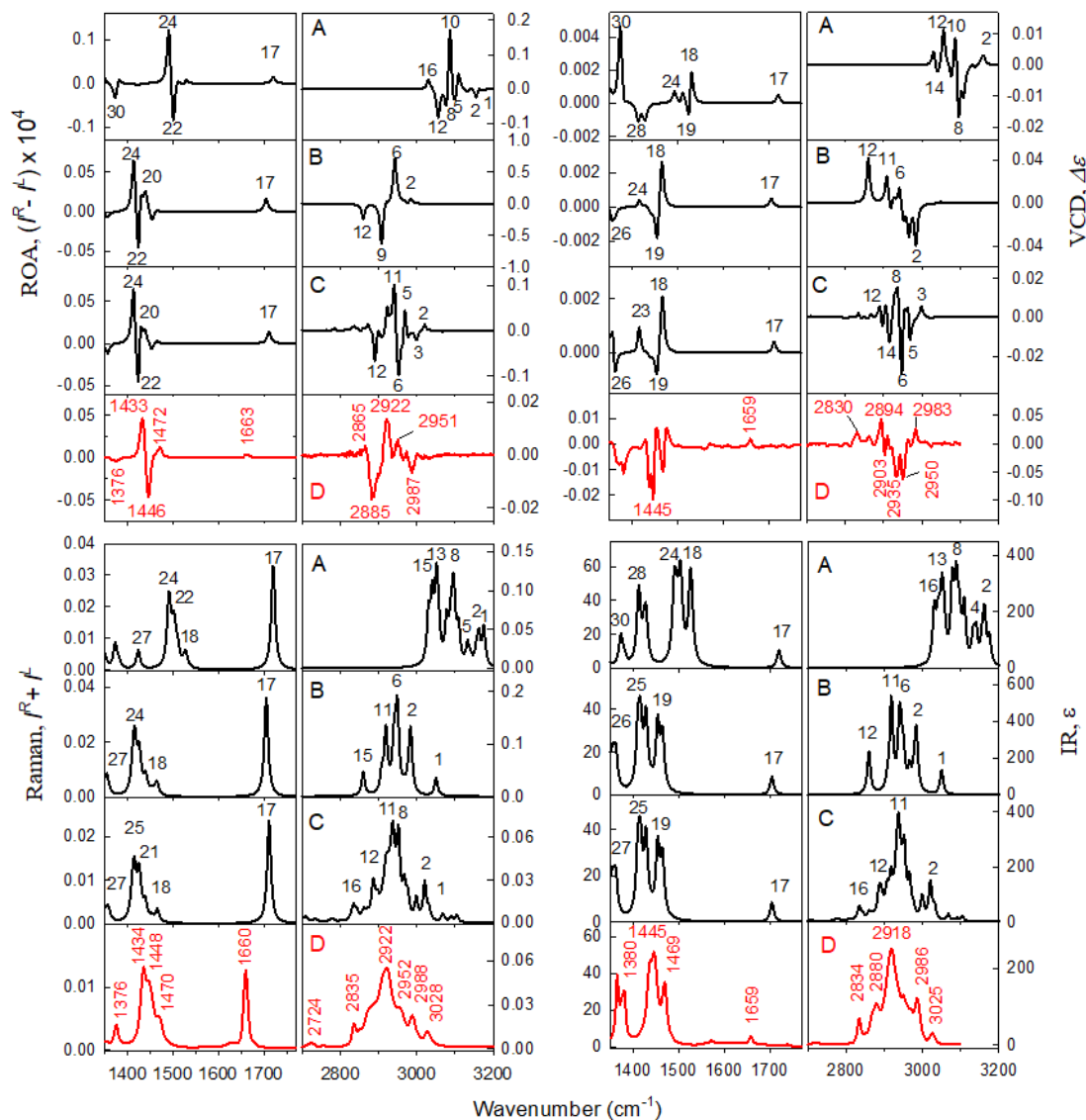


Figure 5.6: ROA, VCD, Raman and IR spectra of (1R)-(+)- α -pinene calculated at the (A) harmonic, (B) PT2 and (C) LVCI (36 modes fixed, $c_1 = 0.002$, $c_2 = 0.1$, 749398 HO states) approximation levels, and (D) experiment, in a low (1350-1770 cm^{-1}) and C-H stretching (2700-3200 cm^{-1}) frequency regions. Redrawn from publication [II] with an added normalization of Raman and ROA spectral intensities.³⁷

The limited VCI computation¹⁵¹ with a limited coupling between the lower- and higher-frequency motions (provided by a parameter c_2) was the most consistent with experiment, both in frequencies and intensity profiles. The LVCI Raman and IR spectra became narrower and dominated by the central signal (mode number 11, ~ 2922 cm^{-1} for Raman) in comparison with the harmonic and PT2 profiles. Most simulated and experimental bands could be linked to each other (**Table 5.1** for an assignment).

For ROA spectra of α -pinene, the relatively strong negative signal observed at 2885 cm^{-1} and the positive band measured at 2922 cm^{-1} are calculated by LVCI at approximately same positions. Around 2951 cm^{-1} , however, the negative ROA signal (associated with the mode number 6) calculated by the LVCI is not observed in the experiment. For VCD, the behavior of the LVCI simulation is similar as for ROA, with the largest discrepancy around 2935 cm^{-1} , where a negative measured signal does not correspond to a positive LVCI signal (mode number 8).

Table 5.1: Calculated (mPW2PLYP/6-311++G**/CPCM level) C-H stretching normal modes for α -pinene. ^a Adapted from publication [II].

mode	1	2	3	4	5	6	7	8
wavenumber (cm^{-1})	3175	3162	3156	3140	3132	3109	3102	3096
assignment	1*	3 ip 2	3	3 op 2	3	3 ip 3	3 op 3	1 ip 2

mode	9	10	11	12	13	14	15	16
wavenumber (cm^{-1})	3090	3087	3078	3056	3051	3045	3040	3030
assignment	3	1 op 1 ip 2	1 op 2	2*	3 ip 3	3 op 3	3	2* ip 1

^a 1 = C-H stretching, 2 = asymmetric CH_2 stretching, 2 = symmetric CH_2 stretching, 3 = asymmetric CH_3 stretching, 3 = symmetric CH_3 stretching, ip = in phase, op = out of phase, * = proximate to double bond

In spite of structural similarity of camphor and fenchone, their experimental spectra, VCD and ROA in particular, are rather different in the C-H stretching region (**Fig. 5.7**). For example, the ROA spectrum for camphor is much simpler than for fenchone, which is nicely reproduced by the LVCI computation. For fenchone, a better agreement between the simulation and experiment is apparent for the IR and VCD spectra than for Raman and ROA spectra. The most visible discrepancies are the shape of the Raman signal, calculated sharper than observed, and the ROA band around 2989 cm^{-1} , where an experimental negative sign is reproduced by LVCI as a weak splitted signal only. For camphor, the agreement is quite good for all four types of spectra.

VCD and IR LVCI intensities approximately (up to 30% difference) resemble the experimental magnitudes for all molecules. For Raman and ROA intensities, which were not measured as absolute values, integral intensities of experimental and calculated LVCI Raman spectra were normalized to unity within the interval $1200\text{-}1500\text{ cm}^{-1}$. The intensity of the harmonic and PT2 spectrum was adjusted to maintain the original integral intensity ratio of the calculated spectra. Same normalization factors were used for the corresponding ROA spectra.³⁷ While LVCI Raman intensities are overestimated about 30%, ROA LVCI intensities are $\sim 2\text{--}4$ times higher than integral intensities of experimental spectra in all cases.

The performance of the LVCI method was tested for α -pinene. The freezing of the lower-frequency vibrations was necessary to reduce the number of the HO states. It is based on the assumption of a limited coupling between the higher- and lower-frequency modes (**Fig. 5.8**). While the C-H stretching modes (last 16 modes in the graphs) exhibit exceptionally large diagonal and off-diagonal anharmonic constants, the coupling of the C-H stretching to the lower-frequency modes is significantly smaller, so they stay relatively isolated from other vibrations.

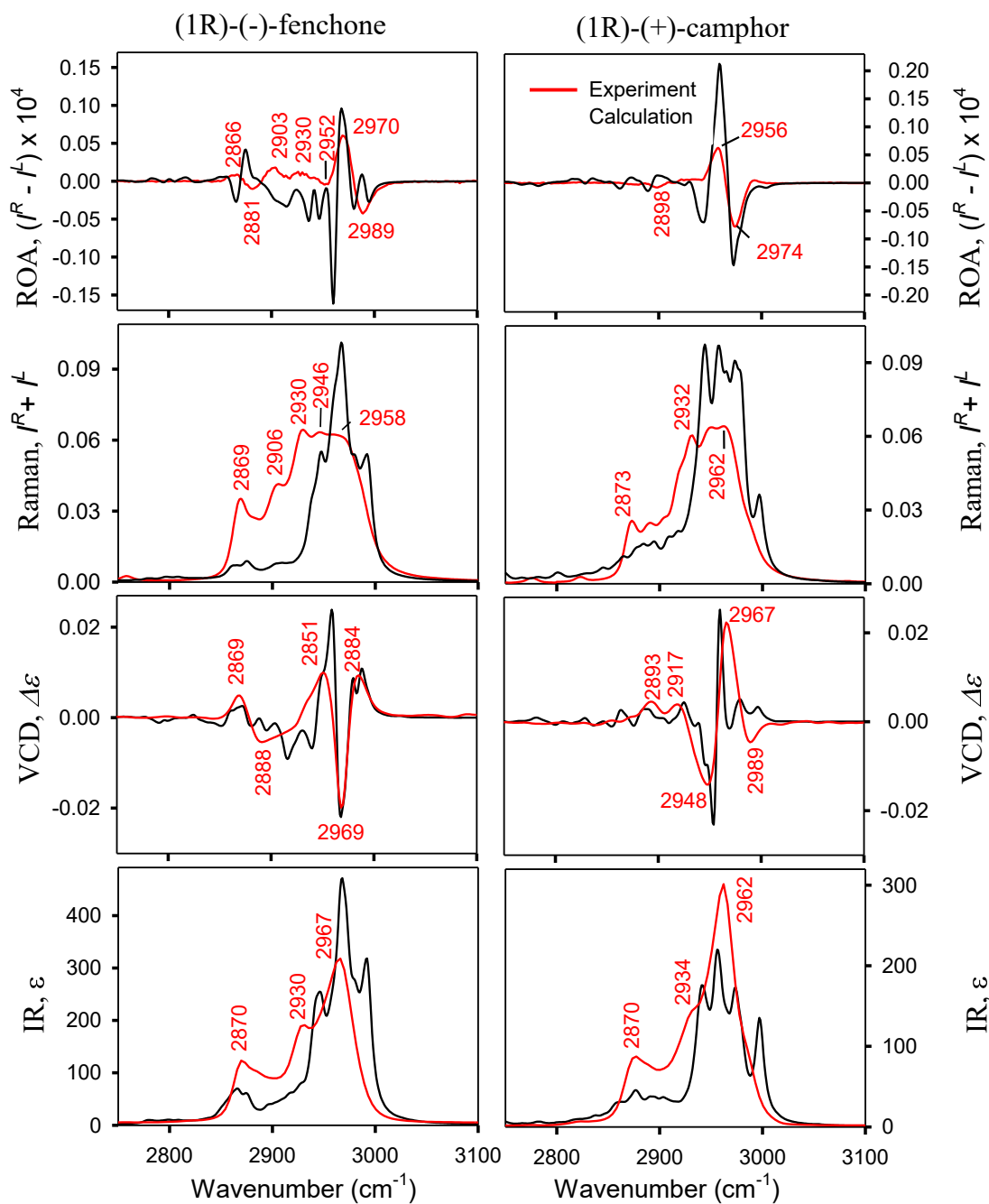


Figure 5.7: Overlaps of the calculated (LVCI with parameters $c_1 = 0.002$, $c_2 = 0.1$) and experimental ROA, Raman, VCD and IR spectra in the C-H stretching region for (1R)-(-)-fenchone (36 modes fixed, 1 086 008 HO states) and (1R)-(+)-camphor (31 modes blocked, 1 906 884 HO states). Redrawn from publication [II] with normalized Raman and ROA spectral intensities.³⁷

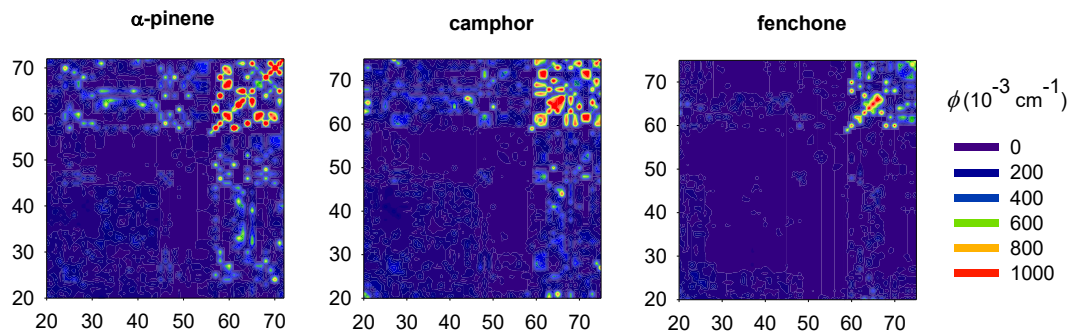


Figure 5.8: Anharmonic coupling (ϕ) between harmonic vibrational modes (for α -pinene, camphor and fenchone), defined for the modes i and j on the x and y axes, as the average of cubic and quartic constants containing these modes (in absolute value, mPW2PLYP//B3LYP/6-311++G**/CPCM calculation, e.g. $|c_{iii}|$, $|c_{ijj}|$, $|d_{ijj}|$, etc.). Adapted from publication [II].

The number of the HO states is dependent not only on the number of blocked vibrations but also on values of coupling parameters c_1 and c_2 (**Fig. 5.9**). The Raman and ROA spectra of α -pinene indicate a good stability and convergence of the transition vibrational frequencies. We started with a one-step selection (with $c_2 = \infty$), where just states interacting with the C-H fundamental vibrations are selected. Even for a relatively weak coupling ($c_1 = 0.0002$) the resultant spectral shape is not very realistic, with a large dispersion of the C-H stretching frequencies. The frequencies are also too high. The two-step HO basis set selection, which adds a second set of states interacting with the first one (provided by c_2 parameter), appears as a more reliable and accurate method. The simulated frequencies and spectral shapes are significantly more realistic, albeit at the expense of the computer memory and time required for much higher number of included HO states.

To summarize, the LVCI method appears as the best simulation method for treating anharmonicities so far, over performing the harmonic and PT2 approaches. The anharmonic corrections improved the experimental-to-calculated relation. We got a correct frequency shift for the C-H stretching vibrations, but not the fine mode splitting. Further development of the LVCI methodology is still needed for ROA and VCD, while a good accuracy was already achieved for Raman and IR spectra. The lower-frequency region ($1350\text{-}1770 \text{ cm}^{-1}$) also significantly benefits from the anharmonic computations. The results also showed that C-H stretching vibrations are

sensitive to the solvent and that empirical dispersion models provide a negligible effect.

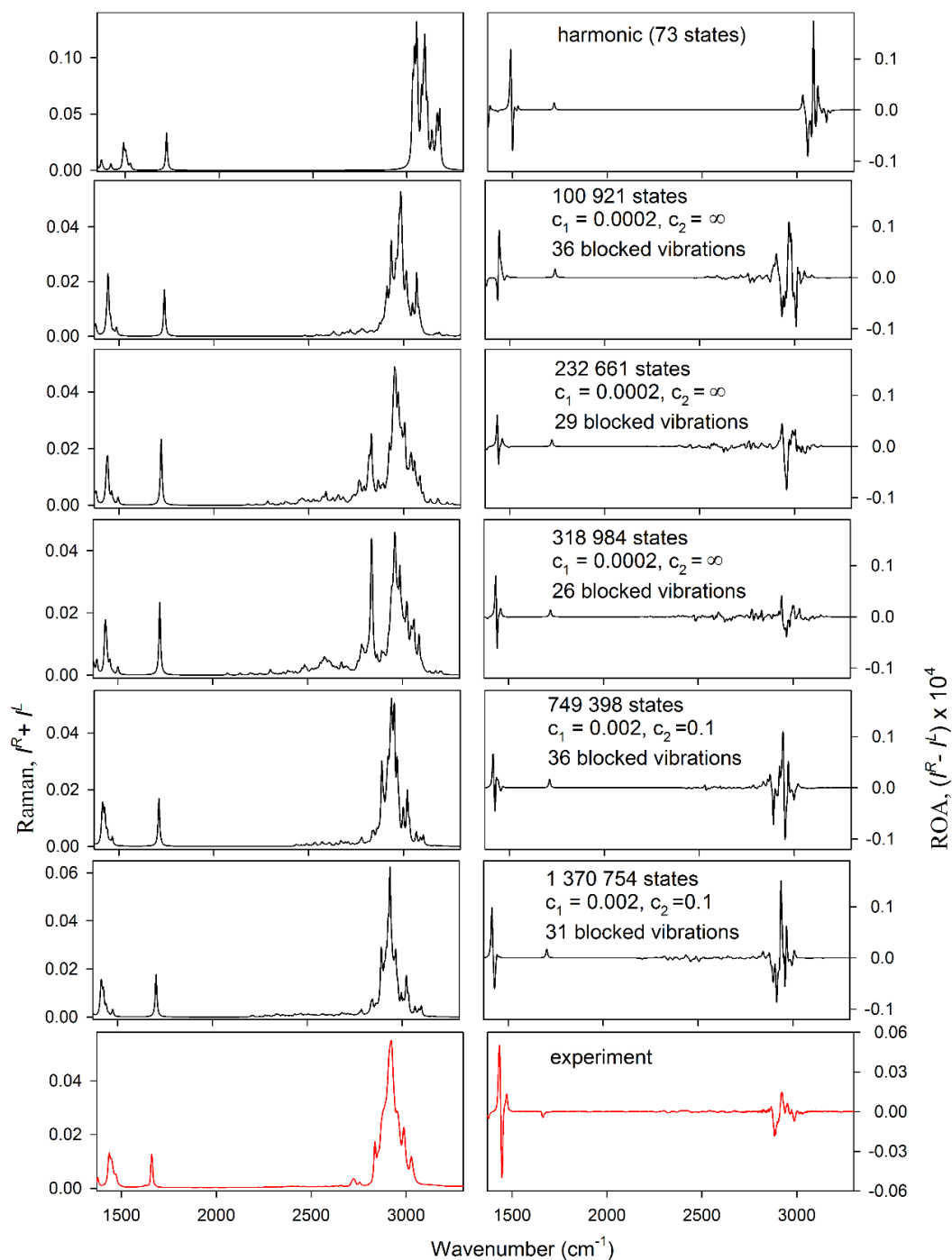


Figure 5.9: Raman and ROA LVCI spectra for (1R)-(+)- α -pinene calculated with different parameters c_1 , c_2 , and a number of blocked vibrations. Bottom: the experimental spectra. Redrawn from publication [II] with an added normalization of Raman and ROA spectral intensities.³⁷

5.3. Tryptophan optical activity

The tryptophan residue plays an important role in peptide conformational studies, especially in those using chiroptical and fluorescence spectroscopic techniques.^{281,282} Tryptophan often exhibits a large optical activity, which interferes with other signals. The contribution of tryptophan to ECD, VCD, ROA and NMR spectra was analyzed in cyclic dipeptides *c*-(Trp-X), where X = Gly, Ala, Trp, Leu, nLeu and Pro (**Fig. 4.3**) in publication [III]. The results were interpreted with the aid of DFT computations and enabled us to better understand the chiral spectral response of Trp residue in larger proteins and to characterize the link between the spectra and molecular structure.

Model cyclic dipeptides were selected as a first step to more complex biomolecular systems as they are more rigid and allow precise computations. Their nature causes rich solvent-solute interactions. The cyclic dipeptides are also known as 2,5-diketopiperazines (DKPs). They have attracted considerable interest because of their potential use in many pharmacological applications, e.g. as antibacterial,²⁸³ antitumor,^{284,285} anticancer,²⁸⁶ and antiviral²⁸⁷ agents. The heterocyclic ring of DKPs can be identified in a variety of biologically active natural products.²⁸⁸ Molecular recognition and thermodynamic properties of DKP derivatives are expected to be useful for understanding the protein folding.²⁸⁹

We were interested in the interaction of Trp residue with the backbone and other side chains of peptides. Such effects are crucial for developing the OA spectroscopic response. A systematic conformational scan was carried out. The conformation of the DKP ring in *c*-(L-Ala-L-Ala) was predicted to be non-planar, with a shallow potential (**Fig. 5.10**). The ring is quite flexible at 300 K ($kT \sim 0.6$ kcal/mol), allowing for large deviations of the ψ and ϕ angles. Two possible puckerings should be taken into account („boat-up“ and „boat-down“) in computations.

We found that the side chains are important for the structure stabilization, and induce non-planarity of the DKP ring (**Fig. 5.11** for *c*-(L-Trp-Gly) and Fig. S2 in publication [III] for other dipeptides). Trp side chains do not move freely but largely oscillate around preferred conformations, which can be categorized according to the values of torsional angles χ_1 and χ_2 . While the extended conformations A and B with $\chi_1 \sim -60^\circ$ (where Trp indole side chain points out from the DKP ring according to **Fig. 4.4**, right) provide two energy minima ($\phi \sim -30$ and 30°), the folded conformations

C and D with $\chi_1 \sim 60^\circ$ (where the Trp indole is above/below the ring) strongly prefer the boat-down ring conformation.

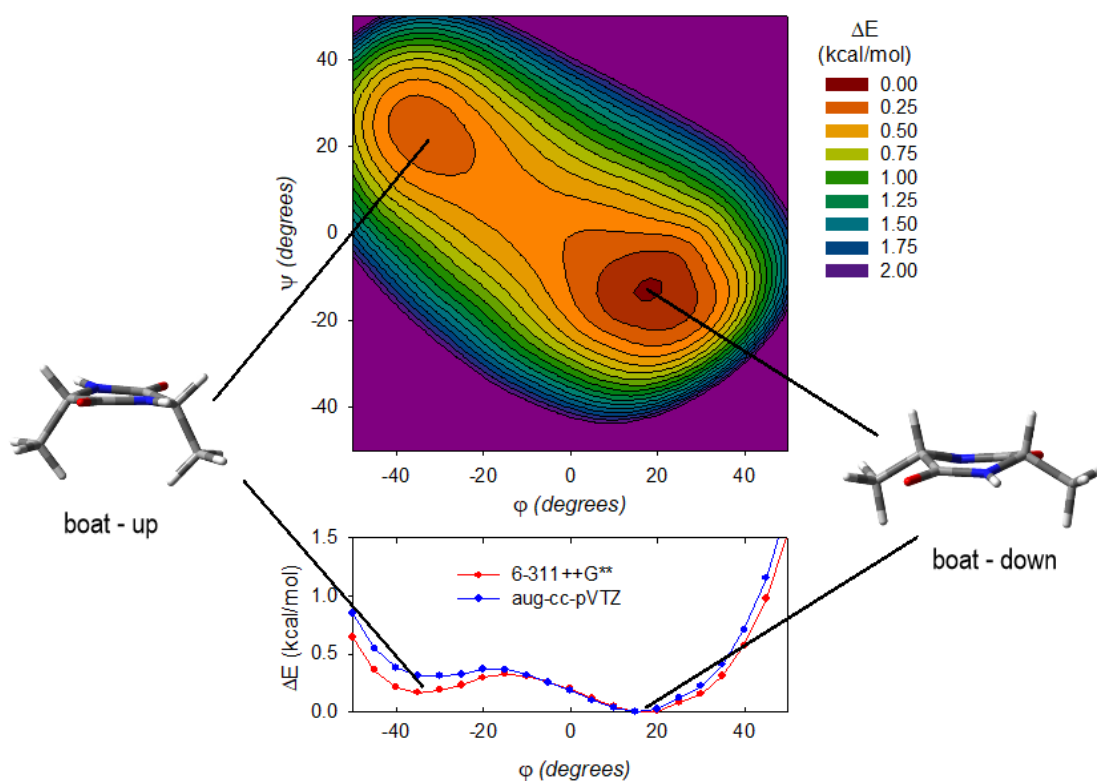


Figure 5.10: Top: calculated 2D potential energy surface for the DKP ring in c-(L-Ala-L-Ala) (ϕ and ψ ; B3LYP/6-311++G**/CPCM(DMSO)). Bottom: corresponding 1D energy scan along the torsion angle ϕ (B3LYP/CPCM(DMSO) with two basis sets). Redrawn from publication [III].

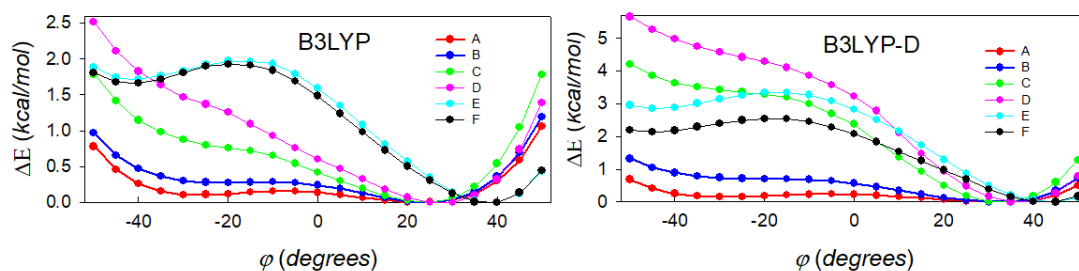


Figure 5.11: Dependence of the relative electronic energies on the torsion angle ϕ for six conformations (A-F) of c-(L-Trp-Gly) defined in Fig. 4.4, calculated at the B3LYP(left) or B3LYP-D(right) /6-311++G**/CPCM(DMSO) levels. Adapted from publication [III].

The energy differences between the two conformations of the DKP ring are notably increased by inclusion of the dispersion correction (eq. 2.27). Such „DFT-D” calculations provide a better description of attractive long-range van der Waals interactions than uncorrected DFT method and significantly change conformer equilibria.^{134,138}

Also the preferred conformation of the Trp side chain is strongly affected by the dispersion correction (**Fig. 5.12** for c-(L-Trp-L-Trp)).

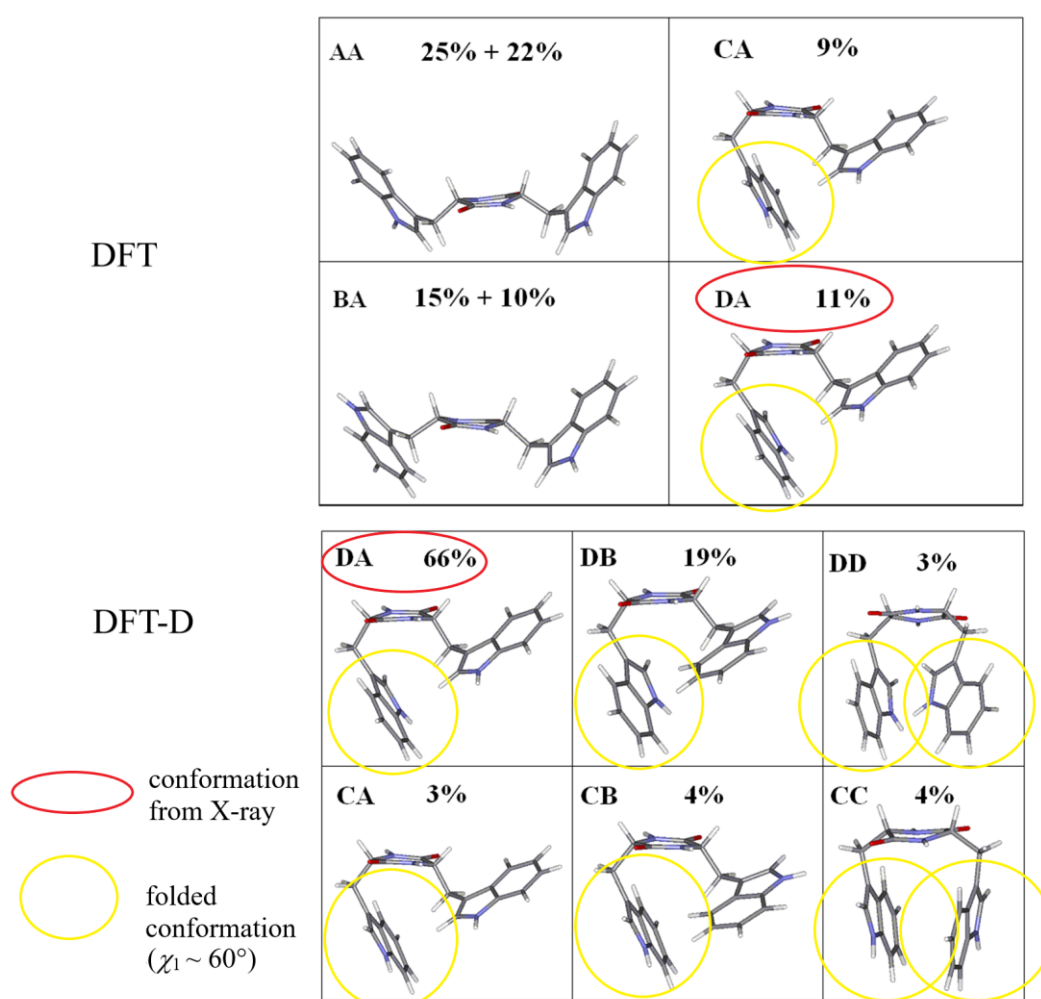


Figure 5.12: Geometries and Boltzmann weights of the most populated conformers of the c-(L-Trp-L-Trp) peptide (Tables 2 and 3 in publication [III] for details). The B3LYP/6-311++G**/CPCM(DMSO) level was used for computations without (DFT, top) and with (DFT-D, at the bottom) correcting for the dispersion interactions. Conformational classes (A-F) of the Trp side chain according to the values of χ_1 and χ_2 angles are defined in **Fig. 4.4**.

The DFT method alone predicts the extended conformers to be the most stable, with a minor but not negligible population of the partially folded ones. The DFT-D approach almost exclusively favors the partially (T-shaped) and completely folded structures, separated from the extended ones by a wide energy margin. The folded structures are favored due to a better description of the $C_{\alpha}\text{-H}\cdots\pi$ intermolecular interaction between the indole group and the DKP ring. The DFT-D results are more consistent with the prevailing T-shaped folded (DA) conformation found in the c-(L-Trp-L-Trp) crystal. The DKP ring was predicted to be almost planar by X-ray crystallography.²⁹⁰ Interestingly, even the c-(L-Trp-Gly) was predicted to be entirely folded by the DFT-D approach, although Gly does not possess any significant polarizable components beyond the DKP ring.

To verify the conformational preferences in real samples, chiroptical spectra (ECD, VCD and ROA) measured for several cyclic dipeptides with tryptophan were compared with spectra obtained by DFT and DFT-D calculations. The geometries and spectra of individual conformers are quite similar (**Fig. 5.13**). The resultant spectrum is thus mostly influenced by the weighting scheme dependent on the relative conformer energies. Spectral contributions of individual conformers are given by their Boltzmann weights (eq. 2.39).

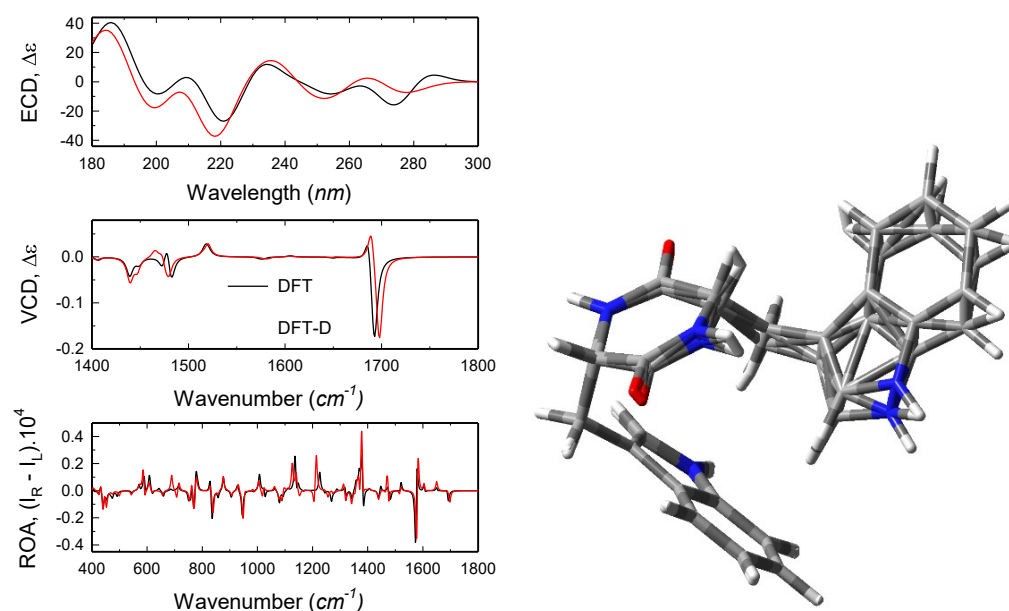


Figure 5.13: Comparison of calculated ECD, VCD and ROA spectra (B3LYP/6-311++G**/CPCM(DMSO)) and geometries (DFT and DFT-D) of the DA conformer of the c-(L-Trp-L-Trp) peptide.

The ECD spectra of c-(Trp-X) dipeptides are dominated by the Trp contributions (π - π^* transitions), even for DKPs with only one Trp. It was suggested that Trp is not interacting significantly with the aliphatic side chain as c-(L-Trp-L-Ala) and c-(L-Trp-L-nLeu) provided almost identical ECD spectra (Fig. 4 in publication [III]). The strongest ECD signal was obtained for c-(L-Trp-L-Trp) with a strong exciton coupling of the Trp residues,²⁹¹ indicating a stable folded conformation. As can be seen in **Fig. 5.14**, the averaging of the conformers has a major impact on the resultant averaged curve and consequently the DFT and DFT-D methods clearly provide very different ECD spectra. The experimental ECD features are better reproduced by the DFT-D computations.

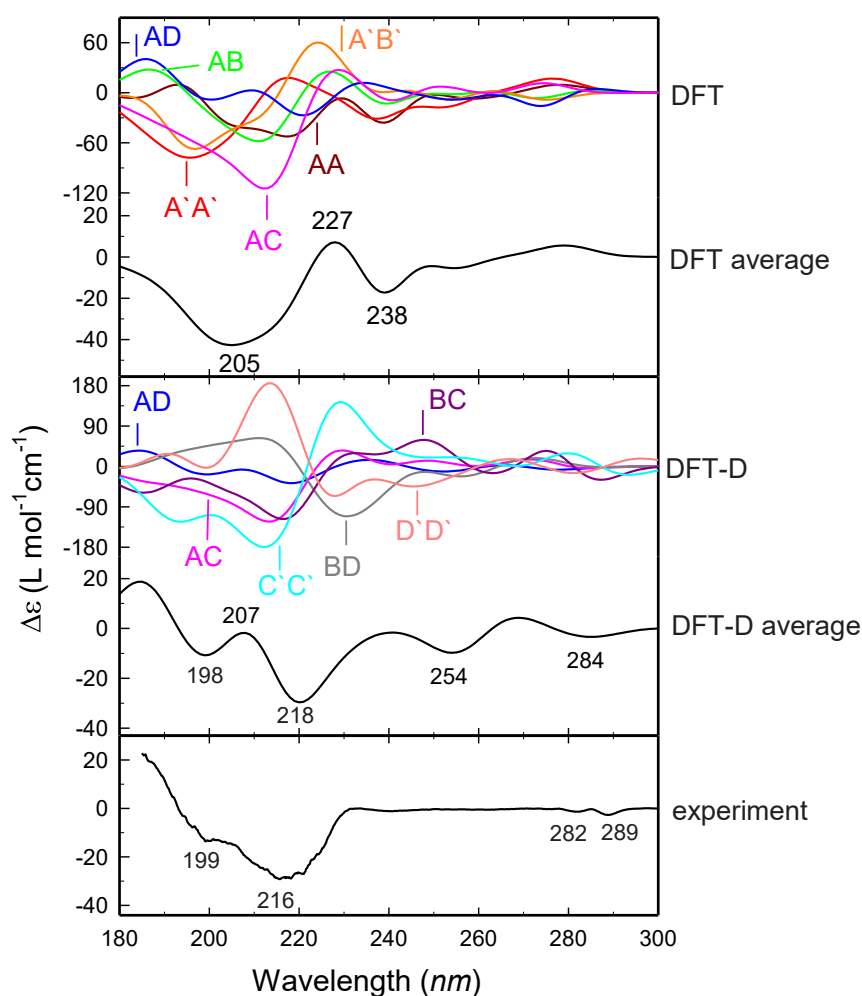


Figure 5.14: Calculated (B3LYP/6-311++G**/CPCM(DMSO), DFT and DFT-D geometries) and experimental ECD spectra of the c-(L-Trp-L-Trp) peptide. Boltzmann weights of different conformers are given in **Fig. 5.12**. Redrawn from publication [III].

The computed ROA and VCD spectra (**Fig. 5.15** and **Fig. 5.16**) of the most stable conformers show a stronger conformational dependence than Raman and IR spectra. The conformer averaging is needed to obtain realistic spectral shapes and intensities. VCD is dominated by the amide modes, well separated from minor Trp contributions (**Fig. 5.15**). However, the relative flatness of the ring makes the VCD weak and subject to artifacts ($g \sim 10^{-5}$ is above but close to our reliable measurement limit). The c-(L-Trp-L-Trp) molecule might have a positive couplet shape (+/-, from lower to higher frequency) in amide I region (C=O stretching) and a negative signal arising from CH₂ motions and amide bands (1430–1530 cm⁻¹) as reproduced correctly by both DFT and DFT-D approaches. The DFT approach overestimates the negative intensities around 1439 cm⁻¹.

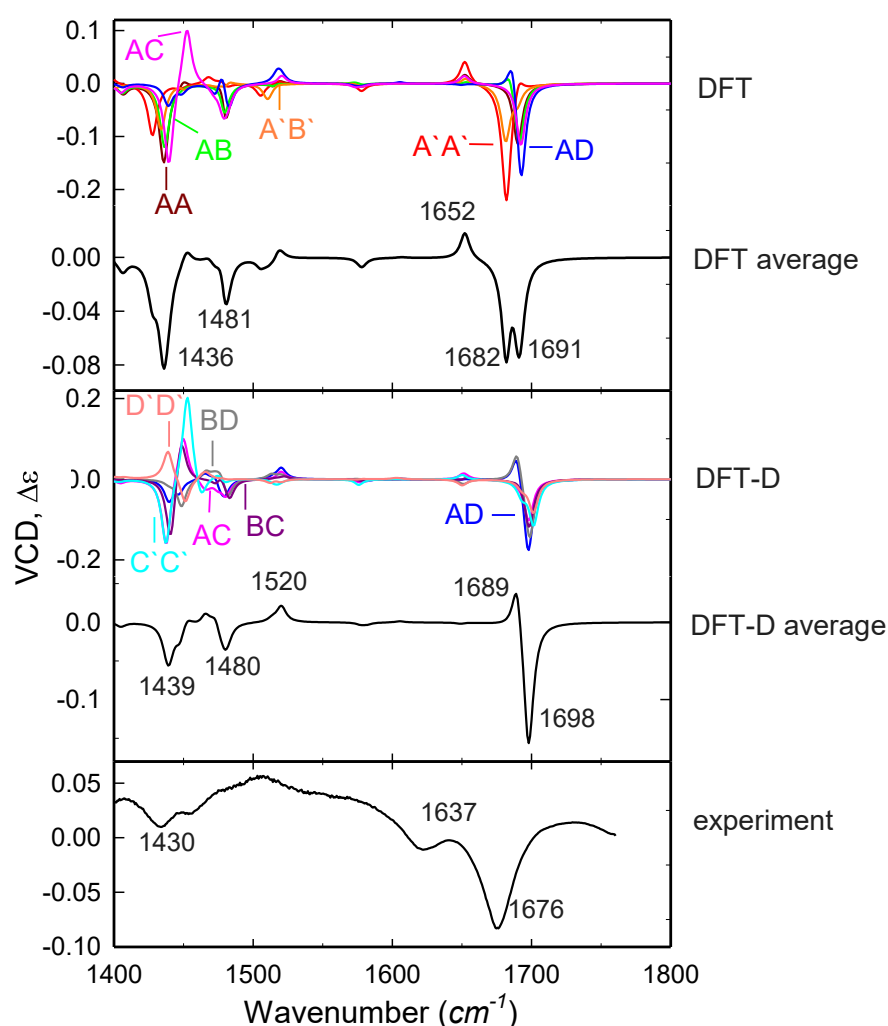


Figure 5.15: Calculated (B3LYP/6-311++G**/CPCM(DMSO)) and experimental VCD spectra of the c-(L-Trp-L-Trp) peptide for DFT and DFT-D geometries. Boltzmann weights of different conformers are in **Fig. 5.12**. Redrawn from publication [III].

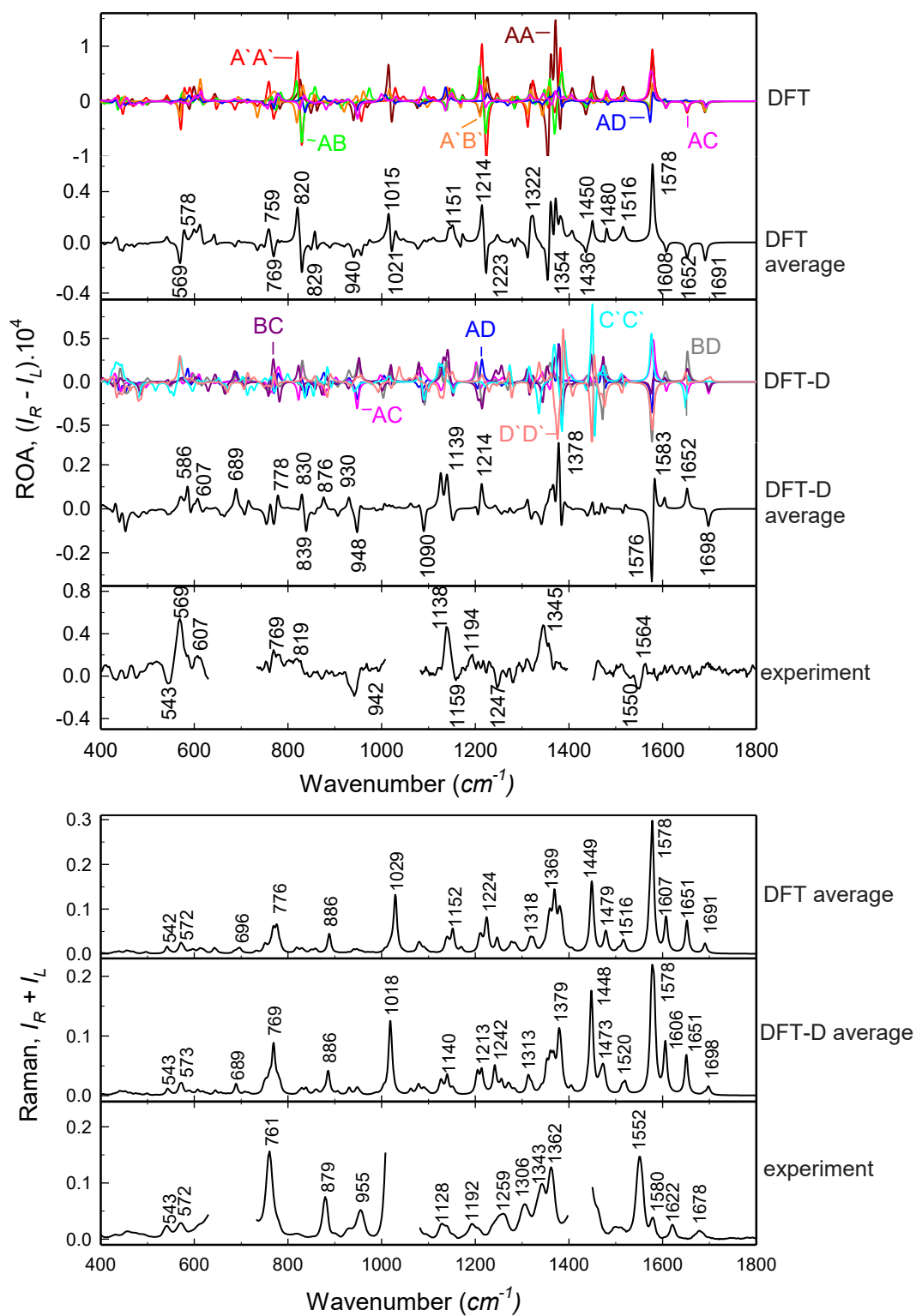


Figure 5.16: Calculated (B3LYP/6-311++G**/CPCM(DMSO)) and experimental ROA and Raman spectra of the c-(L-Trp-L-Trp) peptide for DFT and DFT-D geometries. Boltzmann weights of different conformers are given in Fig. 5.12. Redrawn from publication [III].

The observed Raman spectrum is dominated by the Trp modes and the strongest features are reproduced by both the DFT and DFT-D computations (**Fig. 5.16**). ROA spectra are more sensitive to the Trp side chain conformation, but experimental problems with limited solubility, instability of the samples in the (green) laser light,²⁹² and artifacts associated with the overlap with strong vibrational bands of organic solvents complicated the analysis. In particular, the C=C five-member Trp ring stretching band (experimentally at $\sim 1545\text{--}1560\text{ cm}^{-1}$) appears useful as a unique local probe of the χ_2 angle, which is otherwise difficult to monitor by other methods.¹⁰² A negative ROA band is associated with conformations with $\chi_2 \sim -90^\circ$ and a positive ROA band corresponds to $\chi_2 \sim +90^\circ$. For c-(L-Trp-L-Trp), the prevalence of the T-shaped folded conformers with alternate ($+90^\circ$, -90°) χ_2 values causes partial cancelation and the resultant negative signal is smaller, which can be seen both in the DFT-D and experimental ROA spectra, but not in the DFT average spectrum. For the C-H bending mode at 1350 cm^{-1} (amide III), the predominantly positive experimental ROA signal is better reproduced by the DFT-D model. Also the experimental $+ \cdot -$ pattern within $1100\text{--}1250\text{ cm}^{-1}$ seems to be better reproduced by DFT-D. A negative ROA signal at $920\text{--}942\text{ cm}^{-1}$ is present in both calculations and corresponds to the experimental signal. Also below 900 cm^{-1} both computations mostly reproduced the experimental pattern.

Our study confirmed the advantage of a combination of several spectroscopic techniques. Different spectral types reacted differently on the dispersion correction. Most spectral features were improved when the dispersion was included, which corresponds to similar findings in the past.^{293,137,79} The extended conformation favored by DFT provided poor agreement with the experiment. However, there are also indications that simple adding the dispersion correction to the dielectric solvent model may be an oversimplification. Comparison with experiment suggests that the stability of folded conformers is overestimated for the DFT-D model.

The DFT-D method provided almost the same conformer distribution as the MP2 theory but with a significantly lower computational cost.^{294,295} Also the mPW2PLYP method provided results very similar to DFT-D but it favored more populations of the extended conformers (in total 20%; Table S1 in publication [III]).

A limited accuracy of the DFT-D model in non-aqueous solvents was further supported by the NMR data and the MD conformer ratios lying between the DFT and

DFT-D results. For example, NMR indicated a very flattened boat form of the DKP ring ($\varphi = 9\text{--}12^\circ$, **Table 5.2**), except for c-(L-Trp-L-Pro), for which an opposite pucker ($\varphi = -37^\circ$) was determined. The NMR results agree better with the MD and uncorrected DFT values than with DFT-D. Only for c-(L-Trp-L-Trp), the experimental values are between the DFT and DFT-D results. It seems that DFT-D model overestimates the deformation of the DKP ring.

The spectra and conformer ratios predicted by the CPCM model for solvents of different polarities are almost identical. Only for CHCl_3 the amide I band has a slightly higher frequency (Fig. S1 in publication [III]). However, NMR and MD simulations indicated different conformer ratios for different solvents. The NMR data ($J(\alpha\text{H}-\beta\text{H})$ coupling constants) revealed a significant preference for the folded conformer (with $\chi_1 \sim 60^\circ$) for c-(L-Trp-Gly) and c-(L-Trp-L-Leu) dissolved in DMSO-d_6 and CD_3OD . This finding agrees with the DFT-D results. Extended conformers are strongly preferred in CDCl_3 by all dipeptides. The Trp conformation in c-(L-Trp-L-Trp) could not be determined from NMR data because of the symmetry and fast conformer exchange. MD simulations also indicated that more compact forms are favored in polar solvents (H_2O , DMSO and CH_3OH) and extended forms prevail (90 %) in case of the low-polarity CHCl_3 environment. The NMR spectroscopy and MD simulations are therefore able to reveal finer solvent effects, stemming from the solvent-solute dispersion interactions and hydrogen bonding, which could be only partly included within the DFT/CPCM model.

Table 5.2: Values of φ -angle ($^\circ$) determining the DKP ring conformation in DMSO derived from NMR, MD and Boltzmann averaged values from DFT and DFT-D computations (B3LYP/6-311++G**/CPCM(DMSO)). Adapted from publication [III].

	c-(L-Trp-Gly)		c-(L-Trp-Leu)		c-(L-Trp-L-Pro)	c-(L-Trp-L-Trp)
	Trp	Gly	Trp	Leu	Trp	Trp
φ_{NMR}^a	9	12	9	12	-37	12
φ_{MD}	-	-	-	-	-14	11
φ_{DFT}	7	5	16	18	-37	5
φ_{DFT-D}	36	30	20	16	24	16

^a obtained from the experimental $J(\text{NH}, \alpha\text{H})$ coupling according to ²⁹⁶

Other two studies conducted in collaboration with the University of Tromsø (publication [III'] and [IV']) also demonstrated that the reliability of the spectral interpretation depends on the correct description of the molecular conformation, which is strongly affected by intramolecular interactions. The DFT-D approach was found to be imperative for accurate modelling of the conformer equilibria. Experimental ROA and VCD spectra well correlated with theoretical B3LYP-D spectra for all the absolute configurations (*RS*, *SR*, *SS* and *RR*) of *c*-(Arg-Trp) in publication [III'] and protonated *c*-(Arg-Tyr(OMe)) in publication [IV'].

Our results are in agreement with the later work of dr. Merten et al.,²⁹⁷ in which conformational changes of cyclic tetrapeptides induced by DMSO-*d*₆, CD₃CN and CDCl₃ solvents were studied by VCD. They found that solute–solvent interactions influence the relative population of the conformers and completely change energetic preference and the resultant spectra. Instead of the analysis of the VCD spectra based on energetic differences, they focused on similarities between the experimental and calculated spectral patterns. They concluded that the “explicit” solvation should be considered to account for shifts in conformational distributions and also changes in single-conformer spectra.²⁹⁸

To summarize, the chiroptical spectroscopies supported by theoretical calculations provided useful insight into the conformation of the Trp side chain. It was difficult to balance the dispersion with the solvent and dynamical aspects. Considering the importance of accurate conformer energies, it is not clear that the quality of currently used MD force fields is high enough.

5.4. Circularly polarized luminescence of the europium (III) complex

The interaction of a series of histidine-containing peptides with the racemic $[\text{Eu}(\text{DPA})_3]^{-3}$ complex was monitored in publication [IV] by CPL, in order to understand the binding mode and the role of the main peptide chain. The DPA complex itself exists in two chiral forms (traditionally referred to as “ Λ ” and “ Δ ”), which are normally present in equal amounts. Perturbation of the $\Lambda \rightleftharpoons \Delta$ equilibrium in a presence of chiral component has been suggested as the primary mechanism of chirality induction.

The complexity of the lanthanide complex-peptide interactions nowadays does not allow accurate theoretical calculations due to the necessity to involve non-Born-Oppenheimer phenomena, induced optical activity, open-shell systems and relativity. We have tried to rationalize the measured data by calculations of the binding strength correlated with the CPL intensity.

The effect of the peptide length was studied for His-(Gly) $_n$ peptides, where $n = 1, 2$ and 3 (**Fig. 5.17**). Addition of the peptides to the $\text{Na}_3[\text{Eu}(\text{DPA})_3]$ complex led to a ~30% [for His-(Gly) $_3$] up to 70% (for His-Gly) decrease of the TL compared to the pure complex. The strongest signals both in the $^5\text{D}_0 \rightarrow ^7\text{F}_1$ (~1900 cm^{-1}) and $^5\text{D}_1 \rightarrow ^7\text{F}_2$ (~850 cm^{-1}) regions belongs to the longest His-(Gly) $_3$ peptide, while for His-Gly the CPL is rather weak around 1900 cm^{-1} and hidden in noise at 850 cm^{-1} . His-(Gly) $_2$ provides weaker $^5\text{D}_0 \rightarrow ^7\text{F}_1$ bands with nearly opposite signs. Although the CPL shapes for His-(Gly) $_2$ and His-(Gly) $_3$ are not exact “mirror images”, as a first approximation we can interpret the results as perturbation of the $\Lambda \rightleftharpoons \Delta$ complex enantiomeric equilibrium by the chiral peptide matrices.^{299,300}

The stabilization energies of all complexes are rather low (~2–3 kcal/mol) according to the free energy profiles (**Fig. 5.17**, right). From the relative binding strengths (*s*, eq. 4.9) of His-Gly and His-(Gly) $_2$ no favoring of the Λ or Δ enantiomer within computational accuracy is apparent (**Fig. 5.18**). For His-(Gly) $_3$ at pH ~ 4, however, the Δ binding seems to be more energetically convenient than for Λ . The simulations have confirmed the stronger binding observed for His-(Gly) $_3$. The chirality CPL inversion observed for His-(Gly) $_2$ /His-(Gly) $_3$ was not unambiguously supported by theory, nevertheless we can see that the Λ and Δ His-(Gly) $_2$ forms are predicted to

have about the same probability for $\text{pH} \sim 4$, and the Λ form is preferred at higher pH . The inversion thus can be at least partially explained by a residual presence of the neutral species in the sample. Inspection of geometries obtained close to the energy minima suggested a significant role of the His charge and perhaps a π - π interaction of the His ring with the DPA ligands. In some MD snapshots the interaction of the Gly residues with the complex was apparent as well, which is consistent with relatively high CPL observed for the longest His-(Gly)₃ peptide.

The dependence of the TL and CPL spectra on pH was studied for His-(Gly)₂ (**Fig. 5.19**). The TL is about constant for $\text{pH} \sim 7$ and 10, and dropping by 30–60% for $\text{pH} \sim 4$. The predominantly positive charge of the peptides at $\text{pH} \sim 4$ favors the interaction with the complex and the CPL intensity decreases with increasing pH , which is supported by the MD computations (**Fig. 5.18**).

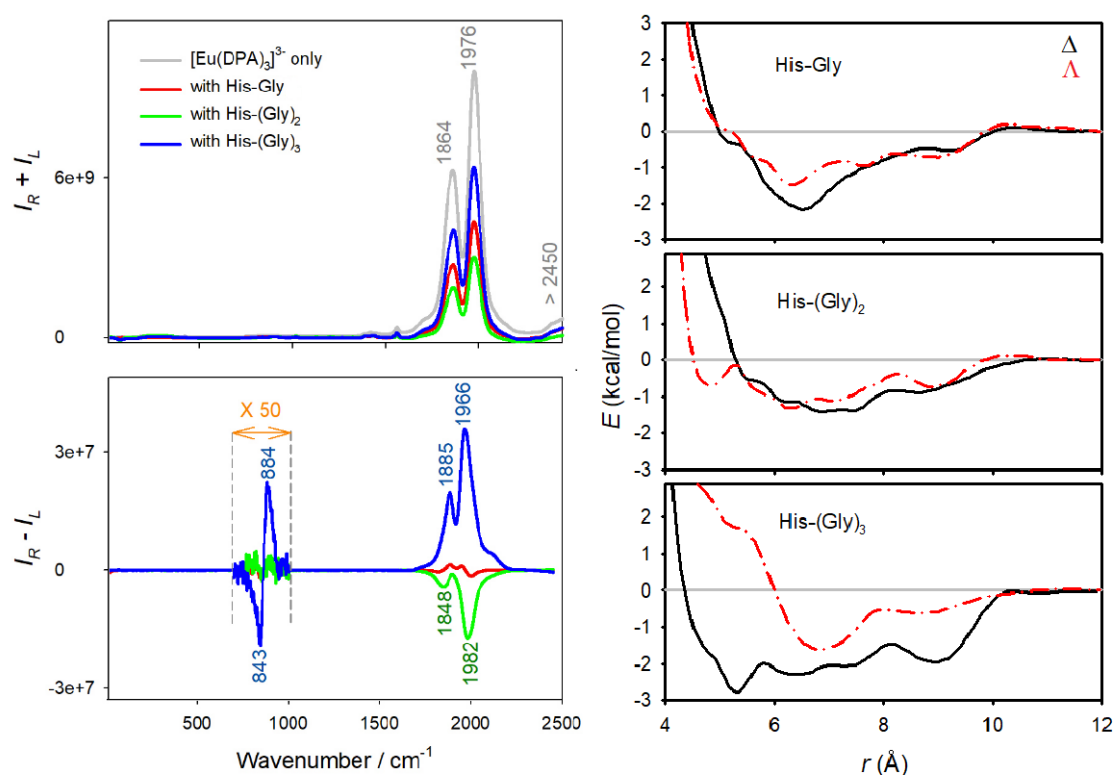


Fig. 5.17: Left: Experimental TL and CPL $[\text{Eu}(\text{DPA})_3]^{3-}$ (4 mM) spectra when chelated with His-(Gly)_n ($n = 1, 2$ and 3; 20 mM, $\text{pH} = 4$). Right: Corresponding calculated free energy profiles for the Δ and Λ forms of $[\text{Eu}(\text{DPA})_3]^{3-}$ complex as dependent on the Eu and $^{\alpha}\text{C}$ of His distance. Redrawn from publication [IV].

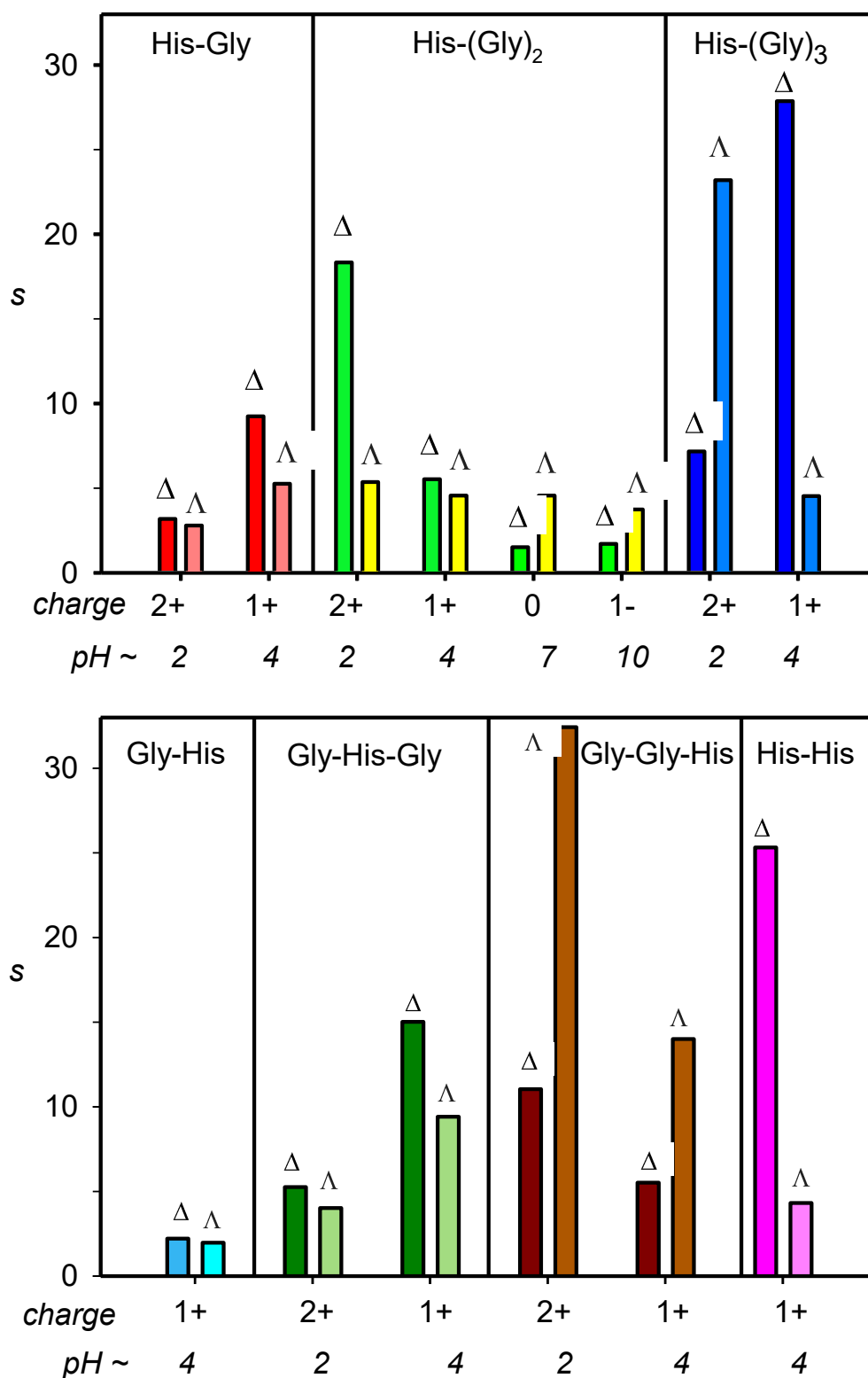


Fig. 5.18: Calculated binding strength of the peptides s , obtained as the ratio (N_B/N_F) of bonded and free complex molecules in the simulation box (eq. 4.9) for different values of pH. Redrawn from publication [IV].

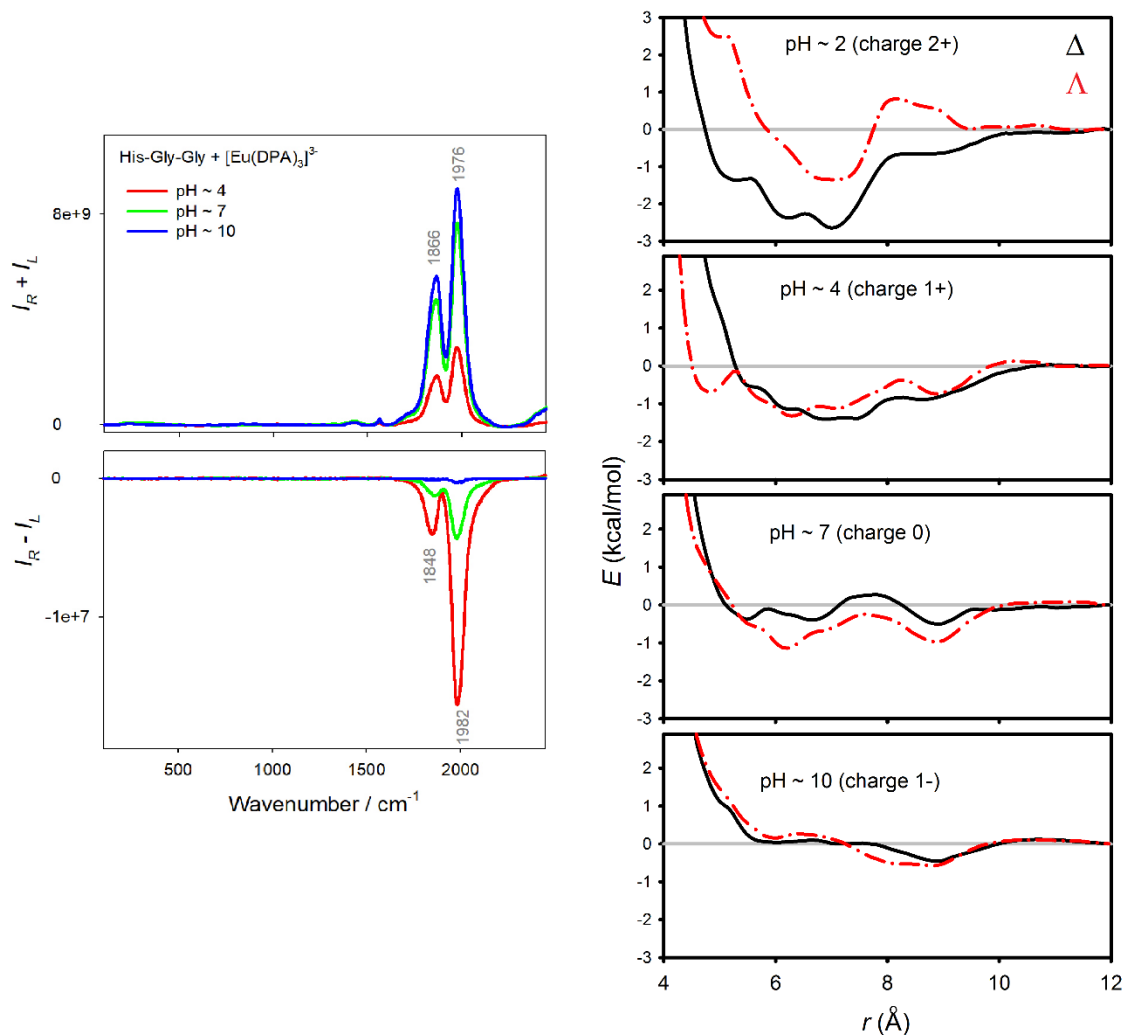


Fig. 5.19: Left: Experimental TL and CPL spectra, mixtures of $[\text{Eu}(\text{DPA})_3]^{3-}$ (4 mM) with His-Gly-Gly (20 mM) at three different pH values. Right: Calculated free energy dependent on Eu-his distance for His-Gly-Gly in complex with Δ and Λ forms of $[\text{Eu}(\text{DPA})_3]^{3-}$ at four different pH values. Redrawn from publication [IV].

The influence of the histidine position in the peptide chain on CPL spectra was investigated for Gly-His, Gly-His-Gly, Gly-Gly-His and His-His peptides (**Fig. 5.20**). The TL intensity decreases gradually for His-Gly-Gly, Gly-His-Gly and Gly-Gly-His. The His residue in the middle (Gly-His-Gly) and at the C-terminus (Gly-Gly-His) induces a weaker CPL signal with nearly opposite sign for the $^5\text{D}_0 \rightarrow ^7\text{F}_1$ transitions compared to His-(Gly)₂. Most probably the His-(Gly)₂ stabilizes the different enantiomer of the complex (Λ).

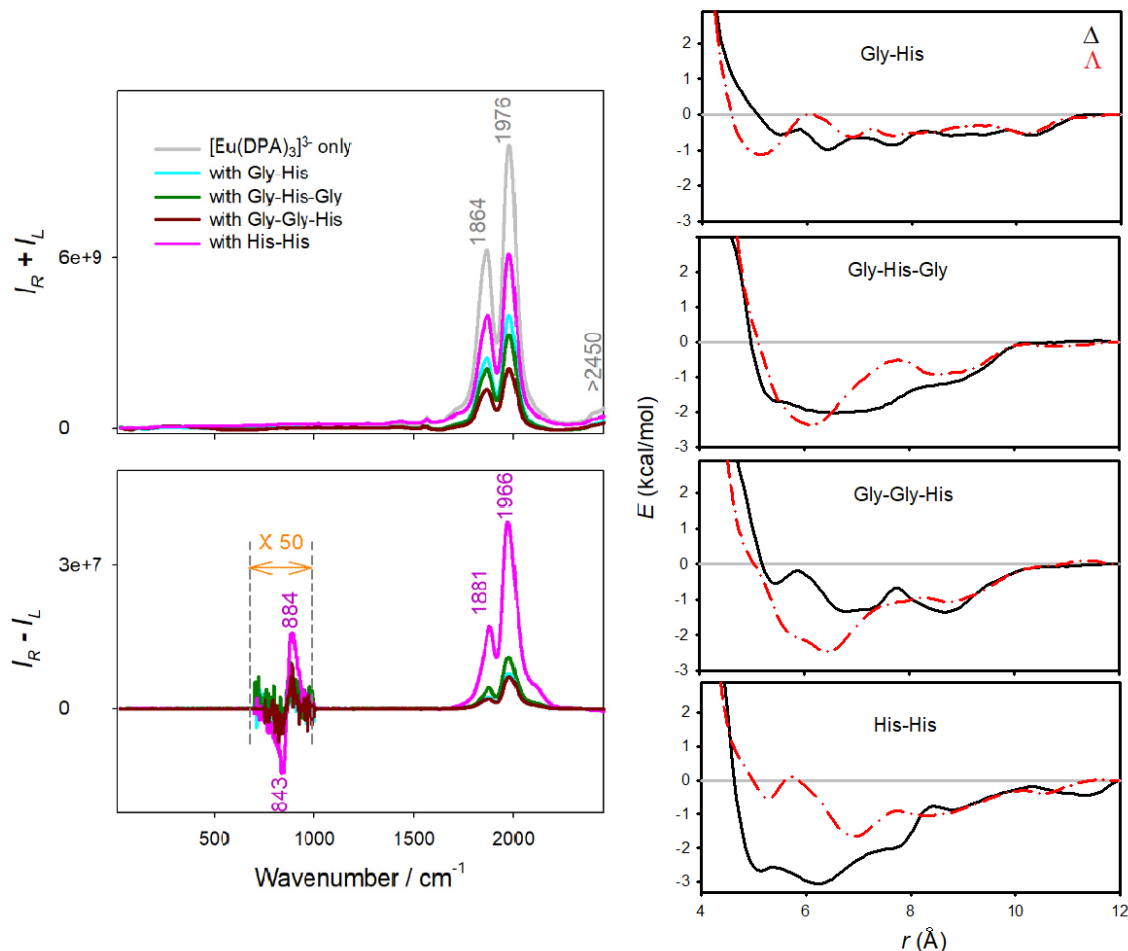


Fig. 5.20: Left: Experimental TL and CPL $[\text{Eu}(\text{DPA})_3]^{3-}$ (4 mM) spectra when chelated with Gly-His, Gly-His-Gly, Gly-Gly-His and His-His (20 mM, pH = 4). Right: Corresponding calculated free energy profiles as dependent on the Eu and ^{13}C of His distance for Δ and Λ forms of $[\text{Eu}(\text{DPA})_3]^{3-}$ complex. Redrawn from publication [IV].

We can speculate that in His-(Gly)₂ the NH_3^+ charge strengthens the binding potency of His, while in Gly-His-Gly and Gly-Gly-His the C-terminal COO^- group weakens it. Most probably other factors, such as dissociation equilibria and van der Waals interactions, also contribute to the electrostatic effects. Free energy profiles provide quite broad and shallow energy “well”, so the “binding” is very weak and the resultant associate may not have a rigid geometry.⁶² The strongest binding is suggested for His-His (**Fig. 5.20**) in agreement with experiment. As the preference of the Λ / Δ form of $[\text{Eu}(\text{DPA})_3]^{3-}$ complex probably correlates with the CPL sign, the theoretical prediction for Gly-Gly-His is therefore not consistent with the experimental observations. Thus the simulations at the present protocol do not seem to be reliable

enough to be used for chirality determination. Nevertheless, they well explain many aspects of the binding, some general trends, and at least suggest that the quite attractive idea of determination of the complex absolute configuration through combination of the theory and experiment is possible.

To summarize, the data indicate a relatively weak binding of the His residue to the $[\text{Eu}(\text{DPA})_3]^{-3}$ complex, with a strong participation of other peptide parts. Longer peptides, low pH and His residue close to the N-peptide terminus favors the binding. The magnitude of the CPL intensity roughly correlates with the MD simulations. The sensitivity of the lanthanide binding to the peptide structure, the large luminescence and optical activity make the technique suitable for probing peptide and protein secondary and tertiary structure.

Conclusions

Our results confirmed that vibrational optical activity and CPL are very sensitive to the molecular structure. In theoretical modelling, special attention should be paid to molecular flexibility and proper conformational averaging, modelling of different solvents and inclusion of vibrational anharmonicities.

The first project focused on solvent models. The normal mode optimization method was applied to an ensemble of clusters of lactamide with a few explicit water molecules. The broadening of the simulated vibrational bands could be efficiently controlled by the normal mode optimization constraint. The most realistic theoretical spectra were obtained for the cutoff frequency $\omega_{max} \sim 200\text{--}300\text{ cm}^{-1}$. This procedure can be rationalized to a large extent by the quantum properties of the vibrations, and provides an efficient means of modeling vibrational properties of molecules in solutions.

The second project was dedicated to VOA spectra of several rigid molecules in the C-H stretching region. The harmonic approach approximately reproduced the experimental spectral patterns. However, more accurate spectral patterns were obtained with the anharmonic corrections implemented via the LVCI formalism. A limited interaction between the C-H stretching and lower-frequency modes was assumed. Many HO states could be included owing to an efficient implementation of the diagonalization procedure. We found that the calculations beyond the harmonic limit also improved the lower-frequency vibrations (e.g., around 1400 cm^{-1}). In the future, we want to extend the computational procedures to hydrated biomolecules, e.g. to estimate the effects of the solvation, conformation and the anharmonic corrections in a consistent way.

In the third project, we studied the role of the dispersion forces for conformer equilibria and dynamics of tryptophan in cyclic dipeptides. The calculations provided a good basis for interpretation of the data obtained from several spectroscopic techniques (ROA, ECD, VCD and NMR). Stable conformers yielded about the same spectra within the DFT and DFT-D approach, but a dispersion DFT correction energetically favored compact folded forms. The dispersion-corrected computations provided spectra closer to the experiment, but still with a limited accuracy, especially for non-aqueous solvents. Most probably, the stability of the folded conformers was

overestimated as also indicated by the NMR data and MD simulations. The 1554 cm^{-1} ROA signal appeared useful as a unique local probe of the χ_2 angle.

The last project was dedicated to lanthanide complexes with histidine-containing peptides. The CPL spectra sensitively reacted on the position of histidine in the peptide chain, which could be rationalized by MD simulations. The interaction of the complex with the peptides was predicted to be rather weak and site-unspecific. Nevertheless, resultant CPL patterns were still quite characteristic for individual peptides. This is promising for future design of similar “smart” probes for chemical imaging of peptides and proteins and other bio-molecular structures. CPL itself was measured using the relatively new “ROA/CPL” methodology, enabling to obtain weak CPL signals immeasurable otherwise.

Quantum-chemical simulations became an integral part of experimental vibrational spectroscopy. This thesis focused on improving the accuracy of the simulations by including anharmonic, solvent, molecular flexibility and dynamics and other finer effects into computations. Accurate interpretation of vibrational spectra (spectral frequencies, intensities and actual band shapes) based on a combination of experimental and theoretical approaches lead to a deeper understanding of molecular structure, dynamics and interactions that govern the peptide and protein spectral features and other physical properties.

Bibliography

1. Mason, S. F., The Development of Theories of Optical Activity and Their Applications. In *Optical Rotatory Dispersion and Circular Dichroism*, Ciardelli, F.; Salvadori, P., Eds. Heydon & Son,: London, 1973; pp 27-40.
2. Barron, L. D., *Molecular Light Scattering and Optical Activity, Second Edition*. Cambridge University Press: Cambridge, 2009.
3. Arrago, D. F., *Mem. de L'Inst.* **1811**, 12 (part 1), 93.
4. Fresnel, A., *Bull. Soc. Philomath.* **1824**, 147.
5. Pasteur, L., *Thésés de chimie et de physique*. Bachelier: Paris, 1847.
6. Fischer, E., Synthese des Traubenzuckers. *Berichte der deutschen chemischen Gesellschaft* **1890**, 23, 799-805.
7. Cahn, R. I., C.; Prelog, V., Specification of Molecular Chirality. *Angewandte Chemie, Intl. Ed.* **1966**, 5 (4), 385-415.
8. Keinan, E. S., I. (eds), *Chemistry for the 21st Century*. Weinheim: Wiley-VCH, 2000.
9. Bettelheim, F.; Brown, W.; Campbell, M.; Farrell, S.; Torres, O., *Introduction to Organic and Biochemistry*. Cengage Learning: 2012.
10. Polavarapu, P. L., Renaissance in Chiroptical Spectroscopic Methods for Molecular Structure Determination. *Chem. Rec.* **2007**, 7 (2), 125-126.
11. Lowry, T. M., *Optical Rotatory Power*. Longmans, Green and Co.: London, 1935.
12. Djerassi, C., *Optical Rotatory Dispersion: Applications to Organic Chemistry*. McGraw-Hill & Company: New York, 1960.
13. Polavarapu, P. L., Protocols for the Analysis of Theoretical Optical Rotations. *Chirality* **2006**, 18, 348-356.
14. Polavarapu, P. L., Kramers–Kronig Transformation for Optical Rotatory Dispersion Studies. *J. Phys. Chem. A* **2005**, 109, 7013-7023.
15. Polavarapu, P. L. P., A. G.; Zhang, P., Kramers-Kronig Transformation of Experimental Electronic Circular Dichroism: Application to the Analysis of Optical Rotatory Dispersion in Dimethyl-L-tartrate. *Chirality* **2006**, 18 (9), 723-732.
16. Riehl, J. P.; Richardson, F. S., Circularly Polarized Luminescence Spectroscopy. *Chem. Rev.* **1985**, 86, 1-16.
17. Riehl, J. P.; Muller, G., Circularly Polarized Luminescence Spectroscopy and Emission-Detected Circular Dichroism. In *Comprehensive Chiroptical Spectroscopy, Volume 1: Instrumentation, Methodologies, and Theoretical Simulations*, Berova, N.; Polavarapu, P. L.; Nakanishi, K.; Woody, R. W., Eds. John Wiley & Sons: Hoboken NJ, USA, 2012; Vol. 1, pp 65-90.
18. Urbanová, M.; Maloň, P., Circular Dichroism Spectroscopy. In *Analytical Methods in Supramolecular Chemistry*, Schalley, C. A., Ed. Wiley-VCH: New York, 2007; p 265.
19. Barron, L. D., In *Chirality at the Nanoscale*, Amabilino, D. B., Ed. Wiley-VCH: New York, 2009; p 1.
20. Barron, L. D.; Bogaard, M. P.; Buckingham, A. D., Raman Scattering of Circularly Polarized Light by Optically Active Molecules. *J. Am. Chem. Soc.* **1973**, 95, 603-605.
21. Hug, W.; Kint, S.; Bailey, G. F.; Schere, J. R., Raman Circular Intensity Differential Spectroscopy. The Spectra of (-)- α -Pinene and (+)- α -Phenylethylamine. *J. Am. Chem. Soc.* **1975**, 97 (5589-5590).

22. Holzwarth, G.; Hsu, E. C.; Mosher, H. S.; Faulkner, T. R.; Moscowitz, A., Infrared Circular Dichroism of Carbon-Hydrogen and Carbon-Deuterium Stretching Modes. Observations. *J. Am. Chem. Soc.* **1974**, *96* (1), 251-252.
23. Nafie, L. A.; Qu, X. H.; Long, F. J.; Freedman, T. B., Optical Design and Sampling Methods for the Measurement of Vibrational Circular Dichroism with a Nicolet Magna FT-IR Spectrometer. *Mikrochim. Acta* **1997**, *S14*, 803-805.
24. Hug, W.; Hangartner, G., A Novel High-Throughput Raman Spectrometer for Polarization Difference Measurements. *J. Raman Spectrosc.* **1999**, *30* (9), 841-852.
25. Blanch, E. W.; Hecht, L.; Barron, L. D., Vibrational Raman Optical Activity of Proteins, Nucleic Acids, and Viruses. *Methods* **2003**, *29* (2), 196-209.
26. Keiderling, T. A., Protein and Peptide Secondary Structure and Conformational Determination with Vibrational Circular Dichroism. *Curr. Opin. Chem. Biol.* **2002**, *6*, 682-688.
27. Bell, A. F.; Hecht, L.; Barron, L. D., Vibrational Raman Optical Activity of DNA and RNA. *J. Am. Chem. Soc.* **1998**, *120*, 5820-5821.
28. Yaffe, N. R.; Almond, A.; Blanch, E. W., A New Route to Carbohydrate Secondary and Tertiary Structure using Raman Spectroscopy and Raman Optical Activity. *J. Am. Chem. Soc.* **2010**, *132* (31), 10654-10655.
29. Blanch, E. W.; Hecht, L.; Syme, C. D.; Volpetti, V.; Lomonosoff, G. P.; Nielsen, K.; Barron, L. D., Molecular Structures of Viruses from Raman Optical Activity *Journal of General Virology* **2002**, *83*, 2593-2600.
30. Polavarapu, P. L., Quantum Mechanical Predictions of Chiroptical Vibrational Properties. *Int. J. Quantum Chem.* **2006**, *106* (8), 1809.
31. Frisch, M. J.; Trucks, G. W.; Schlegel, H. B.; Scuseria, G. E.; Robb, M. A.; Cheeseman, J. R.; Scalmani, G.; Barone, V.; Petersson, G. A.; Nakatsuji, H.; Li, X.; Caricato, M.; Marenich, A. V.; Bloino, J.; Janesko, B. G.; Gomperts, R.; Mennucci, B.; Hratchian, H. P.; Ortiz, J. V.; Izmaylov, A. F.; Sonnenberg, J. L.; Williams; Ding, F.; Lipparini, F.; Egidi, F.; Goings, J.; Peng, B.; Petrone, A.; Henderson, T.; Ranasinghe, D.; Zakrzewski, V. G.; Gao, J.; Rega, N.; Zheng, G.; Liang, W.; Hada, M.; Ehara, M.; Toyota, K.; Fukuda, R.; Hasegawa, J.; Ishida, M.; Nakajima, T.; Honda, Y.; Kitao, O.; Nakai, H.; Vreven, T.; Throssell, K.; Montgomery Jr., J. A.; Peralta, J. E.; Ogliaro, F.; Bearpark, M. J.; Heyd, J. J.; Brothers, E. N.; Kudin, K. N.; Staroverov, V. N.; Keith, T. A.; Kobayashi, R.; Normand, J.; Raghavachari, K.; Rendell, A. P.; Burant, J. C.; Iyengar, S. S.; Tomasi, J.; Cossi, M.; Millam, J. M.; Klene, M.; Adamo, C.; Cammi, R.; Ochterski, J. W.; Martin, R. L.; Morokuma, K.; Farkas, O.; Foresman, J. B.; Fox, D. J., *Gaussian 16*. Wallingford, CT, 2016.
32. Aidas, K.; Angeli, C.; Bak, K. L.; Bakken, V.; Bast, R.; Boman, L.; Christiansen, O.; Cimiraglia, R.; S., C.; Dahle, P.; Dalskov, E. K.; Ekström, U.; Enevoldsen, T.; Eriksen, J. J.; Ettenhuber, P.; Fernández, B.; Ferrighi, L.; Fliegl, H.; Frediani, L.; Hald, K.; Halkier, A.; Hättig, C.; Heiberg, H.; Helgaker, T.; Hennum, A. C.; Hettema, H.; Hjertenæs, E.; Høst, S.; Høyvik, I. M.; Iozzi, M. F.; Jansík, B.; Jensen, H. J.; Jonsson, D.; Jørgensen, P.; Kauczor, J.; Kirpekar, S.; Kjærgaard, T.; W., K.; Knecht, S.; Kobayashi, R.; Koch, H.; Kongsted, J.; Krapp, A.; Kristensen, K.; Ligabue, A.; Lutnæs, O. B.; Melo, J. I.; Mikkelsen, K. V.; Myhre, R. H.; Neiss, C.; Nielsen, C. B.; Norman, P.; Olsen, J.; Olsen, J. M.; Osted, A.; Packer, M. J.; Pawłowski, F.; Pedersen, T. B.; Provasi, P. F.; Reine, S.; Rinkevicius, Z.; Ruden, T. A.; Ruud, K.; Rybkin, V. V.; Sałek, P.; Samson, C. C.; de Merás, A. S.; Saue, T.; Sauer, S. P.; Schimmelpfennig, B.; Sneskov, K.; Steindal, A. H.; Sylvester-Hvid, K. O.; Taylor, P. R.; Teale, A. M.; Tellgren, E. I.; Tew, D. P.; Thorvaldsen, A. J.; Thøgersen, L.; Vahtras, O.; Watson, M. A.; Wilson, D. J.; Ziolkowski, M.; Agren, H., *The Dalton Quantum*

Chemistry Program System. *Wiley Interdiscip Rev Comput Mol Sci.* **2014**, *4* (3), 269-284.

33. Baerends, E. J.; Ziegler, T.; Autschbach, J.; Bashford, D.; Bérces, A.; Bickelhaupt, F. M.; Bo, C.; Boerrigter, P. M.; Cavallo, L.; Chong, D. P.; Deng, L.; Dickson, R. M.; Ellis, D. E.; van Faassen, M.; Fan, L.; Fischer, T. H.; Guerra, C. F.; Franchini, M.; Ghysels, A.; Giammona, A.; van Gisbergen, S. J. A.; Götz, A. W.; Groeneveld, J. A.; Gritsenko, O. V.; Grüning, M.; Gusarov, S.; Harris, F. E.; van den Hoek, P.; Jacob, C. R.; Jacobsen, H.; Jensen, L.; Kaminski, J. W.; van Kessel, G.; Kootstra, F.; Kovalenko, A.; Krykunov, M. V.; van Lenthe, E.; McCormack, D. A.; Michalak, A.; Mitoraj, M.; Morton, S. M.; Neugebauer, J.; Nicu, V. P.; Noodleman, L.; Osinga, V. P.; Patchkovskii, S.; Pavanello, M.; Philipson, P. H. T.; Post, D.; Pye, C. C.; Ravenek, W.; Rodríguez, J. I.; Ros, P.; Schipper, P. R. T.; Schreckenbach, G.; Seldenthuis, J. S.; Seth, M.; Snijders, J. G.; Solà, M.; Swart, M.; Swerhone, D.; te Velde, G.; Vernooijs, P.; Versluis, L.; Visscher, L.; Visser, O.; Wang, F.; Wesolowski, T. A.; van Wezenbeek, E. M.; Wiesenekker, G.; Wolff, S. K.; Woo, T. K.; Yakovlev, A. L. *ADF2013*, SCM, Theoretical Chemistry, Vrije Universiteit: Amsterdam, The Netherlands, 2013.

34. Amos, R. D. *CADPAC: The Cambridge Analytic Derivative Package*, Issue 6.0; SERC Laboratory: Daresbury, UK, 1995.

35. Sutherland, J. C.; Desmond, E. J.; Takacs, P. Z., Versatile Spectrometer for Experiments Using Synchrotron Radiation at Wave-Lengths Greater than 100 Nm. *Nucl. Instruments Methods* **1980**, *172*, 195-199.

36. Wu, T.; You, X. Z.; Bouř, P., Applications of Chiroptical Spectroscopy to Coordination Compounds. *Coord. Chem. Rev.* **2015**, *284* (SI), 1-18.

37. Profant, V.; Pazderková, M.; Pazderka, T.; Maloň, P.; Baumruk, V., Relative Intensity Correction of Raman Optical Activity Spectra Facilitates Extending the Spectral Region. *J. Raman Spectrosc.* **2014**, *45* (7), 603-609.

38. Tu, A. T., Peptide Backbone Conformation and Microenvironment of Protein Side Chains. In *Spectroscopy of Biological Systems*, Clark, R. J. H.; Hester, R. E., Eds. Wiley: Chichester, 1986; pp 47-112.

39. Nafie, L., *Vibrational Optical Activity: Principles and Applications*. Wiley: Chichester, 2011.

40. Polavarapu, P. L., *Chiroptical Spectroscopy. Fundamentals and Applications*. Vanderbilt University: Nashville, Tennessee, USA, 2017.

41. Barron, L. D.; Buckingham, A. D., Rayleigh and Raman Scattering from Optically Active Molecules. *Mol. Phys.* **1971**, *20* (6), 1111-1119.

42. Polavarapu, P. L., Molecular Structure Determination using Chiroptical Spectroscopy: Where We May Go Wrong? *Chirality* **2012**, *24*, 909-920.

43. Barron, L. D.; Buckingham, A. D., Vibrational Optical Activity. *Chem. Phys. Lett.* **2010**, *492*, 199-213.

44. Nafie, L. A.; Freedman, T. B., Dual Circular Polarization Raman Optical Activity. *Chem. Phys. Lett.* **1989**, *154*, 260-266.

45. Nafie, L. A., Circular Polarization Spectroscopy of Chiral Molecules. *J. Mol. Struct.* **1995**, *347*, 83-100.

46. Hecht, L.; Barron, L. D., Instrument for Natural and Magnetic Raman Optical Activity Studies in Right-Angle Scattering. *J. Raman Spectr.* **1994**, *25* (7-8), 445-451.

47. Hecht, L.; Barron, L. D.; Blanch, E. W.; Bell, A. F.; Day, L. A., Raman Optical Activity Instrument for Studies of Biopolymer Structure and Dynamics. *J. Raman Spectrosc.* **1999**, *30* (9), 815-825

48. Hug, W., Virtual Enantiomers as the Solution of Optical Activity's Deterministic Offset Problem. *Appl. Spectrosc.* **2003**, *57* (1), 1-13.
49. Stephens, P. J.; Devlin, F. J.; Cheeseman, J. R., *VCD Spectroscopy for Organic Chemists*. CRC Press: 2012.
50. Nafie, L. A.; Keiderling, T. A.; Stephens, P. J., Vibrational Circular Dichroism. *J. Am. Chem. Soc.* **1976**, *98*, 2715-2723.
51. Nafie, L. A.; Diem, M.; Vidrine, D. W., Fourier Transform Infrared Vibrational Circular Dichroism. *J. Am. Chem. Soc.* **1979**, *101*, 496-498.
52. Keiderling, T. A.; Lakhani, A., Mini Review: Instrumentation for Vibrational Circular Dichroism Spectroscopy, Still a Role for Dispersive Instruments. *Chirality* **2018**, *30* (3), 238-253.
53. Yamamoto, S.; Bouř, P., Detection of Molecular Chirality by Induced Resonance Raman Optical Activity in Europium Complexes. *Angew. Chem. Int. Ed.* **2012**, *51* (44), 11058-11061.
54. Yamamoto, S.; Bouř, P., Transition Polarizability Model of Induced Resonance Raman Optical Activity. *J. Comput. Chem.* **2013**, *34*, 2152-2158.
55. Carr, R.; Evans, N. H.; Parker, D., Lanthanide Complexes as Chiral Probes Exploiting Circularly Polarized Luminescence. *Chem. Soc. Rev.* **2012**, *41*, 7673-7686.
56. Wu, T.; Bouř, P., Specific Circularly Polarized Luminescence of Eu(III), Sm(III), and Er(III) Induced by N-Acetylneuraminic Acid. *Chem. Commun.* **2018**, *54*, 1790-1792.
57. Wu, T.; Kapitán, J.; Mašek, V.; Bouř, P., Detection of Circularly Polarized Luminescence of a Cs-Eu^{III} Complex in Raman Optical Activity Experiments. *Angew. Chem. Int. Ed.* **2015** *54* (49), 14933-14936.
58. Binnemans, K., Interpretation of Europium(III) Spectra. *Coord. Chem. Rev.* **2015**, *295*, 1-45.
59. Wu, T.; Kapitán, J.; Andrushchenko, V.; Bouř, P., Identification of Lanthanide(III) Luminophores in Magnetic Circularly Polarized Luminescence using Raman Optical Activity Instrumentation. *Anal. Chem.* **2017**, *89*, 5043-5049.
60. Parker, D.; Dickins, R. S.; Puschmann, H.; Crossland, J. A.; Howard, K., Being Excited by Lanthanide Coordination Complexes: Aqua Species, Chirality, Excited-State Chemistry, and Exchange Dynamics. *Chem. rev.* **2002**, *102*, 1977-2010.
61. Wu, T.; Kessler, J.; Bouř, P., Chiral Sensing of Amino Acids and Proteins Chelating with EuIII Complexes by Raman Optical Activity Spectroscopy. *Phys. Chem. Chem. Phys.* **2016**, *18*, 23803-23811.
62. Wu, T.; Průša, J.; Kessler, J.; Dračinský, M.; Valenta, J.; Bouř, P., Detection of Sugars via Chirality Induced in Europium(III) Compounds. *Anal. Chem.* **2016**, *88*, 8878-8885.
63. Bijvoet, J. M.; Peerdeman, A. F.; van Bommel, A. J., Determination of the Absolute Configuration of Optically Active Compounds by Means of X-rays. *Nature* **1951**, *168*, 271-272.
64. Keeler, J., *Understanding NMR Spectroscopy, 2nd Edition*. John Wiley & Sons: 2010.
65. Hendrickson, W. A., Determination of Macromolecular Structures from Anomalous Diffraction of Synchrotron Radiation *Science* **1991**, *254* (5028), 51-58.
66. Riek, R.; Fiaux, J.; Bertelsen, E. B.; Horwich, A. L.; Wuthrich, K., Solution NMR Techniques for Large Molecular and Supramolecular Structures. *J. Am. Chem. Soc.* **2002**, *124*, 12144-12153.

67. Burmann, B. M.; Hiller, S., Chaperones and Chaperone-Substrate Complexes: Dynamic Playgrounds for NMR Spectroscopists. *Prog. Nucl. Magn. Reson. Spectrosc.* **2015**, *86-87*, 41-64.
68. Seco, J. M.; Quiñoá, E.; Riguera, R., The Assignment of Absolute Configuration by NMR. *Chem. Rev.* **2004**, *104* (1), 17-118.
69. Wishart, D. S.; Sykes, B. D., The ¹³C Chemical-Shift Index: A Simple Method for the Identification of Protein Secondary Structure using ¹³C Chemical-Shift Data. *J. Biomol. NMR* **1994**, *4*, 171-180.
70. Dobson, C. M., Experimental Investigation of Protein Folding and Misfolding. *Methods* **2004**, *34* (1), 4-14.
71. De Genst, E.; Messer, A.; Dobson, C. M., Antibodies and Protein Misfolding: from Structural Research Tools to Therapeutic Strategies. *Biochim. Biophys. Acta* **2014**, *1844* (11), 1907-1919.
72. Sreerama, N.; Venyaminov, S. Y.; Woody, R. W., Estimation of Protein Secondary Structure from Circular Dichroism Spectra: Inclusion of Denatured Proteins with Native Proteins in the Analysis. *Analyt. Biochem.* **2000**, *287* (2), 252-260.
73. Brooks, W. H.; Guida, W. C.; Daniel, K. G., The Significance of Chirality in Drug Design and Development. *Curr. Top. Med. Chem.* **2011**, *11* (7), 760-770.
74. De Camp, W. H., The FDA Perspective on the Development of Stereoisomers. *Chirality* **1989**, *1* (1), 2-6.
75. Hug, W.; Haesler, J., Is the Vibrational Optical Activity of (R)-[2H1, 2H2, 2H3]-Neopentane Measurable? *Int. J. Quantum Chem.* **2005**, *104*, 695-715.
76. Haesler, J.; Schindelholz, I.; Riguet, E.; Bochet, C. G.; Hug, W., Absolute Configuration of Chirally Deuterated Neopentane. *Nature* **2007**, *446*, 526-529.
77. Polavarapu, P. L., The Absolute Configuration of Bromochlorofluoromethane. *Angew. Chem. Int. Ed.* **2002**, *41* (23), 4544-4546.
78. Polavarapu, P. L., Why is It Important to Simultaneously Use More than One Chiroptical Spectroscopic Method for Determining the Structures of Chiral Molecules? *Chirality* **2008**, *20*, 664-672.
79. Hopmann, K. H.; Šebestík, J.; Novotná, J.; Stensen, W.; Urbanová, M.; Svenson, J.; Svendsen, J. S.; Bouř, P.; Ruud, K., Determining the Absolute Configuration of Two Marine Compounds using Vibrational Chiroptical Spectroscopy. *J. Org. Chem.* **2012**, *77* (2), 858-869.
80. Hecht, L.; Phillips, A. L.; Barron, L. D., Determination of Enantiomeric Excess using Raman Optical Activity. *J. Raman Spectrosc.* **1995**, *26* (8-9), 727-732.
81. Guo, C.; Shah, R. D.; Dukor, R. K.; Freedman, T. B.; Cao, X.; Nafie, L. A., Fourier Transform Vibrational Circular Dichroism from 800 to 10,000 cm⁻¹: Near-IR-VCD Spectral Standards for Terpenes and Related Molecules. *Vib. Spectrosc.* **2006**, *42*, 254-272.
82. Urbanová, M.; Setnička, V.; Volka, K., Measurements of Concentration Dependence and Enantiomeric Purity of Terpene Solutions as a Test of a New Commercial VCD Spectrometer. *Chirality* **2000**, *12*, 199-203.
83. Spencer, K. M.; Edmonds, R. B.; Rauh, R. D.; Carrabba, M. M., Analytical Determination of Enantiomeric Purity Using Raman Optical Activity. *Anal. Chem.* **1994**, *66*, 1269-1273.
84. Hrudíková, J. Monitoring of Enantiomeric Excess by Means of Raman Optical Activity (BSc. Thesis - in Czech). Charles University in Prague, 2007.

85. Berova, N.; Polavarapu, P. L.; Nakanishi, K.; Woody, R. W., *Comprehensive Chiroptical Spectroscopy, Applications in Stereochemical Analysis of Synthetic Compounds, Natural Products and Biomolecules*. Wiley: New Jersey, 2012; Vol. 2.
86. Mensch, C.; Barron, L. D.; Johannessen, C., Ramachandran Mapping of Peptide Conformation Using a Large Database of Computed Raman and Raman Optical Activity Spectra. *Phys Chem. Chem. Phys.* **2016**, *18* (46), 31757-31768.
87. Melcrová, A.; Kessler, J.; Bouř, P.; Kaminský, J., Simulation of Raman Optical Activity of Multi-Component Monosaccharide Samples. *Phys. Chem. Chem. Phys.* **2016**, *18*, 2130-2142.
88. Zhu, F.; Isaacs, N. W.; Hecht, L.; Barron, L. D., Polypeptide and Carbohydrate Structure of an Intact Glycoprotein from Raman Optical Activity. *J. Am. Chem. Soc.* **2005**, *127* (17), 6142-6143.
89. Bell, A. F.; Hecht, L.; Barron, L. D., Vibrational Raman Optical Activity as a Probe of Polyribonucleotide Solution Stereochemistry *J. Am. Chem. Soc.* **1997**, *119* (26), 6006-6013
90. Barron, L. D., The Development of Biomolecular Raman Optical Activity Spectroscopy. *Biomedical Spectroscopy and Imaging* **2015**, *4*, 223-253.
91. Sreerama, N. W., R. W., Circular Dichroism of Peptides and Proteins. In *Circular Dichroism and the Conformational Analysis of Biomolecules*, Nakanishi, K. B., N.; Woody, R. W., Ed. Wiley-VCH: New York, 2000; pp 601-620.
92. Kelly, S. M.; Jess, T. J.; Price, N. C., How to Study Proteins by Circular Dichroism. *Biochim. Biophys. Acta* **2005**, *1751* (2), 119-139.
93. Greenfield, N. J., Using Circular Dichroism Spectra to Estimate Protein Secondary Structure. *Nature Protocols* **2007**, *1* (6), 2876-2890.
94. Berova, N.; Nakanishi, K.; Woody, R. W., *Circular Dichroism Principles and Applications*. Wiley-VCH: New York, 2000.
95. Greenfield, N.; Fasman, G. D., Computed Circular Dichroism Spectra for the Evaluation of Protein Secondary Structure. *Biochemistry* **1969**, *8*, 4108-4116.
96. Greenfield, N. J., Using Circular Dichroism Spectra to Estimate Protein secondary structure. *Nature Protocols* **2006**, *1* (6), 2876-2890.
97. Zhu, F. J.; Isaacs, N. W.; Hecht, L.; Barron, L. D., Raman Optical Activity: A Tool for Protein Structure Analysis. *Structure* **2005**, *13*, 1409-1419.
98. Barron, L. D.; Blanch, E. W.; Hecht, L., Unfolded Proteins Studied by Raman Optical Activity. *Adv. Protein Chem.* **2002**, *62*, 51-90.
99. Barron, L. D.; Blanch, E. W.; McColl, I. H.; Syme, C. D.; Hecht, L.; Nielsen, K., Structure and Behaviour of Proteins, Nucleic Acids and Viruses from Vibrational Raman Optical Activity *Spectrosc. Int. J.* **2003**, *17* (2-3), 101-126.
100. Barron, L. D.; Hecht, L.; Blanch, E. W.; Bell, A. F., Solution Structure and Dynamics of Biomolecules from Raman Optical Activity. *Prog. Biophys. Mol. Biol.* **2000**, *73*, 1-49.
101. Blanch, E. W.; Hecht, L.; Day, L. A.; Pederson, D. M.; Barron, L. D., Tryptophan Absolute Stereochemistry in Viral Coat Proteins from Raman Optical Activity. *J. Am. Chem. Soc.* **2001**, *123* (20), 4863-4864.
102. Jacob, C. R.; Lubber, S.; Reiher, M., Calculated Raman Optical Activity Signatures of Tryptophan Side Chains. *ChemPhysChem* **2008**, *9* (15), 2177-2180.
103. Baumruk, V.; Pančoška, P.; Keiderling, T. A., Predictions of Secondary Structure Using Statistical Analyses of Electronic and Vibrational Circular Dichroism and Fourier Transform Infrared Spectra of Proteins in H₂O. *J. Mol. Biol.* **1996**, *259*, 774-791.

104. Ma, S.; Freedman, T. B.; Dukor, R.; Nafie, L., Near-Infrared and Mid-Infrared Fourier Transform Vibrational Circular Dichroism of Proteins in Aqueous Solution. *Appl. Spectrosc.* **2010**, *64* (6), 615-626.
105. Dukor, R. K. Vibrational Circular Dichroism of Selected Peptides, Polypeptides and Proteins. PhD Thesis, University of Illinois at Chicago, Chicago, Illinois, 1991.
106. Ma, S.; Cao, X.; Mak, M.; Sadik, A.; Walkner, C.; Freedman, T. B.; Lednev, I.; Dukor, R.; Nafie, L., Vibrational Circular Dichroism Shows Unusual Sensitivity to Protein Fibril Formation and Development in Solution. *J. Am. Chem. Soc.* **2007**, *129*, 12364-12365.
107. Kurouski, D.; Lombardi, R. A.; Dukor, R. K.; Lednev, I. K.; Nafie, L. A., Direct Observation and pH Control of Reversed Supramolecular Chirality in Insulin Fibrils by Vibrational Circular Dichroism. *Chem. Commun.* **2010**, *46*, 7154-7156.
108. Kurouski, D.; Lu, X.; Popova, L.; Wan, W.; Shanmugasundaram, M.; Stubbs, G.; Dukor, R. K.; Lednev, I. K.; Nafie, L. A., Is Supramolecular Filament Chirality the Underlying Cause of Major Morphology Differences in Amyloid Fibrils? *J. Am. Chem. Soc.* **2014**, *136* (6), 2302-2312.
109. Blanch, E. W.; McColl, I. H.; Hecht, L.; Nielsen, K.; Barron, L. D., Structural Characterization of Proteins and Viruses using Raman Optical Activity. *Vib. Spectrosc.* **2004**, *35* (1-2), 87-92
110. Pecul, M.; Ruud, K., The Ab Initio Calculation of Optical Rotation and Electric Circular Dichroism. In *Advances in Quantum Chemistry: Response Theory and Molecular Properties*, Sabin, J. R.; Brändas, E.; Jorgen, H.; Jensen, A., Eds. Elsevier, Academic Press: London, 2005; Vol. 50, pp 185-212.
111. Pecul, M.; Ruud, K., Ab Initio Calculation of Vibrational Raman Optical Activity. *Int. J. Quantum Chem.* **2005**, *104*, 816-829.
112. Herrmann, C.; Reiher, M., First-Principles Approach to Vibrational Spectroscopy of Biomolecules. In *Atomistic Approaches in Modern Biology: From Quantum Chemistry to Molecular Simulations*, Reiher, M., Ed. Springer-Verlag Berlin: Berlin, 2007; Vol. 268, pp 85-132.
113. He, Y.; Wang, B.; Dukor, R. K.; Nafie, L. A., Determination of Absolute Configuration of Chiral Molecules Using Vibrational Optical Activity: A Review. *Appl. Spectrosc.* **2011**, *65* (7), 699-723.
114. Kapitán, J.; Baumruk, V.; Kopecký, V., Jr.; Bouř, P., Conformational Flexibility of L-Alanine Zwitterion Determines Shapes of Raman and Raman Optical Activity Spectral Bands. *J. Phys. Chem. A* **2006**, *110*, 4689-4696.
115. Skála, L., *Kvantová Teorie Molekul*. Vydavatelství Karolinum, Charles University: Prague, 1995.
116. Szabo, A.; Ostlund, N. S., *Modern Quantum Chemistry. Introduction to Advanced Electronic Structure Theory*. Dover: New York, 1989.
117. Roothan, C. C. J., New Developments in Molecular Orbital Theory. *Rev. Mod. Phys.* **1951**, *23*, 69-89.
118. Ditchfield, R.; Hehre, W. J.; Pople, J. A., Self-Consistent Molecular-Orbital Methods. IX. An Extended Gaussian-Type Basis for Molecular-Orbital Studies of Organic Molecules. *J. Chem. Phys.* **1971**, *54*, 724-728.
119. Møller, C.; Plesset, M. S., Note on an Approximation Treatment for Many-Electron Systems. *Phys. Rev.* **1934**, *46*, 618-622.
120. Jensen, F., *Introduction to Computational Chemistry. Second Edition*. John Wiley & Sons Ltd.: 2007.

121. Koch, H.; Holthausen, M. C., *Chemist's Guide to Density Functional Theory. Second edition.* Wiley-VCH: Weinheim 2015.
122. Parr, R. G.; Yang, W., *Density-Functional Theory of Atoms and Molecules.* Oxford University Press: New York, 1994.
123. Thomas, L. H., The Calculation of Atomic Fields. *Proc. Cambridge Phil. Soc.* **1927**, *23*, 542-548.
124. Fermi, E., Eine statistische Methode zur Bestimmung einiger Eigenschaften des Atoms und ihre Anwendung auf die Theorie des Periodischen Systems der Elemente. *Z. Physik* **1928**, *48*, 73-79.
125. Dirac, P. A. M., Note on Exchange Phenomena in the Thomas Atom. *Proc. Cambridge Phil. Soc.* **1930**, *26*, 376-385.
126. Hohenberg, P.; Kohn, W., Inhomogeneous Electron Gas. *Phys. Rev. B* **1964**, *136*, 864-871.
127. Kohn, W.; Sham, L. J., Self-Consistent Equations Including Exchange and Correlation Effects. *Phys. Rev. A* **1965**, *140*, 1133-1138.
128. Becke, A., Density-Functional Exchange-Energy Approximation with Correct Asymptotic Behavior. *Phys. Rev. A* **1988**, *38*, 3098-3100.
129. Perdew, J. P.; Chevary, J. A.; Vosko, S. H.; Jackson, K. A.; Pederson, M. R.; Singh, D. J.; Fiolhais, C., Atoms, Molecules, Solids, and Surfaces: Applications of the Generalized Gradient Approximation for Exchange and Correlation. *Phys. Rev. B* **1992**, *46*, 6671-6687.
130. Becke, A. D., Density-Functional Thermochemistry. III. The Role of Exact Exchange. *J. Chem. Phys.* **1993**, *98*, 5648-5652.
131. Lee, C.; Yang, W.; Parr, R. G., Development of the Colle-Salvetti Correlation-Energy Formula into a Functional for the Electron Density. *Phys. Rev. B* **1988**, *37*, 785-789.
132. Cohen, A. J.; Mori-Sanchez, P.; Yang, W., Challenges for Density Functional Theory. *Chem. Rev.* **2012**, *112*, 289-320.
133. Grimme, S., Density Functional Theory with London Dispersion Corrections. *WIREs Comput. Mol. Sci.* **2011**, *1* (2), 211-228.
134. Grimme, S., Accurate Description of van der Waals Complexes by Density Functional Theory Including Empirical Corrections. *J. Comp. Chem.* **2004**, *25* (12), 1463-1473.
135. Grimme, S., Semiempirical GGA-Type Density Functional Constructed with a Long-Range Dispersion Correction. *J. Comput. Chem.* **2006**, *27*, 1787-1799.
136. Chai, J. D.; Head-Gordon, M., Long-range Corrected Hybrid Density Functionals With Damped Atom-Atom Dispersion Corrections. *Phys Chem. Chem. Phys.* **2008**, *10* (44), 6615-6620.
137. Grimme, S.; Antony, J.; Ehrlich, S.; Krieg, H., A Consistent and Accurate Ab Initio Parametrization of Density Functional Dispersion Correction (DFT-D) for the 94 Elements H-Pu. *J. Chem. Phys.* **2010**, *132* (15), 154104.
138. Parchaňský, V.; Matějka, P.; Dolenský, B.; Havlík, M.; Bouř, P., Modeling of a Troger's Tweezer and its Complexation Properties. *J. Mol. Struct.* **2009**, *934*, 117-122.
139. Runge, E.; Gross, E. K. U., Density-Functional Theory for Time-Dependent Systems. *Phys. Rev. Lett.* **1984**, *52*, 997-1000.
140. Bauernschmitt, R.; Ahlrichs, R., Treatment of Electronic Excitations within the Adiabatic Approximation of Time Dependent Density Functional Theory. *Chem. Phys. Lett.* **1996**, *256*, 454.

141. Daněček, P. Anharmonic and Solvation Effects in Vibrational Spectroscopy (PhD. Thesis). PhD., Charles University in Prague, 2007.
142. Harris, D.; Bertolucci, M. D., *Symmetry and Spectroscopy: An Introduction to Vibrational and Electronic Spectroscopy*. Dover Publications: New York, 1989.
143. Pulay, P.; Meyer, W., Comparison of Ab-initio Force Constants of Ethane, Ethylene and Acetylene. *Mol. Phys.* **1974**, *27* (2), 473-490.
144. Bowman, J. M., Self-Consistent Field Energies and Wavefunctions for Coupled Oscillators. *J. Chem. Phys.* **1978**, *68* (2), 608-610.
145. Gerber, R. B.; Ratner, M. A., A semiclassical Self-Consistent Field (SCSCF) Approximation for Eigenvalues of Coupled-Vibration Systems. *Chem. Phys. Lett.* **1979**, *68*, 195-198.
146. Hansen, M. B.; Sparta, M.; Seidler, P.; Toffoli, D.; Christiansen, O., New Formulation and Implementation of Vibrational Self-Consistent Field Theory. *J. Chem. Theory Comput.* **2010**, *6*, 235-248.
147. Fujisaki, H.; Yagi, K.; Hirao, K.; Straub, J. E., Quantum Dynamics of N-Methylacetamide Studied by the Vibrational Configuration Interaction Method. *Chem. Phys. Lett.* **2007**, *443*, 6-11.
148. Chakraborty, A.; Truhlar, D. G.; Bowman, J. M.; Carter, S., Calculation of Converged Rovibrational Energies and Partition Function for Methane using Vibrational–Rotational Configuration Interaction. *J. Chem. Phys.* **2004**, *121*, 2071.
149. Neff, M.; Rauhut, G., Toward Large Scale Vibrational Configuration Interaction Calculations. *J. Chem. Phys.* **2009**, *131*, 124129.
150. Norris, L. S.; Ratner, M. A.; Roitberg, A. E.; Gerber, R. B., Møller-Plesset Perturbation Theory Applied to Vibrational Problems. *J. Chem. Phys.* **1996**, *105* (24), 11261-11267.
151. Daněček, P.; Bouř, P., Comparison of the Numerical Stability of Methods for Anharmonic Calculations of Vibrational Molecular Energies. *J. Comput. Chem.* **2007**, *28* (10), 1617-1624.
152. Ten, G. N.; Nechaev, V. V.; Krasnoshchekov, S. V., Interpretation of Vibrational IR Spectrum of Uracil using Anharmonic Calculation of Frequencies and Intensities in Second-Order Perturbation Theory. *Opt. Spectrosc.* **2010**, *108* (1), 37-44.
153. Christiansen, O., Vibrational Coupled Cluster Theory. *J. Chem. Phys.* **2004**, *120*, 2149-2159.
154. Bouř, P. *S4, Program for Anharmonic Vibrational Properties*, Academy of Sciences: Prague, 2010.
155. Bloino, J.; Biczysko, M.; Barone, V., Anharmonic Effects on Vibrational Spectra Intensities: Infrared, Raman, Vibrational Circular Dichroism, and Raman Optical Activity. *J. Phys. Chem. A* **2015**, *119* (49), 11862-11874.
156. Frisch, M. J.; Trucks, G. W.; Schlegel, H. B.; Scuseria, G. E.; Robb, M. A.; Cheeseman, J. R.; Scalmani, G.; Barone, V.; Mennucci, B.; Petersson, G. A.; Nakatsuji, H.; Caricato, M.; Li, X.; Hratchian, H. P.; Izmaylov, A. F.; Bloino, J.; Zheng, G.; Sonnenberg, J. L.; Hada, M.; Ehara, M.; Toyota, K.; Fukuda, R.; Hasegawa, J.; Ishida, M.; Nakajima, T.; Honda, Y.; Kitao, O.; Nakai, H.; Vreven, T.; Montgomery, J. A.; Peralta, J. E.; Ogliaro, F.; Bearpark, M.; Heyd, J. J.; Brothers, E.; Kudin, K. N.; Staroverov, V. N.; Kobayashi, R.; Normand, J.; Raghavachari, K.; Rendell, A.; Burant, J. C.; Iyengar, S. S.; Tomasi, J.; Cossi, M.; Rega, N.; Millam, J. M.; Klene, M.; Knox, J. E.; Cross, J. B.; Bakken, V.; Adamo, C.; Jaramillo, J.; Gomperts, R.; Stratmann, R. E.; Yazyev, O.; Austin, A. J.; Cammi, R.; Pomelli, C.; Ochterski, J. W.; Martin, R. L.; Morokuma, K.; Zakrzewski, V. G.; Voth, G. A.; Salvador, P.; Dannenberg, J. J.;

- Dapprich, S.; Daniels, A. D.; Farkas, O.; Foresman, J. B.; Ortiz, J. V.; Cioslowski, J.; Fox, D. J. *Gaussian 09*, Revision D01; Gaussian, Inc.: Wallingford CT, USA, 2009.
157. Pulay, P., Analytical Derivative Techniques and the Calculation of Vibrational Spectra. In *Modern electronic structure theory*, Yarkony, D. R., Ed. World Scientific: Singapore, 1995; Vol. 2, pp 1191-1240.
158. Bouř, P.; Sopková, J.; Bednářová, L.; Maloň, P.; Keiderling, T. A., Transfer of Molecular Property Tensors in Cartesian Coordinates: A New Algorithm for Simulation of Vibrational Spectra. *J. Comput. Chem.* **1997**, *18*, 646-659.
159. Yamamoto, S.; Li, X.; Ruud, K.; Bouř, P., Transferability of Various Molecular Property Tensors in Vibrational Spectroscopy. *J. Chem. Theory Comput.* **2012**, *8* (3), 977-985.
160. Bouř, P.; Kubelka, J.; Keiderling, T. A., Quantum Mechanical Models of Peptide Helices and Their Vibrational Spectra. *Biopolymers* **2002**, *65*, 45-69.
161. Hilario, J.; Kubelka, J.; Keiderling, T. A., Optical Spectroscopic Investigations of Model Beta-Sheet Hairpins in Aqueous Solution *J. Am. Chem. Soc.* **2003**, *125* (25), 7562-7574.
162. Yamamoto, S.; Kaminský, J.; Bouř, P., Structure and Vibrational Motion of Insulin from Raman Optical Activity Spectra. *Anal. Chem.* **2012**, *84*, 2440-2451.
163. *Spartan16* (www.wavefun.com/products/spartan.html), Wavefunction, Inc.: Irvine, CA.
164. *Conflex program* (www.conflex.net), CONFLEX Corporation: Tokyo, Japan.
165. *HyperChem(TM) Professional 8.0* (<http://www.hyper.com>), Hypercube, Inc.: Gainesville, Florida, USA.
166. Kaminský, J.; Kapitán, J.; Baumruk, V.; Bednářová, L.; Bouř, P., Interpretation of Raman and Raman Optical Activity Spectra of a Flexible Sugar Derivative, the Gluconic Acid Anion. *J. Phys. Chem. A* **2009**, *113*, 3594-3601.
167. Alder, B. J.; Wainwright, T. E., Studies in Molecular Dynamics. I. General Method. *J. Chem. Phys.* **1959**, *31*, 459-466.
168. Verlet, L., Computer Experiments on Classical Fluids. I. Thermodynamical Properties of Lennard-Jones Molecules. *Phys. Rev.* **1967**, *159* (1), 201-214.
169. Pluhařová, E. Molekulové Simulace Nukleace Ledu (MSc. Thesis - in czech). Charles University in Prague, Prague, 2010.
170. Kumar, S.; Rosenberg, J. M.; Bouzida, D.; Swendsen, R. H.; Kollman, P., The Weighted Histogram Analysis Method for Free-Energy Calculations on Biomolecules. I. The Method. *J. Comp. Chem.* **1992**, *13*, 1011-1021.
171. Roux, B., The Calculation of the Potential of Mean Force using Computer Simulations. *Comp. Phys. Commun.* **1995**, *91*, 275-282.
172. Mennucci, B.; Cappelli, C.; Cammi, R.; Tomasi, J., Modeling Solvent Effects on Chiroptical Properties. *Chirality* **2011**, *23* (9), 717-729.
173. Jalkanen, K. J.; Nieminen, R. M.; Knapp-Mohammady, M.; Suhai, S., Vibrational Analysis of Various Isotopomers of L-alanyl-L-alanine in Aqueous solution: Vibrational Absorption, Vibrational Circular Dichroism, Raman, and Raman Optical Activity Spectra *Int. J. Quantum Chem.* **2003**, *92* (2), 239-259.
174. Klamt, A.; Schuurmann, G., COSMO: A New Approach to Dielectric Screening in Solvent with Explicit Expression for the Screening Energy and Its Gradient. *J. Chem. Soc. Perkin Trans.* **1993**, *2*, 799-805.
175. Tomasi, J.; Mennucci, B.; Cammi, R., Quantum Mechanical Continuum Solvation Models. *Chem. Rev.* **2005**, *105*, 2999-3093.

176. Barone, V.; Cossi, M., Quantum Calculations of Molecular Energies and Energy Gradients in Solution by a Conductor Solvent Model. *J. Phys. Chem. A* **1998**, *102* (11), 1995-2001.
177. Cossi, M.; Rega, N.; Scalmani, G.; Barone, V., Energies, Structures, and Electronic Properties of Molecules in Solution with the C-PCM Solvation Model. *J. Comput. Chem.* **2002**, *24* (6), 669-681.
178. Kapitán, J.; Baumruk, V.; Kopecký, V., Jr.; Pohl, R.; Bouř, P., Proline Zwitterion Dynamics in Solution, Glass and Crystalline State. *J. Am. Chem. Soc.* **2006**, *128* (41), 13451-13462.
179. Cheeseman, J. R.; Shaik, M. S.; Popelier, P. L. A.; Blanch, E. W., Calculation of Raman Optical Activity Spectra of Methyl- β -D-Glucose Incorporating a Full Molecular Dynamics Simulation of Hydration Effects. *J. Am. Chem. Soc.* **2011**, *133* (13), 4991-4997.
180. Deplazes, E.; vanBronswijk, W.; Zhu, F.; Barron, L. D.; Ma, S.; Nafie, L. A.; Jalkanen, K. J., A Combined Theoretical and Experimental Study of the Structure and Vibrational Absorption, Vibrational Circular Dichroism, Raman and Raman Optical Activity Spectra of the L-Histidine Zwitterion *Theor. Chem. Acc.* **2008**, *119*, 155-176.
181. Luber, S., Solvent Effects in Calculated Vibrational Raman Optical Activity Spectra of α -Helices. *J. Phys. Chem. A* **2013**, *117*, 2760-2770.
182. Šebek, J.; Kejík, Z.; Bouř, P., Geometry and Solvent Dependence of the Electronic Spectra of the Amide Group and Consequences for Peptide Circular Dichroism. *J. Phys. Chem. A* **2006**, *110*, 4702-4711.
183. Hopmann, K. H.; Ruud, K.; Pecul, M.; Kudelski, A.; Dračinský, M.; Bouř, P., Explicit versus Implicit Solvent Modeling of Raman Optical Activity Spectra. *J. Phys. Chem. B* **2011**, *115*, 4128-4137.
184. Urago, H.; Suga, T.; Hirata, T.; Kodama, H.; Unno, M., Raman Optical Activity of a Cyclic Dipeptide Analyzed by Quantum Chemical Calculations Combined with Molecular Dynamics Simulations. *J. Phys. Chem. B* **2014**, *118*, 6767.
185. Mutter, S. T.; Zielinski, F.; Popelier, P. L. A.; Blanch, E. W., Calculation of Raman Optical Activity Spectra for Vibrational Analysis. *Analyst* **2015**, *140* (9), 2944-2956.
186. Bouř, P.; Keiderling, T. A., Partial Optimization of Molecular Geometry in Normal Coordinates and Use as a Tool for Simulation of Vibrational Spectra. *J. Chem. Phys.* **2002**, *117*, 4126-4132.
187. Bouř, P., Convergence Properties of the Normal Mode Optimization and its Combination with Molecular Geometry Constraints. *Collect. Czech. Chem. Commun.* **2005**, *70*, 1315-1340.
188. Pulay, P.; Fogarasi, G., Geometry Optimization in Redundant Internal Coordinates. *J. Chem. Phys.* **1992**, *96*, 2856-2860.
189. Atkins, P. W.; Barron, L. D., Rayleigh Scattering of Polarized Photons by Molecules. *Molecular Physics* **1969**, *16* (5), 453-466.
190. Placzek, G., The Rayleigh and the Raman Scattering. In *Handbuch der Radiologie*, Marx, E., Ed. Akademische Verlagsgesellschaft: Leipzig, 1934; Vol. 6, p 205.
191. Li, H.; Nafie, L. A., Simultaneous Acquisition of All Four Forms of Circular Polarization Raman Optical Activity: Results for α -Pinene and Lysozyme. *J. Raman Spectrosc.* **2012**, *43* (1), 89-94.
192. Kapitán, J. Theoretical and Experimental Development of Raman Optical Activity as a Stereochemical Probe for Aqueous Environment (PhD. Thesis-in Czech). Charles University in Prague, 2006.

193. Hrudíková, J. Raman Optical Activity and Conformational Flexibility of Peptides in Solution (MSc. Thesis - in Czech). Charles University in Prague, 2009.
194. Ruud, K.; Thorvaldsen, J., Theoretical Approaches to the Calculation of Raman Optical Activity Spectra. *Chirality* **2009**, *21* (1E), E54-E67.
195. Polavarapu, P. L., Ab Initio Vibrational Raman and Raman Optical Activity Spectra. *J. Phys. Chem.* **1990**, *94*, 8106-8112.
196. Bose, P. K.; Barron, L. D.; Polavarapu, P. L., Ab Initio and Experimental Vibrational Raman Optical Activity in (+)-(R)-Methylthiirane. *Chem. Phys. Lett.* **1989**, *155* (4-5), 423-429.
197. Amos, R. D., Electric and Magnetic Properties of CO, HF, HCl, and CH₃F. *Chem. Phys. Lett.* **1982**, *87*, 23-26.
198. Helgaker, T.; Ruud, K.; Bak, K. L.; Joergensen, P.; Olsen, J., Vibrational Raman Optical Activity Calculations using London Atomic Orbitals. *Faraday Discuss.* **1994**, *99*, 165-180.
199. Ruud, K.; Helgaker, T.; Bouř, P., Gauge-Origin Independent Density-Functional Theory Calculations of Vibrational Raman Optical Activity. *J. Phys. Chem. A* **2002**, *106* (32), 7448-7455.
200. Hehre, W. J.; Ditchfield, R.; Pople, J. A., Further Extensions of Gaussian-Type Basis Sets for use in Molecular Orbital Studies of Organic Molecules. *J. Chem. Phys.* **1971**, *56*, 2257-2261.
201. Dunning, T. H. J., Gaussian Basis Sets for Use in Correlated Molecular Calculations. I. The Atoms Boron Through Neon and Hydrogen. *J. Chem. Phys.* **1989**, *90*, 1007.
202. Woon, E. D.; Dunning, T. H. J., Gaussian Basis Sets for use in Correlated Molecular Calculations. IV. Calculation of Static Electrical Response Properties. *J. Chem. Phys.* **1994**, *100*, 2975.
203. Liegeois, V.; Ruud, K.; Champagne, B., An Analytical Derivative Procedure for the Calculation of Vibrational Raman Optical Activity Spectra. *J. Chem. Phys.* **2007**, *127*, 204105.
204. Thorvaldsen, A. J.; Gao, B.; Ruud, K.; Fedorovsky, M.; Zuber, G.; Hug, W., Efficient Calculation of ROA Tensors with Analytical Gradients and Fragmentation. *Chirality* **2012**, *24* (12), 1018-1030.
205. London, F., Théorie Quantique des Courants Interatomiques dans les Combinaisons Aromatiques. *J. Phys. Radium* **1937**, *8*, 397-409.
206. Ditchfield, R., Self-Consistent Perturbation Theory of Diamagnetism I. A Gauge-Invariant LCAO Method for N. M. R. Chemical Shifts. *Mol. Phys.* **1974**, *27*, 789-807.
207. Benda, L.; Štěpánek, J.; Kaminský, J.; Bouř, P., Spectroscopic Analysis: Ab initio Calculation of Chiroptical Spectra. In *Comprehensive Chirality*, Carreira, E. M.; Yamamoto, H., Eds. Elsevier: Amsterdam, 2012; Vol. 8, pp 520-544.
208. Pecul, M.; Rizzo, A., Raman Optical Activity Spectra: Basis Set and Electron Correlation Effects. *Molecular Physics* **2003**, *101* (13), 2073-2081.
209. Hug, W., Visualizing Raman and Raman Optical Activity Generation in Polyatomic Molecules *Chem. Phys.* **2001**, *264* (1), 53-69
210. Zuber, G.; Hug, W., Rarefied Basis Sets for the Calculation of Optical Tensors. 1. The Importance of Gradients on Hydrogen Atoms for the Raman Scattering Tensor. *J. Phys. Chem. A* **2004**, *108* (11), 2108-2118
211. Reiher, M.; Liegeois, V.; Ruud, K., Basis Set and Density Functional Dependence of Vibrational Raman Optical Activity Calculations. *J. Phys. Chem. A* **2005**, *109*, 7567-7574.

212. Cheeseman, J. R.; Frisch, M. J., Basis Set Dependence of Vibrational Raman and Raman Optical Activity Intensities. *J. Chem. Theory Comput.* **2011**, *7* (10), 3323-3334.
213. Šebek, J.; Kapitán, J.; Šebestík, J.; Baumruk, V.; Bouř, P., L-Alanyl-L-Alanine Conformational Changes Induced by pH As Monitored by the Raman Optical Activity Spectra. *J. Phys. Chem. A* **2009**, *113*, 7760-7768.
214. Daněček, P.; Kapitán, J.; Baumruk, V.; Bednářová, L.; Kopecký, V., Jr.; Bouř, P., Anharmonic Effects in IR, Raman and Raman Optical Activity Spectra of Alanine and Proline Zwitterions. *J. Chem. Phys.* **2007**, *126*, 224513.
215. Rosenfeld, L., Quantenmechanische Theorie der Natürlichen Optischen Aktivität von Flüssigkeiten und Gasen. *Z. Phys.* **1929**, *52*, 161-174.
216. Stephens, P. J., Theory of Vibrational Circular Dichroism. *J. Phys. Chem.* **1985**, *89*, 748-752.
217. Amos, R. D.; Handy, N. C.; Jalkanen, K. J.; Stephens, P. J., Efficient Calculation of Vibrational Magnetic Dipole Transition Moments and Rotational Strengths. *Chem. Phys. Lett.* **1987**, *133*, 21.
218. Nafie, L. A.; Freedman, T. B., Vibronic Coupling Theory of Infrared Vibrational Transitions. *J. Chem. Phys.* **1983**, *78*, 7108-7116.
219. Stephens, P. J., Gauge Dependence of Vibrational Magnetic Transition Moments and Rotational Strengths. *J. Phys. Chem.* **1987**, *91*, 1712-1715.
220. Cheeseman, J. R.; Frisch, M. J.; Devlin, F. J.; Stephens, P. J., Ab Initio Calculation of Atomic Axial Tensors and Vibrational Rotational Strengths Using Density Functional Theory. *Chem. Phys. Lett.* **1996**, *252*, 211-220.
221. Pedersen, J. M.; Hansen, A. E., Ab initio Calculation and Display of the Rotary Strength Tensor in the Random Phase Approximation. Method and Model Studies. *Chem. Phys. Lett.* **1995**, *246* (1-2), 1-8.
222. Autschbach, J.; Seth, M.; Ziegler, T., Development of a Sum-Over-States Density Functional Theory for Both Electric and Magnetic Static Response Properties. *J. Chem. Phys.* **2007**, *126*, 174103.
223. Casida, M. E.; Huix-Rotllant, M., Progress in Time-Dependent Density Functional Theory. *Ann. Rev. Phys. Chem.* **2012**, *63*, 287-323.
224. Ruud, K.; Helgaker, T., Optical Rotation Studied by Density-Functional and Coupled-Cluster Methods. *Chem. Phys. Lett.* **2002**, *352* (5-6), 533-539.
225. Cheeseman, J. R.; Frisch, M. J.; Devlin, F. J.; Stephens, P. J., Hartree-Fock and Density Functional Theory ab Initio Calculation of Optical Rotation Using GIAOs: Basis Set Dependence. *J. Phys. Chem. A* **2000**, *104*, 1039-1046.
226. Kuppens, T.; Langenaeker, W.; Tollenaere, J. P.; Bultinck, P., Determination of the Stereochemistry of 3-hydroxymethyl-2,3-dihydro-[1,4]dioxino[2,3-b]-pyridine by Vibrational Circular Dichroism and the Effect of DFT Integration Grids. *J. Phys. Chem. A* **2003**, *107*, 542-443.
227. Polavarapu, P. L.; Covington, C. L., Comparison of Experimental and Calculated Chiroptical Spectra for Chiral Molecular Structure Determination. *Chirality* **2014**, *26* (9), 539-552.
228. Anderson, M. P.; Uvdal, P., New Scale Factors for Harmonic Vibrational Frequencies Using the B3LYP Density Functional Method with the Triple- ζ Basis Set 6-311+G(d,p). *J. Phys. Chem. A* **2005**, *109* (12), 2937-2941.
229. Debie, E.; De Gussem, E.; Dukor, R. K.; Herrebout, W.; Nafie, L. A.; Bultinck, P., A Confidence Level Algorithm for the Determination of Absolute Configuration using Vibrational Circular Dichroism or Raman Optical Activity. *Chem. Phys. Chem.* **2011**, *12*, 1542-1549.

230. Covington, C. L.; Polavarapu, P. L., Similarity in Dissymmetry Factor Spectra: A Quantitative Measure of Comparison between Experimental and Predicted Vibrational Circular Dichroism. *J. Phys. Chem. A* **2013**, *117*, 3377-3386.
231. Buděšínský, M.; Daněček, P.; Bednářová, L.; Kapitán, J.; Baumruk, V.; Bouř, P., Comparison of Quantitative Conformer Analyses by Nuclear Magnetic Resonance and Raman Optical Activity Spectra for Model Dipeptides. *J. Phys. Chem. A* **2008**, *112*, 8633-8640.
232. Parchaňský, V.; Kapitán, J.; Kaminský, J.; Šebestík, J.; Bouř, P., Ramachandran Plot for Alanine Dipeptide as Determined from Raman Optical Activity. *J. Phys. Chem. Lett.* **2013**, *4*, 2763-2768.
233. Jungwirth, J.; Šebestík, J.; Šafařík, M.; Kapitán, J.; Bouř, P., Quantitative Determination of Ala-Ala Conformer Ratios in Solution by Decomposition of Raman Optical Activity Spectra. *J. Phys. Chem. B* **2017**, *121*, 8956-8964.
234. Zuk, W. M.; Freedman, T. B.; Nafie, L. A., Vibrational CD Studies of the Solution Conformation of Simple Alanyl Peptides as a Function of pH. *Biopolymers* **1989**, *28* (11), 2025-2044.
235. Julínek, O.; Lindner, W.; Urbanová, M., Study of Stereoselective Interactions of Carbamoylated Quinine and Quinidine with 3,5-Dinitrobenzoyl alpha-Amino Acids Using VCD Spectroscopy in the Region of C-H Stretching Vibrations. *Chirality* **2011**, *23* (4), 354-360.
236. Bouř, P., Anharmonic Corrections to Vibrational Energies of Molecules: Water and Dideuteriooxirane. *J. Phys. Chem.* **1994**, *98*, 8862-8865.
237. Longhi, G.; Abbate, S.; Gangemi, R.; Giorgio, E.; Rosini, C., Fenchone, Camphor, 2-Methylenefenchone and 2-Methylenecamphor: A Vibrational Circular Dichroism Study. *J. Phys. Chem. A* **2006**, *110* (15), 4958-4968.
238. Kaledin, A. L.; Bowman, J. M., Full Dimensional Quantum Calculations of Vibrational Energies of N-Methyl Acetamide. *J. Phys. Chem. A* **2007**, *111*, 5593-5598.
239. Devlin, F. J.; Stephens, P. J.; Cheeseman, J. R.; Frisch, M. J., Ab Initio Prediction of Vibrational Absorption and Circular Dichroism Spectra of Chiral Natural Products using Density Functional Theory - Alpha-Pinene. *J. Phys. Chem.* **1997**, *101*, 9912-9924.
240. Pearlman, D. A.; Case, D. A.; Caldwell, J. W.; Ross, W. S.; Cheatham, T. E.; Debolt, S.; Ferguson, D.; Seibel, G.; Kollman, P., Amber, A Package of Computer programs for Applying Molecular Mechanics, Normal-Mode Analysis, Molecular-Dynamics and Free-Energy Calculations to Simulate the Structural and Energetics Properties of Molecules. *Comput. Phys. Commun.* **1995**, *91* (1-3), 1-41.
241. Case, D. A.; Cheatham, I. T. E.; Darden, T.; Gohlke, H.; Luo, R.; Merz, J. K. M.; Onufriev, A.; Simmerling, C.; Wang, B.; Woods, R., The Amber Biomolecular Simulation Programs. *J. Comput. Chem.* **2005**, *26*, 1668-1688.
242. Car, R.; Parrinello, M., Unified Approach for Molecular Dynamics and Density-Functional Theory. *Phys. Rev. Lett.* **1985**, *55*, 2471-2474.
243. Bouř, P. *Qgrad*, Academy of Sciences, Prague: Prague, 2006.
244. Broyden, C. G., The Convergence of a Class of Double-Rank Minimization Algorithms 1. General Considerations. *J. Inst. Math. Appl.* **1970**, *6*, 76.
245. Fletcher, R., A New Approach to Variable Metric Algorithm. *Comput. J.* **1970**, *13*, 317.
246. Goldfarb, D., A Family of Variable-Metric Methods Derived by Variational Means. *Math. Comput.* **1970**, *24*, 23.
247. Shanno, D. F., Conditioning of Quasi-Newton Methods for Function Minimization. *Math. Comput.* **1970**, *24*, 647.

248. Schlegel, H. B., Geometry Optimization on Potential Energy Surfaces. In *Modern Electronic Structure Theory*, Yarkony, D. R., Ed. World Scientific: Singapore, 1995; pp 459-500.
249. Banerjee, A.; Adams, N.; Simons, J.; Shepard, R., Search for Stationary-Points on Surface. *J. Phys. Chem.* **1985**, *89*, 52-57.
250. Simons, J.; Nichols, J., Strategies for Walking on Potential-Energy Surfaces Using Local Quadratic Approximations. *Int. J. Quantum Chem., Quantum Chem. Symp.* **1990**, *24*, 263.
251. Baker, J.; Hehre, W. J., Geometry Optimization in Cartesian Coordinates: The End of the Z-Matrix? *J. Comput. Chem.* **1991**, *12* (5), 606-610.
252. Baker, J., Techniques for Geometry Optimization: A Comparison of Cartesian and Natural Internal Coordinates. *J. Comput. Chem.* **1993**, *14*, 1085-1100.
253. Perdew, J. P.; Burke, K.; Wang, Y., Generalized Gradient Approximation for the Exchange-Correlation Hole of a Many-Electron System. *Phys. Rev. B* **1996**, *54*, 16533-16539.
254. Yanai, T.; Tew, D.; Handy, N. C., A New Hybrid Exchange-Correlation Functional using the Coulomb-Attenuating Method (CAM-B3LYP). *Chem. Phys. Lett.* **2004**, *393*, 51-57.
255. Schwabe, T.; Grimme, S., Double-Hybrid Density Functionals with Long-Range Dispersion Corrections: Higher Accuracy and Extended Applicability. *Phys. Chem. Chem. Phys.* **2007**, *9* (26), 3397-3406.
256. Klamt, A., Conductor-Like Screening Models for Real Solvents: A New Approach to the Quantitative Calculation of Solvation Phenomena. *J. Phys. Chem.* **1995**, *99*, 2224-2235.
257. Papoušek, D.; Aliev, M. R., *Molecular Vibrational/Rotational Spectra*. Academia: Prague, 1982.
258. Dračinský, M.; Bouř, P., Vibrational Averaging of the Chemical Shift in Crystalline α -Glycine. *J. Comput. Chem.* **2012**, *33*, 1080-1089.
259. Matsunaga, N.; Chaban, G. M.; Gerber, R. B., Degenerate Perturbation Theory Corrections for the Vibrational Self-Consistent Field Approximation: Method and Applications. *J. Chem. Phys.* **2002**, *117* (8), 3541-3547.
260. Samsonyuk, A.; Scheurer, C., Configuration Space Partitioning and Matrix Buildup Scaling for the Vibrational Configuration Interaction Method. *J. Comput. Chem.* **2013**, *34*, 27-37.
261. Mitin, A. V., Iterative Methods for the Calculation of a Few of the Lowest Eigenvalues and Corresponding Eigenvectors of the $AX = \lambda BX$ Equation with Real Symmetric Matrices of Large Dimension. *J. Comput. Chem.* **1994**, *15* (7), 747-751.
262. Davidson, E. R., The Iterative Calculation of a Few of the Lowest Eigenvalues and Corresponding Eigenvectors of Large Real-Symmetric Matrices. *J. Comput. Phys.* **1975**, *17*, 87-94.
263. Grimme, S., Accurate Description of van der Waals Complexes by Density Functional Theory Including Empirical Corrections. *J. Comput. Chem.* **2004**, *25*, 1463-1473.
264. Kapitán, J.; Baumruk, V.; Kopecký, V., Jr.; Bouř, P., Demonstration of the Ring Conformation in Polyproline by the Raman Optical Activity. *J. Am. Chem. Soc.* **2006**, *128*, 2438-2443.
265. Altona, C.; Sundaralingam, M., Conformational Analysis of the Sugar Ring in Nucleosides and Nucleotides. New Description using the Concept of Pseudorotation. *J. Am. Chem. Soc.* **1972**, *94*, 8205-8212.

266. Han, S. J.; Kang, Y. K., Pseudorotation in Heterocyclic Five-Membered Rings: Tetrahydrofuran and Pyrrolidine. *J. Mol. Struct. (THEOCHEM)* **1996**, *369*, 157-165.
267. Vokáčová, Z.; Šponer, J.; Šponer, J. E.; Sychrovský, V., Theoretical Study of the Scalar Coupling Constants across the Noncovalent Contacts in RNA Base Pairs: The Cis- and Trans-Watson-Crick/Sugar Edge Base Pair Family *J. Phys. Chem. B* **2007**, *111* (36), 10813-10824.
268. Wang, J.; Wolf, R. M.; Caldwell, J. W.; Kollman, P. A.; Case, D. A., Development and Testing of a General Amber Force Field. *J. Comput. Chem.* **2005**, *25* (9), 1157-1174.
269. Maier, J. A.; Martinez, C.; Kasavajhala, K.; Wickstrom, L.; Hauser, K. E.; Simmerling, C., ff14SB: Improving the Accuracy of Protein Side Chain and Backbone Parameters from ff99SB. *J. Chem. Theory Comput.* **2015**, *11* (8), 3696-3713.
270. Jorgensen, W. L.; Chandrasekhar, J.; Madura, J. D., Comparison of Simple Potential Functions for Simulating Liquid Water. *J. Chem. Phys.* **1983**, *79*, 926-935.
271. Kumar, S.; Bouzida, D.; Swendsen, R. H.; Kollman, P. A.; Rosenberg, J. M., The Weighter Histogram Analysis Methods for Free-Energy Calculations on Biomolecules.1. The Method. *J. Comput. Chem.* **1992**, *13* (8), 1011-1021.
272. Roux, B., The Calculation of Potential of Mean Force Using Computer Simualtions. *Comput. Phys. Commun.* **1995**, *91* (1-3), 275-282.
273. Hanzlíková, J.; Praus, P.; Baumruk, V., Raman Optical Activity Spectrometer for Peptide Studies. *J. Mol. Struct.* **1999**, *480-481*, 431-435.
274. Bouř, P. *SC95*, Academy of Sciences: Prague, 1994-2009.
275. Lakhani, A.; Malon, P.; Keiderling, T. A., Comparison of Vibrational Circular Dichroism Instruments: Development of a New Dispersive VCD. *Appl. Spectrosc.* **2009**, *63* (7), 775-785.
276. Lakhani, A.; Roy, A.; De Poli, M.; Nakaema, M.; Formaggio, F.; Toniolo, C.; Keiderling, T. A., Experimental and Theoretical Spectroscopic Study of 3(10)-Helical Peptides Using Isotopic Labeling to Evaluate Vibrational Coupling. *J. Phys. Chem. B* **2011**, *115*, 6252-6264.
277. Kessler, J.; Dračinský, M.; Bouř, P., Parallel Variable Selection of Molecular Dynamics Clusters as a Tool for Calculation of Spectroscopic Properties. *J. Comput. Chem.* **2013**, *34*, 366-371.
278. Štěpánek, P.; Bouř, P., Multi-scale Modeling of Electronic Spectra of Three Aromatic Amino Acids: Importance of Conformational Averaging and Explicit Solute-Solvent Interactions. *Phys. Chem. Chem. Phys.* **2014**, *16*, 20639-20649.
279. Kaminský, J.; Kříž, J.; Bouř, P., On the Magnetic Circular Dichroism of Benzene. A Density-Functional Study. *J. Chem. Phys.* **2017**, *146*, 144301.
280. Cappelli, C.; Bloino, J.; Lipparini, F.; Barone, V., Toward Ab Initio Anharmonic Vibrational Circular Dichroism Spectra in the Condensed Phase. *J. Phys. Chem. Lett.* **2012**, *3* (13), 1766-1773.
281. Pan, C. P.; Barkley, M. D., Conformational Effects on Tryptophan Fluorescence in Cyclic Hexapeptides *Biophys. J.* **2004**, *86* (6), 3828-3835
282. Edelhoch, H., Spectroscopic Determination of Tryptophan and Tyrosine in Proteins. *Biochemistry* **1967**, *6* (7), 1948-1954.
283. Tischman, J. A.; Oefner, R. E.; Luna, M. G. D.; Kazaoka, M., Competitive Induction and Enhancement of Indole and a Diketopiperazine in Marine Bacteria. *Mar. Biotechnol.* **2004**, *6*, 215-220.
284. Kanzaki, H.; Imura, D.; Nitoda, T.; Kawazu, K., Enzymatic Conversion of Cyclic Dipeptides to Dehydro Derivatives That Inhibit Cell Division. *J. Biosci. Bioeng.* **2000**, *90*, 86-89.

285. Nicholson, B.; Lloyd, G. K.; Miller, B. R.; Palladino, M. A.; Kiso, Y.; Hayashi, Y.; Neuteboom, S. T. C., Npi-2358 Is a Tubulin-Depolymerizing Agent: In-Vitro Evidence for Activity as a Tumor Vascular-Disrupting Agent. *Anti-Cancer Drug Des.* **2006**, *17*, 25-31.
286. Brauns, S. C.; Milne, P.; Naudé, R.; Venter, M. V. D., Selected Cyclic Dipeptides Inhibit Cancer Cell Growth and Induce Apoptosis in Ht-29 Colon Cancer Cells. *AntiCancer Res.* **2004**, *24*, 1713-1720.
287. Sinha, S.; Srivastava, R.; Clercq, E. D.; Singh, R. K., Synthesis and Antiviral Properties of Arabino and Ribonucleosides of 1,3-Dideazaadenine, 4-Nitro-1, 3-Dideazaadenine and Diketopiperazine. *Nucleotides Nucleic Acids* **2004**, *23*, 1815-1824.
288. Martins, M. B.; Carvalho, I., Diketopiperazines: Biological Activity and Synthesis. *Tetrahedron* **2007**, *63* (40), 9923-9932.
289. Brady, G. P.; Sharp, K. A., Energetics of Cyclic Dipeptide Crystal Packing and Solvation. *Biophys. J.* **1997**, *72*, 913-927.
290. Grant, G. D.; Hunt, A. L.; Milne, P. J.; Roos, H. M.; Joubert, J. A., The Structure and Conformation of the Tryptophanyl Diketopiperazines Cyclo(Trp-Trp).C₂H₆SO and Cyclo(Trp-Pro). *J. Chem. Crystall.* **1999**, *29* (4), 435-447.
291. Roy, A.; Bouř, P.; Keiderling, T. A., Modeling of the Circular Dichroism for a Tryptophan Zipper Peptide with TD-DFT of Coupled Aromatic Residues. *Chirality* **2009**, *21* (1E), E163-E171.
292. Keiderling, T. A.; Kubelka, J.; Hilario, J., Vibrational Circular Dichroism of Biopolymers. Summary of Methods and Applications. In *Vibrational Spectroscopy of Polymers and Biological Systems*, Braiman, M.; Gregoriou, V., Eds. CRC Press: Boca Raton, 2006; pp 253-324.
293. Dabkowska, I.; Gonzalez, H. V.; Jurečka, P.; Hobza, P., Stabilization Energies of the Hydrogen-Bonded and Stacked Structures of Nucleic Acid Base Pairs in the Crystal Geometries of CG, AT, and AC DNA Steps and in the NMR Geometry of the 5'-d(GCGAAGC)-3' Hairpin: Complete Basis Set Calculations at the MP2 and CCSD(T) Levels. *J. Phys. Chem. A* **2005**, *109* (6), 1131-1136.
294. Piacenza, M.; Grimme, S., Van der Waals Complexes of Polar Aromatic Molecules: Unexpected Structures for Dimers of Azulene. *J. Am. Chem. Soc.* **2005**, *127* (42), 14841-14848.
295. Parac, M.; Etinski, M.; Peric, M.; Grimme, S., A Theoretical Investigation of the Geometries and Binding Energies of Molecular Tweezer and Clip Host-Guest Systems. *J. Chem Theory Comput.* **2005**, *1*, 1110-1118.
296. Huvaere, K.; Skibsted, L. H., Light-Induced Oxidation of Tryptophan and Histidine. Reactivity of Aromatic N-heterocycles toward Triplet-Excited Flavins. *J. Am. Chem. Soc.* **2009**, *131* (23), 8049-8060.
297. Merten, C.; Li, F.; Bravo-Rodriguez, K.; Sanchez-Garcia, E.; Xu, Y.; Sanderb, W., Solvent-Induced Conformational Changes in Cyclic Peptides: A Vibrational Circular Dichroism Study. *Phys. Chem. Chem. Phys.* **2014**, *16*, 5627-5633.
298. Merten, C., Vibrational Optical Activity as Probe for Intermolecular Interactions. *Phys Chem. Chem. Phys.* **2017**, *19*, 18803-18812.
299. Bünzli, J. C. G.; Piguet, C., Taking Advantage of Luminescent Lanthanide Ions. *Chem. Soc. Rev.* **2005**, *34*, 1048-1077.
300. Muller, G.; Muller, F. C.; Maupin, C. L.; Riehl, J. P., The Measurement of the Fluorescence Detected Circular Dichroism (FD CD) from a Chiral Eu(III) System *Chem Commun.* **2005**, 3615-3617.

List of figures

Fig. 1.1: Two enantiomers of alanine	6
Fig. 1.2: Four experimental forms of ROA	10
Fig. 1.3: Definition of CD: energy-level polarization diagram	11
Fig. 1.4: Definition of CPL: energy-level polarization diagram.....	13
Fig. 2. 1: Harmonic and exact potential of the C-H stretching vibration	29
Fig. 2. 2: Typical steps required for calculations of chiroptical spectra.....	30
Fig. 2.3: Intramolecular and intermolecular energy contributions	33
Fig. 4.1: (S)-lactamide	48
Fig. 4.2: (1R)-(+)- α -pinene, (1R)-(-)-fenchone and (1R)-(+)-camphor	50
Fig. 4.3: Cyclic dipeptides c-(L-Trp-X).....	53
Fig. 4.4: Potential energy scan and conformer geometries for c-(L-Trp-L-Trp).....	54
Fig. 4.5: [Eu(DPA) ₃] ³⁻ complex and peptides containing histidine	56
Fig. 5.1: Calculated and experimental Raman and ROA spectra of (S)-lactamide ...	62
Fig. 5.2: Simulated (S)-lactamide Raman bandwidths for different ω_{max}	62
Fig. 5.3: Changes of torsional angles of (S)-lactamide for different ω_{max}	63
Fig. 5.4: Solvent dependence of calculated Raman, ROA, IR, VCD spectra of (1R)-(+)-camphor	65
Fig. 5.5: Harmonic and anharmonic frequency errors for fenchone.....	66
Fig. 5.6: Calculated and experimental Raman, ROA, IR and VCD spectra of (1R)-(+)- α -pinene	67
Fig. 5.7: LVCI and experimental Raman, ROA, IR and VCD spectra of (1R)-(-)-fenchone and (1R)-(+)-camphor	70
Fig. 5.8: Anharmonic coupling between harmonic vibrational modes.....	71
Fig. 5.9: Raman and ROA LVCI spectra of (1R)-(+)- α -pinene	72
Fig. 5.10: 1D and 2D potential energy scan for the DKP ring in c-(L-Ala-L-Ala) ...	74
Fig. 5.11: Potential energy scan for six conformations of c-(L-Trp-Gly)	74
Fig. 5.12: Conformations of c-(L-Trp-L-Trp) preferred by DFT and DFT-D calculations	75
Fig. 5.13: Calculated ECD, VCD and ROA spectra for DFT and DFT-D geometries of the T-shaped conformer of the c-(L-Trp-L-Trp) peptide.....	76
Fig. 5.14: Calculated and experimental ECD spectra of the c-(L-Trp-L-Trp)	77
Fig. 5.15: Calculated and experimental VCD spectra of c-(L-Trp-L-Trp).....	78

Fig. 5.16: Calculated and experimental ROA and Raman spectra of the c-(L-Trp-L-Trp) peptide.....	79
Fig. 5.17: Experimental TL and CPL spectra and calculated free energies for complexes of $[\text{Eu}(\text{DPA})_3]^{3-}$ with His-(Gly) $_n$ peptides	84
Fig. 5.18: Calculated binding strength of peptides	85
Fig. 5.19: Experimental TL and CPL spectra and calculated free energies for $[\text{Eu}(\text{DPA})_3]^{3-}$ with His-Gly-Gly at three different pH values.....	86
Fig. 5.20: Experimental TL and CPL spectra and calculated free energies for $[\text{Eu}(\text{DPA})_3]^{3-}$ with Gly-His, Gly-His-Gly, Gly-Gly-His and His-His peptides	87

List of tables

Table 1.1: Comparison of chiroptical techniques.....	8
Table 5.1: Calculated C-H stretching normal modes for α -pinene.....	68
Table 5.2: Puckering of the DKP ring in DMSO derived from NMR, MD, DFT and DFT-D calculations	81

List of abbreviations

AAT	atomic axial tensor
AcCN	acetonitrile
AO	atomic orbital
APT	atomic polar tensor
B3LYP	Becke's 1993 three-parameter hybrid functional with Lee-Yang-Parr correlation functional
BPW91	Becke's 1988 functional with Perdew-Wang correlation functional
B-O	Born-Oppenheimer
CC	coupled clusters
CCD	charge-coupled device
CCl ₄	carbon tetrachloride
CCSD(T)	coupled clusters theory assuming only single, double and partially triple excitations
CD	circular dichroism
CD ₃ OD	deuterated methanol
CDCl ₃	deuterated chloroform
CHCl ₃	chloroform
CH ₃ OH	methanol
CI	configurational interaction
CID	circular intensity difference
COSMO	conductor-like screening model
CPCM	COSMO-PCM solvent model
CPMD	Car-Parrinello molecular dynamics
CPL	circularly polarized luminescence
DFT	density functional theory
DCP	dual circular polarization
DMSO	dimethylsulfoxide
DMSO-d ₆	deuterated dimethylsulfoxide
DPKs	2,5-diketopiperazines
ECD	electronic circular dichroism
EE	enantiomeric excess

Eu	europium
FDCD	fluorescence detected circular dichroism
FF	force field
FT	Fourier-transform
GGA	generalized gradient approximation
GIAO	gauge-independent atomic orbitals
Gly	glycine
GTO	gaussian-type orbitals
HF	Hartree-Fock
His	histidine
HO	harmonic oscillator
ICP	incident circular polarization
IOCB	Institute of Organic Chemistry and Biochemistry
IR	infrared absorption
LCP	left-handed circularly polarized
LVCI	limited vibrational configuration interaction
MD	molecular dynamics
MFP	magnetic field perturbation
MO	molecular orbital
MP2	Møller-Plesset perturbation theory of the second order
NMO	normal mode optimization
NMR	nuclear magnetic resonance
OA	optical activity
ORD	optical rotatory dispersion
PCM	polarizable continuum solvent model
PES	potential energy surface
PEM	photoelastic modulator
PT2	second order perturbation method
RCP	right-handed circularly polarized
ROA	Raman optical activity
QM/MM	quantum mechanics/molecular mechanics
SCP	scattered circular polarization
SD	Slater determinant
SCF	self-consistent field

TFE	2,2,2-trifluoroethanol
TD-DFT	time-dependent density functional theory
Trp	tryptophan
UV	ultra violet
VCD	vibrational circular dichroism
VCI	vibrational configuration interaction
VOA	vibrational optical activity
WHAM	weighted histogram analysis method

List of publications

The results, presented in this thesis, follow four already published works.

[I] Hudecová, J.; Hopmann, K. H.; Bouř, P., Correction of Vibrational Broadening in Molecular Dynamics Clusters with the Normal Mode Optimization Method. *J. Phys. Chem. B* **2012**, *116*, 336-342

DOI: 10.1021/jp208785a, **IF** 3.607, **Cited** 22×

My contribution: DFT computations, their analysis and discussions of the results. Preparation of the manuscript part.

[II] Hudecová, J.; Profant, V.; Novotná, P.; Baumruk, V.; Urbanová, M.; Bouř, P., CH Stretching Region: Computational Modeling of Vibrational Optical Activity. *J. Chem. Theory Comput.* **2013**, *9*, 3096–3108

DOI: 10.1021/ct400285n, **IF** 5.310, **Cited** 12×

My contribution: Anharmonic computations (perturbational and variational methods), analysis and preparation of the manuscript.

[III] Hudecová, J.; Horníček, J.; Buděšínský, M.; Šebestík, J.; Šafařík, M.; Zhang, G.; Keiderling, T. A.; Bouř, P., Three Types of Induced Tryptophan Optical Activity Compared in Model Dipeptides: Theory and Experiment. *ChemPhysChem* **2012**, *13* (11), 2748-2760

DOI: 10.1002/cphc.201200201, **IF** 3.349, **Cited** 8x

My contribution: All *ab-initio* computations (geometry optimization, conformer selection, generation of the spectra) and data interpretation. Acquiring and data processing of all Raman and ROA spectra. Measurement of some ECD, IR and VCD spectra with help of G. Zhang. Major contribution to analysis of the results and preparation of the manuscript.

[IV] Brichtová, E. ; Hudecová, J.; Vršková, N.; Šebestík, J.; Bouř, P.; Wu T. Binding of Lanthanide Complexes to Histidine-Containing Peptides Inspected by Raman Optical Activity Spectroscopy. **2018** accepted to *Chemistry - A European Journal*

DOI: 10.1002/chem.201800840, **IF** 5.317

My contribution: Rationalization of observed data by molecular dynamics simulations – WHAM profiles of complexation energy and writing of corresponding part of the manuscript, discussions of the results.

I was involved in five other projects that are not directly discussed in the thesis. All of them deals with the ROA method. There is one reviewing article (II'), three publications (I', III' IV'), for which I provided Raman and ROA measurements, and one publication mostly based on my Master Thesis¹⁹³ (V').

[I'] Wu, T.; Hudecová, J.; Bouř, P., Comparison of Electronic and Vibrational Optical Activity of a Europium(III) Complex. *Chem. Eur. J.* **2015**, *21* (15), 5807-5813

DOI: 10.1002/chem.201406266, **IF** 5.771, **Cited** 5×

My contribution: help with the ROA experiment.

[II'] Hudecová, J.; Bouř, P. Vibrational Optical Activity: Experimental Background and Computer Simulations, *Chemické listy* 2014, **108** (4), 285-292

IF 0.272 **Cited** 0×

My contribution: Writing of part of the manuscript.

[III'] Li, X.; Hopmann, K. H.; Hudecová, J.; Isaksson, J.; Novotná, J.; Stensen, W.; Andrushchenko, V.; Urbanová, M.; Svendsen, J. S.; Bouř, P.; Ruud, K., Determination of Absolute Configuration and Conformation of a Cyclic Dipeptide by NMR and Chiral Spectroscopic Methods. *J. Phys. Chem. A* **2013**, *117* (8), 1721–1736

DOI: 10.1021/jp311151h, **IF** 2.775, **Cited** 27×

My contribution: measurement of ECD and Raman + ROA spectra of four diastereomers, data processing, writing of appropriate part of manuscript.

[IV'] Li, X.; Hopmann, K. H.; Hudecová, J.; Stensen, W.; Novotná, J.; Urbanová, M.; Svendsen, J. S.; Bouř, P.; K., R., Absolute Configuration of a Cyclic Dipeptide Reflected in Vibrational Optical Activity: Ab Initio and Experimental Investigation. *J. Phys. Chem. A* **2012**, *116*, 2554-2563

DOI: 10.1021/jp211454v, **IF** 2.771, **Cited** 17×

My contribution: Raman and ROA experiment for four diastereomers: measurement, processing, writing of a part of the manuscript about ROA experiment.

[V] Hudecová, J.; Kapitán, J.; Baumruk, V.; Hammer, R. P.; Keiderling, T. A.; Bouř, P., Side Chain and Flexibility Contributions to the Raman Optical Activity Spectra of a Model Cyclic Hexapeptide. *J. Phys. Chem. A* **2010**, *114*, 7642-7651

DOI: 10.1021/jp104744a, **IF** 2.64, **Cited** 21×

My contribution: MD and DFT computations, their analysis and discussions of the results. Raman and ROA measurement of Phe-D-Pro dipeptide. Preparation of all figures and writing of a part of the manuscript.

I presented my work at 13 international conferences and workshops, giving 3 talks and 10 poster presentations. The published works were 112 times cited to 15th June 2018.

A. Attachments

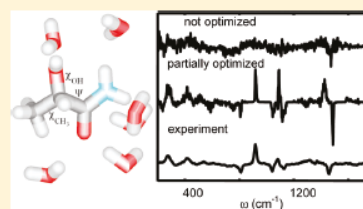
A1. Publication [I]

Hudecová, J.; Hopmann, K. H.; Bouř, P., Correction of Vibrational Broadening in Molecular Dynamics Clusters with the Normal Mode Optimization Method. *J. Phys. Chem. B* **2012**, *116*, 336-342

Correction of Vibrational Broadening in Molecular Dynamics Clusters with the Normal Mode Optimization Method

Jana Hudecová,^{†,‡} Kathrin H. Hopmann,[§] and Petr Bouřný,[†][†]Institute of Organic Chemistry and Biochemistry, Academy of Sciences, Flemingovo nám. 2, 166 10 Prague, Czech Republic[‡]Institute of Physics, Charles University, Ke Karlovu 5, 12116 Prague 2, Czech Republic[§]Department of Chemistry, Centre for Theoretical and Computational Chemistry, University of Tromsø, N-9037 Tromsø, Norway

ABSTRACT: Vibrational properties of solutions are frequently simulated with clusters of a solute and a few solvent molecules obtained during molecular dynamics (MD) simulations. The raw cluster geometries, however, often provide unrealistic vibrational band broadening, for both ab initio and empirical force fields. In this work, partial optimization in normal-mode coordinates is used on empirical basis to reduce the broadening. The origin of the error is discussed on a simplified two-dimensional system, which indicates that the problem is caused by the anharmonic MD potential, mode coupling, and neglect of quantum effects. Then the procedure of partial geometry optimization on Raman and Raman optical activity (ROA) spectra is applied and analyzed for the solvated lactamide molecule. Comparison to experiment demonstrates that the normal-mode partial optimization technique with a suitable frequency limit can significantly reduce the broadening error. For lactamide, experimental and simulated vibrational bandwidths are compared; the most realistic theoretical spectra are obtained for partially optimized clusters with the vibrational wavenumber cutoff of about 200 cm⁻¹.



■ INTRODUCTION

Computations of solution properties with clusters containing explicit solvent molecules became popular because of the superior results to vacuum or simpler polarizable continuum models (PCM),^{1–4} availability of accurate molecular dynamics (MD) force fields,⁵ feasible ab initio dynamical schemes,^{6–8} and the steady increase of computer power. For example, we found that the explicit solvent model is needed to accurately simulate NMR parameters of solvated molecules,^{4,9} and polarized continuum models (PCM) are often inadequate to describe hydrogen bonding or temperature effects on the vibrational properties of the peptide amide group.^{10,11}

In vibrational spectroscopy, a combination of quantum and molecular dynamics methods is often needed in larger cluster computations to calculate realistic band shapes. In particular, polar molecules, such as peptide models, exhibit large inhomogeneous band broadening, for example in IR,^{12,13} VCD,¹⁴ or two-dimensional^{15,16} (2D) spectroscopic techniques. The band-shape modeling lends the peptide vibrational spectroscopy an enhanced structural sensitivity. This mostly originates from vibrational coupling among the individual amide chromophores, resulting in delocalized modes, which can give rise to complex, asymmetric band shapes.^{17,18} For example, β -sheet peptide conformations exhibit different IR band shape of the carbonyl stretching mode than α -helices. The solvent has also a dramatic effect on the amide and other vibrational frequencies.^{19,20} In the vibrational optical activity techniques,²¹ the structural sensitivity enhancement is mostly achieved through the spectral sign pattern.^{22,23} Nevertheless, for the case of flexible and polar molecule with many overlapping transitions, the band-shape modeling with explicit solvent is also necessary.²⁴

The instantaneous normal-mode approximation investigated in the present study provides a convenient way to compute the vibrational frequencies and intensities for the condensed phase at the harmonic level.²⁵ Second energy derivatives and the harmonic vibrations are estimated with MD snapshot geometries. While such approach is a useful approximation for some liquids,^{26,27} in a recent study²⁸ we observed unrealistic inhomogeneous broadening of simulated Raman and Raman optical activity (ROA) bands when raw clusters were used to simulate two hydrated molecules, lactamide and 2-aminopropan-1-ol. The problem persisted both for classical MD or Car–Parrinello molecular dynamics (CPMD)⁶ snapshots.

For completeness, we should also mention the time-dependent approaches of band-shape generation, frequently used to model vibrational linear or 2D spectra.^{15,29} These are based on the semiclassical line-shape theory, and the line width is controlled through a phenomenological decay function.^{30,31} In a static averaging approximation, for example, the absorption profile is calculated from individual MD snapshots and the resultant electrostatic potentials.¹³ This typically leads to too broad bands, which can be improved by many techniques,³² discussion of which goes beyond the scope of this work.

But also in the instantaneous normal-mode approximation, most coordinates are too dispersed if compared to quantum-mechanical uncertainty, as the MD cluster geometries are based on classical mechanics. We therefore propose to efficiently

Received: September 12, 2011

Revised: October 21, 2011

Published: December 01, 2011

reduce the consequent spectral broadening by a partial optimization of the cluster geometries.^{11,28} In particular, the normal-mode optimization algorithm³³ seems to be very suitable for this purpose, as it was found particularly robust for clusters,³⁴ it is numerically stable, and it does not require manual definition of the coordinates. For larger molecules, for example, we used it to fix the desired conformations of peptides³⁵ and large DNA³⁶ molecules, whereas the normal mode's degrees of freedom important for the spectrum could be relaxed.

For the clusters investigated in the present study, the extent of the partial optimization is crucial for realistic results. The geometry of MD clusters cannot be optimized completely to avoid collapse to an energy minimum, implying a loss of the structural information obtained by the dynamics. In the normal-mode partial optimization, this can be controlled by a sole parameter, the maximal harmonic normal-mode frequency (ω_{\max}), below which the normal modes are fixed. By fixing the shallow modes, such motions as molecular translations and rotations are restricted. However, the limit has been used on an ad hoc basis so far. In particular, neither the relation of ω_{\max} to the resulting bandwidths nor the effect on molecular coordinates has been established. To rationalize the choice of this parameter, in this study we perform Raman spectral simulation based on 100 snapshots of lactamide in a box of water molecules obtained previously by a CPMD simulation,²⁸ and monitor the resultant inhomogeneous broadening. The coordinate changes occurring during the partial optimization were monitored, and the simulated bandwidths were compared to experimental Raman spectra.

To better understand the origin of the broadening in the instantaneous normal-mode approximation, we also constructed a model two-dimensional system, where the classical MD results could be compared to benchmark vibrational configuration interaction (VCI) computation. As shown below, already the model 2D Hamiltonian exhibits band broadening; this is primarily caused by the anharmonic character of the potential and coupling of the vibrational modes. However, the results on the lactamide also document that the error can be efficiently reduced by the partial optimization, and that this empirical procedure can be at least partially justified by physical arguments. In particular, the low-frequency vibrations (solvent translations, torsions, etc.) that are temperature-excited are treated classically, using the MD coordinate dispersion, whereas higher-energy vibrations (bending and stretching modes) need to be fully optimized.

METHODS

A Model of the Anharmonic Coupling. To obtain a deeper insight into the role of anharmonicities in MD potential and spectra calculated within the instantaneous normal-mode approximation, we considered a two-dimensional model system with a potential $V = (\omega_1/2)q_1^2 + (\omega_2/2)q_2^2 + (d_{1122}/24)q_1^2q_2^2$, where q_i denote the dimensionless normal-mode coordinates³⁷ and cm^{-1} are used as energy units. The harmonic parameters were inspired by a B3LYP³⁸/6-31G** computation³⁹ of a hydrogen-bonded water dimer,¹⁰ with the frequencies $\omega_1 = 28 \text{ cm}^{-1}$ and $\omega_2 = 3712 \text{ cm}^{-1}$ corresponding to a water wagging and OH stretching mode, respectively. By choice we wanted to mimic a coupling of low ($\omega \ll kT$, where kT is the Boltzmann quantum) and high ($\omega \gg kT$) frequency modes. The quartic anharmonic constant was set to $d_{1122} = 448 \text{ cm}^{-1}$. The constant was chosen rather arbitrarily; nevertheless, its magnitude corresponds to usual anharmonic coupling constants in molecules.⁴⁰

To mimic the MD procedure, the classical instantaneous spectra were simulated for 90×90 coordinates equidistantly chosen on the 2D $q_1 \times q_2$ potential energy surface, within $q_{\min} = -2$ and $q_{\max} = 2$. At each point an effective MD frequency of the second mode was calculated as a second derivative of the potential, $\omega_2' = \partial^2 V / \partial q_2^2$. The resulting spectral band was weighted by the corresponding Boltzmann factor for 50 and 300 K. An arbitrary dipole strength was introduced, constant within the coordinate space. Individual transitions were summed and convoluted with Lorentzian band 10 cm^{-1} wide (full widths at half-height, fwhh) to smooth the resultant curve.

For the same system, quantum transition frequencies were obtained by vibrational configuration interaction (VCI)⁴¹ done in the harmonic oscillator basis involving 51 states, and the spectrum was generated similarly as for the classical case using Boltzmann weighting of the initial states. For the first and second normal mode, 10 and 5 times excited states were included, respectively. The S4 program⁴² was used for the VCI computation. A constant intensity of the $|00\rangle \rightarrow |01\rangle$ transition was assumed, similarly as for the MD model; i.e., the intensity anharmonicities (second dipole derivatives) were neglected.

Normal-Mode Optimization. In the vicinity of an energy minimum, we can introduce a molecular harmonic vibrational Hamiltonian given in a matrix form by³⁷

$$H = \frac{1}{2}(\Delta \mathbf{x}^t \mathbf{M} \Delta \mathbf{x} + \Delta \mathbf{x}^t \mathbf{f} \Delta \mathbf{x}) \quad (1)$$

where \mathbf{M} is diagonal matrix of atomic masses m_i , $\Delta \mathbf{x}$ is the vector of atomic displacements with respect to the equilibrium positions, $\Delta x_i = x_i - x_i^0$, superscript t denotes transpose matrices, and \mathbf{f} is the Cartesian force field. Conveniently, mass-weighted coordinates are introduced as $X_i = (m_i)^{1/2} \Delta x_i$, so that $f_{ij} = (m_i m_j)^{1/2} F_{ij}$, and $H = \frac{1}{2}(\dot{\mathbf{X}}^t \mathbf{X} + \mathbf{X}^t \mathbf{F} \mathbf{X})$. Finally, the normal-mode coordinates Q_i are typically introduced by

$$\mathbf{X} = \mathbf{s} \mathbf{Q} \quad (2)$$

where the transformation matrix satisfies $\mathbf{s}^t \mathbf{s} = \mathbf{I}$, $\mathbf{s}^t \mathbf{F} \mathbf{s} = \mathbf{\Lambda}$; \mathbf{I} is the unit matrix, and $\mathbf{\Lambda}$ is a diagonal matrix ($\Lambda_{ij} = \omega_i^2 \delta_{ij}$) containing squares of the normal-mode frequencies ω_i . The Hamiltonian then becomes a sum of harmonic oscillators:

$$H = \sum_i \frac{1}{2}(\dot{Q}_i^2 + \omega_i^2 Q_i^2) \quad (3)$$

Equation 3 is usually used to obtain vibrational molecular energies. However, using the linear transformation between the Cartesian displacements and the normal-mode coordinates

$$\Delta x_\mu = \sum_i \frac{1}{\sqrt{m_\mu}} s_{\mu i} Q_i = \sum_i S_{\mu i} Q_i \quad (4)$$

we can use the Q_i coordinates during the optimization in place of the more usual internal redundant^{43,44} or Cartesian coordinates. In the QGRAD⁴⁵ program interfaced to Gaussian,³⁹ initial Cartesian force field can be estimated on a lower level, and it is continuously updated by the "BGFS"⁴⁶⁻⁴⁹ formula from Cartesian gradients

$$\mathbf{f}^{(i+1)} = \mathbf{f}^{(i)} - \left(\frac{\Delta \mathbf{g}^t \Delta \mathbf{g}}{\mathbf{d}\mathbf{x}^t \Delta \mathbf{g}} + \frac{(\mathbf{f}^{(i)} \mathbf{d}\mathbf{x})^t \mathbf{d}\mathbf{x} \mathbf{f}^{(i)}}{\mathbf{d}\mathbf{x}^t \mathbf{f}^{(i)} \mathbf{d}\mathbf{x}} \right) \quad (5)$$

where $\Delta \mathbf{g}$ and $\mathbf{d}\mathbf{x}$ are gradient and coordinate increments between the steps i and $i + 1$.

The actual optimization is performed in normal modes, using the RFO^{50–54} updating. New normal-mode displacements are

$$d\mathbf{Q}^{(i+1)} = -\frac{2\mathbf{g}^{(i)}}{\Lambda_{ii} + \sqrt{\Lambda_{ii}^2 + 4(\mathbf{g}^{(i)})^2}} \quad (6)$$

so that updated Cartesian coordinates may be obtained as $\mathbf{x}^{(i+1)} = \mathbf{x}^{(i)} - \mathbf{S}d\mathbf{Q}^{(i+1)}$. Further details can be found in the previous works.^{33,34} Note that this scheme also enables a full optimization of the system. In the restricted normal-mode optimization adopted in this work, some modes (with $\omega_i \in (\omega_{\min}, \omega_{\max})$) are kept constant ($dQ_i = 0$).

Lactamide Raman and ROA Spectra. The geometry CPMD snapshots were selected randomly from a 48 ps simulation performed previously.²⁸ From the snapshots, clusters containing (S)-lactamide and 3–9 hydrogen-bonded waters closer than 3.6 Å to a lactamide atom were selected. This approximation well included the effect of the first hydration shell on the vibrational properties of lactamide; more distant water molecules did not influence the signal significantly. All computations were performed at the B3LYP/6-311++G**/CPCM level of theory, using the continuum model to simulate the effect of the more distant waters, not explicitly included in the computations. The constrained normal-mode optimization was repeated for seven values of ω_{\max} : 10, 20, 50, 100, 200, 300, and 600 cm^{-1} . In addition, we also studied the raw nonoptimized CPMD snapshots corresponding to infinite ω_{\max} . To fix large imaginary frequencies occasionally exhibited by some CPMD geometries, a lower limit $\omega_{\min} = -300 \text{ cm}^{-1}$ was introduced and kept constant.

For the $8 \times 100 = 800$ optimized and raw geometries, Raman backscattered line intensities⁵⁵ were calculated by Gaussian, and the water signal (corresponding polarizability derivatives) was deleted. Smoother spectra were generated by summing the 100 cluster signals and performing a convolution (e.g., ref 56, eq 3) with Lorentzian bands 2 cm^{-1} wide, which were much narrower than the inhomogeneous broadening.

For selected lactamide vibrational bands (528, 813, and 920 cm^{-1}), theoretical bandwidths (fwhh) were obtained from the simulated spectra by fitting with Lorentzian bands. The bands were chosen at frequencies where overlap of multiple vibrational transitions was minimal, and the fitting with the symmetric function was reasonable. By comparing whole spectral shapes, we deduce that their broadening reflects behavior of the spectral signals within the entire range of frequencies. For the fitting, we used an iterative procedure, comparing integral mean quadratic deviations of spectral intensities with the ideal Lorentzian profile.

RESULTS AND DISCUSSION

Two-Dimensional Model. The simpler 2D model Hamiltonian well documents the limits of the instantaneous normal-mode approximation used in MD. In Figure 1, absorption spectra are simulated for the two-dimensional model using the classical and quantum approach. We can already see some common errors introduced by the classical approximation. First, the quantum theory provides a few transitions only, whereas the classical approach generates a continuous spectrum (approximated by the high line density corresponding to the coordinate grid). This is apparent namely for the lower temperature (50 K, upper part of Figure 1), where even the lowest energy vibration (with the frequency ω_1) predominantly remains in the ground state, and VCI provides one transition only. For 300 K (lower part of Figure 1)

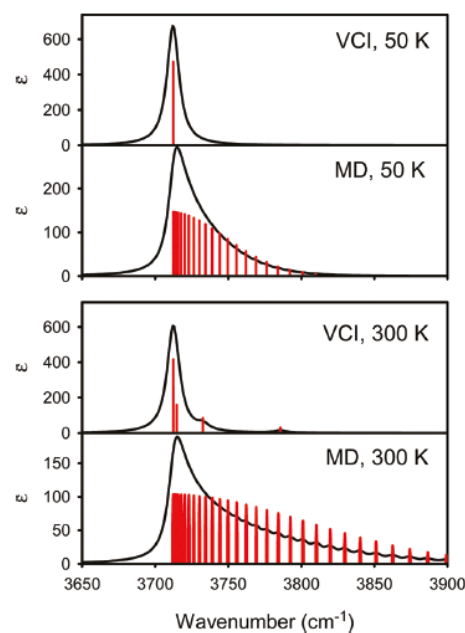


Figure 1. Absorption spectra (ϵ , in arbitrary units) of the 2D model simulated by the quantum (VCI) and classical (MD) approaches at 50 and 300 K.

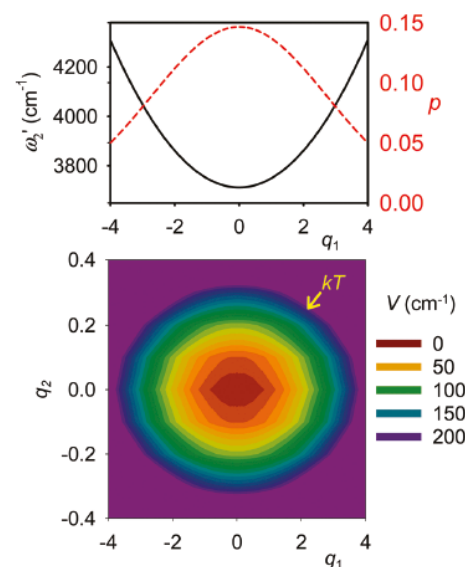


Figure 2. Model 2D potential (bottom, $V = (\omega_1/2)q_1^2 + (\omega_2/2)q_2^2 + (d_{1122}/24)q_1^2q_2^2$, approximate accessible energy at 300 K is indicated by kT), effective harmonic frequency of the second mode $\omega_2' = \partial^2 V / \partial q_2^2$ and Boltzmann probability p for 300 K as dependent on q_1 (top).

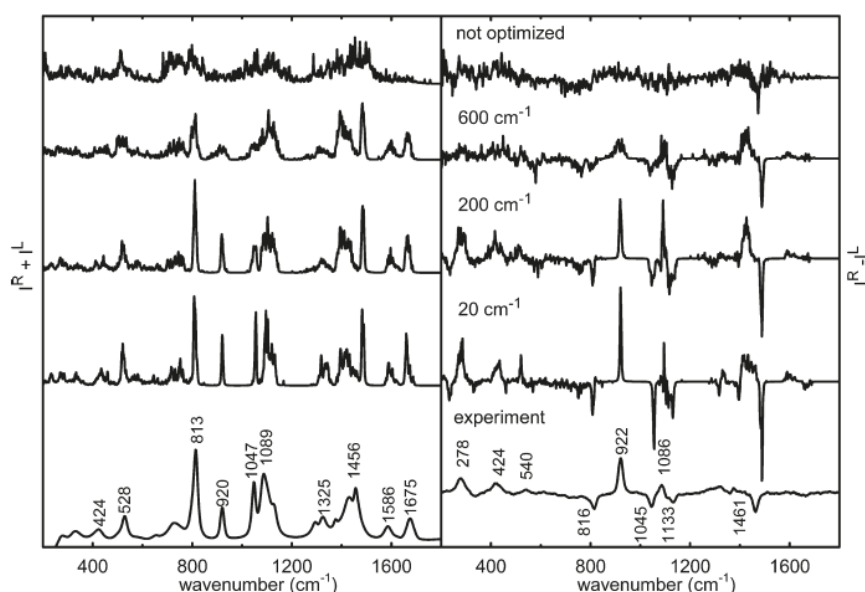


Figure 3. Lactamide solution backscattered Raman (left, $I^R + I^L$) and ROA (right, $I^R - I^L$) spectra simulated with the partially optimized CPMD clusters. The ω_{\max} cutoffs and the experimental spectrum in H_2O with positions of principal peaks are indicated.

more quantum transitions appear; the system starts to exhibit the classical distribution of vibrational frequencies.

The MD spectral shape in Figure 1 can be easily understood on the basis of the potential analyzed in Figure 2. We see that the “molecule” can explore a relatively large part of the potential energy surface, limited approximately by the Boltzmann kT limit. Consequently, different harmonic frequencies equal to the potential second derivatives are obtained for the higher-frequency mode (q_2). For our coupling term, the effective MD frequencies are limited by the lower limit for $q_1 = 0$, i.e., $\omega_2' \geq \omega_2$. However, in the adiabatic quantum model, for $\hbar\omega_2 \gg kT$, only one transition frequency (for 50 K, Figure 1) or a transition with limited number of satellite bands (300 K, Figure 1) is possible.

Another quantum effect, the shift of the maximal frequency, is quite small (1 cm^{-1} , Figure 1), and can be neglected in this case. However, it can be quite large in real molecules,⁵⁷ and except for a partial diagonal correction it cannot be simulated within the instantaneous normal-mode and harmonic schemes. Finally, even for the higher temperature of 300 K the classical bandwidth based on the MD/instantaneous normal-mode approach is still larger than those obtained by the more rigorous VCI calculation.

The example potential was chosen to be simple to enable the benchmark VCI computation. For real systems, we can expect that other anharmonic contributions not included in the simplified 2D Hamiltonian, such as diagonal and cubic terms,⁵⁷ would lead to a more complicated behavior. The 2D model is thus not able to fully explain the MD broadening effects in large clusters; nevertheless, it convincingly indicates that anharmonic coupling terms in the vibrational Hamiltonian cause significant differences between the quantum (VCI) and classical (MD) results.

Solvated Lactamide. Also in the lactamide spectra direct exploitation of MD geometries leads to overestimation of the broadening and quite unrealistic spectral shapes. The spectra

simulated from the raw snapshots, the optimized snapshots with ω_{\max} of 600, 200, and 20 cm^{-1} , and the experimental²⁸ spectra measured in aqueous solution are compared in Figure 3 (left, Raman; right, Raman optical activity, ROA). Clearly, the results for raw nonoptimized clusters (top in Figure 3) are unusable for a detailed assignment of the lactamide bands. Similarly as for the model system (Figure 1), the raw MD instantaneous normal-mode approach overestimates the anharmonic force field terms and causes too wide dispersion of the harmonic frequencies.

On the other hand, the partial optimization of cluster geometries leads to a radical improvement. For $\omega_{\max} = 600 \text{ cm}^{-1}$ many of the experimental intensity features for wavenumbers above 800 cm^{-1} are reproduced (Figure 3). However, the bands are still too broad, and no improvement is apparent below 600 cm^{-1} . The Raman band at $\sim 528 \text{ cm}^{-1}$ became even broader for $\omega_{\max} = 600 \text{ cm}^{-1}$ than for the nonoptimized case, which can be explained by the coupling of the complicated 528 cm^{-1} vibrations with higher-frequency modes. For $\omega_{\max} = 200 \text{ cm}^{-1}$ (Figure 3), most of the Raman and ROA intensity features are well developed, and the bandwidths are realistic within the entire wavenumber region. For $\omega_{\max} = 20 \text{ cm}^{-1}$ individual bands can be recognized as well, but most bandwidths become too narrow if compared to the experiment. $\omega_{\max} = 10 \text{ cm}^{-1}$ (not shown) provided virtually the same spectra as $\omega_{\max} = 20 \text{ cm}^{-1}$. Note that simulations in vacuum or a continuum solvent model would provide line spectra only, without any information about the broadening.

The optimizations with too low ω_{\max} become less economic in terms of the required computer time. Note that the normal-mode coordinates, similar to Cartesian coordinates, are in general not suitable for complete molecular optimizations as they do not follow the covalent bond network.³⁴ Thus, whereas the optimization of 100 clusters (without the frequency calculation)

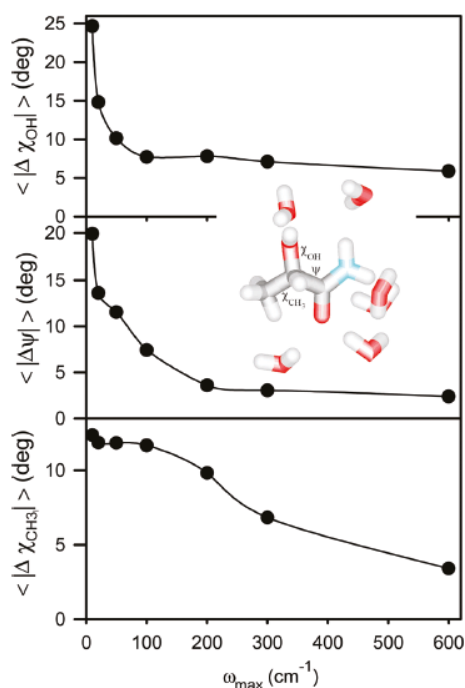


Figure 4. Average absolute changes of three (S)-lactamide torsional angles during the optimization, as obtained for seven values of ω_{\max} . The averages were obtained from 100 CPMD clusters; the angles $\chi_{\text{OH}} = \angle(\text{C}=\text{O}\text{COH})$, $\psi = \angle(\text{NCCC})$, and $\chi_{\text{CH}_3} = \angle(\text{CCCH})$ are indicated in the randomly chosen snapshot.

required 28 days of CPU time (3 GHz, Intel 5160) for the 600 cm^{-1} limit, 89 and 212 days were needed for 200 and 20 cm^{-1} , respectively. We also attempted a full optimization of the clusters, which provided results very close to those obtained with the lowest ω_{\max} limits (10 and 20 cm^{-1}). However, many clusters could not be fully optimized because of a lack convergence of the optimization algorithm. The full geometries also do not reflect well the desired dynamical geometry distribution at 300 K; therefore, we do not include these results in the analysis.

The effect of the optimization limit on the relaxation of molecular coordinates is documented in Figure 4. Here, average changes of the χ_{OH} , ψ , and χ_{CH_3} torsional angles are plotted for seven ω_{\max} values. The OH rotation is associated with the shallowest potential, and thus remains fixed for most of the optimization models. The rotation is released for $\omega_{\max} < 100 \text{ cm}^{-1}$, when the change increases steeply. The ψ angle responds more gradually, and it is starting to change already for $\omega_{\max} < 300 \text{ cm}^{-1}$. The CH_3 rotation exhibits the most developed sigmoidal “melting” pattern with a transition frequency at about 250 cm^{-1} . This value also well corresponds to the harmonic normal-mode frequency of this motion.²⁸

A detailed coordinate dispersion is documented on the ψ and χ_{OH} angles in Figure 5. For 10 randomly selected clusters the optimized torsional angles were extracted for each value of ω_{\max} . During the optimization, the original broad distribution of ψ (within $\sim 105^\circ$ – 150° for the selected clusters) becomes

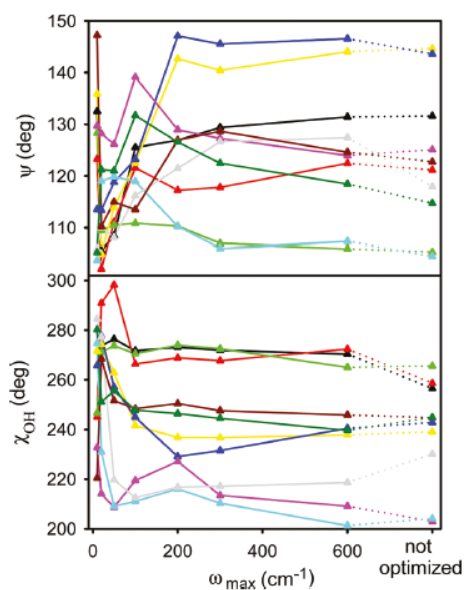


Figure 5. Dependence of the optimized (S)-lactamide ψ and χ_{OH} angles on ω_{\max} in 10 randomly chosen clusters.

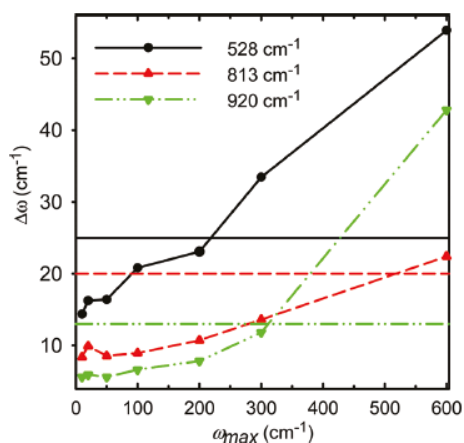


Figure 6. Simulated lactamide Raman bandwidths ($\Delta\omega$) as calculated for different ω_{\max} for the bending (528 cm^{-1}), NH_2 wagging (813 cm^{-1}), and C–C/C–O stretching (920 cm^{-1}) vibrational modes. Experimental widths²⁸ are indicated by the horizontal lines.

narrower, adopting values mostly within $\sim 102^\circ$ – 130° for $\omega_{\max} < 200 \text{ cm}^{-1}$. This reflects the intrinsic molecular potential driving motion of this angle. On the other hand, for χ_{OH} the dispersion ($\sim 200^\circ$ – 270° for nonoptimized clusters, and 210° – 290° for $\omega_{\max} = 20 \text{ cm}^{-1}$) does not change much during the optimizations. This can be explained by the stabilizing effect of the surrounding water molecules that make hydrogen bonds to the OH group. The water positions do not change even for low values of ω_{\max} .

The computed bandwidths for three nonoverlapping peaks with central frequencies at 528, 813, and 920 cm^{-1} are plotted in Figure 6 as obtained with the seven values of ω_{max} . The experimental widths, indicated by the horizontal lines, were lowered by 3 cm^{-1} to account for the instrument broadening. We consider this value to be a lower limit of the correction because of the instrument low-resolution setup optimized for ROA measurement, and the crude CCD detection of the wavenumbers where 1 pixel corresponds to about 3 cm^{-1} .

The comparison is also hampered by the experimental noise and transition overlap. Typically, each simulated band contains not only the dominant transition but also satellites. Nevertheless, in Figure 6, we can see that an optimal ω_{max} can be estimated at least approximately from the crossing of the simulated bandwidth curve with the experimental line, ranging from $\omega_{\text{max}} \sim 200 \text{ cm}^{-1}$ (for the 528 cm^{-1} band) to $\sim 500 \text{ cm}^{-1}$ (813 cm^{-1} band). A similar analysis of the ROA spectra and the direct Raman and ROA spectral comparison in Figure 3 suggest that an optimal ω_{max} value is close to the lower limit of the interval, within 200–300 cm^{-1} , curiously, this range comprises the Boltzmann temperature quantum ($kT \approx 208 \text{ cm}^{-1}$ at 300 K).

We think that a relation of the limit to kT is quite obvious for the reasons discussed above, although the actual empirical value found here may be a coincidence. Unfortunately, comparison with rigorous results, such as the VCI computation for the dimer, cannot be presently done for larger clusters to determine the relation more closely. On the other hand, the spectral profiles (cf. Figure 3) change very slowly with ω_{max} ; thus in a wide interval around the optimal value the spectra can be simulated realistically enough to allow for the normal-mode assignment and estimation of most of the solvent inhomogeneous normal-mode broadening.

CONCLUSIONS

The raw cluster simulations based on classical and ab initio molecular dynamics provide too wide vibrational bands and unrealistic geometry dispersion of the higher-frequency motions. On the two-dimensional model, we could show that this may be primarily caused by the coupling of vibrational modes and anharmonic force field terms. Geometries and, consequently, the effective harmonic normal-mode frequencies vary too much in the molecular dynamics trajectories. For the lactamide, we showed that the broadening of the vibrational bands simulated for an ensemble of clusters can be efficiently controlled by the normal mode optimization constraint. The resultant spectra exhibit not only better bandwidths but also relative intensities if compared to the experiment. The only empirical parameter, the cutoff of the vibrational frequencies in the constrained optimization, could be obtained by comparison of selected peaks in the experimental and simulated spectra. The empirical procedure of partial optimization could be to a large extent rationalized by the quantum properties of the vibrations, and provides an efficient means of modeling vibrational properties of molecules in solutions.

AUTHOR INFORMATION

Corresponding Author

*E-mail: bour@uochb.cas.cz

ACKNOWLEDGMENT

The study was performed with support from the Academy of Sciences, Grant Agency of the Czech Republic (P208/11/0105),

the Grant Agency of Charles University (126310), the MSMT (LH11033), and Norwegian Supercomputing Program (Notur). We thank Prof. Kenneth Ruud for the discussion on this topic.

REFERENCES

- (1) Tomasi, J.; Mennucci, B.; Cammi, R. *Chem. Rev.* **2005**, *105*, 2999.
- (2) Mennucci, B.; Martínez, J. M. *J. Phys. Chem. B* **2005**, *109*, 9818.
- (3) Bouř, P.; Michalík, D.; Kapitán, J. *J. Chem. Phys.* **2005**, *122*, 144501.
- (4) Dračinský, M.; Kaminský, J.; Bouř, P. *J. Phys. Chem. B* **2009**, *113*, 14698.
- (5) Kamiya, N.; Watanabe, Y. S.; Ono, S.; Higo, J. *Chem. Phys. Lett.* **2005**, *401*, 312.
- (6) Car, R.; Parrinello, M. *Phys. Rev. Lett.* **1985**, *55*, 2471.
- (7) Lippert, G.; Hutter, J.; Parrinello, M. *Mol. Phys.* **1997**, *92*, 477.
- (8) Grimme, S.; Antony, J.; Ehrlich, S.; Krieg, H. *J. Chem. Phys.* **2010**, *132*, 154104.
- (9) Dračinský, M.; Bouř, P. *J. Chem. Theory Comput.* **2010**, *6*, 288.
- (10) Bouř, P.; Keiderling, T. A. *J. Chem. Phys.* **2003**, *119*, 11253.
- (11) Kaminský, J.; Bouř, P.; Kubelka, J. *J. Phys. Chem. A* **2011**, *115*, 30.
- (12) Yang, S.; Cho, M. *J. Chem. Phys.* **2005**, *123*, 134503.
- (13) Grahnen, J. A.; Amunson, K. E.; Kubelka, J. *J. Phys. Chem. B* **2010**, *114*, 13011.
- (14) Choi, J. H.; Kim, J. S.; Cho, M. *J. Chem. Phys.* **2005**, *122*, 174903.
- (15) Choi, J. H.; Cheon, S.; Lee, H.; Cho, M. *Phys. Chem. Chem. Phys.* **2008**, *10*, 3839.
- (16) Jeon, J.; Cho, M. *New J. Phys.* **2010**, *12*, 065001.
- (17) Miyazawa, T.; Blout, E. R. *J. Am. Chem. Soc.* **1961**, *83*, 712.
- (18) Krimm, S.; Bandekar, J. *Adv. Protein Chem.* **1986**, *38*, 181.
- (19) Torii, H.; Tatsumi, T.; Tasumi, M. *J. Raman Spectrosc.* **1998**, *29*, 537.
- (20) Kubelka, J.; Keiderling, T. A. *J. Phys. Chem. A* **2001**, *105*, 10922.
- (21) Barron, L. D. *Molecular Light Scattering and Optical Activity*; Cambridge University Press: Cambridge, UK, 2004.
- (22) Haesler, J.; Schindelholz, I.; Riguier, E.; Bochet, C. G.; Hug, W. *Nature* **2007**, *446*, 526.
- (23) Polavarapu, P. L. *Angew. Chem., Int. Ed.* **2002**, *41*, 4544.
- (24) Cheeseman, J. R.; Shaik, M. S.; Popelier, P. L. A.; Blanch, E. W. *J. Am. Chem. Soc.* **2011**, *133*, 4991.
- (25) Keyes, T. J. *J. Phys. Chem. A* **1997**, *101*, 2921.
- (26) Ahlborn, H.; Space, B.; Moore, P. B. *J. Chem. Phys.* **2000**, *112*, 8083.
- (27) Bouř, P. *Chem. Phys. Lett.* **2002**, *365*, 82.
- (28) Hopmann, K. H.; Ruud, K.; Pecul, M.; Kudelski, A.; Dračinský, M.; Bouř, P. *J. Phys. Chem. B* **2011**, *115*, 4128.
- (29) Kwac, K.; Lee, K. K.; Han, J.; Oh, K. I.; Cho, M. *J. Chem. Phys.* **2008**, *128*, 105106.
- (30) Gorbunov, R. D.; Nguyen, P. H.; Kobus, M.; Stock, G. *J. Chem. Phys.* **2007**, *126*, 054509.
- (31) Choi, J. H.; Lee, H.; Lee, K. K.; Hahn, S.; Cho, M. *J. Chem. Phys.* **2007**, *126*, 045102.
- (32) Joutsuka, T.; Ando, K. *J. Chem. Phys.* **2011**, *134*, 204511.
- (33) Bouř, P.; Keiderling, T. A. *J. Chem. Phys.* **2002**, *117*, 4126.
- (34) Bouř, P. *Collect. Czech. Chem. Commun.* **2005**, *70*, 1315.
- (35) Yamamoto, S.; Watarai, H.; Bouř, P. *ChemPhysChem* **2011**, *12*, 1509.
- (36) Andrushchenko, V.; Bouř, P. *J. Phys. Chem. A* **2007**, *111*, 9714.
- (37) Papoušek, D.; Aliev, M. R. *Molecular Vibrational/Rotational Spectra*; Academia: Prague, 1982.
- (38) Becke, A. D. *J. Chem. Phys.* **1993**, *98*, 5648.
- (39) Frisch, M. J.; Trucks, G. W.; Schlegel, H. B.; Scuseria, G. E.; Robb, M. A.; Cheeseman, J. R.; Scalmani, G.; Barone, V.; Mennucci, B.; Petersson, G. A.; Nakatsuji, H.; Caricato, M.; Li, X.; Hratchian, H. P.; Izmaylov, A. F.; Bloino, J.; Zheng, G.; Sonnenberg, J. L.; Hada, M.; Ehara, M.; Toyota, K.; Fukuda, R.; Hasegawa, J.; Ishida, M.; Nakajima, T.

Honda, Y.; Kitao, O.; Nakai, H.; Vreven, T.; Montgomery, J., J. A.; Peralta, J. E.; Ogliaro, F.; Bearpark, M.; Heyd, J. J.; Brothers, E.; Kudin, K. N.; Staroverov, V. N.; Kobayashi, R.; Normand, J.; Raghavachari, K.; Rendell, A.; Burant, J. C.; Iyengar, S. S.; Tomasi, J.; Cossi, M.; Rega, N.; Millam, J. M.; Klene, M.; Knox, J. E.; Cross, J. B.; Bakken, V.; Adamo, C.; Jaramillo, J.; Gomperts, R.; Stratmann, R. E.; Yazyev, O.; Austin, A. J.; Cammi, R.; Pomelli, C.; Ochterski, J. W.; Martin, R. L.; Morokuma, K.; Zakrzewski, V. G.; Voth, G. A.; Salvador, P.; Dannenberg, J. J.; Dapprich, S.; Daniels, A. D.; Farkas, O.; Foresman, J. B.; Ortiz, J. V.; Cioslowski, J.; Fox, D. J. *Gaussian 09, Revision A.02*; Gaussian, Inc.: Wallingford, CT, 2009.

- (40) Barone, V. J. *Phys. Chem. A* **2004**, *108*, 4146.
- (41) Daněček, P.; Bouř, P. *J. Comput. Chem.* **2007**, *28*, 1617.
- (42) Bouř, P. *S4, program for anharmonic vibrational properties*; Academy of Sciences: Prague, 2010.
- (43) Peng, C.; Ayala, P. Y.; Schlegel, H. B.; J., F. M. *J. Comput. Chem.* **1996**, *17*, 49.
- (44) Pulay, P.; Fogarasi, G. *J. Chem. Phys.* **1992**, *96*, 2856.
- (45) Bouř, P. *Qgrad*; Academy of Sciences, Prague: Prague, 2006.
- (46) Broyden, C. G. *J. Inst. Math. Appl.* **1970**, *6*, 76.
- (47) Fletcher, R. *Comput. J.* **1970**, *13*, 317.
- (48) Goldfarb, D. *Math. Comput.* **1970**, *24*, 23.
- (49) Shanno, D. F. *Math. Comput.* **1970**, *24*, 647.
- (50) Schlegel, H. B. Geometry optimization on potential energy surfaces. In *Modern electronic structure theory*; Yarkony, D. R., Ed.; World Scientific: Singapore, 1995; p 459.
- (51) Banerjee, A.; Adams, N.; Simons, J.; Shepard, R. J. *Phys. Chem.* **1985**, *89*, 52.
- (52) Simons, J.; Nichols, J. *Int. J. Quantum Chem., Quantum Chem. Symp.* **1990**, *24*, 263.
- (53) Baker, J.; Hehre, W. J. *J. Comput. Chem.* **1991**, *12*, 606.
- (54) Baker, J. *J. Comput. Chem.* **1993**, *14*, 1085.
- (55) Polavarapu, P. L. *Vibrational spectra: principles and applications with emphasis on optical activity*; Elsevier: Amsterdam, 1998; Vol. 85.
- (56) Buděšínský, M.; Daněček, P.; Bednářová, L.; Kapitán, J.; Baumruk, V.; Bouř, P. *J. Phys. Chem. A* **2008**, *112*, 8633.
- (57) Daněček, P.; Kapitán, J.; Baumruk, V.; Bednářová, L.; Kopecký, V., Jr.; Bouř, P. *J. Chem. Phys.* **2007**, *126*, 224513.

A2. Publication [II]

Hudecová, J.; Profant, V.; Novotná, P.; Baumruk, V.; Urbanová, M.; Bouř, P., CH
Stretching Region: Computational Modeling of Vibrational Optical Activity. *J. Chem.
Theory Comput.* **2013**, *9*, 3096–3108

CH Stretching Region: Computational Modeling of Vibrational Optical Activity

Jana Hudecová,^{†,§} Václav Profant,[†] Pavlína Novotná,[‡] Vladimír Baumruk,[†] Marie Urbanová,[‡] and Petr Bour^{*,§}

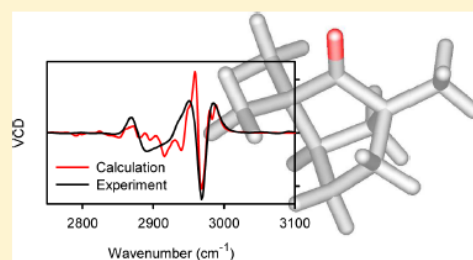
[†]Faculty of Mathematics and Physics, Institute of Physics, Charles University, Ke Karlovu 5, 12116, Prague 2, Czech Republic

[‡]Department of Physics and Measurements and Department of Analytical Chemistry, Institute of Chemical Technology, Technická 5, 16628 Prague, Czech Republic

[§]Institute of Organic Chemistry and Biochemistry, Academy of Sciences, Flemingovo náměstí 2, 16610 Prague, Czech Republic

Supporting Information

ABSTRACT: Most organic compounds provide vibrational spectra within the CH stretching region, yet the signal is difficult to interpret because of multiple difficulties in experiment and modeling. To better understand various factors involved, the ability of several harmonic and anharmonic computational approaches to describe these vibrations was explored for α -pinene, fenchone, and camphor as test compounds. Raman, Raman optical activity (ROA), infrared absorption (IR), and vibrational circular dichroism (VCD) spectra were measured and compared to quantum chemical computations. Surprisingly, the harmonic vibrational approach reasonably well reproduced the measured spectral patterns, including the vibrational optical activity (VOA). The CH stretching, however, appeared to be more sensitive to the basis set and solvent variations than lower-frequency vibrations. For a higher accuracy in frequencies and spectral shapes, anharmonic corrections were necessary. Accurate harmonic and anharmonic force fields were obtained with the mPW2PLYP double-hybrid functional. A limited vibrational configuration interaction (LVCI) where the CH stretching motion was decoupled from other vibrations provided the best simulated spectra. A balanced harmonic oscillator basis set had to be used, containing also states indirectly interacting with fundamental vibrations. A simpler second-order perturbational approach (PT2) appeared less useful. The modeling provided unprecedented agreement with experimental vibrational frequencies; spectral shapes were reproduced less faithfully. The possibility of *ab initio* interpretation of the CH spectral region for relatively large molecules further broadens the application span of vibrational spectroscopy.



INTRODUCTION

The CH stretching region is traditionally considered as a range of wavenumbers approximately within 2500–3400 cm^{-1} comprising mostly fundamental transitions of the CH valence vibrational motions. Unlike NH, OH or SH stretching vibrations also present in this interval, CH stretching bands are not prone to broadening by hydrogen bonding. Because of the high relative strength of the CH bond and small hydrogen mass, fundamental CH stretching energies are well-separated from other molecular vibrations and can be easily identified in the spectra. They provide rich information not only about molecular stereochemistry^{1,2} but also about intermolecular interaction³ as the hydrogen atoms form large parts of molecular surfaces. For a deuterated system containing the CD bonds (vibrating lower than CH, around 2200 cm^{-1}) even a solute–solvent chirality induction was observed lately.⁴ Near-infrared vibrational circular dichroism was proposed for online monitoring of a chemical reaction.⁵

On the other hand, the bond strengths of different CH groups in a molecule are quite similar, which causes overlapping of

vibrational bands, and makes the interpretation difficult. Measurements in the CH stretching region are often connected with unusual spectrometer setups. For example, although particularly useful stereochemical information can be obtained from the vibrational optical activity (VOA),^{6–8} the CH stretching signal may be weak and prone to artifacts.^{9–11}

The potential energy surface governing the hydrogen stretching motion is strongly anharmonic. CH bonds and the coupling terms between them cannot be simply described by quadratic force constants. This often prevents reliable simulation and consequent interpretation of experimental data.^{10,12–18} In the past, for example, simpler models or empirical rules were proposed for VOA simulations in this region.^{9,19} Some spectral shapes could be reasonably well modeled at the harmonic level, which, however, led to huge frequency errors.^{10,20} Obviously, the lower-frequency (around 1400 cm^{-1}) vibrations also profit from an eventual anharmonic correction.²⁰ So far, in spite of

Received: April 6, 2013

Published: May 29, 2013

considerable progress in computational methodology,^{15,21–24} simulations of the CH stretching properties are in general considered to be unreliable.

A significant progress was achieved lately by incorporating the solvent environment to the density functional theory (DFT) simulations of vibrational circular dichroism (VCD).^{20,25,26} Even then the anharmonic corrections, although helpful for energies, did not lead to a general improvement in spectral shapes.²⁶ A mixed message about the performance of the harmonic approximation has thus been obtained in the past. As shown below, some of the confusion can be explained by the stability of the harmonic pattern even when hundreds of thousands of harmonic oscillator (HO) states are allowed to interact within the anharmonic scheme. As shown below, however, these states have to be chosen in a balanced way. This study also suggests that the perturbational approach (PT2) used previously²⁶ may not be sufficient to treat the anharmonicities, especially for the vibrational optical activity, and should be replaced by the more universal vibrational configuration interaction.

In the first part of this paper, we systematically investigate various factors influencing the quality of both the harmonic and anharmonic computed force fields with respect to the CH stretching behavior. It turns out, for example, that the CH stretching motion is very sensitive to the choice of the basis set and electronic computational level used. Unlike in previous studies, the “complete set” of IR, Raman, Raman optical activity (ROA), and VCD is simulated and compared to experiment to avoid accidental agreement/disagreement of the spectra. In particular, the vibrational optical activity (VCD, ROA) is very sensitive to variations of computational parameters,²⁷ structure, and molecular force field. For ROA, high-quality experimental spectra in the CH stretching region could be measured, owing to a spectrometer expansion by three grating systems, correction of the intensities against a fluorescence standard, and a careful baseline subtraction. Original VCD spectra were acquired as well, on a spectrometer dedicated to this region.

For the anharmonic computations, we obtained the best results using the limited vibrational configuration method (LVCI) and a limited coupling between the lower- and higher-frequency motions. A faster degeneracy-corrected second order perturbation (PT2)¹⁵ method lead to improvement in frequencies only, without credible intensity reproduction. The LVCI procedure and the limited coupling have been suggested in many variants previously.^{12,21,23,28} Our implementation^{15,29} allows for a fast diagonalization of a very large vibrational Hamiltonian matrix ($\sim 10^6$ of HO basis states) and a consistent spectra generation in a “double-anharmonic” approximation where the energy and intensity tensor derivatives are evaluated up to the fourth and second order, respectively.

It is also important to note that the agreement between the computation and experiment would not be possible without the latest availability of the double-hybrid density functionals³⁰ combining the MP2³¹ method with DFT.³² For relatively large molecules, we are thus getting so far the most balanced converged simulated spectral shapes that considerably improve the harmonic procedure if compared to experiment. Obviously, some discrepancies remain, and we see this study as a step toward full understanding of the molecular vibrational behavior.

METHODS

Spectra Measurement. Raman and ROA incident circular polarized light (ICP) spectra of neat α -pinene, neat fenchone, and 0.2 M CCl_4 solution camphor were acquired on a

spectrometer³³ built at the Charles University, Prague. It is based on the 514.5 nm laser excitation wavelength. Owing to three interchangeable gratings and intensity correction using a fluorescence standard (National Institute of Standards and Technology, USA), a wide wavenumber range ($\sim 50 \dots 3400 \text{ cm}^{-1}$) became accessible. The laser power was set to 500 mW, the total acquisition time was about 20 h for each sample and grating, and the measurements were performed using low-volume quartz cells with antireflectively coated windows. Raw ROA spectra were filtered by Fourier transform to suppress quasiperiodic high-frequency CCD signal. For camphor, the solvent (CCl_4) signal was subtracted. For Raman spectra, the empty cell signal was subtracted and the baseline was slightly straightened by a polynomial fit. ROA artifacts were eliminated by measuring and averaging both enantiomers without further correction. The measurement of both enantiomers was particularly important for the CH stretching signal, where the circular intensity difference³⁴ (CID) ratio of the ROA and Raman signals is as small as $\sim 5 \times 10^{-5}$. Spectra of the (1R)-(+)- α -pinene, (1R)-(-)-fenchone, and (1R)-(+)-camphor enantiomers (Figure 1) are presented.

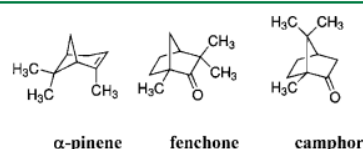


Figure 1. Studied molecules: (1R)-(+)- α -pinene (2,6,6-trimethylbicyclo[3.1.1]hept-2-ene), (1R)-(-)-fenchone (1,3,3-trimethylbicyclo[2.2.1]heptan-2-one), and (1R)-(+)-camphor (1,7,7-trimethylbicyclo [2.2.1]heptan-2-one).

VCD and IR spectra were measured on a FTIR IFS 66/S spectrometer equipped with a PMA 37 VCD/IRRAS module (Bruker, Germany). The samples were placed in a demountable cell (A145, Bruker, Germany) composed of KBr and CaF_2 windows separated by a 6, 50, or 100 μm Teflon spacer with a spectral resolution of 4 or 8 cm^{-1} , and averages of 6–16 blocks of 3686 scans were used. The spectra were corrected for the baseline and artifacts as for ROA. The experimental conditions for all compounds and spectral ranges are summarized in Supporting Information Table S1.

Electronic and Harmonic Vibrational Computations. α -Pinene, fenchone, and camphor geometries were optimized by energy minimization using the Gaussian09 program.³⁵ The Raman, ROA, IR, and VCD spectra were calculated at the same level within the harmonic approximation also by Gaussian. Various quantum chemical models and functionals (HF, MP2,³¹ B2PLYP, B3LYP, BPW91, B3PW91,³⁶ CAM-B3LYP,³⁷ mPW2PLYP,³⁰ and dispersion-corrected^{30,38} mPW2PLYP = “mPW2PLYP-D”) and basis sets (6-31G, D95, 6-31G*, TZV, 6-31+G*, 6-31G**, D95**, TZVP, 6-31++G**, D95+**, 6-31++G**, cc-pVTZ, and aug-cc-pVTZ) were combined in order to investigate the behavior of the CH stretching vibrations. Computation of the ROA intensity tensors is not implemented within mPW2PLYP; thus they were calculated at the DFT B3LYP/6-311++G**/COSMO level. Previous experience suggests that the error associated with such simplification would be very small.^{39–41}

The molecular environment was accounted for by the COSMO⁴² dielectric model. For a deeper insight, nine different

solvents of a broad scale of relative dielectric constants (ϵ_r , given in parentheses, see also Supporting Information Table S2) were used for camphor (vacuum (1), argon (1.43), carbon tetrachloride (2.23), chloroform (4.71), dichloromethane (8.93), 2-hexanone (14.14), methanol (32.61), water (78.36), and formamide (108.94)). The experimental conditions were mimicked by $\epsilon_r = 2.23$ (camphor solution in carbon tetrachloride), $\epsilon_r = 2.69$ (neat α -pinene, using Gaussian parameters for pentanoic acid), and $\epsilon_r = 12.51$ (neat fenchone, using Gaussian parameters for 1-hexanol). A spherical polarization factor⁴³ defined as $\eta = (\epsilon_r - 1)/(2\epsilon_r + 1)$ was conveniently used as the principal solvent characteristic, as many spectroscopic properties are approximately linear in η . All theoretical spectral profiles were generated by a convolution of calculated intensities with a Lorentzian function 10 cm^{-1} wide (full width at half-maximum). Incident circular polarized (ICP) Raman and ROA spectral profiles were adjusted by a Boltzmann factor⁴⁴ to 298 K and expressed as intensity sums ($I^R + I^L$, Raman) and differences ($I^R - I^L$, ROA) for the right- and left-circular polarized lights. Note that in experiment absolute Raman and ROA intensities are not measured; therefore, the computed and experimental intensities were scaled to have similar magnitudes. The IR absorption (ϵ) and VCD ($\Delta\epsilon$) spectra are expressed in the standard units of $\text{L}\cdot\text{cm}^{-1}\cdot\text{mol}^{-1}$. No scaling was applied to computed frequencies.

Anharmonic Corrections. We used a limited Taylor expansion of the vibrational potential, where the anharmonic part is given by

$$W(Q_1, \dots, Q_M) = \frac{1}{6} \sum_{i=1}^M \sum_{j=1}^M \sum_{k=1}^M c_{ijk} Q_i Q_j Q_k + \frac{1}{24} \sum_{i=1}^M \sum_{j=1}^M \sum_{k=1}^M \sum_{l=1}^M d_{ijkl} Q_i Q_j Q_k Q_l \quad (1)$$

where Q_i are the normal mode coordinates, c_{ijk} and d_{ijkl} are the cubic and quartic constants. All cubic and semidiagonal ("ijk", etc.) quartic constants were obtained by two-step differentiation of the second energy derivatives. The differentiation was performed in dimensionless⁴⁵ normal mode coordinates q_i , with a step of $\Delta q_i = \Delta Q_i \times 1000/\omega_i$, where $\Delta Q_i = 0.05$ atomic units, and the harmonic frequency ω_i is in inverse centimeters. The variable step size prevents too small displacements for the lowest-frequency modes.⁴⁶

The PT2 and LVCI schemes were used for anharmonic corrections to vibrational energies and spectral intensities. Within PT2, the harmonic vibrational energy for each state n , E_n^0 , is corrected by $E_n^{(1)} = W_{nn}$ and by a second-order term,

$$E_n^{(2)} = \sum_{m \neq n} A_{mn} \quad (2)$$

where $A_{mn} = [E_m - E_n \pm ((E_m - E_n)^2 + 4W_{mn}^2)^{1/2}]/2$, the plus sign holds for $E_n > E_m$ and minus sign for $E_n < E_m$, and $W_{mn} = \langle n | W | m \rangle$. Similarly, the PT2 wave function was considered as $\psi_n' = \psi_n - \sum_{m \neq n} A_{mn} W_{mn}^{-1} \psi_m$, ψ_n is the unperturbed state.

The spectral properties were considered to be dependent on the coordinates to second order as

$$P = P_0 + \sum_i P_{1,i} Q_i + \frac{1}{2} \sum_{i,j} P_{2,ij} Q_i Q_j \quad (3)$$

where P is the electric dipole moment (for IR) or the polarizabilities (α , G , A , for Raman and ROA intensities). For VCD, we also used the dependence of the magnetic dipole moment on the coordinates and momenta Π_i ,

$$m = m_0 + \sum_i A_{1,i} \Pi_i + \frac{1}{2} \sum_{i,j} A_{2,ij} (\Pi_i Q_j + Q_j \Pi_i) \quad (4)$$

$A_{1,i}$ is the axial tensor. Note that within the magnetic field perturbation theory, the magnetic derivatives can be treated in the same way as for the coordinate derivatives, i.e. within the Born–Oppenheimer approximation.⁴⁷

Transitional PT2 dipole moments and polarizabilities^{34,48} were obtained as $\langle i | P | 0 \rangle / (N_i N_0)^{1/2}$ (for a transition $\psi_0' \rightarrow \psi_i'$), with renormalization factors $N_i = 1 + \sum_{j \neq i} |\langle i | W | j \rangle|^2 E_j^{-2}$, $E_{ij} = E_i - E_j$.

In LVCI, vibrational wave function was expanded to the HO wave functions, $\Phi_\epsilon = \sum_f C_f^e \psi_f$. As in previous studies,^{15,21} several criteria were employed to limit the number of HO basis functions. The lowest-frequency normal modes (e.g., up to mode number 36) were not excited, and only states (f) oblying $W_{fn} > c_1 |E_n - E_f|$ were included, where c_1 is an interaction parameter and n is a ground or fundamental state. A second set of HO basis functions (f') was added based on coefficient c_2 , interacting with the already chosen basis ($W_{f'f} > c_2 |E_{f'} - E_f|$). Hamiltonian elements with too energy-separated states ($|H_{ij}| < 10^{-4} |E_i - E_j|$) were excluded as well.

Up to five-times excited wave functions were used, and the coefficients C_f^e and associated energies E_ϵ were obtained from the Hamiltonian matrix by Mitin's version⁴⁹ of the Davidson⁵⁰ diagonalization procedure. Previously, a Fourier transform (FT) based procedure for large matrix diagonalization was also proposed for generation of anharmonic molecular spectra.²⁹ In this study, we prefer the Davidson approach because it provides exact eigenstates without the need to calibrate the FT convergence,²⁹ and allows us to include anharmonic (second-order) derivatives of the intensity tensors.

Diagonalization Algorithm. For LVCI, the large Hamiltonian diagonalization is of central importance for the spectra generation. We provide a brief description of the algorithm:

- (1) Select the HO states $\{\psi_n\}$ based on the restrictions above and calculate elements of the vibrational Hamiltonian H_{ij} . Save indices and values for the large elements only.
- (2) Load them in memory (e.g., in an array a , for each row i recorded in $a_{ms} \dots a_{ms+nj}$, keep a number of these elements n_j , starting index m_j , and the column index in an array j).
- (3) To solve the eigenvalue problem, $H \cdot c^\lambda = E_\lambda c^\lambda$, set $\lambda = 0$ and $M = M_{\max} = 10$. Set d to a unit vector and $E_d = 0$.
- (4) Increment λ by 1. For $\lambda > 1$, set $d = \sum_{j=1}^M w_j^2 X_j$ and $E_d = z_2$.
- (5) Set $c^\lambda = d$ and $E_\lambda = E_d$. Orthogonalize c^λ to vectors $\{c^\mu\}_{\mu=1, \dots, \lambda-1}$ and normalize so that $|c^\lambda| = 1$.
- (6) Construct "gradient vectors"⁴⁹ $\{x_j\}_{j=1, \dots, M}$ as $x_1 = c^\lambda$ or $x_j = H \cdot x_{j-1} - E_j x_{j-1}$ (for $J > 1$), orthonormalize each against the previous gradient vectors $\{x_k\}_{k=1, \dots, j-1}$ and eigenvectors $\{c^\mu\}_{\mu=1, \dots, \lambda-1}$. If $|x_j| < \text{tolerance}$, record E^λ and c^λ ; if also $E^\lambda < E_{\text{lim}}$ ($E_{\text{lim}} \sim 2400 \text{ cm}^{-1}$ for $E^1 \sim -800 \text{ cm}^{-1}$), go to 4; else, stop. Typically, tolerance ~ 1 .
- (7) Search for a new eigenvector λ as a combination of the gradient vectors, $c^\lambda = \sum_{j=1}^M w_j X_j$; Construct $A_{ij} = x_i \cdot H \cdot x_j$ and solve the reduced dimension ($M \times M$) eigenproblem $A \cdot w^L = z_L w^L$.

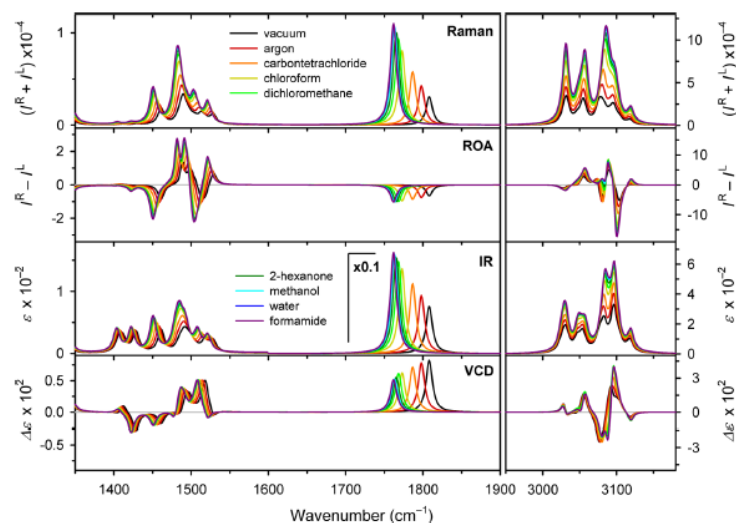


Figure 2. Solvent dependence of the calculated (B3LYP/6-311++G**/COSMO) (1R)-(+)-camphor Raman, ROA, IR, and VCD spectra.

- (8) Check if the subspace is not redundant: for $K = 4 \dots M$, if $|w^K| < 10^{-10}$ reduce M by 1 (if still larger than 3). But if $|w^K| > 10^{-10}$ and $M < M_{\max}$, increase M by 1.
- (9) Set $E_d = z_1$ (lowest eigenvalue) and $d = \sum_{j=1}^M w_j^2 x_j$. Go to 5.

The restriction to the large H_{ij} elements (steps 1 and 2) provided significant memory saving enabling real time computation without a data swapping on the disk. For the dimension of 1 086 008 used in the camphor computation, for example, from the total of 589 707 231 036 elements, 561 913 420 (~0.05%) were selected, requiring about 6.7 GB of memory only. The possibility to keep the Hamiltonian and eigenvectors in memory enables efficient parallelization of the code. As another enhancement, only large eigenvector elements ($|C_i^j| > 10^{-4}$) were kept in memory, which had a negligible effect on the precision but significantly reduced the computational time needed for the multiple vector orthonormalization procedures (steps 5 and 6).

RESULTS AND DISCUSSION

Experimental Spectra. The experimental spectra (Figure S1) of α -pinene, fenchone, and camphor are consistent with previous data.^{4,10,20,51–55} The VOA measurements in the high-frequency CH stretching region required special care to minimize artifacts. In particular, the measurement of ROA was difficult because of the low ROA/Raman circular intensity difference (ratio of ROA and Raman intensities, CID)³⁴ which is given by the relatively large Raman signal of the C–H stretching modes. An example of the artifact removal is shown for α -pinene in Figure S2. The problems of the artifacts in ROA measurement are discussed in detail in ref 56. Currently, both enantiomers have to be available for acquiring reliable ROA spectra in the CH stretching region, some of which could also be verified by comparison with previous measurements.^{51,56}

Solvent Dependence of Spectral Intensities. The dependence of the spectra on the solvent environment in the computations has often been neglected in the past, which can lead to very poor agreement to experiment. For example, only about 25% of average spectral VCD intensities could be reproduced by vacuum computation on terpenes.⁵³ It is generally

believed that the interaction of the aliphatic CH group with a solvent is limited; this is, however, not true in terms of the absolute spectral intensities. We choose camphor for the solvent testing as this molecule is normally in a solid state and it is usually dissolved for VOA measurement.

As can be seen in Figure 2, although stretching frequencies do not significantly change under solvent variations, the intensities vary for all the Raman, ROA, IR, and VCD spectral types in the CH region at least to the same extent as for other vibrations. Already the argon environment causes a notable (~10–20%) increase of the intensities. The increase approximately saturates for solvents more polar than 2-hexanone, where the calculated Raman/ROA and IR/VCD intensities are respectively about four and two times larger than in vacuum. Relative CID ratios for different vibrational bands are also varying with solvent polarity. On average, however, CID magnitudes remain rather constant throughout the entire spectral region. The fact that the magnitudes of the Raman and ROA spectra, for example, react to the environment in the same way thus contributed to previous successes of the vacuum-based VOA modeling.^{57,58}

The dependence of integral Raman and IR intensities on the solvent polarity plotted in Figure 3 (upper two panels) reveals that the CH stretching vibrations are significantly more influenced than the rest, except for the carbonyl stretching. In Figure 3 (bottom), we also compare the dependencies of the isotropic electric dipole polarizability (α), dipole moment, and the magnetic (G') and quadrupole (A) polarizabilities³⁴ on the polarization factor η . As expected, the dependencies are about linear. The G' tensor is the least and A is the most sensitive to the polarity. Therefore, the similar increase in magnitudes of the Raman (dependent on derivatives of α) and ROA (dependent on α , G' , and A derivatives) intensities with the polarity appears rather accidental, given by the balance of the G' and A contributions.

Similar intensity changes as for CH stretching occur in the lower-frequency region below 1900 cm^{-1} , where they are additionally accompanied by notable changes of vibrational frequencies (Figure 3; individual transition frequencies are

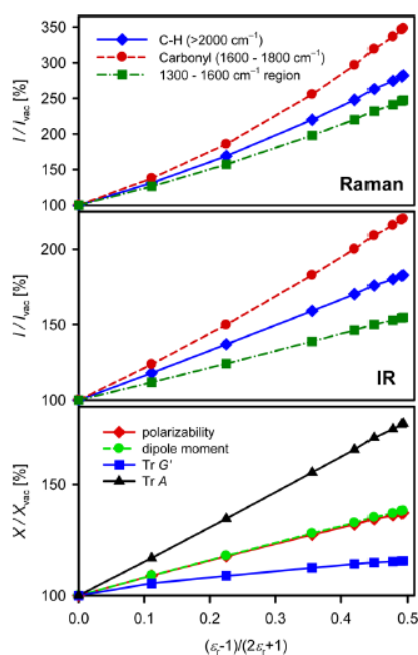


Figure 3. Dependence of calculated integral Raman and IR (IR)-(+)-camphor spectral intensities, dipole moment, and isotropic polarizabilities on the solvent polarization factor, relative to vacuum. For the A -tensor, we define $\text{Tr } A \equiv \sum_{\alpha=1,3} A_{\alpha\alpha\alpha}$

extracted in Supporting Information Figure S3). The C=O stretching band ($\sim 1770 \text{ cm}^{-1}$) exhibits the largest shifts, about 50 cm^{-1} for the entire range of solvents. As discussed before,^{59–62} even larger shifts can occur experimentally because of the inadequacy of the continuum models for the carbonyl group forming hydrogen bonds. Whereas the increasing solvent polarity causes mostly downshift of the lower-frequency modes, the CH band positions can change both up- and downward, occasionally changing their ordering.

The relative band intensities are rather conserved under the environment variation. For camphor the ROA CH stretching region spectra were the most sensitive to the solvent variation as the change in solvent polarity causes sign flip for a band around 3070 cm^{-1} . For VCD, the signs do not change, but band positions and relative intensities do.

Frequencies, Functionals, and Basis Sets. Comparison of the harmonic frequencies obtained with different methods provides indication of their computational reliability. The Raman and ROA fenchone spectra and the error of average harmonic CH stretching frequencies calculated at 12 approximation levels are summarized in Figure 4. Clearly all the electronic methods significantly overestimate the CH stretching frequencies if compared to experiment, HF being the extreme case with an error of 260 cm^{-1} . On the other hand, compared to mPW2PLYP³⁰ as the most advanced and accurate approach, all the DFT methods provide the harmonic frequencies too low, obviously still with a large deviation ($70\text{--}160 \text{ cm}^{-1}$) from experiment. This can only be improved by the PT2 and LVCI anharmonic corrections, included at the mPW2PLYP level, giving the average errors as 35 and 5 cm^{-1} , respectively.

Interestingly, the empirical dispersion correction,^{30,63} designed to treat longer-range dispersion interactions inadequately described by some older DFT approaches,⁶⁴ had an ambiguous effect on the spectra. In comparison with the uncorrected computations, it made slightly worse the lowest ($< \sim 1200 \text{ cm}^{-1}$) and improved the higher-frequency region. The influence of the dispersion in the CH region is rather negligible (Figure 4).

More importantly, the performance of the harmonic level is much better for spectral shapes than for frequencies. As apparent from Figure 4, various functionals give similar intensity profiles, including the vibrational optical activity. Principal spectral features can thus be approximately modeled within the harmonic approach also for the CH stretching. As discussed previously, this approach can be combined, for example, with empirical scaling of the frequencies.^{65,66}

The basis set convergence of the ROA and Raman spectra in the CH stretching and lower-frequency regions is analyzed in Figure 5. The normalized spectral overlap error comprises deviations of frequencies and intensities. Apparently, for the Raman and IR spectra, the convergence is reasonably smooth both for the CH and lower-frequency vibrations. The ROA and VCD spectra in the CH region (blue records in the panels) do not improve much with increasing basis set size before the 6-311++G** basis set is used. This indicates that the simulated VOA CH stretching spectra might be more sensitive not only to the proper inclusion of the solvent environment (see above), but also to the basis set. The split-valence triple- ζ 6-311++G** basis set brings an improvement mostly to the valence electrons determining vibrational frequencies; sole ROA intensities, for example, would be sufficiently described by the D95++** basis and similar sets including the diffuse functions.^{27,39,67}

From a practical point of view, usage of basis sets larger than 6-311++G** thus appears unnecessary, as this is associated with a sharp increase of computational time. From Figure 5, we also see that for approximate computations a proper choice of the basis set can lead to significant time savings, because smaller basis sets sometime provide better results than larger ones. For convenience, we list the computational times needed for ROA spectra computation with different basis sets in Supporting Information Table S3.

For the following anharmonic modeling, we use the mPW2PLYP/6-311++G**/COSMO method for force field, which allows for both the harmonic and anharmonic force field term calculations in a reasonable time in a consistent way. Note that the B3LYP/6-311++G**/COSMO level is used for the intensities.

Comparison of the Anharmonic Approaches for α -Pinene. α -Pinene is the smallest of the three models and permissible for extended vibrational tests. The behavior of the harmonic, PT2, and LVCI computational method used for the spectral simulations is documented in Figure 6. All the Raman, ROA, IR, and VCD spectra are shown within $1350\text{--}1770$ and $2700\text{--}3200 \text{ cm}^{-1}$, to capture the differences between the low-frequency and CH stretching regions. The indicated normal mode numbers correspond to Table 1. For LVCI, the normal mode number was assigned according to the dominant expansion coefficients.

The harmonic computation provides the CH stretching frequencies too high. Although the simulated harmonic spectral profiles are close to experiment, a band-to-band comparison at this level can be done only in the lower-frequency region. The PT2 computation corrects most of the frequency error.

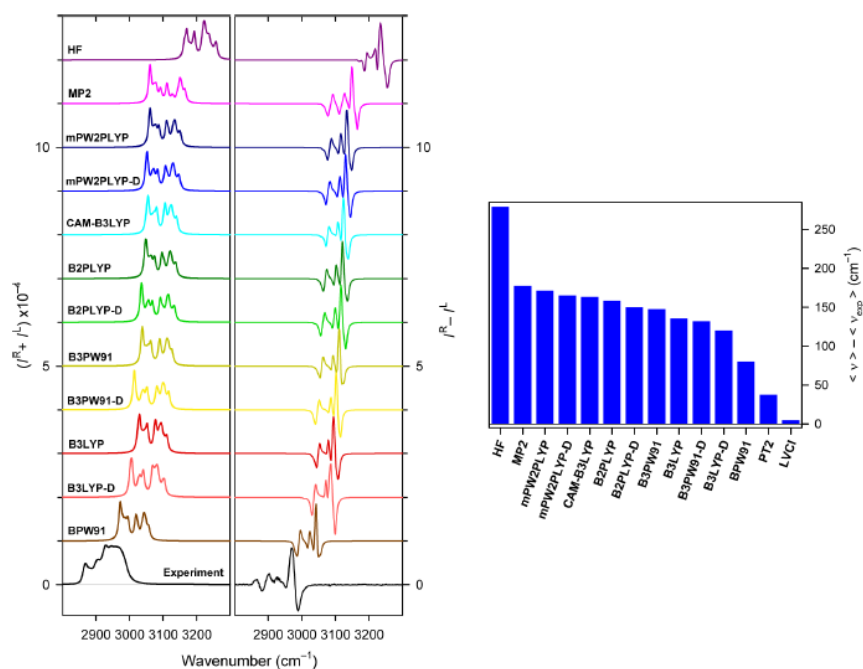


Figure 4. (left) Raman and ROA (IR)-(-)-fenchone spectra calculated by various harmonic methods, with the 6-311+G** basis set. (right) Average harmonic (HF...BPW91) and anharmonic (PT2 and LVCI, for the mPW2PLYP force field) frequency errors.

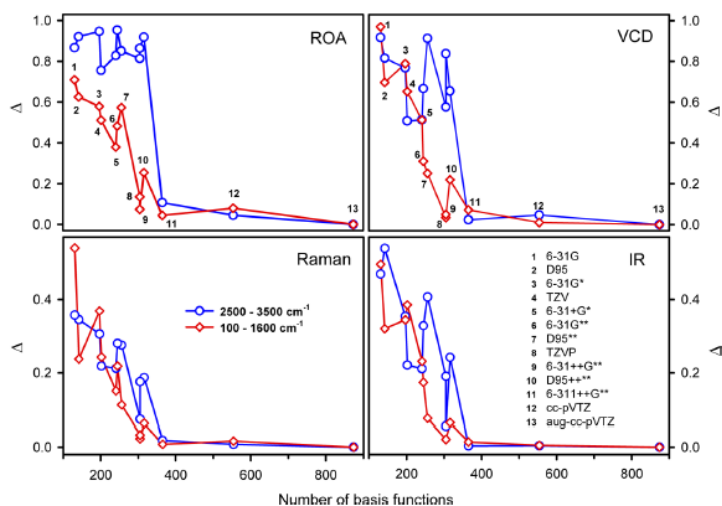


Figure 5. Basis set convergence of spectral errors, calculated for the four (IR)-(-)-fenchone spectral types using the B3LYP functional and aug-cc-pVTZ reference ($\Delta = 1 - |fS_{ref} dv| / [(fS_{ref}^2 dv)^{1/2} (fS^2 dv)^{1/2}]$).

To our surprise, the 1350–1770 cm⁻¹ region also significantly benefited from the anharmonic computations. This wavenumber range comprises mostly the C–H bending modes, and is traditionally considered as harmonic. For example, mode number 24, shifted from the harmonic position at 1492 to 1418 cm⁻¹, is then only somewhat lower than experiment (1434

cm⁻¹). The C=C stretching band (mode number 17) is rather indifferent to anharmonicity corrections. Its position calculated too high if compared to experiment can be attributed most probably to an error of the mPW2PLYP/6-311++G**/COSMO force field. Possibly, also higher-order terms, not included in the potential (1) may play a role. Additionally, the LVCI

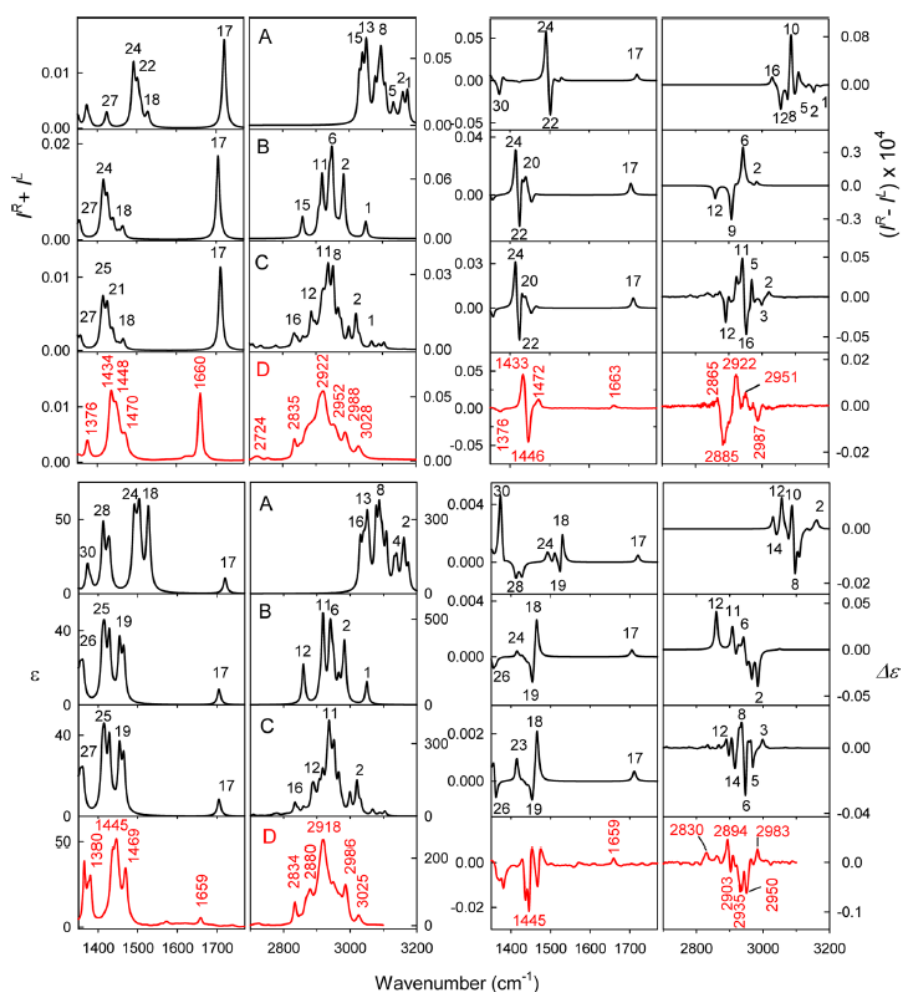


Figure 6. Raman, ROA, IR, and VCD spectra of (1R)-(+)- α -pinene calculated at the (A) harmonic, (B) PT2, and (C) LVCI (36 modes fixed, $c_1 = 0.002$, $c_2 = 0.1$, 749398 HO states) approximation levels and (D) experiment, in low (1350–1770 cm^{-1}) and CH (2700–3200 cm^{-1}) frequency regions. The indicated mode numbers correspond to Table 1.

computational method has been primarily optimized for the CH stretching region. In particular, the HO states potentially important for the C=C vibration could not be included in the Hamiltonian because of the size limits.

In the C–H stretching region the PT2 computation is still inadequate to reproduce the observed spectral shapes, although it improves the harmonic Raman and IR spectral shapes. The mode ordering is mostly conserved within PT2.

The LVCI computation is the most consistent with experiment, providing both reasonable frequencies and intensity profiles. This is visible namely for the Raman and IR spectra, where most simulated and experimental bands can be assigned also in the CH stretching region. In comparison with the harmonic profiles, the LVCI spectra become narrower and dominated by the central signal (vibration number 11, $\sim 2922 \text{ cm}^{-1}$ for Raman). For ROA and VCD the intensity errors are more apparent than for IR and Raman scattering. This is given in

general by the higher sensitivity of the polarized spectroscopies to molecular vibrations, i.e. to the eigenvectors of the LVCI Hamiltonian. Nevertheless, the simulation allows one to understand the underlying vibrational patterns. For ROA, for example (see also Figure 7, top, for detailed overlap of the simulation and experiment), the relatively strong negative signal observed at 2885 cm^{-1} is readily reproduced by LVCI at approximately the same position (with a strong participation of the fundamental mode number 12; note, however, that beyond the harmonic approximation the concept of vibrational normal modes becomes irrelevant). Similarly, the positive experimental band at 2922 cm^{-1} is reproduced by LVCI, with a participation of the normal mode 11. Around 2951 cm^{-1} , however, the negative LVCI ROA signal associated with the mode number 16 is overestimated by the computation.

For VCD, the behavior of the LVCI simulation is similar as for ROA, with the largest discrepancy around 2935 cm^{-1} , where a

Table 1. Calculated (mPW2PLYP/6-311++G***/COSMO) CH Stretching Normal Modes^a

mode	α -pinene	fenchone	camphor
1	3175 1*	3150 3 ip 2 ip 3 ip 2	3158 3
2	3162 3 ip 2	3148 3 ip 2 op 3 ip 2	3141 3 ip 2
3	3156 3	3140 2 ip 2 ip 2 op 3 ip 3	3136 2 ip 2 ip 2
4	3140 3 op 2	3135 2 op 2 ip 2 op 3 ip 3	3135 3
5	3132 3	3132 3 op 3 op 2	3133 3
6	3109 3 ip 3	3131 3, 3 op 3	3130 2 op 2 ip 2
7	3102 3 op 3	3130 3, 3 op 3 op 2	3123 3 ip 3
8	3096 1 ip 1 ip 2	3130 3 op 2	3118 1, 2 op 2
9	3090 3	3118 1 ip 2, 2	3116 3 op 3
10	3087 1 op 1 ip 2	3115 1, 2 op 2	3113 1, 2 op 2
11	3078 1 op 2	3090 2 ip 2 ip 2 op 1	3090 1 op 2 ip 2 ip 2
12	3056 2*	3082 2 op 2 ip 2	3088 2 ip 2 op 2
13	3051 3 ip 3	3073 2 op 2	3080 2 op 2
14	3045 3 op 3	3062 ip 3	3063 ip 3 ip 3
15	3040 2* ip 1	3059 op 3	3060 ip 3 ip 3
16	3030	3058	3056 3 op 3

- ^a
- 1 - CH stretching
 - 2 - asymmetric CH₂ stretching
 - 2 - symmetric CH₂ stretching
 - 3 - asymmetric CH₃ stretching
 - 3 - symmetric CH₃ stretching
 - ip in phase
 - op out of phase
 - * proximate to double bond

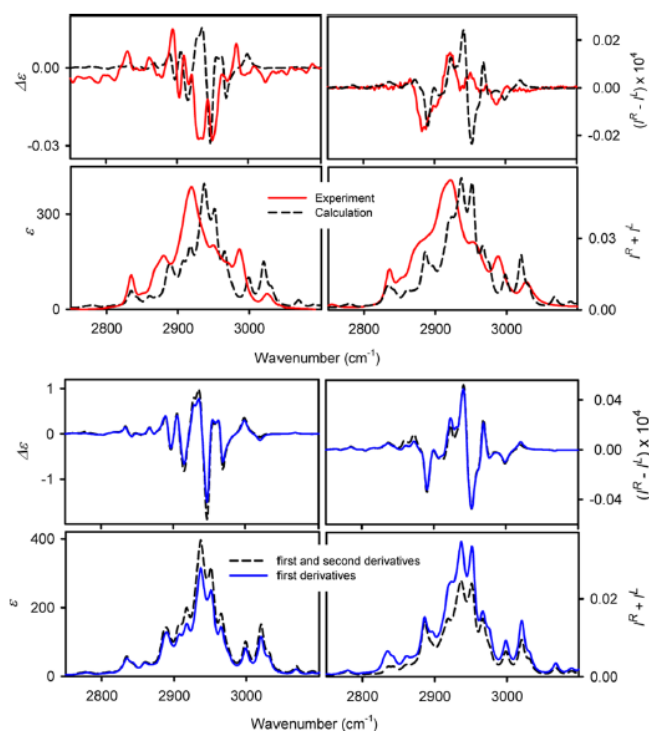


Figure 7. (top) Calculated (LVCI) and experimental VCD, IR, Raman, and ROA (1R)-(+)- α -pinene spectra in the CH stretching region. (bottom) Calculated spectra with and without contribution of the second intensity tensor derivatives.

negative signal is measured, but a positive one (mode number 8) is simulated. Overall, however, the convergence of the LVCI method to the experiment is quite apparent for all the spectral types. The simulation also justifies the above comparison of the harmonic ROA and VCD patterns to experiments, as even under

LVCI some principal intensity profiles are conserved if compared to the harmonic limit. This suggests that the anharmonic interactions/potential shape only rarely causes changes in the mode ordering (e.g., via Fermi resonances). Instead, the CH stretching vibrations, for example, interact with a pool of other

molecular vibrations, which causes an approximately uniform shift of the frequencies. There is a remaining frequency error of about $5\text{--}10\text{ cm}^{-1}$ of the LVCI computation, most probably given by the limited Taylor expansion of the potential, error of the electronic quantum-chemical approach, and approximation in the vibrational LVCI approach.

For IR and VCD the magnitude of the measured and computed intensities is directly comparable. For the absorption (Figure 6, left, bottom) all the computational models provide peak heights (for the bandwidth of 10 cm^{-1}) comparable with the experiment; the accuracy seems worse for the CH stretching region (where the calculated intensities are by about 30% overestimated) than below 1800 cm^{-1} . The anharmonic PT2 and LVCI anharmonic corrections do not seem to significantly change the harmonic integral IR intensities. The VCD intensities obtained with different models (Figure 6, right, bottom) vary more and a detailed qualitative comparison is problematic. On average, the harmonic VCD intensities appear underestimated (by $\sim 50\%$) if compared to experiment, which is significantly repaired by the anharmonic corrections.

The spectra simulated with and without the second derivatives of the intensity tensors (transitional electric and magnetic dipole moment, and the α , G' , and A polarizabilities,⁵⁴ Figure 7, bottom) are very similar. Rather surprisingly, for the VOA intensities (VCD, ROA) generally considered very sensitive to computational parameters the contribution of the second derivatives is relatively smaller than for the IR and Raman spectra. Finally, we see that the second derivative contributions can both increase (IR) and decrease (Raman) the integral intensities. They mostly improve the agreement of the simulations with the experiment, and their computation requires relatively small computational effort in comparison with the energy derivatives.

Anharmonic Coupling Between Normal Modes and Convergence of the LVCI Results. The freezing of the lower-frequency vibrations is necessary to reduce the number of the HO states. Similar mode separation appeared useful, for example, in the modeling of the tryptophan chromophore.⁶⁸ It is based on the assumption of a limited coupling between the higher- and lower-frequency modes. At least partially, it can be justified on the basis of the anharmonic coupling defined as an average of the dimensionless cubic and quartic constants containing two modes i and j ($|c_{iii}| + |c_{jjj}| + |c_{ijj}| + |d_{iii}| + \dots$). Indeed (Supporting Information Figure S4), the CH stretching modes (last 16 modes in the graphs) exhibit exceptionally large diagonal and off-diagonal anharmonic constants and are thus relatively isolated from other vibrations. The coupling of the CH stretching to the lower-frequency modes is significantly smaller, and even smaller is the diagonal and off-diagonal coupling within the modes with frequency below 2000 cm^{-1} . The coupling increases again for the very-low energy ($<300\text{ cm}^{-1}$, not shown) modes, such as the methyl torsions, where, however, the limited Taylor expansion of the potential (eq 1) is not applicable.

LVCI computations with a variable number of the HO states (with various coupling parameters c_1 and c_2 and number of blocked vibrations, e.g. Supporting Information Figure S5 with the Raman and ROA spectra of (1R)-(+)- α -pinene) indicate a good stability and convergence of the transition vibrational frequencies; however, the intensities are very sensitive and require a relatively large number of states to be included, especially for the one-step selection with $c_2 = 0$. This makes the computations extremely computer memory and time demanding.

On the other hand, the two-step HO basis set selection appears as a more reliable and accurate method. The role of the second parameter for the simulated Raman spectra of α -pinene is documented in Figure 8. If just states interacting with the CH

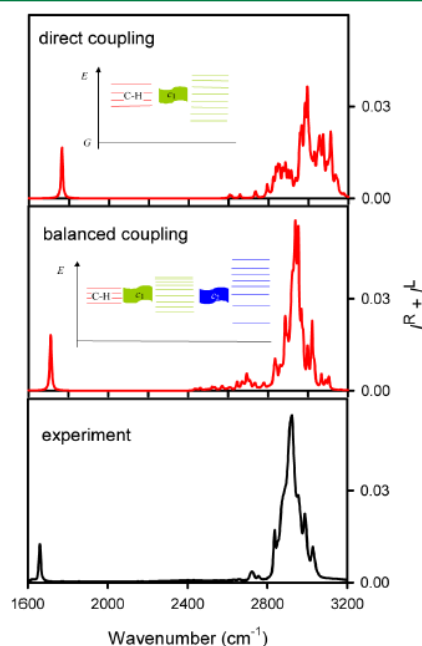


Figure 8. Raman spectra of α -pinene calculated by the LVCI method with one ($c_1 = 0.002$, $c_2 = \infty$) and two ($c_1 = 0.002$, $c_2 = 0.1$) step selection of the HO basis states and the experiment. The first method causes an unrealistic spread of state energies, whereas the second one provides more balanced coupling and spectra of the states of interest (CH stretching).

fundamental vibrations are selected, even for a relatively weak coupling ($c_1 = 0.002$), the resultant spectral shape is not very realistic, with a large dispersion of the CH stretching frequencies. The frequencies are also too high. This can be prevented by including the second set of states interacting with the first one, for $c_2 = 0.1$. Then the simulated frequencies and spectral shapes are significantly more realistic, albeit at the expense of the computer resources required (14 986 vs 749 398 states included). This approach leads to a more reliable convergence, where spectral intensities are less sensitive to the number of states included (see also Supporting Information Figures S5 and S6) than in the one step LVCI state selection.

On the basis of the perturbation formalism,⁶⁹ one may expect that adding a third set of states interacting with the two would further improve the data. This is not possible to explore for our systems (the total number of the states would be enormous) and implementation limited to 5-times excited states. On the other hand, from the large value of c_2 (0.1) we see that a significant improvement was already achieved by including the largest interactions, suggesting that further changes would bring minor effects only, with respect to all sources of errors. The possibility to vary the c_1 and c_2 coefficients arbitrarily makes the three-stage state selection obsolete as well.

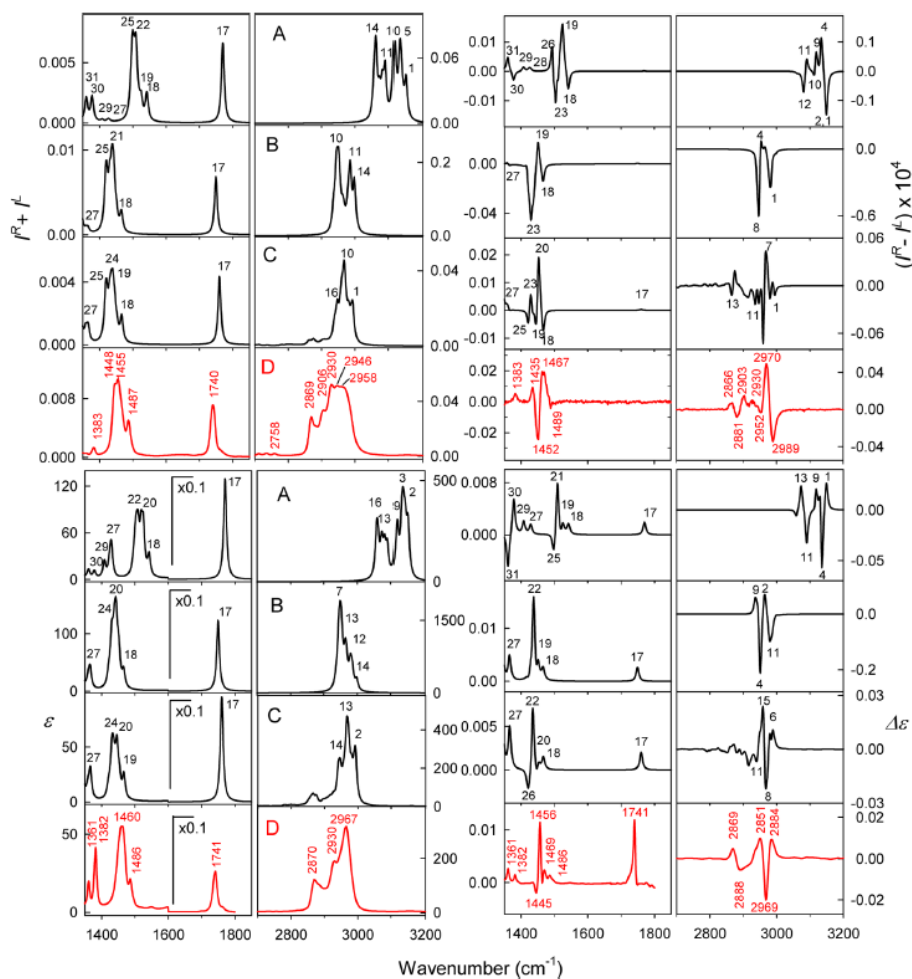


Figure 9. (IR)-(-)-Fenchone Raman, ROA, IR, and VCD spectra calculated at the (A) harmonic, (B) PT2, and (C) LVCI approximations (36 modes fixed, $c_1 = 0.002$, $c_2 = 0.1$, 1 086 008 HO states) and (D) experiment in low (1350–1850 cm^{-1}) and CH (2700–3200 cm^{-1}) frequency regions. The indicated mode numbers correspond to Table 1.

Fenchone and Camphor Spectra. The behavior of the other two molecules with respect to the spectral modeling of the CH stretching vibrations is similar to α -pinene (Figures 9 and 10, detailed overlaps between the calculation and experiment are plotted in Supporting Information Figure S7). The computations were slightly more demanding than for α -pinene because of the presence of the carbonyl group. For fenchone (Figure 9), the most visible discrepancies between the LVCI simulation and experiment are the shape of the Raman CH stretching signal, predicted to be sharper than observed, and the ROA band around 2989 cm^{-1} , the experimental negative sign of which is reproduced as a weak split signal only. At the level of visual comparison, a better agreement between the simulation and experiment is apparent for the IR and VCD spectra that for Raman/ROA.

For camphor (Figure 10), the intensity of the highest-frequency negative ROA signal at 2974 cm^{-1} is underestimated

as well. In spite of structural similarity of camphor and fenchone, their spectra, in particular VCD and ROA, are rather different. For example, camphor ROA is much simpler than for fenchone, which is well reproduced by the LVCI computation, but not by the lower-level harmonic and PT2 approaches. For fenchone, the relative Raman and IR intensities of the C=O stretching band are smaller than for camphor, which is reproduced by all the computations.

The computational times can well be estimated for the electronic problem, where the harmonic force field is the most demanding part (for example, 188 h for camphor and the mPW2PLYP/6-311++G**/COSMO computation if recalculated to one E7330 2.40 GHz processor). Both the PT2 and LVCI methods need the same anharmonic force constants present in eq 1, which requires the time for the harmonic force field to be multiplied twice by the number of modes (resulting to the total of about 1175 CPU days in this case). Computational

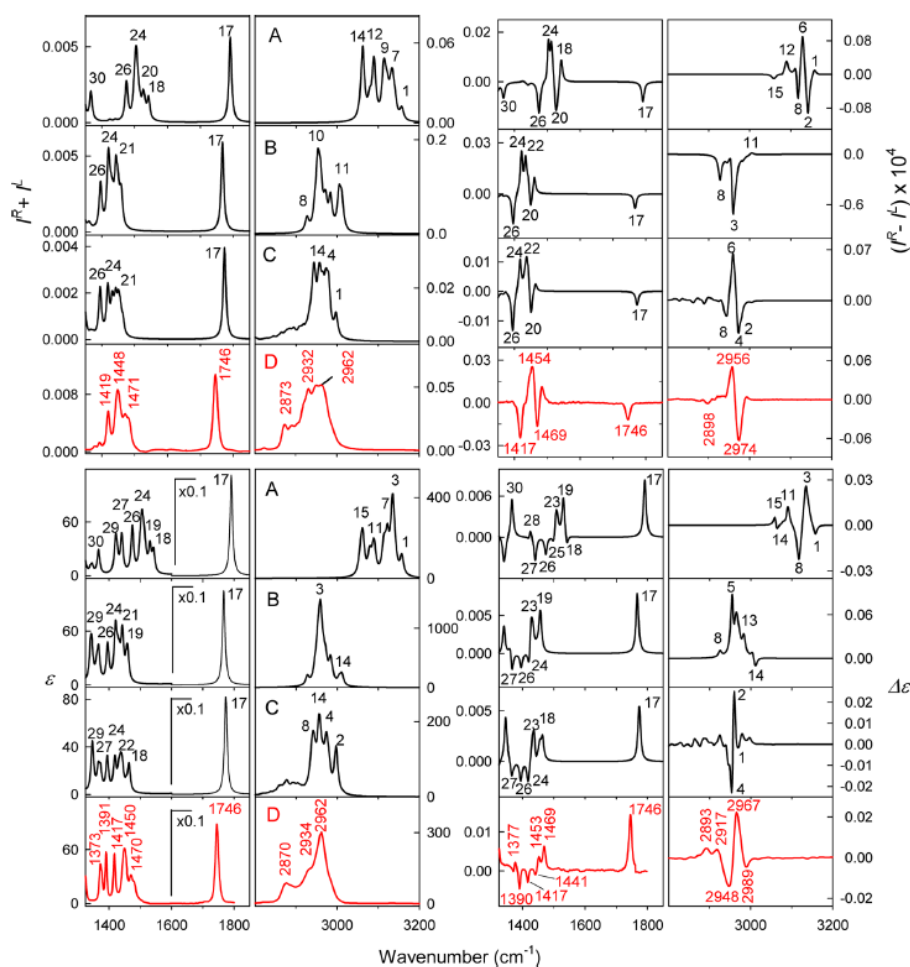


Figure 10. (IR)-(+)-Camphor Raman, ROA, IR, and VCD spectra calculated at the (A) harmonic, (B) PT2, and (C) LVCI approximations (31 modes fixed, $\epsilon_1 = 0.002$, $\epsilon_2 = 0.1$, 1 906 884 HO states) and (D) experiment in low (1350–1850 cm^{-1}) and CH (2800–3200 cm^{-1}) frequency regions. The indicated mode numbers correspond to Table 1.

times needed for the PT2 and LVCI vibrational procedures vary significantly. In our implementation, the PT2 correction took about 1 min and the LVCI camphor computation (Figure 10) took about 6 days.

In the spirit of the previous study of Cappelli et al. focused on the PT2 method,²⁶ we consider the possibility of reliable LVCI computations as a next step in reproduction of the CH stretching signal in organic molecules. This is clearly desirable as the harmonic approaches do not capture important spectral features and the link between the spectral shapes and structures. Apart of the dimensionality of the problem, many obstacles remain to be solved in the future, such as the role of the lowest-energy vibrations (e.g., methyl torsions), potentially requiring an explicit quantum state temperature averaging and extension of the limited Taylor expansion-based anharmonic approach.

CONCLUSIONS

We acquired high-quality ROA spectra of three terpene molecules, and by comparing the four spectral types with computations, we could assess performance of the computational approaches for detailed CH stretching modeling. Contrary to general belief, we found that the CH stretching spectral intensities are very dependent on the solvent environment and are also slightly more sensitive to the basis set choice than the lower-frequency vibrations.

For the simulation beyond the harmonic limit, a limited interaction between the CH stretching and lower-frequency modes was assumed. This could be partially justified by analysis of the anharmonic intermode coupling. Owing to an efficient implementation of the diagonalization procedure, the limited vibrational configuration interaction provided converged spectral patterns very well reproducing the experimental frequencies and intensities. In spite of occasional problems namely for the

vibrational optical activity spectral features, the LVCI scheme appears as the best simulation method so far, over performing the harmonic and second-order perturbational approaches. The computations in part justify previous modeling efforts based on the harmonic limit, as the most distinct spectral features survive also beyond the harmonic approximation. A future accuracy improvement is desirable; nevertheless the results clearly indicate that the LVCI simulation of the vibrational optical activity beyond the harmonic limit are possible and bring precious information about molecular structure and the spectroscopic response.

■ ASSOCIATED CONTENT

Supporting Information

Experimental and computational details including all experimental spectra and solvent dependence of the calculated results. This material is available free of charge via the Internet at <http://pubs.acs.org>.

■ AUTHOR INFORMATION

Corresponding Author

*E-mail: bour@uochb.cas.cz.

Notes

The authors declare no competing financial interest.

■ ACKNOWLEDGMENTS

This study was performed with the support from the Academy of Sciences (M200550902), Grant Agency of the Czech Republic (P208/11/0105), Grant Agency of Charles University (126310), and the Ministry of Education (LH11033).

■ REFERENCES

- Hug, W.; Haesler, J. *Int. J. Quantum Chem.* **2005**, *104*, 695–715.
- Zuk, W. M.; Freedman, T. B.; Nafie, L. A. *Biopolymers* **1989**, *28*, 2025–2044.
- Juřinec, O.; Lindner, W.; Urbanová, M. *Chirality* **2011**, *23*, 354–360.
- Debie, E.; Jaspers, L.; Bultinck, P.; Herrebout, W.; Veken, B. V. D. *Chem. Phys. Lett.* **2008**, *450*, 426–430.
- Guo, C.; Shah, R. D.; Mills, J.; Dukor, R. K.; Cao, X.; Freedman, T. B.; Nafie, L. *Chirality* **2006**, *18*, 775–782.
- Keiderling, T. A.; Kubelka, J.; Hilario, J., Vibrational circular dichroism of biopolymers. Summary of methods and applications. In *Vibrational spectroscopy of polymers and biological systems*; Braiman, M., Gregoriou, V., Eds.; CRC Press: Boca Raton, 2006; pp 253–324.
- Nafie, L. *Vibrational optical activity: Principles and applications*; Wiley: Chichester, 2011.
- Benda, L.; Štěpánek, J.; Kaminský, J.; Bouř, P. Spectroscopic Analysis: Ab initio Calculation of Chiroptical Spectra. In *Comprehensive Chirality*; Carreira, E. M., Yamamoto, H., Eds.; Elsevier: Amsterdam, 2012; Vol. 8, pp 520–544.
- Polavarapu, P. L.; Nafie, L. *J. Chem. Phys.* **1980**, *73*, 1567–1575.
- Longhi, G.; Abbate, S.; Gangemi, R.; Giorgio, E.; Rosini, C. *J. Phys. Chem. A* **2006**, *110*, 4958–4968.
- Guo, C.; Shah, R. D.; Dukor, R. K.; Freedman, T. B.; Cao, X.; Nafie, L. *A. Vib. Spectrosc.* **2006**, *42*, 254–272.
- Bounouar, M.; Scheurer, C. *Chem. Phys.* **2006**, *323*, 87–101.
- Parčhaňský, V.; Bouř, P. *J. Chem. Phys.* **2010**, *133*, 044117.
- Daněček, P.; Kapitán, J.; Baumruk, V.; Bednářová, L.; Kopecký, V., Jr.; Bouř, P. *J. Chem. Phys.* **2007**, *126*, 224513.
- Daněček, P.; Bouř, P. *J. Comput. Chem.* **2007**, *28*, 1617–1624.
- Bouř, P. *J. Phys. Chem.* **1994**, *98*, 8862–8865.
- Kaledin, A. L.; Bowman, J. M. *J. Phys. Chem. A* **2007**, *111*, 5593–5598.
- Romanowski, H.; Bowman, J. M.; Harding, L. B. *J. Chem. Phys.* **1985**, *82*, 4155–4165.
- Laux, L.; Pultz, V.; Abbate, S.; Havel, H. A.; Overend, J.; Moscovitz, A. *J. Am. Chem. Soc.* **1982**, *104*, 4276–4278.
- Devlin, F. J.; Stephens, P. J.; Cheeseman, J. R.; Frisch, M. J. *J. Phys. Chem.* **1997**, *101*, 9912–9924.
- Samsonyuk, A.; Scheurer, C. *J. Comput. Chem.* **2013**, *34*, 27–37.
- Choi, J. H.; Cho, M. *J. Chem. Theory Comput.* **2011**, *7*, 4097–4103.
- Hanson-Heine, M. W. D.; George, M. W.; Besley, N. A. *J. Chem. Phys.* **2012**, *136*, 224102.
- Carbonniere, P.; Lucca, T.; Pouchan, C.; Rega, N.; Barone, V. *J. Comput. Chem.* **2005**, *26*, 384–388.
- Polyanichko, A. M.; Andrushchenko, V.; Bouř, P.; Wieser, H., Vibrational Circular Dichroism Studies of Biological Macromolecules and their Complexes. In *Circular Dichroism: Theory and Spectroscopy*; Rodgers, D. S., Ed.; Nova: Hauppauge, NY, 2011.
- Cappelli, C.; Bloino, J.; Lippardini, F.; Barone, V. *J. Phys. Chem. Lett.* **2012**, *3*, 1766–1773.
- Cheeseman, J. R.; Frisch, M. J. *J. Chem. Theory Comput.* **2011**, *7*, 3323–3334.
- Barone, V. *J. Chem. Phys.* **2005**, *122*, 014108.
- Ivani, L.; Bouř, P. *J. Chem. Theory Comput.* **2010**, *6*, 2095–2102.
- Schwabe, T.; Grimme, S. *Phys. Chem. Chem. Phys.* **2007**, *9*, 3397–3406.
- Møller, C.; Plesset, M. S. *Phys. Rev.* **1934**, *46*, 618–622.
- Parr, R. G.; Yang, W. *Density-functional theory of atoms and molecules*; Oxford University Press: New York, 1994.
- Hanzlíková, J.; Praus, P.; Baumruk, V. *J. Mol. Struct.* **1999**, *480–481*, 431–435.
- Barron, L. D. *Molecular Light Scattering and Optical Activity*; Cambridge University Press: Cambridge, 2004.
- Frisch, M. J.; Trucks, G. W.; Schlegel, H. B.; Scuseria, G. E.; Robb, M. A.; Cheeseman, J. R.; Scalmani, G.; Barone, V.; Mennucci, B.; Petersson, G. A.; Nakatsuji, H.; Caricato, M.; Li, X.; Hratchian, H. P.; Izmaylov, A. F.; Bloino, J.; Zheng, G.; Sonnenberg, J. L.; Hada, M.; Ehara, M.; Toyota, K.; Fukuda, R.; Hasegawa, J.; Ishida, M.; Nakajima, T.; Honda, Y.; Kitao, O.; Nakai, H.; Vreven, T.; Montgomery, J. J. A.; Peralta, J. E.; Ogliaro, F.; Bearpark, M.; Heyd, J. J.; Brothers, E.; Kudin, K. N.; Staroverov, V. N.; Kobayashi, R.; Normand, J.; Raghavachari, K.; Rendell, A.; Burant, J. C.; Iyengar, S. S.; Tomasi, J.; Cossi, M.; Rega, N.; Millam, J. M.; Klene, M.; Knox, J. E.; Cross, J. B.; Bakken, V.; Adamo, C.; Jaramillo, J.; Gomperts, R.; Stratmann, R. E.; Yazyev, O.; Austin, A. J.; Cammi, R.; Pomelli, C.; Ochterski, J. W.; Martin, R. L.; Morokuma, K.; Zakrzewski, V. G.; Voth, G. A.; Salvador, P.; Dannenberg, J. J.; Dapprich, S.; Daniels, A. D.; Farkas, O.; Foresman, J. B.; Ortiz, J. V.; Cioslowski, J.; Fox, D. J. *Gaussian 09*, Revision B01, Gaussian, Inc.: Wallingford CT, 2009.
- Perdew, J. P.; Burke, K.; Wang, Y. *Phys. Rev. B* **1996**, *54*, 16533–16539.
- Yanai, T.; Tew, D.; Handy, N. C. *Chem. Phys. Lett.* **2004**, *393*, 51–57.
- Grimme, S. *J. Comput. Chem.* **2006**, *27*, 1787–1799.
- Zuber, G.; Hug, W. *J. Phys. Chem. A* **2004**, *108*, 2108–2118.
- Ruud, K.; Helgaker, T.; Bouř, P. *J. Phys. Chem. A* **2002**, *106*, 7448–7455.
- Ruud, K.; Thorvaldsen, J. *Chirality* **2009**, *21*, E54–E67.
- Klamt, A. COSMO and COSMO-RS. In *The Encyclopedia of Computational Chemistry*; Schleyer, P. R., Allinger, N. L., Clark, T., Gasteiger, J., Kollman, P. A., Schaefer, H. F., III, Schreiner, P. R., Eds.; John Wiley & Sons: Chichester, 1998; Vol. 1, pp 604–615.
- Buckingham, A. D. *Proc. R. Soc. (London) A* **1956**, *238*, 235–244.
- Polavarapu, P. L. *Vibrational spectra: principles and applications with emphasis on optical activity*; Elsevier: Amsterdam, 1998; Vol. 85.
- Papoušek, D.; Aliev, M. R. *Molecular Vibrational/Rotational Spectra*; Academia: Prague, 1982.
- Dračínský, M.; Bouř, P. *J. Comput. Chem.* **2012**, *33*, 1080–1089.
- Stephens, P. J. *J. Phys. Chem.* **1985**, *89*, 748–752.
- Polavarapu, P. L. *Vibr. Spectra Struct.* **1984**, *13*, 103–160.

- (49) Mitin, A. V. *J. Comput. Chem.* **1994**, *15*, 747–751.
- (50) Davidson, E. R. *J. Comput. Phys.* **1975**, *17*, 87–94.
- (51) Hug, W.; Kint, S.; Bailey, G. F.; Schere, J. R. *J. Am. Chem. Soc.* **1975**, *97*.
- (52) Hecht, L.; Che, D.; Nafie, L. A. *J. Phys. Chem.* **1992**, *96*, 4266–4270.
- (53) Bouř, P.; McCann, J.; Wieser, H. *J. Phys. Chem. A* **1998**, *102*, 102–110.
- (54) Bouř, P.; Baumruk, V.; Hanzlíková, J. *Collect. Czech. Chem. Commun.* **1997**, *62*, 1384–1395.
- (55) Devlin, F. J.; Stephens, P. J.; Cheeseman, J. R.; Frisch, M. R. *J. Am. Chem. Soc.* **1996**, *118*, 6327–6328.
- (56) Hug, W. *Appl. Spectrosc.* **1981**, *35*, 115–124.
- (57) Haesler, J.; Schindelholz, I.; Riguet, E.; Bochet, C. G.; Hug, W. *Nature* **2007**, *446*, 526–529.
- (58) Luber, S.; Reiher, M. *J. Phys. Chem. B* **2010**, *114*, 1057–1063.
- (59) Kubelka, J.; Keiderling, T. A. *J. Phys. Chem. A* **2001**, *105*, 10922–10928.
- (60) Bouř, P.; Keiderling, T. A. *J. Phys. Chem. B* **2005**, *109*, 23687–23697.
- (61) Kubelka, J.; Huang, R.; Keiderling, T. A. *J. Phys. Chem. B* **2005**, *109*, 8231–8243.
- (62) Ganim, Z.; Chung, H. S.; Smith, A. W.; Deflores, L. P.; Jones, K. C.; Tokmakoff, A. *Acc. Chem. Res.* **2008**, *41*, 432–441.
- (63) Grimme, S.; Antony, J.; Ehrlich, S.; Krieg, H. *J. Chem. Phys.* **2010**, *132*, 154104.
- (64) Šponer, J.; Hobza, P. *Collect. Czech. Chem. Commun.* **2003**, *68*, 2231–2282.
- (65) Scott, A. P.; Radom, L. *J. Phys. Chem.* **1996**, *100*, 16502–16513.
- (66) Merrick, J. P.; Moran, D.; Radom, L. *J. Phys. Chem. A* **2007**, *111*, 11683–11700.
- (67) Reiher, M.; Liegeois, V.; Ruud, K. *J. Phys. Chem. A* **2005**, *109*, 7567–7574.
- (68) Kabeláč, M.; Hobza, P.; Špirko, V. *Phys. Chem. Chem. Phys.* **2009**, *11*, 3921–3926.
- (69) Szabo, A.; Ostlund, N. S. *Modern quantum chemistry. Introduction to advanced electronic structure theory*; Dover: New York, 1989.

The CH Stretching Region: Computational Modeling of Vibrational Optical Activity

**Jana Hudecová, Václav Profant, Pavlína Novotná, Vladimír Baumruk,
Marie Urbanová, and Petr Bouř**

Table S1. Experimental conditions used for the IR and VCD measurement

Table S2. Relative permittivity and polarization factor of the solvents used in calculations.

Table S3. Computational times for different basis sets.

Figure S1. The experimental spectra.

Figure S2. ROA artifact removal.

Figure S3. Calculated frequency shifts as dependent on the polarization factor.

Figure S4. Anharmonic coupling between harmonic vibrational modes.

Figure S5. LVCI dependence on the number of HO states, α -pinene.

Figure S6. LVCI dependence on the number of HO states, camphor.

Figure S7. Overlaps between experiment and computation, fenchone and camphor.

Table S1. Experimental conditions used for the IR and VCD measurement^a

	region (cm ⁻¹)	solvent	cell	resolution (cm ⁻¹)	c (M)	l (μm)
fenchone	2000 - 3800	neat	CaF ₂	8	6.24	6
	1600 - 1800	neat	KBr	4	6.24	6
	850 - 1600	neat	KBr	4	6.24	50
camphor	2000 - 3800	CCl ₄	CaF ₂	8	0.6	50
	1600 - 1800	CCl ₄	KBr	4	0.13	50
	825 - 1600	CCl ₄	KBr	4	0.6	100
α-pinene	2700 - 3100	CH ₂ Cl ₂	CaF ₂	4	1.45	6
	800 - 1800	neat	KBr	4	6.30	50

^a concentration (*c*), spacer width (*l*).

2

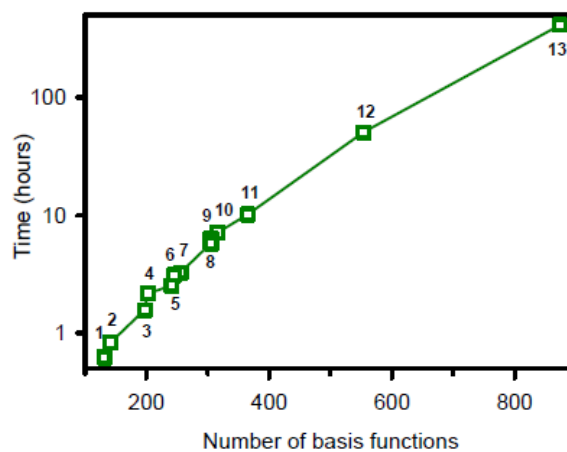
Table S2. Relative permittivity and the polarization factor of the solvents used in calculations.

Solvent	ϵ_r	$(\epsilon_r - 1)/(2\epsilon_r + 1)$
vacuum	1.00	0.000
argon	1.43	0.111
carbon tetrachloride	2.23	0.225
chloroform	4.71	0.356
dichloromethane	8.93	0.420
2-hexanone	14.14	0.449
methanol	32.61	0.477
water	78.36	0.490
formamide	108.94	0.493

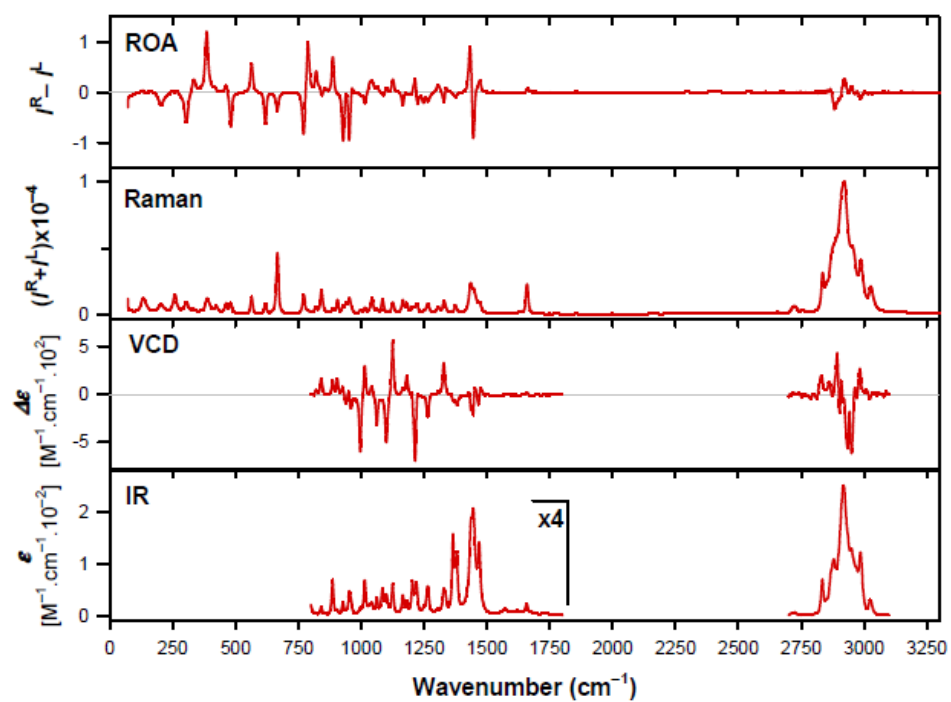
3

Table S3. Approximate computational times for different basis sets, fenchone B3LYP ROA (frequencies and tensors) Gaussian 09 computation, ~ 3GHz cpu.

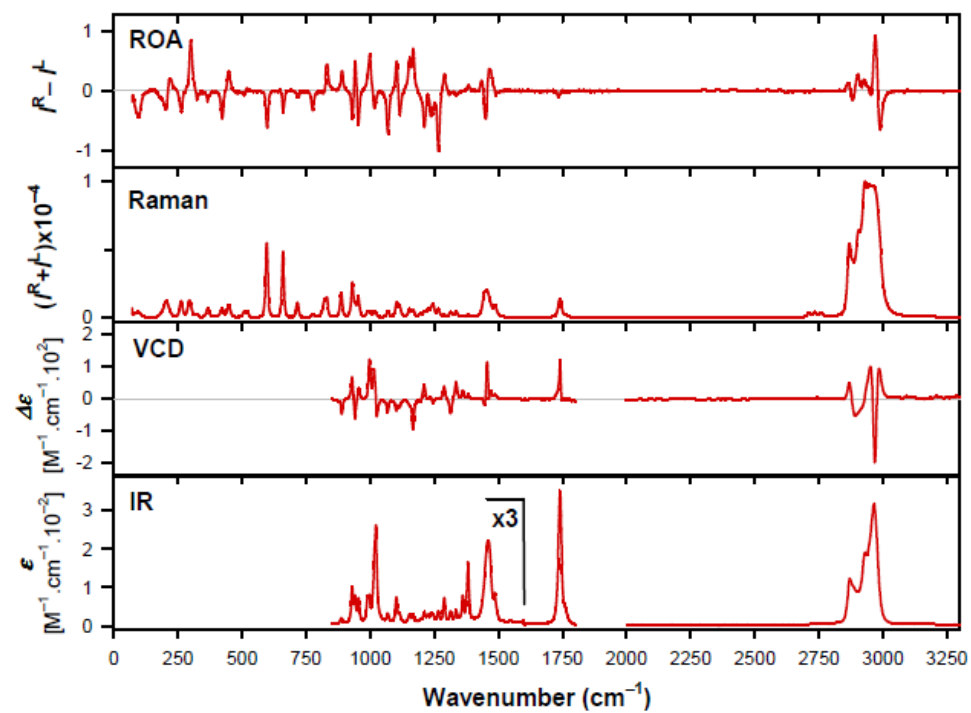
#	basis set	t (h)
1	6-31G	0.6
2	D95	0.8
3	6-31G*	1.6
4	TZV	2.2
5	6-31+G*	2.5
6	6-31G**	3.1
7	D95**	3.3
8	TZVP	5.8
9	6-31++G**	6.4
10	D95+++**	7.1
11	6-311++G**	10.2
12	cc-pVTZ	50.7
13	aug-cc-pVTZ	410.8



(1R)-(+)- α -pinene:



(1R)-(-)-fenchone:



(1R)-(+)-camphor:

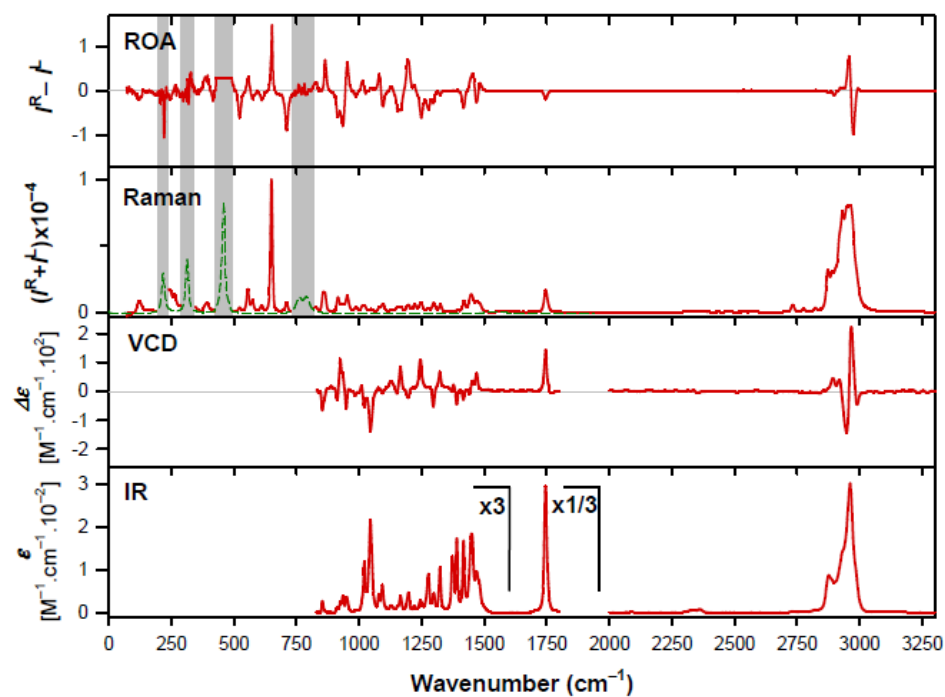


Figure S1. All measured spectra, i.e. Raman scattering, ROA, IR and VCD of (1R)-(+)- α -pinene, (1R)-(-)-fenchone, and (1R)-(+)-camphor (from the top). For camphor, the CCl_4 solvent bands are displayed in green and the Raman and ROA spectra are not reliable in these regions. In some spectral region factors by which the intensity was multiplied are indicated. IR and VCD experimental conditions are summarized in **Table S1**.

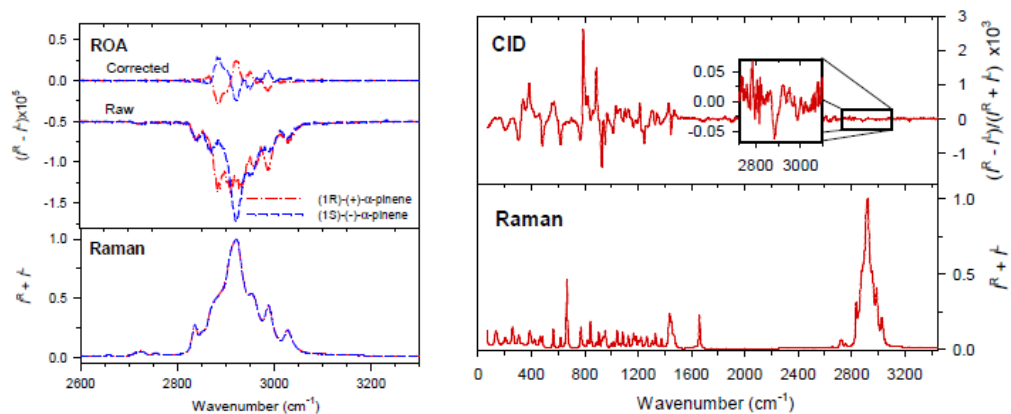


Figure S2. Left: Example of the artifact removal in the CH stretching region for α -pinene. Whereas the experimental Raman spectra (bottom) of the R and S enantiomers are indistinguishable at this scale, raw ROA spectra (top) are contaminated by the Raman signal. Right: Raman spectrum and the CID ratio within the entire range of frequencies.

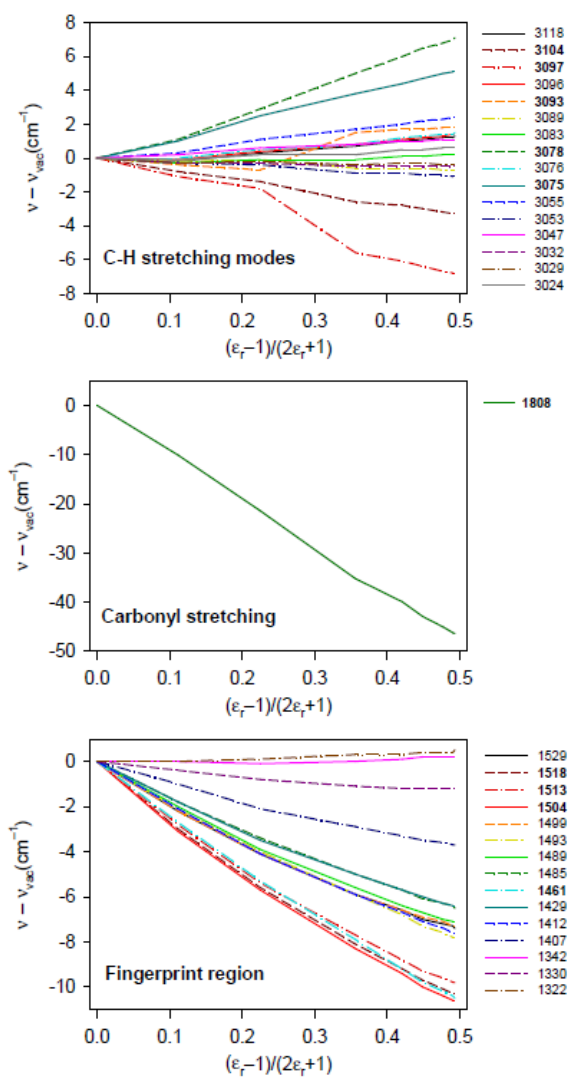


Figure S3. Calculated (B3LYP/6-311++G**/COSMO) frequency shifts of selected (1R)-(+)-camphor vibrational modes as dependent on the solvent polarization factor (see Table S2).

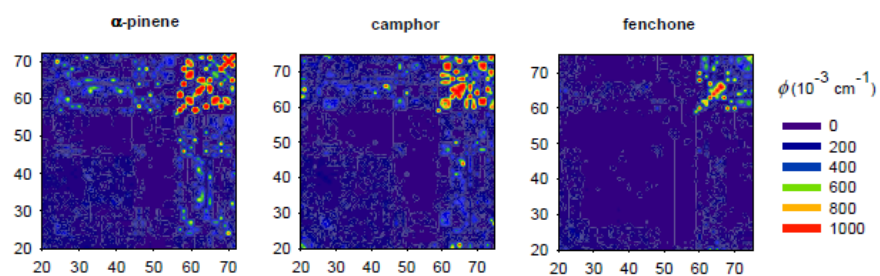


Figure S4. Anharmonic coupling (ϕ) between harmonic vibrational modes. For the modes i and j on the x and y axes, ϕ is defined as the average of cubic and quartic constants containing these modes (in absolute value, BPW2PLYP/ B3LYP/ 6-311++G**/ COSMO calculation, e.g. $|c_{iii}|$, $|c_{ijj}|$, $|d_{ijj}|$, etc.). The large coupling among the C-H stretching modes is recognizable at the upper right corner in the graphs.

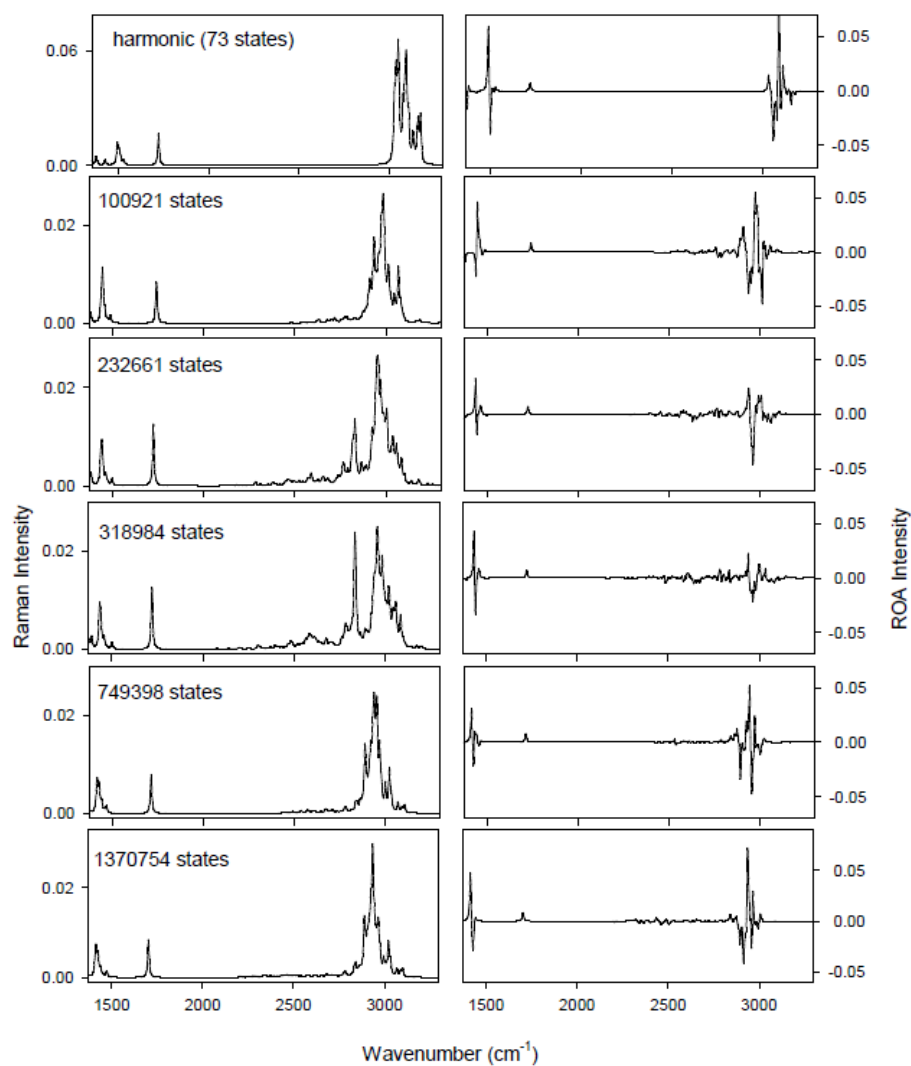


Figure S5. α -pine(1R)-(+)- α -pinene, Raman and ROA spectra calculated with 100921 ($c_1 = 0.0002$, $c_2 = \infty$, 36 blocked vibrations), 232661 ($c_1 = 0.0002$, $c_2 = \infty$, 29 blocked), 318984 ($c_1 = 0.0002$, $c_2 = \infty$, 26 blocked), 749398 ($c_1 = 0.002$, $c_2 = 0.1$, 36 blocked) states.), and 1370754 ($c_1 = 0.002$, $c_2 = 0.1$, 31 blocked) HO states.

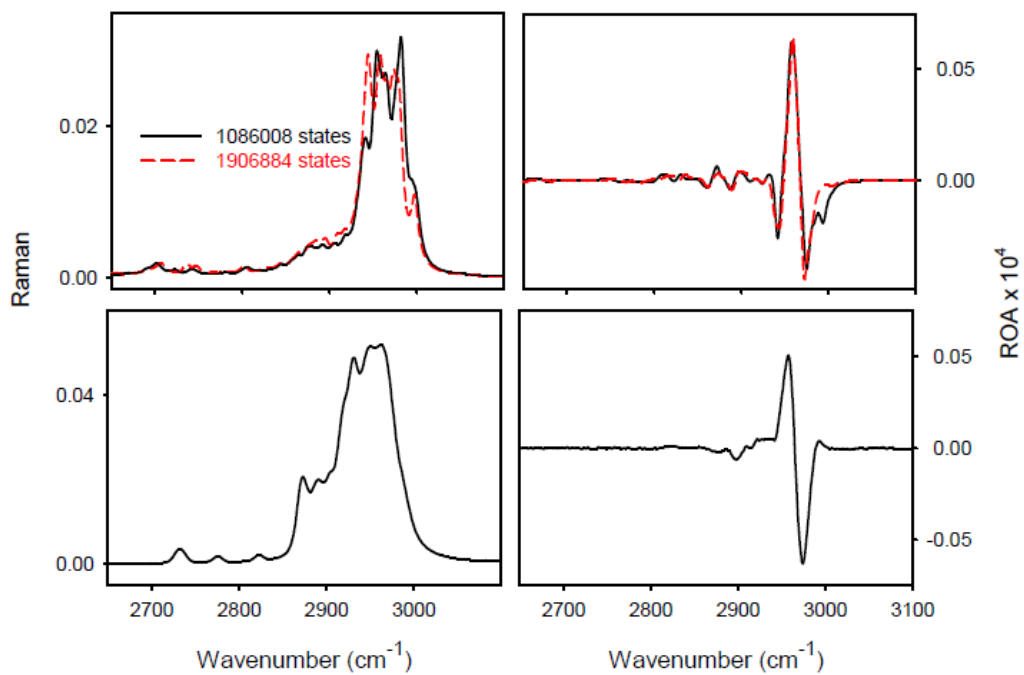


Figure S6. Simulated Raman and ROA (1R)-(+)-camphor spectra for 1086008 (36 modes blocked) and 1906884 (31 modes blocked) LVCI HO states (top, with $c_1 = 0.002$, $c_2 = 0.1$), and the experiment (bottom).

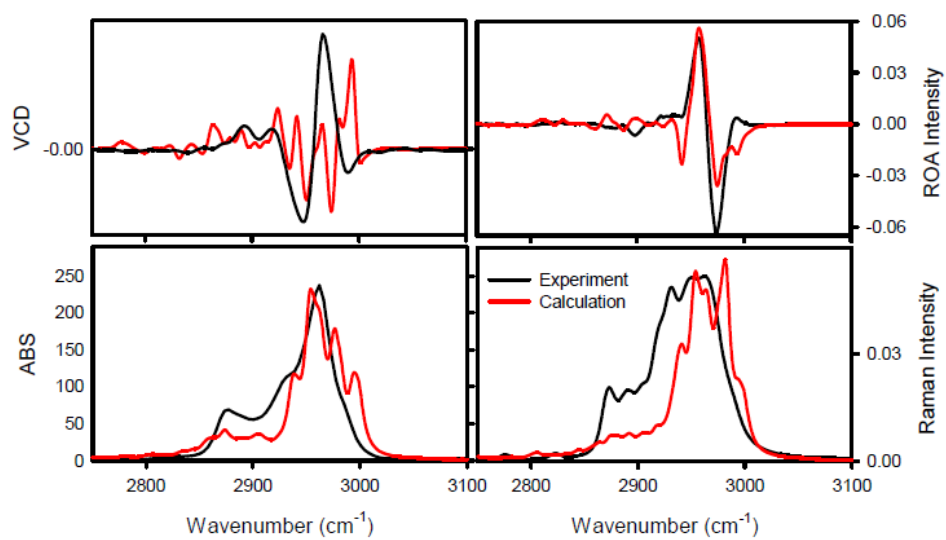
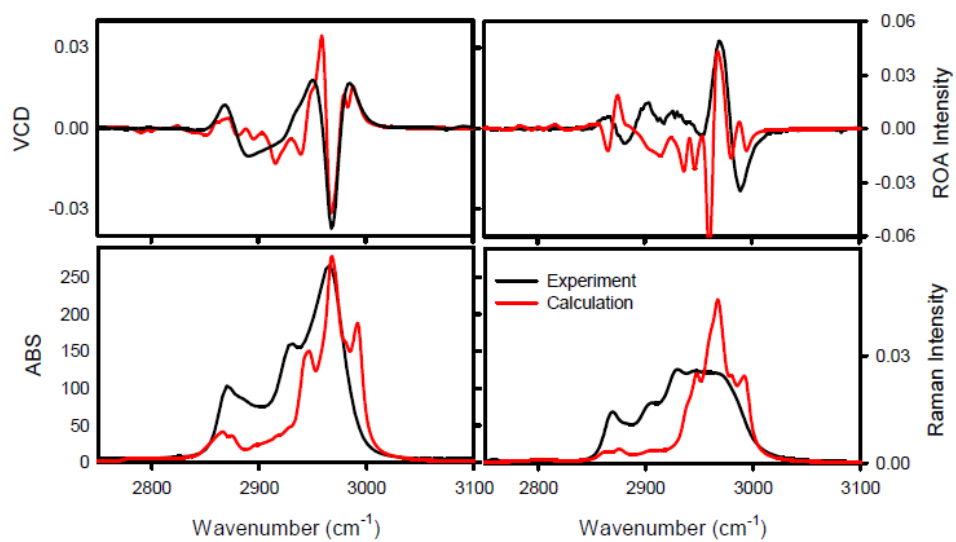


Figure S7. Overlaps of the calculated and experimental spectra in the CH stretching region for (1R)-(-)-fenchone (top) and (1R)-(+)-camphor (bottom).

A3. Publication [III]

Hudecová, J.; Horníček, J.; Buděšínský, M.; Šebestík, J.; Šafařík, M.; Zhang, G.; Keiderling, T. A.; Bouř, P., Three types of induced tryptophan optical activity compared in model dipeptides: Theory and experiment. *ChemPhysChem* **2012**, *13* (11), 2748-2760

Three Types of Induced Tryptophan Optical Activity Compared in Model Dipeptides: Theory and Experiment

Jana Hudecová,^{*,[a, b]} Jan Horníček,^[a] Miloš Buděšínský,^[a] Jaroslav Šebestík,^[a] Martin Šafařík,^[a] Ge Zhang,^[c] Timothy A. Keiderling,^[c] and Petr Bour^{*,[a]}

The tryptophan (Trp) aromatic residue in chiral matrices often exhibits a large optical activity and thus provides valuable structural information. However, it can also obscure spectral contributions from other peptide parts. To better understand the induced chirality, electronic circular dichroism (ECD), vibrational circular dichroism (VCD), and Raman optical activity (ROA) spectra of Trp-containing cyclic dipeptides c-(Trp-X) (where X = Gly, Ala, Trp, Leu, nLeu, and Pro) are analyzed on the basis of experimental spectra and density functional theory (DFT) computations. The results provide valuable insight into the molecular conformational and spectroscopic behavior of Trp. Whereas the ECD is dominated by Trp π - π^* transitions, VCD is dominated by the amide modes, well separated from minor Trp contributions. The ROA signal is the most complex.

However, an ROA marker band at 1554 cm^{-1} indicates the local χ_2 angle value in this residue, in accordance with previous theoretical predictions. The spectra and computations also indicate that the peptide ring is nonplanar, with a shallow potential so that the nonplanarity is primarily induced by the side chains. Dispersion-corrected DFT calculations provide better results than plain DFT, but comparison with experiment suggests that they overestimate the stability of the folded conformers. Molecular dynamics simulations and NMR results also confirm a limited accuracy of the dispersion-DFT model in nonaqueous solvents. Combination of chiral spectroscopies with theoretical analysis thus significantly enhances the information that can be obtained from the induced chirality of the Trp aromatic residue.

1. Introduction

The tryptophan (Trp) residue plays an important role in peptide conformational studies, especially those using chiral and fluorescence spectroscopic techniques.^[1–8] The aromatic chromophore has an easily detectable spectral response. This is both convenient and a problem, as electronic circular dichroism (ECD) arising from Trp can interfere with that due to the peptide backbone and bias secondary structure analyses, while its fluorescence overlaps that of other aromatics. Coupling between Trp and other aromatic residues leads to a particularly large ECD that can be used for tertiary structure analyses.^[7–11]

Trp also has distinctive vibrational spectral properties.^[12,13] Its bands can be selectively enhanced in Raman spectra^[2] and used for surface-enhanced studies.^[14] Although the aromatic side chain in Trp is planar, strong Raman optical activity (ROA) features have been identified in some peptides and confirmed theoretically as being due to the chiral orientation of the adjacent covalent link.^[15]

The Trp residue has many biological functions, including participation in ion transfer^[16] and providing a signal or anchor for pores formed from transmembrane helices, which often terminate in Trp. Quinacrine drugs were suggested to interact with tryptophans.^[17] Often, short secondary structures containing these residues are stabilized by a hydrophobic collapse.^[18]

In this work, a series of small Trp-containing cyclic dipeptides was synthesized and subjected to spectroscopic and computational studies, in order to understand the side-chain role in the ECD, vibrational circular dichroism (VCD), and ROA spectra, and to monitor the Trp conformational properties in solu-

tion. The cyclic dipeptides (sometimes called 2,5-diketopiperazines, DKPs, after the central six-membered ring) are favored for model studies^[19–21] as they are more rigid than linear peptides and are reasonably small, thereby facilitating the use of more accurate computations.

In particular, we were interested in the interaction of the Trp residue with the backbone and other side-chain parts of peptides, as such effects are crucial for developing ROA and ECD spectroscopic responses. As shown below, they provide complementary, but not identical, information about the structure to that obtained with NMR spectroscopy, which can be often reconciled only with complex theoretical modeling of molecu-

[a] J. Hudecová, J. Horníček, Dr. M. Buděšínský, Dr. J. Šebestík, M. Šafařík, Dr. P. Bour
Institute of Organic Chemistry and Biochemistry
Academy of Sciences
Flemingovo náměstí 2, 16610 Prague 6 (Czech Republic)
Fax: (+420) 220183123
E-mail: hudecova@uochb.cas.cz
bour@uochb.cas.cz

[b] J. Hudecová
Institute of Physics, Faculty of Mathematics and Physics
Charles University
Ke Karlovu 5, 12116 Prague 2 (Czech Republic)

[c] G. Zhang, Dr. T. A. Keiderling
Department of Chemistry
University of Illinois at Chicago
845 W. Taylor St., Chicago, IL 60607-7061 (USA)

Supporting information for this article is available on the WWW under <http://dx.doi.org/10.1002/cphc.201200201>.

lar behavior. For symmetric molecules, such as the cyclic dipeptide *c*-(L-Trp-L-Trp), NMR spectroscopy cannot discriminate among the conformational variants of individual side chains, thus making the optical techniques, in particular ROA, in principle more suitable in this case.

However, the ROA spectral features are not necessarily local, and the side-chain contributions are mostly overlapped with the backbone signal.^[22,23] Only some ROA bands can be associated with local molecular parts. Fortunately, for Trp, such a band exists at 1554 cm⁻¹, and its conformational dependence on the χ_2 side-chain dihedral angle can be reliably interpreted with computations.^[15] For ECD, the Trp-Trp exciton coupling is generally believed to indicate a fixed and close mutual position. This was only partially confirmed by our modeling, as a large signal was observed in mono-Trp peptides (e.g. *c*-(Trp-Ala)) as well.

Peptide structural studies through chiral spectroscopies profit from the improved reliability and performance of the computational tools. The ECD spectra, for example, can be nowadays routinely simulated using time-dependent density functional theory (TDDFT)^[24–26] for fairly large molecules, including the aromatic residues in peptides.^[10,11]

Also, information about local molecular structure in the vibrational optical activity spectra can be fully grasped only when supported by the simulations.^[27,28] For VCD theory, the most important milestones were perhaps the development of the magnetic field perturbation theory of Stephens,^[29,30] and its implementation within the gauge-independent atomic orbitals (GIAOs)^[31] and the DFT methodology.^[32]

Similarly to VCD, the GIAOs should be used for ROA.^[33] Although implemented within DFT,^[34] ROA calculations have for a long time been hampered by the necessity to compute derivatives of some tensors numerically. This obstacle was lifted only recently by implementation of fully analytical schemes in publicly available programs.^[35–40]

Our study also confirms the advantage of analysis of data from a combination of several spectroscopic techniques to characterize molecular behavior.^[41,42] Especially, the vibrational methods provide new insight into details of peptide secondary structure.^[43–48] However, the spectral interpretations and computations are still challenging, in particular for the proper representation of solvent involvement, conformational averaging, and balance of dispersion force.^[49–51]

As indicated in previous studies the dispersion should be added to most DFT biomolecular studies.^[52–56] This is true also for the Trp-containing dipeptides, although the benefit of the correction within a simplified solvent model may be limited.

Experimental Section

Synthesis: The synthesis started from N-protected (benzyloxycarbonyl, Z, and fluorenylmethoxycarbonyl, Fmoc) and C-protected (hydrochlorides of corresponding methyl esters) amino acids obtained from Merck, Czech Republic. Linear dipeptide precursors were prepared from Z-L-Trp-OH or Fmoc-D-Trp-OH and HCH-X-OMe peptides (X = Gly, Ala, Trp, Leu, nLeu, and Pro) using standard BOP activation^[57] with 3 equiv diisopropylethylamine. Cyclic dipep-

ptides *c*-(L-Trp-L-X) were obtained from Z-L-Trp-X-OMe, whereas *c*-(D-Trp-D-X) compounds were prepared from Fmoc-D-Trp-D-X-OMe, since different blocking groups were available for L- and D-Trp. The peptides were purified by column chromatography (Merck silica gel 60, CHCl₃/MeOH 25:1 or 10:1). Cyclization of the L series was achieved by 5 h of hydrogenolysis^[58] on Pd sponge in MeOH with continual heating to 50 °C for 15–40 h. The Pd sponge was removed by filtration and washed with MeOH, acetonitrile (AcCN) or DMSO depending on the product solubility. The solvent was evaporated, and the product was crystallized several times from MeOH.

The cyclic D series peptides were obtained in two steps. First, the Fmoc group was removed using 1,8-diazabicyclo[5.4.0]undec-7-ene (DBU)/EtSH/AcCN (2:20:78) mixture^[59] for 1 h, which was followed by extraction of the amine form between 1% HCl and diethyl ether. The aqueous solutions were adjusted to pH 8 with saturated NaHCO₃. Free amine was taken to EtOAc. After drying with Na₂SO₄ and evaporation of the solvent, the residue was heated in MeOH for 24–72 h. The precipitated cyclic form was filtered off and recrystallized from MeOH. In cases of low conversion, the remaining amino component was removed with Dowex-50 in MeOH.

Because of limited solubilities of the various cyclic dipeptides, a relatively wide range of solvents had to be used for the experimental NMR spectroscopy, ECD, VCD, and ROA, as summarized in Table 1.

Table 1. Overview of solvents used for the experimental spectra.

Compound	NMR	ECD	IR/VCD	Raman/ROA
<i>c</i> -(L-Trp-Gly)	[D ₂]DMSO, CD ₃ OD, CDCl ₃	–	DMSO	DMSO
<i>c</i> -(D-Trp-Gly)	–	–	DMSO	DMSO
<i>c</i> -(L-Trp-L-Ala)	–	TFE, AcCN	–	–
<i>c</i> -(L-Trp-L-Trp)	[D ₂]DMSO, CD ₃ OD	AcCN	DMSO, AcCN	DMSO, CH ₃ OH, DMSO
<i>c</i> -(D-Trp-D-Trp)	–	AcCN	DMSO, AcCN	DMSO
<i>c</i> -(L-Trp-L-Leu)	[D ₂]DMSO, CD ₃ OD	–	–	CH ₃ OH
<i>c</i> -(L-Trp-L-nLeu)	–	TFE, AcCN	–	–
<i>c</i> -(L-Trp-L-Pro)	[D ₂]DMSO, CD ₃ OD	AcCN	DMSO, AcCN	–
<i>c</i> -(D-Trp-D-Pro)	–	AcCN	DMSO, AcCN	DMSO

NMR Spectroscopy: ¹H and ¹³C NMR spectra of *c*-(L-Trp-Gly), *c*-(L-Trp-L-Trp), *c*-(L-Trp-L-Leu), and *c*-(L-Trp-L-Pro) were measured on a Bruker Avance II NMR spectrometer (¹H at 600.13 and ¹³C at 150.9 MHz) equipped with a 5 mm cryo-probe. The spectra of all cyclic dipeptides were measured at 300 K in DMSO, CD₃OD, and CDCl₃. For structural assignment of proton and carbon signals (using natural ¹³C occurrence), a combination of homo- and heteronuclear 2D NMR spectra (H,H-COSY, H,C-HSQC and H,C-HMBC) was used. The NOE contacts were determined from 2D H,H-ROESY spectra (mixing time 300 ms).

ECD Spectra: Electronic CD spectra for *c*-(L-Trp-L-Ala), *c*-(L-Trp-L-Trp), *c*-(D-Trp-D-Trp), *c*-(L-Trp-L-nLeu), *c*-(L-Trp-L-Pro), and *c*-(D-Trp-D-Pro) samples were measured using a Jasco J-810 spectropolarimeter. Samples were studied in 0.1 cm path length quartz cells,

using concentrations of about 0.2 mg mL⁻¹ in AcCN or 2,2,2-trifluoroethanol (TFE). c-(Trp-Gly) was not sufficiently soluble under these conditions. Each spectrum was obtained as an average of six scans taken with a band pass of 1 nm and scanning speed of 50 nm min⁻¹. The experimental spectra are expressed in $\Delta\epsilon$ (L mol⁻¹ cm⁻¹); for this purpose the concentration was determined by the Trp UV absorption.

VCD Spectra: VCD spectra of the D and L forms of c-(Trp-Gly), c-(Trp-Trp), and c-(Trp-Pro) were measured using a homemade dispersive instrument separately described in detail.^[60] The corresponding IR spectra were recorded on the same samples using a Vertex 80 FTIR (Bruker) spectrometer.

Samples were prepared by dissolving the peptides in DMSO or AcCN (not shown), to a concentration of about 10 mg mL⁻¹, and placing the solutions in a sealed cell composed of two CaF₂ windows separated by a 100 μ m spacer. Spectra were obtained as the average of six scans and were corrected by subtraction of an identically obtained spectrum of the solvent. Most VCD signals were in general quite weak and comparable in intensity to the instrumental artifact signals developed with this high-refractive-index solvent. The VCD spectra are therefore presented as the difference of enantiomers, or (L-D)/2. Similarly, IR spectra are presented as their sum, or (L+D)/2.

ROA and Raman Spectra: All cyclic dipeptides were dissolved in DMSO or methanol to concentrations of 50–150 mg mL⁻¹, and the spectra were measured with a backscattering SCP BioTools μ -Chiral Raman-2X instrument equipped with an Opus diode-pumped solid-state laser operating at 532 nm.^[61,62] The laser power was set to 50–100 mW, and power at the sample was 30–60 mW. Higher powers would cause a faster degradation of the samples. Residual fluorescence was quenched by leaving the sample in the laser beam for a few hours before measurement. The total acquisition time was about 20 h for each sample. For most samples, ROA spectra from two or three independent measurements were averaged. Solvent bands were subtracted from the Raman spectra, and minor baseline corrections were made. In the case of strong solvent scattering, affected wavenumber regions were deleted from the spectra. In this work we analyzed only the ROA of c-(Trp-Trp) and c-(Trp-Gly), where both enantiomers were available and meas-

urable; the spectra are then presented as the difference (L-D)/2, as for VCD.

DFT Geometries: Lowest-energy conformations of selected dipeptides (Tables 2 and 3) were obtained by geometry optimization with the Gaussian program,^[63] mostly using the B3LYP^[64] functionals and 6-311++G** basis set. For some tests, the aug-cc-pVTZ standard basis sets, MP2,^[65] MPW2PLYP,^[54,66] B3PW91,^[67] and BPW91^[68] methods were used as specified below (Table S1, Supporting Information). The conductor-like polarizable continuum model (CPCM)^[69] was used with AcCN (relative permittivity, $\epsilon_r=36$), CHCl₃ ($\epsilon_r=4.7$), TFE ($\epsilon_r=27$), CH₃OH ($\epsilon_r=33$), and DMSO ($\epsilon_r=47$) parameters for computations on the c-(L-Trp-L-Trp) molecule. The solvent variations, however, had only a minor effect on the resultant spectra and relative conformer energies, as documented in Figure S1 in the Supporting Information. For calculations of other molecules

Table 2. Selected geometry parameters,^[a] relative energies,^[b] and Boltzmann weights^[c] of the most populated conformers,^[d] calculated at the B3LYP/6-311++G**/CPCM(DMSO) level.

Conformation ^[e]		χ_1	χ_2	ϕ	ψ	ΔE	η
c-(Trp-Gly)							
A		-61	103	23	-16	0	35
A'		-60	106	-25	17	0.1	32
B		-59	-87	22	-16	0.7	11
D		62	-92	28	-19	0.7	11
C		63	89	25	-17	0.9	8
c-(Trp-Ala)							
A		-60	103	18	-12	0	39
A'		-60	106	-28	19	0.1	32
B		-59	-87	18	-13	0.7	11
B'		-57	-83	-25	15	1.1	6
D		63	-89	17	-12	1.1	6
C		63	90	14	-9	1.1	6
c-(Trp-Leu)							
A3	Trp	-61	103	15	-11	0	45
	Leu	-63	172	16	-11		
B3		-58	-88	18	-13	0.7	13
		-63	172	18	-14		
A8		-61	103	20	-15	0.9	9
		-167	64	27	-21		
D3		62	-89	16	-11	1.1	7
		-62	174	14	10		
C3		64	90	13	-9	1.2	6
		-63	173	16	-11		
c-(Trp-Trp)							
AA	Trp 1	-61	102	16	-10	0	25
	Trp 2	-61	102	16	-10		
A'A'		-59	105	-19	11	0.1	22
		-60	105	-19	12		
AB		-61	103	16	-11	0.7	15
		-58	-88	15	-10		
A'B'		-60	105	-12	6	1	10
		-58	-84	-10	5		
AD		-60	103	16	-10	0.9	11
		62	-90	17	-11		
c-(Trp-Pro) ^[f]							
	(<i>P</i> , θ_m)						
A' S	(302.4, 38.2)	-60	108	-37	31	0	64
B' S	(302.7, 38.3)	-58	-82	-36	31	1	12
A' N	(75.9, 36.1)	-59	108	-41	36	1.1	10
B' S	(300.3, 38.1)	-63	-22	-39	33	1.5	5
C' S	(303.9, 38.2)	54	80	-35	30	1.9	3

[a] Torsion angles χ_1 , χ_2 , ϕ , and ψ , in degrees, defined in Figure 1, for L,L enantiomers for DFT structures. [b] ΔE , in kcal mol⁻¹. [c] Including degeneracy; in %. [d] Conformers with relative energy $\Delta E < 2$ kcal mol⁻¹ are specified. [e] Notation of peptide conformation is specified in Figure 2. [f] Type of proline puckering: S or N defined by phase *P* and amplitude θ_m .

Table 3. Selected geometry parameters, relative energies, and Boltzmann weights of the most populated conformers, calculated at the B3LYP-D/6-311++G**/CPCM(DMSO) level.^[a]

Conformation	χ_1	χ_2	ϕ	ψ	ΔE	η	
c-(Trp-Gly)							
D	60	-90	37	-24	0	76	
C	61	87	33	-23	0.7	23	
c-(Trp-Ala)							
D	62	-90	24	-15	0	55	
C	63	94	21	-11	0.1	43	
c-(Trp-Leu)							
D3	Trp	64	-93	22	-18	0	64
	Leu	-50	-175	13	-9		
C3		65	91	18	-11	0.8	17
		-55	178	20	-13		
C8		61	98	20	-9	1.5	5
		-176	54	26	-15		
D2		64	-93	20	-15	1.6	4
		-74	64	20	-15		
c-(Trp-Trp)							
AD		-56	103	17	-8	0	66
		64	-89	22	-13		
BD		-64	-90	10	-1	0.8	19
		66	-81	23	-12		
BC		-59	-96	11	-7	1.7	4
		72	102	13	-4		
C'C'		67	92	-18	10	1.3	4
		64	83	-13	6		
D'D'		62	-83	-2	1	1.4	3
		56	-96	-16	12		
AC		-57	103	19	-10	1.8	3
		64	93	19	-10		
c-(Trp-Pro)	(P, θ_m)						
D	(4.0, 39.7)	62	-91	26	-18	0	86
C	(326.8, 41.9)	65	88	21	-12	1.4	8

[a] Symbols same as in Table 2.

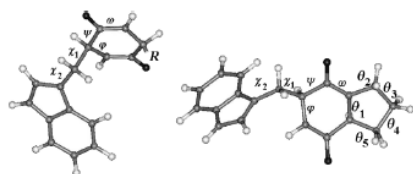
nates were allowed to relax. This revealed four minima; the angle χ_1 favors values around -60° and 60° , and χ_2 prefers -90° and 90° .

Based on these scans, c-(L-Trp-Gly), c-(L-Trp-L-Ala), c-(L-Trp-L-Leu), c-(L-Trp-L-Trp), and c-(L-Trp-L-Pro) dipeptide geometries were generated with starting values χ_1 of about -60° , 60° , and 180° , $\chi_2 \approx -90^\circ$ and 90° (these conformations are depicted in Figure 2) together with two possible ring conformations, $\phi \approx -25^\circ$ and 25° , and optimized by energy minimization (with B3LYP or B3LYP-D and CPCM(DMSO)/6-311++G**). For c-(L-Trp-L-Trp), c-(L-Trp-L-Leu), and c-(L-Trp-L-Pro), the conformation of the second side chain was also investigated systematically; for Leu, the χ_1' and χ_2' torsion angles were set at -60° , 60° or 180° for beginning the optimization; similarly, we used the S and N conformations^[71-74] of the proline five-membered ring.

Generation of the Spectra: Harmonic IR, VCD, Raman, and ROA intensities were computed with the Gaussian programs at the same level of theory as for optimized structures. The B3LYP functional with a medium-sized basis

only the DMSO ϵ_r value (or CHCl_3 value for checking of conformer preference) was used with both the normal and dispersion-corrected (B3LYP-D)^[54,66,70] B3LYP functional.

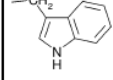
A two-dimensional scan was performed for c-(L-Ala-L-Ala) to investigate the inner ring potential energy surface (PES). Torsion angles ϕ and ψ (Figure 1, Table 4) were scanned in the range from -50°

**Figure 1.** Characteristic coordinates of the c-(L-Trp-X), X = Gly, L-Ala, L-Leu, L-nLeu, L-Trp, and c-(L-Trp-L-Pro) cyclic dipeptides.

to $+50^\circ$ with a step of 5° at the B3LYP/CPCM(DMSO)/6-311++G** level. Because of the relatively simple single-valley PES that resulted from the 2D scan, for the other dipeptides we performed a relaxed 1D scan along the ϕ angle only.

For c-(L-Trp-L-Trp) at the B3LYP/6-311G** level, the Trp side-chain conformation was investigated by a scan along torsion angles χ_1 and χ_2 , from -180° to $+165^\circ$ with 15° increments; other coordi-

Table 4. R on cyclic dipeptides.

R	peptide
-H	c-(L-Trp-Gly)
-CH ₃	c-(L-Trp-L-Ala)
-CH ₂ CH(CH ₃) ₂	c-(L-Trp-L-Leu)
-(CH ₂) ₃ CH ₃	c-(L-Trp-L-nLeu)
	c-(L-Trp-L-Trp)

set has been found very convenient for analogous spectral simulations in many previous studies.^[75-78] An excitation frequency of 532 nm was used for backscattered Raman and ROA dynamic (frequency-dependent) polarizabilities. Relative Raman and ROA spectral $S(\omega)$ shapes were obtained by convoluting the calculated intensities (I) with Lorentzian bands $\Delta = 8 \text{ cm}^{-1}$ wide, and multiplying by a temperature-correction factor for $T = 298 \text{ K}$, so that the spectrum from each mode i can be represented as [Eq. (1)]:

$$S(\omega) = I \left[1 - \exp\left(-\frac{\omega_i}{kT}\right) \right]^{-1} \frac{1}{\omega_i} \left[4 \left(\frac{\omega - \omega_i}{\Delta} \right)^2 + 1 \right]^{-1} \quad (1)$$

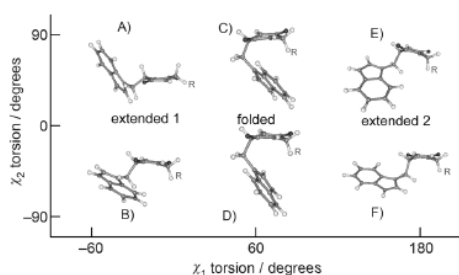


Figure 2. Conformational classes (A–F) of the Trp-containing dipeptides (see also Table 2 for conformer energies). The canonical angles (χ_1, χ_2 ; Figure 1) are A(–60, 90°), B(–60, –90°), C(60, 90°), D(60, –90°), E(180, 90°), and F(180, –90°).

where k is the Boltzmann constant and ω_i the vibrational frequency. Similarly, for VCD ($S(\omega) = \Delta\varepsilon$) and IR spectroscopy ($S(\omega) = \varepsilon$) [Eq. (2)]:

$$S(\omega) = cJ \frac{2\omega_i}{\Delta\nu} \left[4 \left(\frac{\omega - \omega_i}{\Delta} \right)^2 + 1 \right]^{-1} \quad (2)$$

where $S(\omega)$ is in units of $\text{mol}^{-1}\text{Lcm}^{-1}$, J is the rotational/dipole strength in debyes², and $c = 108$ for IR and 435 for VCD. Contributions of individual conformers were averaged using Boltzmann weights based on the sum of electronic and zero-point energies (ZPEs).

ECD spectra were generated from the dipole and rotational strengths calculated with Gaussian programs using the TDDFT method (B3LYP or B3LYP-D/CPCM(DMSO)/6-311++G**), and convoluted with Gaussian bands 15 nm wide. Surprisingly, the CAM-B3LYP^[79] functional, sometimes claimed to be superior to B3LYP for ECD,^[80] performed much worse for our system, and was thus not used.

Molecular Dynamics: An alternate solvent model was explored for c-(L-Trp-L-Trp) and c-(L-Trp-L-Pro), by running molecular dynamics (MD) simulations with the Amber10 program package^[81] and using the Amber99 force field. Missing force-field parameters in the cyclic dipeptide ring were derived from a Hartree-Fock (HF)/6-31G* calculation with Gaussian, using the "POP=MK" keyword. DMSO and chloroform force fields were obtained from the extended Amber database (<http://www.pharmacy.manchester.ac.uk/bryce/amber>). The solute molecule was surrounded by solvent molecules (DMSO, methanol, chloroform, or water) up to a distance of 8–14 Å. A four-step equilibration^[82] was carried out, followed by a 50 ns (100 ns for c-(L-Trp-L-Trp) in water) production run, using NpT ensembles and 1 fs integration time. Snapshots were taken each 5 ps and divided into three groups for c-(L-Trp-L-Trp) (folded: CC, CD, and DD; partially folded: AC, AD, BC, BD, CE, CF, DE, and DF; and extended: AA, AB, AE, AF, BB, BE, BF, EE, EF, and FF), and into two groups for c-(L-Trp-L-Pro) (folded: C, D; and extended: A, B, E, F; see Figure 2), according to the values of the χ_1 and χ_2 Trp angles. The relative conformer populations were normalized to 100%. From three independent MD runs for c-(L-Trp-L-Trp) the population error thus obtained was estimated as 20%.

2. Results and Discussion

Dipeptide Ring Geometry

It is known that the cyclic dipeptidic unit is normally quite flexible, and its conformation is very dependent on the amino acid side-chain type and interactions.^[83] For example, c-(L-Ala-L-Ala) in a crystal is puckered, whereas c-(L-Ala-D-Ala) is nearly flat.^[84] The peptide ring in the c-(L-Trp-L-Trp) crystal structure is also flat.^[85] This is in agreement with the computed one- and two-dimensional PESs for c-(L-Ala-L-Ala), displayed in Figure 3.

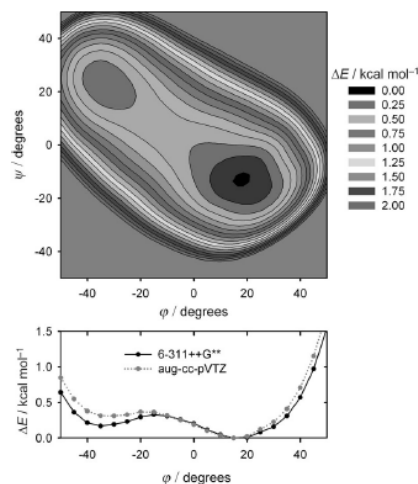


Figure 3. Top: calculated 2D (ϕ, ψ , B3LYP/CPCM(DMSO)/6-311++G**) PES for the inner ring in c-(L-Ala-L-Ala). Bottom: the corresponding 1D energy scan along the torsion angle ϕ [B3LYP/CPCM(DMSO)].

Clearly, the potential is shallow, and at 300 K ($kT \approx 0.6$ kcal mol^{-1}) the ring is quite flexible, thus allowing for large deviations of the ψ and ϕ angles. The other principal angles in the dipeptide ring (ψ' and ϕ') adopt similar values to ψ and ϕ during the ring deformation. Minor variations were caused by the 6-311++G** and aug-cc-pVTZ basis set change (Figure 3, bottom). The flat ring-deformation potential is undoubtedly caused by a partial conjugation of the amide-bond π -electronic systems and strongly anharmonic out-of-plane amide deformation energy, as observed, for example, for the *N*-methylacetamide (NMA) molecule.^[86]

Other peptides (c-(Gly-Gly), c-(L-Ala-L-Ala), c-(L-Ala-Gly), and c-(L-Leu-Gly)) showed a similar dependence (other 1D surfaces are shown in Figure S2, Supporting Information), although a closer look reveals finer differences between the dipeptides. Unlike c-(L-Ala-L-Ala), c-(Gly-Gly) exhibits two minima with the same energy, which reflects the symmetry of the molecule. The L-Leu enforces a stronger preference for the global minimum. The relative energies are notably changed by switching on the dispersion correction (bottom of Figure S2); if included, for ex-

ample, the difference in the two minima of *c*-(L-Ala-L-Ala) increases by $\approx 0.4 \text{ kcal mol}^{-1}$ and the dipeptide ring becomes more twisted.

For *c*-(L-Trp-Gly), the relative energy differences between the two dipeptide ring conformers ($\phi \approx -40$ and 40°) also strongly depend on the conformation of the side chains, as documented in Figure S3 in the Supporting Information. For some conformers (C and D, Figure 2), the $\phi \approx -40^\circ$ minimum is missing; for A and B this minimum is very shallow.

Conformations of the Dipeptides

In Tables 2 and 3 we list the lowest-energy conformers ($\Delta E < 2 \text{ kcal mol}^{-1}$) for the *c*-(L-Trp-Gly), *c*-(L-Trp-L-Ala), *c*-(L-Trp-L-Leu), *c*-(L-Trp-L-Trp), and *c*-(L-Trp-L-Pro) dipeptides as obtained by a systematic conformer search. The B3LYP/CPCM(DMSO)/6-311++G** approximation level was used with (DFT-D) and without (DFT) correcting for the dispersion interactions.

The conformers can be approximately categorized according to the values of χ_1 and χ_2 as “extended” (marked as A, B, E, F), where the Trp indole side ring points out from the dipeptide ring, or “folded” (marked as C, D), where the Trp indole is above/below the ring, potentially stabilized by interaction with the other amino acid side chain (Figure 2).

Rather contradictory conformational analysis results are obtained with the DFT and DFT-D approaches (Tables 2 and 3), using the CPCM solvent model with DMSO parameters. When DMSO was replaced by chloroform in the model, only minor changes in conformer populations appeared (mostly less than $\pm 5\%$). Typically, the DFT method alone predicts that the extended conformers are most stable, with a minor but not negligible population ($\approx 20\%$) of the folded ones. DFT-D almost exclusively favors the folded structures, separated from the extended ones by a wide energy margin. Interestingly, even the *c*-(L-Trp-Gly) is predicted to be entirely folded by DFT-D, although Gly does not possess any significant polarizable component beyond the DKP ring. The results are nevertheless consistent with previous studies, which clearly document the large effect of including the dispersion correction, and the significant energy changes computed with this force.^[53,54,66,70,87]

For *c*-(L-Trp-Gly), Boltzmann populations obtained at other approximation levels (including B3LYP, BPW91, B3PW91, MP2, MPW2PLYP) are summarized in Table S1 in the Supporting Information. The uncorrected DFT results (B3LYP, BPW91, B3PW91) are very similar, and favor all the extended conformers A and A'. Likewise, the dispersion correction always switches the equilibrium to the folded structures C and D. The MP2 theory provides almost the same conformer distribution as the DFT-D methods. The MPW2PLYP results are also very similar to those from DFT-D; yet we see that some population of the A, A', B, and B' conformers (in total 20%) is allowed by the MPW2PLYP method, unlike for MP2 and DFT-D ($< 1\%$). This reflects the well-known fact that the plain MP2 correction tends to overestimate the dispersion correction if compared to HF or older DFT formulations.^[53,54,66]

NMR Results

NMR spectra allow for the use of more variable experimental conditions, in particular different kinds of solvents. In most cases NMR spectroscopy can monitor the conformation of a cyclic dipeptide, and verify theoretical structural predictions.^[88,89] The analysis of the $J(\text{NH}, {}^1\text{H})$ vicinal couplings and the resultant ϕ angles in $[\text{D}_6]\text{DMSO}$ are summarized in Table 5.

Table 5. Experimental $J(\text{NH}, {}^1\text{H})$ coupling constants [Hz] in DMSO, the inner-ring ϕ angle [$^\circ$] in DMSO, MD-averaged ϕ values (for *c*-(L-Trp-L-Trp)) in DMSO, and Boltzmann-averaged ϕ values from DFT and DFT-D computations (B3LYP/CPCM(DMSO)/6-311++G**).

	<i>c</i> -(L-Trp-Gly)		<i>c</i> -(L-Trp-L-Leu)		<i>c</i> -(L-Trp-L-Pro)	<i>c</i> -(L-Trp-L-Trp)
	Trp	Gly	Trp	Leu	Trp	Trp
J	2.6	2.9; 0.9	2.6	2.9	≈ 0.8	2.9
$\phi_{\text{exp}}^{\text{[a]}}$	9	12	9	12	-37	12
ϕ_{MD}	-	-	-	-	-14	11
ϕ_{DFT}	7	5	16	18	-37	5
$\phi_{\text{DFT-D}}$	36	30	20	16	24	16

[a] Obtained from the coupling according to ref. [100], with coefficients $A = 7.0$, $B = -1.1$, $C = 0.55$.

Table 5 also includes averaged ϕ values from the MD run ϕ_{MD} (for *c*-(L-Trp-L-Trp) and *c*-(L-Trp-L-Pro)) and Boltzmann-weighted DFT and DFT-D (B3LYP/CPCM(DMSO)/6-311++G**) results. Except for *c*-(L-Trp-L-Pro), NMR data indicate a very flattened boat form of the dipeptide ring ($\phi = 9\text{--}12^\circ$). This agrees better with the uncorrected DFT and MD values than with DFT-D, but for *c*-(L-Trp-L-Trp), the experimental values lie between the DFT and DFT-D results. For *c*-(L-Trp-L-Pro) an opposite pucker ($\phi = -37^\circ$) was determined by NMR spectroscopy than for the other dipeptides, in agreement with a previous observation for a similar *c*-(L-Phe-L-Pro) compound (-49°).^[90] This value is also nicely reproduced by DFT ($\phi = -37^\circ$), but again not as well by DFT-D (Boltzmann average, $\phi = 24^\circ$).

The amino acid side-chain conformation can be deduced from the $J({}^1\text{H}, {}^1\text{H})$ and NOE ($\text{NH}, {}^1\text{H}$) values. The coupling constants and resultant approximate populations of the χ_1 rotamers are listed in Table 6; the solvents included $[\text{D}_6]\text{DMSO}$, CD_3OD , and CDCl_3 (see also Table 1). Note that two β -protons (referred to as R and S) provide individual NMR signals. The NMR data thus indicate a significant preference for the folded rotamer (where $\phi \approx 60^\circ$) in *c*-(L-Trp-Gly) and *c*-(L-Trp-L-Leu). In the case of *c*-(L-Trp-L-Leu) this leads to strong shielding of the Leu ${}^1\text{H}$ (3.39 and 3.57 ppm) and ${}^1\text{H}$ protons (0.62 and -0.05 ppm in DMSO, and 0.66 and -0.20 ppm in CD_3OD) due to a ring current effect of Trp. Folded conformers also prevail in *c*-(L-Trp-L-Pro), but only at about half the population, 46–52%; in CDCl_3 extended conformers are strongly preferred. These facts are somewhat inconsistent with the dipeptide ring analysis, in that they agree more with the DFT-D results than with DFT. Nevertheless, they can be explained by the overestimation of the effects of dispersion in the DFT-D method. In particular, the Trp residue is mostly folded, as predicted by DFT-D, but it does not deform the inner ring so much. This is

Table 6. Experimental $J(^1\text{H}, ^2\text{H})$ coupling constants [Hz] and χ_1 -rotamer populations η [%].^[a]

	c-(L-Trp-Gly) Trp			c-(L-Trp-L-Leu) Trp			Leu			c-(L-Trp-L-Pro) Trp			c-(L-Trp-L-Trp) Trp		
	^2H	R	S	R	S	R	S	R	S	R	S	R	S	R	S
J , DMSO	4.7		4.6	4		4.8	9.4		4.7	4.7		5.8	4.3		6.6
J , CD ₃ OD	3.8		4.6	3.6		4.6	10		4.3	≈ 5		≈ 5	3.9		7.4
J , CDCl ₃	–		–	3.9		8	10.2		3.7	3.8		10.9	3.7		8
χ_1 [°]	AB	EF	CD	AB	EF	CD	–60	180	60	–60	180	60	–60	180	60
η , DMSO [%]	21	17	62	10	23	67	75	17	8	20	34	46	15	43	42
η , CD ₃ OD [%]	11	16	73	5	21	74	83	12	5	23	25	52	11	53	36
η , CDCl ₃ [%]	–	–	–	11	60	29	84	6	10	10	90	0	9	60	31

[a] According to ref. [101], $J(^1\text{H}, ^2\text{H}) = 5.86 - 1.86 \cos(\tau) + 3.81 \cos(2\tau) + 0.37 \sin(\tau)$, where $\tau = \chi(^1\text{H}, \text{C}, \text{C}, ^2\text{H})$.

also consistent with the prevailing conformation in the c-(L-Trp-L-Trp) crystal, for example, where a T-shaped folded conformation was found (indicated as AD in Tables 2 and 3), but the inner ring is almost planar.^[b5] The NMR data for the Trp conformation in c-(L-Trp-L-Trp) are not usable for reliable prediction; because of the symmetry, the Trp residues are not resolved by NMR spectroscopy and are subject to fast conformer exchange.

The χ_2 Trp angle can in principle be derived from the observed NOE values. However, our measured data indicate strong NOE contacts of Trp R- ^2H with both HN protons, thus implying a fast flipping around the $^2\text{C}-^1\text{C}$ bond, which prevents a reliable prediction.

Molecular Dynamics

The MD simulations with explicit solvent provide an alternative to the DFT-D/CPCM model. In spite of the large error of the populations ($\approx 20\%$, see the Experimental Section), the MD results (Table 7) clearly indicate a more complicated picture.

Table 7. Conformer populations [%] for c-(L-Trp-L-Trp) and c-(L-Trp-L-Pro) obtained by MD/Amber10 simulations in different solvents.

c-(L-Trp-L-Trp)	Population ^[a]					
	extended	partially folded	folded			
water	1	92	7			
DMSO	45	55	0			
CH ₃ OH	7	93	0			
CHCl ₃	90	10	0			
c-(L-Trp-L-Pro)	Population					
	extended conformation			folded		
χ_1	–60°		180°		60°	
	A	B	E	F	C	D
water	14	21	4	2	30	28
DMSO	8	8	8	3	45	28
CH ₃ OH	26	15	1	1	23	34
CHCl ₃	41	45	0	0	11	3

[a] Folded conformers: CC, CD, and DD; partially folded: AC, AD, BC, BD, CE, CF, DE, and DF; and extended conformers: AA, AB, AE, AF, BB, BE, BF, EE, EF, and FF (see Figure 2).

Unlike with DFT-D/CPCM (Table 3), for c-(L-Trp-L-Trp) the extended structures may be additionally present in MD. In the low-polarity CHCl₃ environment the extended forms prevail (90%). On the other hand, more polar solvents (DMSO, H₂O, MeOH) strongly favor more compact forms, in agreement with the hydrophobic collapse known for some Trp-containing peptides. In water (first line in Table 7) even the fully stacked parallel L-Trp-L-Trp folded conformers appear (7%), but the edge-on-face L-Trp-L-Trp interaction is still more probable (92%), as commonly found in the Trp-containing peptides and proteins.^[18,91–94]

The MD-predicted preferences of the Trp side-chain position for c-(L-Trp-L-Pro) are in agreement with the NMR results (Table 6), also favoring extended conformers in CHCl₃. For c-(L-Trp-L-Trp) the results cannot be compared to NMR data because of molecular symmetry. The behavior in CH₃OH is very similar to that in water according to MD, that is, the ratio of extended and folded conformers is close to 50:50. In DMSO the folded conformers slightly prevail in MD (73:27); in NMR the ratio was 46:54. Thus, we see that the MD simulations reveal finer solvent effects than DFT-D/CPCM, which had almost the same conformer ratios for all solvents, although the MD results are limited by the force field inaccuracy.

ECD Spectra

The experimental spectra of c-(L-Trp-L-Ala), c-(L-Trp-L-Trp), c-(L-Trp-L-nLeu), and c-(L-Trp-L-Pro) in AcCN are plotted in Figure 4. Due to interfering absorbance of DMSO in the UV region, it was necessary to employ different solvents for ECD than for the vibrational spectra (VCD and ROA). The ECD spectra for these molecules have the unique characteristic that they are dominated almost completely by the Trp contributions, even for DKPs with only one Trp residue. The differences between the ECD in AcCN and TFE (mostly ≈ 5 nm shift, but preserving the general shape, Figure S4, Supporting Information) were relatively minor, and less than the differences between the various molecules. Such solvent effects would be difficult to model.^[95]

The c-(L-Trp-L-Pro) is the outlier, which corresponds to a distortion of the peptide ring and consequently the interaction of

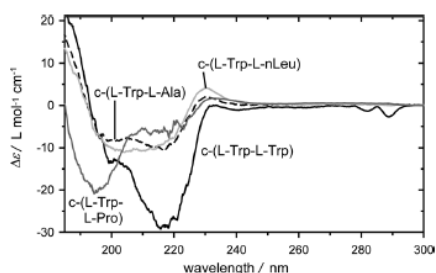


Figure 4. Experimental ECD spectra of *c*-(L-Trp-L-Ala), *c*-(L-Trp-L-Trp), *c*-(L-Trp-L-nLeu), and *c*-(L-Trp-L-Pro), all measured in AcCN. For analogous TFE results, see Figure S4 in the Supporting Information.

the Trp with the rest of the molecule caused by the constraints due to the Pro pyrrole ring. The near identical ECD for *c*-(L-Trp-L-Ala) and *c*-(L-Trp-L-Leu) suggests that the Trp is not interacting significantly with the aliphatic side chain, at least in these solvents. The much larger ECD seen for *c*-(L-Trp-L-Trp) in AcCN than for the other peptides (Figure 4) suggests a strong exciton coupling of the Trp residues,¹¹ and thus indicates a significant contribution from a stable interacting or folded conformation. This is further confirmed by the negative ECD at 290 nm, which is not seen for the other dipeptides.

The main features of the ECD spectra are reproduced for *c*-(L-Trp-L-Ala), *c*-(L-Trp-L-Trp), and *c*-(L-Trp-L-Pro) by the B3LYP/CPCM(DMSO)/6-311++G** computations (Figure 5). The averaging of contributions from thermally populated conformers had a minor influence on the total absorption, but had a major impact on the resultant averaged ECD, and consequently the DFT and DFT-D methods clearly provide very different ECD

spectra (Figure 5). Individual conformer ECD (e.g. conformer C of *c*-(L-Trp-L-Ala) calculated with and without the dispersion, see Figure 5) are quite similar; thus, the resultant spectrum is mostly influenced by the weighting scheme dependent on the relative conformer energies (Tables 2 and 3).

For all molecules, it is clear that the conformer averaging is needed to obtain realistic spectral shapes and absolute intensities. It is also apparent that the balance of populated conformers changes the predicted ECD band shape by shifting the spectral band overlap, thus making the relative energetics more critical than the spectral prediction for each conformer.

IR and VCD Spectra

The experimental VCD and IR spectra of *c*-(L-Trp-Gly), *c*-(L-Trp-L-Trp), and *c*-(L-Trp-L-Pro) in DMSO are compared in Figure 6. We also measured spectra in other solvents, but in AcCN the *c*-(Trp-Trp) and *c*-(Trp-Pro) developed added bands which may be indicative of aggregation at IR concentrations. Such data are not presented. The amide I (C=O stretching, 1600–1700 cm⁻¹) IR spectrum has a relatively sharp band at 1670–80 cm⁻¹ for *c*-(L-Trp-Gly) and *c*-(L-Trp-L-Trp), but the *c*-(L-Trp-L-Pro) exhibits a broadening due to the Trp-Pro link being a tertiary amide with a lower amide I frequency.^{19,89} The main VCD signal is very weak and predominantly negative in the amide I region. It has some contributions from other underlying modes, which arise from the aromatic Trp side chain. The *c*-(L-Trp-L-Trp) molecule might have a positive couplet shape (+/-, from lower to higher frequency), but this is not clear in the experiment due to a baseline distortion.

The *c*-(L-Trp-L-Pro) VCD is surprisingly weak, considering the expected distortion of its peptide ring, with the amide I VCD being above but near to our measurement limits. (Most spec-

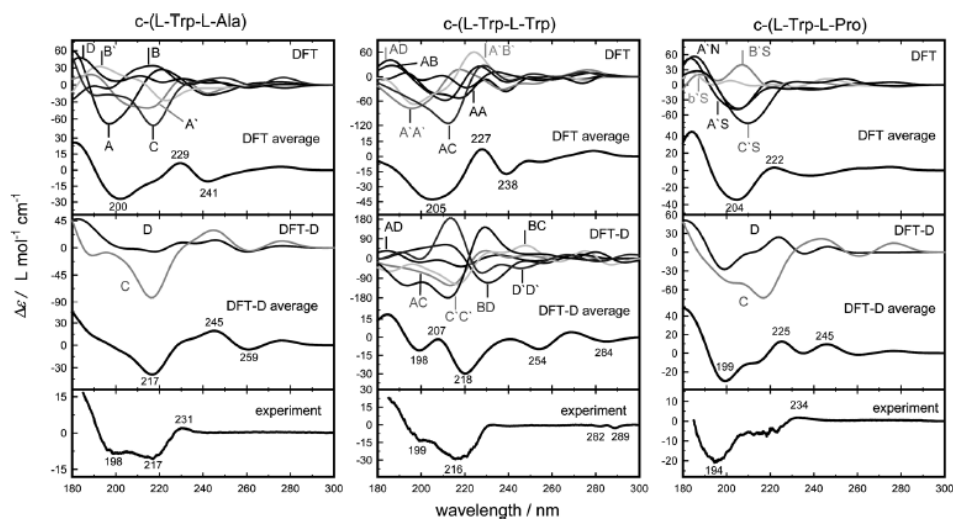


Figure 5. Calculated (B3LYP/CPCM(DMSO)/6-311++G**, DFT, and DFT-D geometries) and experimental ECD spectra of *c*-(L-Trp-L-Ala), *c*-(L-Trp-L-Trp), and *c*-(L-Trp-L-Pro). Relative abundances (Boltzmann weights) of different conformers are given in Tables 2 and 3.

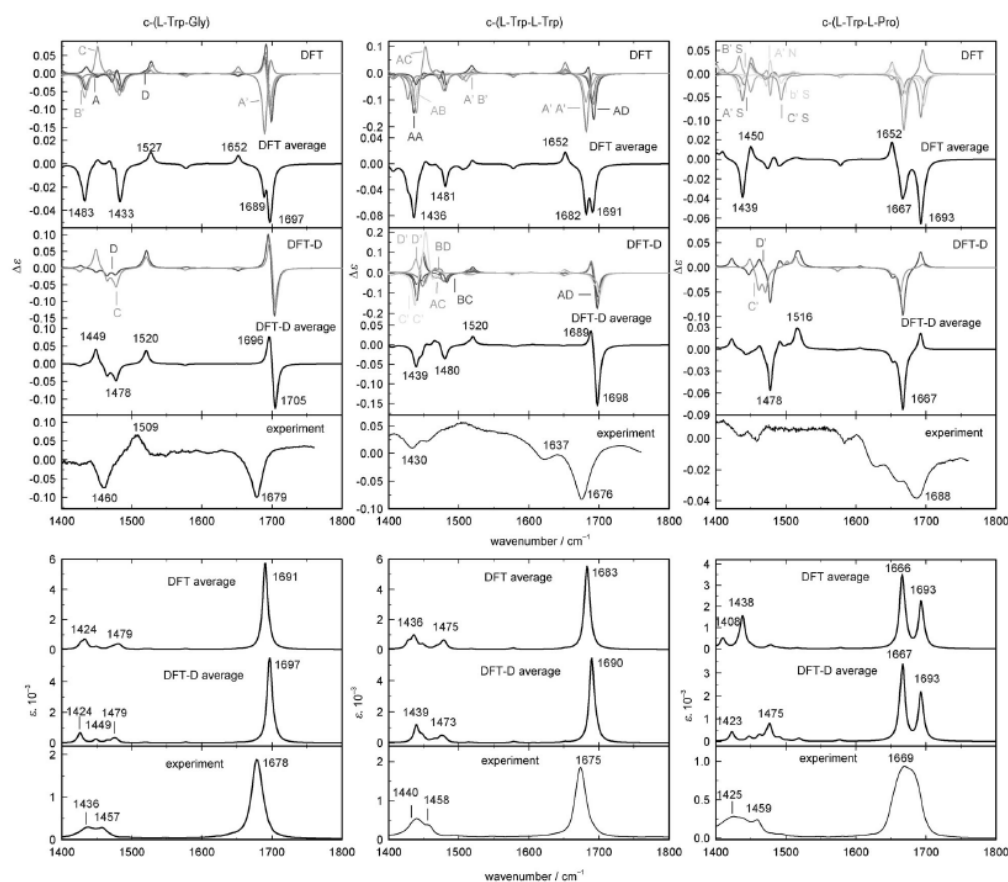


Figure 6. Calculated (B3LYP/CPCM(DMSO)/6-311 ++G**, DFT, and DFT-D) and experimental VCD and IR spectra of *c*-(L-Trp-Gly), *c*-(L-Trp-L-Trp), and *c*-(L-Trp-L-Pro) in DMSO. Experimental intensities are only approximate due to concentration error. Relative abundances (Boltzmann weights) of different conformers are given in Tables 2 and 3.

tra are measured with $A \approx 0.5$ for the amide I, so $\Delta\epsilon/\epsilon$ of 10^{-5} is above but close to our reliable measurement limit.) Such weak VCD spectra are subject to distortion through absorption artifacts, so that we limited our experimental VCD measurements to those samples for which we have both D,D and L,L isomers. In addition to amide I, there is a significant VCD signal arising from CH_2 motions and amide II bands ($1430\text{--}1530\text{ cm}^{-1}$), although this region is broader and more complex resulting in the IR and VCD patterns being less characteristic and not easily separable into local modes.^[96]

The spectral simulations (Figure 6) reproduce many of the observed dependencies, with the IR and VCD predictions being very good aside from small frequency shifts as are expected for DFT. For example, in *c*-(L-Trp-Gly) the amide I VCD computed with the DFT calculation is predominantly negative. While many of the individual conformers have couplet amide I shapes, the negative lobes tend to dominate and, when weighted by population, prove to be the larger contributions.

The positive signal at 1652 cm^{-1} predicted by DFT might correspond to the very weak experimental feature at 1630 cm^{-1} . DFT-D provides a conservative couplet for amide I, in both C and D conformers, which does not reflect experiment. For the region $1400\text{--}1550\text{ cm}^{-1}$ (combination of CH_2 and amide II modes), on the other hand, neither method is in good agreement, but several conformers give rise to a positive band higher in frequency than a negative band, which is seen experimentally. After averaging, the DFT-D VCD curve is perhaps in better agreement with the experimental amide II than the DFT. The overlap and mixing of amide II (C-N-H deformation) and CH_2 modes is difficult to reproduce correctly by computations, as we have also found in previous model calculations.^[97]

For *c*-(L-Trp-L-Trp) both DFT and DFT-D approaches provide the basic VCD pattern correctly (mostly negative amide I and a negative amide II region), although the calculated dispersion of the negative intensities around 1439 cm^{-1} is too large. In *c*-(L-Trp-L-Pro) the amide I VCD is predominantly negative and

broader than in *c*-(L-Trp-Gly) and *c*-(L-Trp-L-Trp), which is reproduced by the DFT calculations but not by the DFT-D results.

ROA Spectra

The ROA measurements were often hampered by the sample fluorescence (Table 1) and known instability of the Trp compounds in the (green) laser light.^[98] The best experimental Raman and ROA spectra were obtained for 150 mg mL⁻¹ (*c*-(L-Trp-L-Trp) and *c*-(D-Trp-D-Trp)) and 50 mg mL⁻¹ (*c*-(L-Trp-Gly) and *c*-(D-Trp-Gly)) solutions in DMSO.

In Figure 7 the ROA and Raman spectra are shown, together with the corresponding DFT and DFT-D computations. The computations reproduce the strongest features in the ob-

served Raman spectrum well. Both compounds have very similar Raman intensity patterns, which are dominated by the Trp modes (see the assignment in Table 8). Similar domination of the spectra by aromatic residues was observed previously for a model peptide.^[22] The ROA spectra are more complex, but many observed features can be explained by the calculation. For example, the C=C five-membered Trp ring stretching band (experimentally at ≈ 1554 cm⁻¹) exhibits a negative ROA signal. This is, however, provided only by the dispersion model. On the other hand, DFT-D overestimates the relative intensity.

As discussed before,^[15] although coming from the nonchiral chromophore, the ROA for this vibration is extremely sensitive to the Trp side-chain conformation, that is, the χ_2 angle. In particular, a negative ROA band is associated with conformations

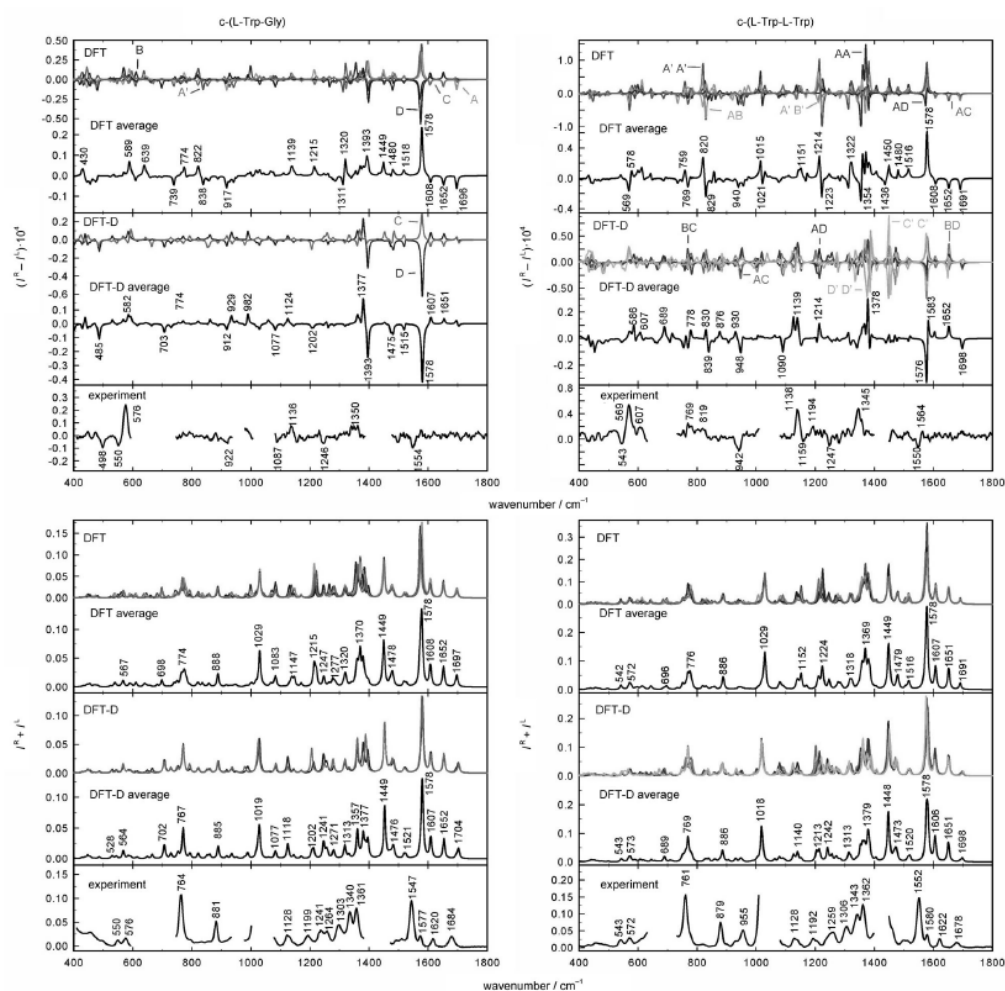


Figure 7. Calculated (B3LYP/PCPM(DMSO)/6-311++G*, DFT, and DFT-D geometries) and experimental ROA ($l_r - l_l$) and Raman ($l_r + l_l$) spectra of *c*-(L-Trp-Gly) and *c*-(L-Trp-L-Trp) in DMSO. The intensity of the experimental spectra is relative, only the ratio ROA/Raman is meaningful.

Table 8. Assignment of the most intense Raman bands.^[a]

c-(Trp-Gly) DFT-D ^[b]	c-(Trp-Gly) Exp.	c-(Trp-Trp) Exp.	Vibrations
1704	1684	1678	A I, out of phase
1695	1684	1678	A I, in phase
1652	1620	1622	$\nu(\text{C}=\text{C})$, $\nu(\text{C}=\text{N})$ Trp
1607	1577	1580	$\nu(\text{C}=\text{C})$, $\nu(\text{C}=\text{N})$ Trp
1578	1547	1552	$\nu(\text{C}=\text{C})$, Trp 5-membered ring
1449			amide II
1377	1361	1362	amide III
1357	1340	1343	$\nu(\text{C}=\text{C})$, Trp
1312	1303	1306	Trp, 5-membered ring breathing
1271	1264	1259	$\nu(\text{C}=\text{C})$, phenyl ring in Trp
1241	1241		$\nu(\text{C}=\text{N})$ Trp, $\delta(\text{CH})$
1202	1199	1192	$\delta(\text{CH})$, aliphatic
1118	1128	1128	$\nu(\text{C}-\text{N})$ in amides
1019		≈ 1020	$\nu(\text{C}=\text{C})$, phenyl ring in Trp
982		955	$\nu(\text{C}-\text{C})$ in amides, $\delta(\text{CH})$
885	881	879	$\nu(\text{C}=\text{C})$, $\nu(\text{C}=\text{N})$ Trp
767	764	761	$\nu(\text{C}=\text{C})$, $\nu(\text{C}=\text{N})$ Trp
564	576	572	$\nu(\text{C}=\text{C})$, $\nu(\text{C}=\text{N})$ Trp, out of plane amide NH
528	550	543	dipeptide ring deformation

[a] Frequencies in cm^{-1} . [b] B3LYP-D/CPM(DMSO)/6-311++G** level.

with $\chi_2 \approx -90^\circ$, which is in agreement with the prevalent conformer population of this isomer predicted for c-(L-Trp-Gly) (Table 3). For c-(L-Trp-L-Trp) the prevalence of the T-shaped folded conformers with alternate ($+90^\circ$, -90°) χ_2 values causes partial cancelation and the resultant negative signal is smaller, which can be seen in both the theoretical and experimental ROA spectra.

Around 1350 cm^{-1} (CH bending, amide III) the predominantly positive experimental ROA signal is better reproduced by DFT-D for c-(L-Trp-L-Trp), but by DFT for c-(L-Trp-Gly). Within $1100\text{--}1250 \text{ cm}^{-1}$ the experimental “+ + - -” pattern seems to be better reproduced by DFT-D for both peptides. A negative ROA signal at $920\text{--}942 \text{ cm}^{-1}$ is present in both experiments and all calculations. Below 900 cm^{-1} , the differences in the spectra provided by DFT and DFT-D are minor; nevertheless, both computations mostly reproduced the sign pattern observed experimentally. The large experimental positive ROA intensity at 576 and 569 cm^{-1} for c-(L-Trp-Gly) and c-(L-Trp-L-Trp), respectively, is not fully reproduced by the computation, which can be explained by an anharmonic character of the NH out-of-plane deformation.^[99]

DFT versus DFT-D

To summarize the role of the dispersion at the spectral simulations, we can conclude that adding the physically correct van der Waals interaction significantly changes conformer equilibria. Most spectral features were improved when the dispersion was included, in line with similar investigations in the past.^[52-56] However, there are also indications that only adding the correction to the dielectric solvent model may be an oversimplification. This is supported by the NMR data and the MD

conformer ratios lying between DFT and DFT-D. Different spectral types (e.g. ECD, VCD, and ROA) also reacted differently in the dispersion correction; for VCD, for example, DFT-D provided bands that were too narrow due to the limited number of folded conformers. To better balance these complex dispersion, flexibility, and solvent effects remains a challenge for the future.

3. Conclusions

We have systematically compared the ECD, VCD, and ROA spectra of Trp-containing cyclic dipeptides. The results enable us to better understand the chiral spectral response of this residue in larger proteins and to characterize the link between the spectra and molecular structure. The Trp chromophore, although not intrinsically chiral if isolated from the backbone, dominated in the ECD and ROA dipeptide spectra. Especially surprising was the large Trp ECD signal of c-(L-Trp-L-Ala), as this molecule contains only one Trp residue without an exciton coupling between identical oscillators. Only for VCD can the interference between the side- and main-chain signals be avoided. However, the relative flatness of the ring makes the VCD weak and subject to artifacts.

The DFT computations provided a reliable basis for spectral interpretation. Dipeptide theoretical PESS, however, were strongly influenced by the presence or absence of the dispersion correction. Stable conformers yielded about the same spectra with DFT and DFT-D, but the dispersion energetically favored the compact folded forms. In general, the corrected computations also provided better spectra. Nevertheless, several indications appeared pointing to an overestimation of the dispersion effect within the CPCM solvent model. This was also confirmed by the NMR data and MD simulations, which revealed finer solvent effects, stemming from the solvent-solute dispersion and hydrogen bonding, that could be only partially included within DFT.

The chiral spectroscopies, at least in principle, eliminate the problems associated with measurements of symmetric molecules in solutions and unstable conformers by NMR spectroscopy. However, some experiments were hampered by limited solubility and instability of the dipeptides with Trp, and artifacts associated with the overlap with solvent vibrational bands. The ROA spectra appeared to be the most sensitive to the Trp side-chain conformation. Specific Trp marker bands could be found within the entire spectral region. In particular, the 1554 cm^{-1} ROA signal appeared useful as a unique local probe of the χ_2 angle, which is also otherwise difficult to monitor by other methods. Overall, we can conclude that the chiral spectroscopies provide very detailed information about the peptide structure, which must be, however, supported by theoretical modeling.

Acknowledgements

This study was performed with support from the Czech National Grant Agency (P208/11/0105), the Grant Agency of Charles Uni-

versity (126310), and the Ministry of Education (LH11033). The work at UIC was supported in part by a grant from the National Science Foundation (CHE 07 18543 to T.A.K.) and T.A.K. in part by a Research Award from the Alexander von Humboldt Stiftung.

Keywords: circular dichroism · conformation analysis · density functional calculations · peptides · Raman spectroscopy

- [1] H. Edelhoch, *Biochemistry* **1967**, *6*, 1948–1954.
 [2] R. P. Rava, T. G. Spiro, *J. Am. Chem. Soc.* **1984**, *106*, 4062–4064.
 [3] L. S. Itzhaki, P. A. Evans, C. M. Dobson, S. E. Radford, *Biochemistry* **1994**, *33*, 5212–5220.
 [4] S. M. O'Malley, M. J. McDonald, *J. Protein Chem.* **1994**, *13*, 561–567.
 [5] E. Bismuto, I. Sirangelo, G. Irace, E. Gratton, *Biochemistry* **1996**, *35*, 1173–1178.
 [6] C. P. Pan, M. D. Barkley, *Biophys. J.* **2004**, *86*, 3828–3835.
 [7] R. W. Woody, *Eur. Biophys. J.* **1994**, *23*, 253–262.
 [8] R. A. Sendak, D. M. Rothwarf, W. J. Wedemeyer, W. A. Houry, H. A. Scheraga, *Biochemistry* **1996**, *35*, 12978–12992.
 [9] D. M. Rogers, D. M. Hirst, *Biochemistry* **2004**, *43*, 11092–11102.
 [10] D. M. Rogers, N. A. Besley, P. O'Shea, J. D. Hirst, *J. Phys. Chem. B* **2005**, *109*, 23061–23069.
 [11] A. Roy, P. Bouř, T. A. Keiderling, *Chirality* **2009**, *21*, E163–E171.
 [12] B. Hernández, F. Pflüger, A. Adenier, S. G. Kriglik, M. Ghomi, *J. Phys. Chem. B* **2010**, *114*, 15319–15330.
 [13] S. D. Dieng, J. P. M. Schelvis, *J. Phys. Chem. A* **2010**, *114*, 10897–10905.
 [14] A. E. Aliaga, I. Osorio-Roman, P. Leyton, C. Garrido, J. Carcamo, C. Canulef, F. Celis, G. Diaz, E. Clavijo, J. S. Gomez-Jeria, M. M. Campos-Vallette, *J. Raman Spectrosc.* **2009**, *40*, 164–169.
 [15] C. R. Jacob, S. Lubner, M. Reiher, *ChemPhysChem* **2008**, *9*, 2177–2180.
 [16] W. Hu, T. A. Cross, *Biochemistry* **1995**, *34*, 14147–14155.
 [17] A. Saravanamuthu, T. J. Vickers, C. S. Bond, M. R. Peterson, W. N. Hunter, A. H. Fairlamb, *J. Biol. Chem.* **2004**, *279*, 29493–29500.
 [18] A. G. Cochran, N. J. Skelton, M. A. Starovasnik, *Proc. Natl. Acad. Sci. USA* **2001**, *98*, 5578–5583.
 [19] P. Bouř, V. Sychrovský, P. Maloň, J. Hanzlíková, V. Baumruk, J. Pospíšek, M. Buděšínský, *J. Phys. Chem. A* **2002**, *106*, 7321–7327.
 [20] N. A. Besley, M. J. Brienne, J. D. Hirst, *J. Phys. Chem. B* **2000**, *104*, 12371–12377.
 [21] J. Fleischhauer, J. Grötzinger, B. Kramer, P. Krüger, A. Wollmer, R. W. Woody, E. Zobel, *Biophys. Chem.* **1994**, *49*, 141–152.
 [22] J. Hudcová, J. Kapitán, V. Baumruk, R. P. Hammer, T. A. Keiderling, P. Bouř, *J. Phys. Chem. A* **2010**, *114*, 7642–7651.
 [23] S. Yamamoto, M. Straka, H. Watarai, P. Bouř, *Phys. Chem. Chem. Phys.* **2010**, *12*, 11021–11032.
 [24] C. Jamorski, M. E. Casida, D. R. Salahub, *J. Chem. Phys.* **1996**, *104*, 5134–5147.
 [25] F. Furche, R. Alhrichs, *J. Chem. Phys.* **2004**, *121*, 12772–12773.
 [26] F. Furche, R. Alhrichs, C. Wachsmann, E. Weber, A. Sobanski, F. Vögtle, S. Grimme, *J. Am. Chem. Soc.* **2000**, *122*, 1717–1724.
 [27] L. A. Nafie, *Annu. Rev. Phys. Chem.* **1997**, *48*, 357–386.
 [28] P. L. Polavarapu, *Chem. Rev.* **2007**, *7*, 125–126.
 [29] P. J. Stephens, *J. Phys. Chem.* **1985**, *89*, 748–752.
 [30] P. J. Stephens, *J. Phys. Chem.* **1987**, *91*, 1712–1715.
 [31] K. L. Bak, F. J. Devlin, C. S. Ashvar, P. R. Taylor, M. J. Frisch, P. J. Stephens, *J. Phys. Chem.* **1995**, *99*, 14918–14922.
 [32] J. R. Cheeseman, M. J. Frisch, F. J. Devlin, P. J. Stephens, *Chem. Phys. Lett.* **1996**, *252*, 211–220.
 [33] T. Helgaker, K. Ruud, K. L. Bak, P. Joergensen, J. Olsen, *Faraday Discuss.* **1994**, *99*, 165–180.
 [34] K. Ruud, T. Helgaker, P. Bouř, *J. Phys. Chem. A* **2002**, *106*, 7448–7455.
 [35] V. Liégeois, K. Ruud, B. Champagne, *J. Chem. Phys.* **2007**, *127*, 204105.
 [36] M. Pecul, K. Ruud, *Int. J. Quantum Chem.* **2005**, *104*, 816–829.
 [37] K. Ruud, J. Thorvaldsen, *Chirality* **2009**, *21*, E54–E67.
 [38] J. R. Cheeseman, M. S. Shaik, P. L. A. Popelier, E. W. Blanch, *J. Am. Chem. Soc.* **2011**, *133*, 4991–4997.
 [39] J. R. Cheeseman, M. J. Frisch, *J. Chem. Theory Comput.* **2011**, *7*, 3323–3334.
 [40] J. R. Cheeseman in *Calculation of Molecular Chiroptical Properties Using Density Functional Theory*, University of Groningen, Groningen, **2007**, p. INV3.
 [41] P. L. Polavarapu, *Chirality* **2008**, *20*, 664–672.
 [42] F. Wang, C. Zhao, P. L. Polavarapu, *Biopolymers* **2004**, *75*, 85–93.
 [43] T. Weymuth, C. R. Jacob, M. Reiher, *ChemPhysChem* **2011**, *12*, 1165–1175.
 [44] C. Herrmann, K. Ruud, M. Reiher, *ChemPhysChem* **2006**, *7*, 2189–2196.
 [45] S. Yamamoto, J. Kaminsky, P. Bouř, *Anal. Chem.* **2012**, *84*, 2440–2451.
 [46] S. Lubner, M. Reiher, *J. Phys. Chem. B* **2010**, *114*, 1057–1063.
 [47] C. R. Jacob, S. Lubner, M. Reiher, *J. Phys. Chem. B* **2009**, *113*, 6558–6573.
 [48] C. Merten, L. D. Barron, L. Hecht, C. Johannessen, *Angew. Chem.* **2011**, *123*, 10149–10152; *Angew. Chem. Int. Ed.* **2011**, *50*, 9973–9976.
 [49] M. Pecul, E. Lamparska, C. Capelli, L. Frediani, K. Ruud, *J. Phys. Chem. A* **2006**, *110*, 2807–2815.
 [50] K. H. Hopmann, K. Ruud, M. Pecul, A. Kudelski, M. Dračinský, P. Bouř, *J. Phys. Chem. B* **2011**, *115*, 4128–4137.
 [51] B. Mennucci, C. Cappelli, R. Cammi, J. Tomasi, *Chirality* **2011**, *23*, 717–729.
 [52] I. Dabkowska, H. V. Gonzalez, P. Jurečka, P. Hobza, *J. Phys. Chem. A* **2005**, *109*, 1131–1136.
 [53] S. Grimme, J. Antony, S. Ehrlich, H. Krieg, *J. Chem. Phys.* **2010**, *132*, 154104.
 [54] S. Grimme, *J. Comput. Chem.* **2006**, *27*, 1787–1799.
 [55] K. H. Hopmann, J. Šebestík, J. Novotná, W. Stensen, M. Urbanová, J. Svenson, J. S. Svendsen, P. Bouř, K. Ruud, *J. Org. Chem.* **2012**, *77*, 858–869.
 [56] X. Li, K. H. Hopmann, J. Hudcová, W. Stensen, J. Novotná, M. Urbanová, J. S. Svendsen, P. Bouř, K. Ruud, *J. Phys. Chem. A* **2012**, *116*, 2554–2563.
 [57] J. Ježek, R. Markošová, *Collect. Czech. Chem. Commun.* **1994**, *59*, 671–706.
 [58] E. Wünsch, *Methoden der Organischen Chemie (Houben-Weyl)*, Thieme, Stuttgart, **1974**.
 [59] J. E. Sheppeck, H. Kar, H. Hong, *Tetrahedron Lett.* **2000**, *41*, 5329–5333.
 [60] A. Lakhani, A. Roy, M. De Poli, M. Nakaema, F. Formaggio, C. Toniolo, T. A. Keiderling, *J. Phys. Chem. B* **2011**, *115*, 6252–6264.
 [61] W. Hug, G. Hangartner, *J. Raman Spectrosc.* **1999**, *30*, 841–852.
 [62] W. Hug, *Appl. Spectrosc.* **2003**, *57*, 1–13.
 [63] Gaussian 09 (Revision B01), M. J. Frisch, G. W. Trucks, H. B. Schlegel, G. E. Scuseria, M. A. Robb, J. R. Cheeseman, G. Scalmani, V. Barone, B. Mennucci, G. A. Petersson, H. Nakatsuji, M. Caricato, X. Li, H. P. Hratchian, A. F. Izmaylov, J. Bloino, G. Zheng, J. L. Sonnenberg, M. Hada, M. Ehara, K. Toyota, R. Fukuda, J. Hasegawa, M. Ishida, T. Nakajima, Y. Honda, O. Kitao, H. Nakai, T. Vreven, J. Montgomery, J. E. Peralta, F. Ogliaro, M. Bearpark, J. J. Heyd, E. Brothers, K. N. Kudin, V. N. Staroverov, R. Kobayashi, J. Normand, K. Raghavachari, A. Rendell, J. C. Burant, S. S. Iyengar, J. Tomasi, M. Cossi, N. Rega, J. M. Millam, M. Klene, J. E. Knox, J. B. Cross, V. Bakken, C. Adamo, J. Jaramillo, R. Gomperts, R. E. Stratmann, O. Yazyev, A. J. Austin, R. Cammi, C. Pomelli, J. W. Ochterski, R. L. Martin, K. Morokuma, V. G. Zakrzewski, G. A. Voth, P. Salvador, J. J. Dannenberg, S. Dapprich, A. D. Daniels, O. Farkas, J. B. Foresman, J. V. Ortiz, J. Cioslowski, D. J. Fox, Gaussian, Inc., Pittsburgh, PA, **2009**.
 [64] A. D. Becke, *J. Chem. Phys.* **1993**, *98*, 5648–5652.
 [65] C. Møller, M. S. Plesset, *Phys. Rev.* **1934**, *46*, 618–622.
 [66] T. Schwabe, S. Grimme, *Phys. Chem. Chem. Phys.* **2007**, *9*, 3397–3406.
 [67] J. P. Perdew, K. Burke, Y. Wang, *Phys. Rev. B* **1996**, *54*, 16533–16539.
 [68] A. Becke, *Phys. Rev. A* **1988**, *38*, 3098–3100.
 [69] J. Tomasi, B. Mennucci, R. Cammi, *Chem. Rev.* **2005**, *105*, 2999–3093.
 [70] S. Grimme, *J. Comput. Chem.* **2004**, *25*, 1463–1473.
 [71] J. Kapitán, V. Baumruk, V. Kopecký, Jr., P. Bouř, *J. Am. Chem. Soc.* **2006**, *128*, 2438–2443.
 [72] J. Kapitán, V. Baumruk, V. Kopecký, Jr., R. Pohl, P. Bouř, *J. Am. Chem. Soc.* **2006**, *128*, 13451–13462.
 [73] C. Altona, M. Sundaralingam, *J. Am. Chem. Soc.* **1972**, *94*, 8205–8212.
 [74] S. J. Han, Y. K. Kang, *J. Mol. Struct.: THEOCHEM* **1996**, *369*, 157–165.
 [75] E. E. Zvereva, A. R. Shagidullin, S. A. Katsyuba, *J. Phys. Chem. A* **2011**, *115*, 63–69.
 [76] M. Reiher, V. Liégeois, K. Ruud, *J. Phys. Chem. A* **2005**, *109*, 7567–7574.
 [77] J. Haesler, I. Schindelholz, E. Riguet, C. G. Bochet, W. Hug, *Nature* **2007**, *446*, 526–529.

- [78] S. Yamamoto, H. Watarai, P. Bouř, *ChemPhysChem* **2011**, *12*, 1509–1518.
- [79] T. Yanai, D. Tew, N. C. Handy, *Chem. Phys. Lett.* **2004**, *393*, 51–57.
- [80] O. Julínek, M. Krupička, W. Lindner, M. Urbanová, *Phys. Chem. Chem. Phys.* **2010**, *12*, 11487–11497.
- [81] D. A. Case, I. T. E. Cheatham, T. Darden, H. Gohlke, R. Luo, J. K. M. Merz, A. Onufriev, C. Simmerling, B. Wang, R. Woods, *J. Comput. Chem.* **2005**, *26*, 1668–1688.
- [82] Z. Vokáčová, J. Šponer, J. E. Šponer, V. Sychrovský, *J. Phys. Chem. B* **2007**, *111*, 10813–10824.
- [83] A. P. Mendham, T. J. Dines, M. J. Snowden, B. Z. Chowdhry, *J. Raman Spectrosc.* **2009**, *40*, 1478–1497.
- [84] E. Sletten, *J. Am. Chem. Soc.* **1970**, *92*, 172–177.
- [85] G. D. Grant, A. L. Hunt, P. J. Milne, H. M. Roos, J. A. Joubert, *J. Chem. Crystallogr.* **1999**, *29*, 435–447.
- [86] V. Andrushchenko, P. Matějka, D. T. Anderson, J. Kaminský, J. Horníček, L. O. Paulson, P. Bouř, *J. Phys. Chem. A* **2009**, *113*, 9727–9736.
- [87] V. Parchaňský, P. Matějka, B. Dolenský, M. Havlík, P. Bouř, *J. Mol. Struct.* **2009**, *934*, 117–122.
- [88] M. J. O. Anteunis, *Bull. Soc. Chim. Belg.* **1978**, *87*, 627–650.
- [89] M. Buděšínský, J. Symerský, J. Ječný, J. van Hecke, N. Hosten, M. J. O. Anteunis, F. Borremans, *Int. J. Pept. Protein Res.* **1992**, *39*, 123–130.
- [90] M. Buděšínský, I. Čísařová, J. Podlaha, F. Borremans, J. C. Martins, M. Waroquier, E. Pauwels, *Acta Crystallogr. Sect. B* **2010**, *66*, 662–677.
- [91] R. Huang, L. Wu, D. McElheny, P. Bouř, A. Roy, T. A. Keiderling, *J. Phys. Chem. B* **2009**, *113*, 5661–5674.
- [92] P. Bouř, T. A. Keiderling, *J. Phys. Chem. B* **2005**, *109*, 23687–23697.
- [93] W. Y. Yang, J. W. Pitera, W. C. Swope, M. Gruebele, *J. Mol. Biol.* **2004**, *336*, 241–251.
- [94] S. J. Russell, T. Blandl, N. J. Skelton, A. G. Cochran, *J. Am. Chem. Soc.* **2003**, *125*, 388–395.
- [95] J. Šebek, Z. Kejik, P. Bouř, *J. Phys. Chem. A* **2006**, *110*, 4702–4711.
- [96] T. A. Keiderling, J. Kubelka, J. Hilario in *Vibrational Circular Dichroism of Biopolymers: Summary of Methods and Applications* (Eds.: M. Braiman, V. Gregoriou), CRC, Boca Raton, **2006**, pp. 253–324.
- [97] J. Kubelka, T. A. Keiderling, *J. Phys. Chem. A* **2001**, *105*, 10922–10928.
- [98] K. Huvaere, L. H. Skibsted, *J. Am. Chem. Soc.* **2009**, *131*, 8049–8060.
- [99] C. N. Tam, P. Bouř, J. Eckert, F. R. Trouw, *J. Phys. Chem. A* **1997**, *101*, 5877–5884.
- [100] J. M. Schmidt, M. Blümel, F. Löhr, H. Rüterjans, *J. Biomol. NMR* **1999**, *14*, 1–12.
- [101] J. M. Schmidt, *J. Biomol. NMR* **2007**, *37*, 287–301.

Received: March 8, 2012

Revised: April 27, 2012

Published online on June 15, 2012

Supporting Information

© Copyright Wiley-VCH Verlag GmbH & Co. KGaA, 69451 Weinheim, 2012

Three Types of Induced Tryptophan Optical Activity Compared in Model Dipeptides: Theory and Experiment

Jana Hudecová,^{*,[a, b]} Jan Horníček,^[a] Miloš Buděšínský,^[a] Jaroslav Šebestík,^[a] Martin Šafařík,^[a] Ge Zhang,^[c] Timothy A. Keiderling,^[c] and Petr Bouř^{*,[a]}

cphc_201200201_sm_miscellaneous_information.pdf

Table S1. Boltzmann weights (%) of the most populated conformers of c-(L-Trp-Gly) based on electronic energies calculated with different functionals, for the CPCM(DMSO) solvent model. The A-F conformers are defined in **Figure 2** in the main text.

	A	A'	B	B'	C	D	E	F
B3LYP/6-311++G**	35	32	11	0	7	11	1	3
BPW91/6-311++G**	39	34	11	0	5	7	1	3
B3PW91/6-311++G**	31	32	9	6	8	11	1	2
B3LYP-D/6-311++G**	1	0	0	0	23	76	0	0
BPW91-D/6-311++G**	1	1	1	0	22	75	0	0
B3PW91-D/6-311++G**	0	0	0	0	21	79	0	0
MP2/6-31++G**	0	0	0	0	33	67	0	0
MPW2PLYP/6-31++G**	7	7	4	2	29	50	0	1

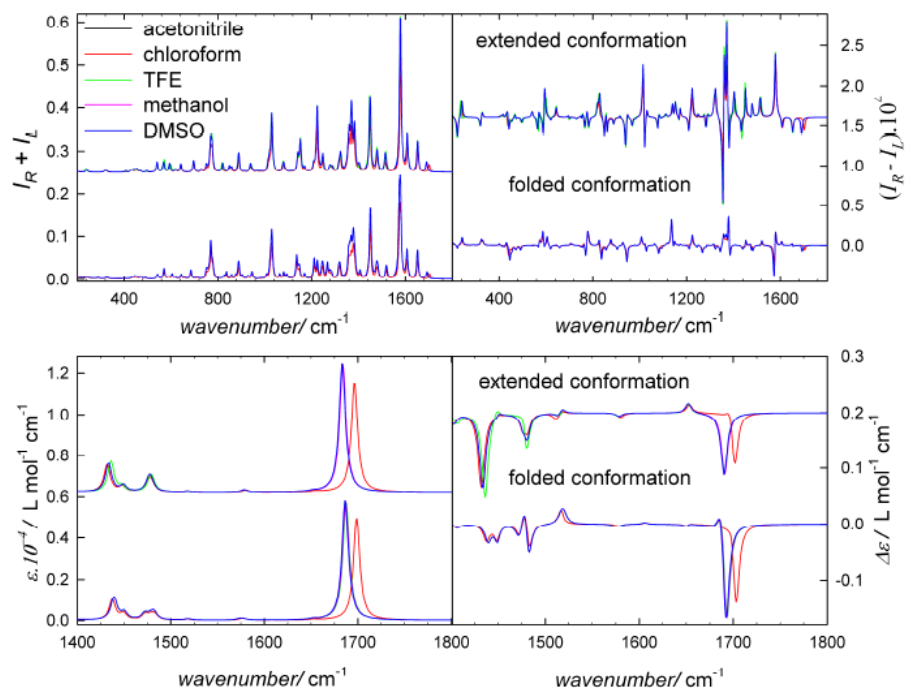


Figure S1. Raman, ROA, IR and VCD spectra computed (B3LYP/CPCM/6-311++G**) for different solvents (some of them are indistinguishable at this scale) for two conformations of c-(L-Trp-L-Trp): extended (AA, up in each panel) conformation and folded conformation (AD, down), see **Table 2**.

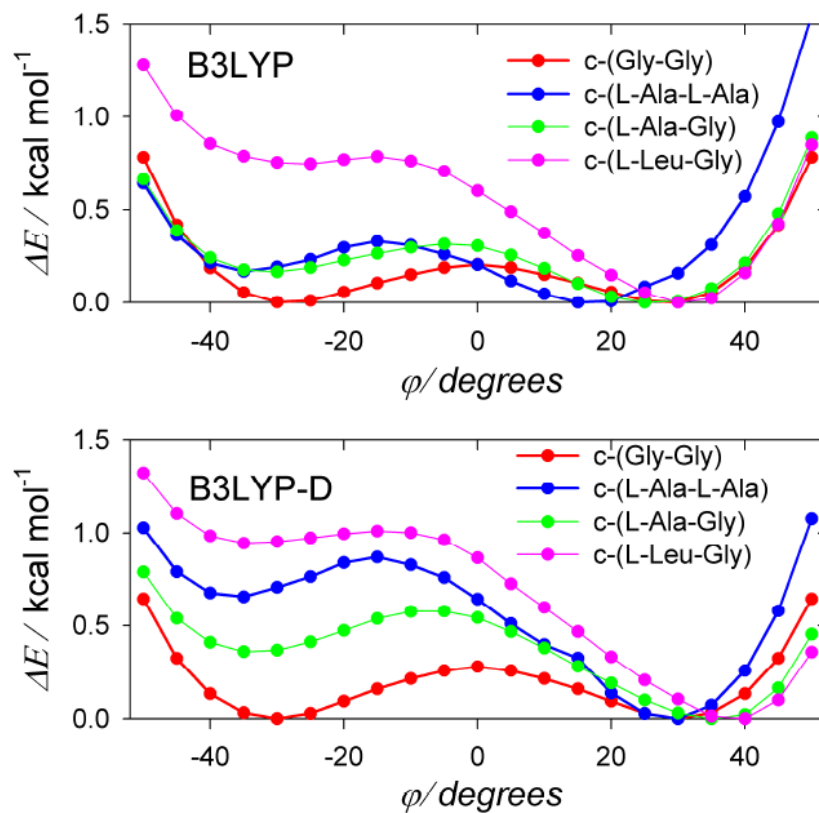


Figure S2. Calculated dependence of the relative electronic energies (B3LYP or B3LYP-D/CPCM(DMSO)/6-311++G**) on the ϕ -angle in the c-(Gly-Gly), c-(L-Ala-L-Ala), c-(L-Ala-Gly), and c-(L-Leu-Gly) (lowest-energy conformation with $\chi_1 \sim -60^\circ$, $\chi_2 \sim 180^\circ$) peptides.

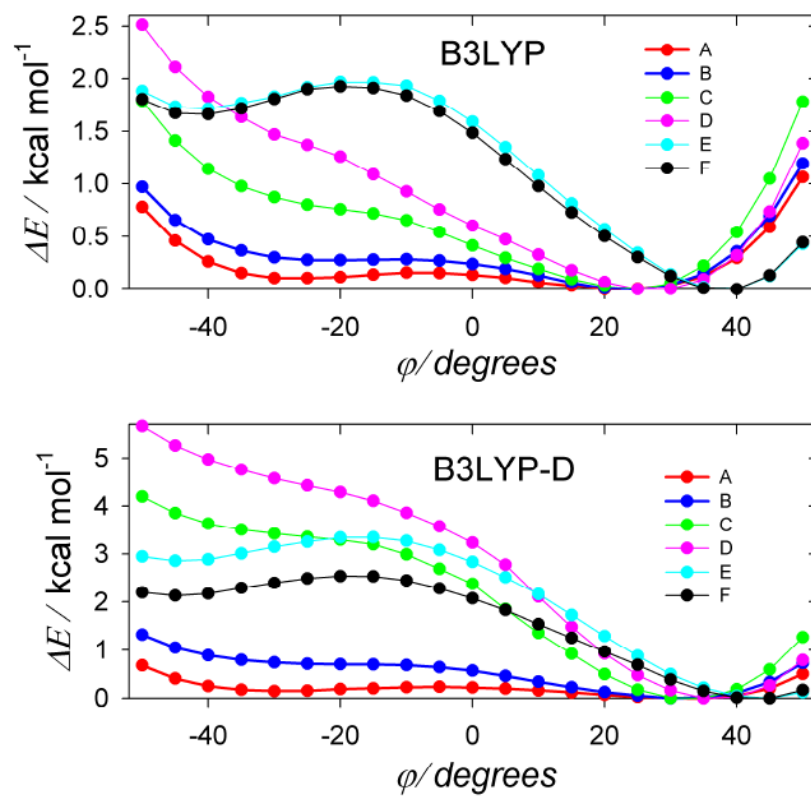


Figure S3. Calculated 1D scans (B3LYP or B3LYP-D/CPCM(DMSO)/ 6-311++G**, see Figure S2) for six conformations of c-(L-Trp-Gly) defined in Figure 3, Table 2 and 3.

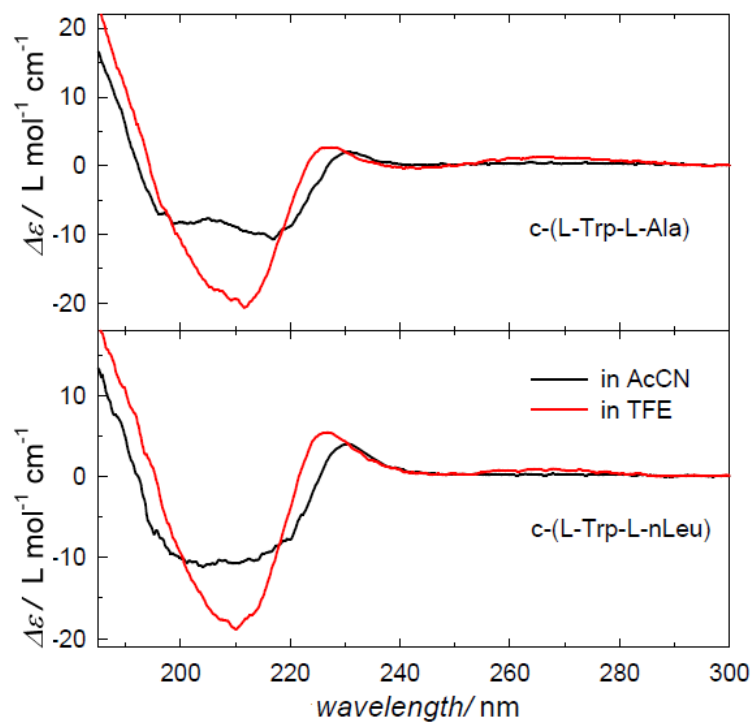


Figure S4. Experimental ECD spectra of c-(L-Trp-L-Ala) and c-(L-Trp-L-nLeu) measured in AcCN (black) and TFE (red).

A4. Publication [IV]

Brichtová, E. ; Hudecová, J.; Vršková, N.; Šebestík, J.; Bouř, P.; Wu T. Binding of Lanthanide Complexes to Histidine-Containing Peptides Inspected by Raman Optical Activity Spectroscopy. **2018** accepted to *Chemistry - A European Journal*

Lanthanide Probe

Binding of Lanthanide Complexes to Histidine-Containing Peptides Probed by Raman Optical Activity Spectroscopy

Eva Brichtová,^[a, b] Jana Hudecová,^[a, c] Nikola Vršková,^[a] Jaroslav Šebestík,^[a] Petr Bour,^[a, b] and Tao Wu^{*[a]}

Abstract: Lanthanide complexes are used as convenient spectroscopic probes for many biomolecules. Their binding to proteins is believed to be enhanced by the presence of histidine, but the strength of the interaction significantly varies across different systems. To understand the role of peptide length and sequence, short histidine-containing peptides have been synthesized (His-Gly, His-Gly-Gly, His-Gly-Gly-Gly, Gly-His, Gly-His-Gly, His-His, and Gly-Gly-His) and circularly polarized luminescence (CPL) induced at the [Eu(dpa)₃]³⁻ complex has been measured by means of a Raman optical activity (ROA) spectrometer. The obtained

data indicate relatively weak binding of the histidine residue to the complex, with a strong participation of other parts of the peptide. Longer peptides, low pH, and a histidine residue close to the *N*-peptide terminus favor the binding. The binding strengths are approximately proportional to the CPL intensity and roughly correlate with predictions based on molecular dynamics (MD) simulations. The specificity of lanthanide binding to the peptide structure and its intense luminescence and high optical activity make the ROA/CPL technique suitable for probing secondary and tertiary structures of peptides and proteins.

Introduction

Luminescent labels of living cell components attract attention because of many applications in analytical biochemistry and imaging.^[1] Many of them are based on europium and other lanthanides as these metals exhibit extremely rich luminescence spectra, which are very dependent on the environment.^[1a, 2] Circularly polarized luminescence (CPL), that is, different emission of left- and right-circularly polarized light, is even more sensitive to the probed structure than the total luminescence (TL) alone.^[3]

Lanthanide compounds are thus used to label protein molecules to study their structure, function, and dynamics.^[4] Quite often, however, the actual mode of the lanthanide–protein binding is not known, or the interaction is not sufficiently specific. Combinations of lanthanide tags and proteins have therefore been investigated by X-ray crystallography, fluorescence spectroscopy, and NMR spectrometry.^[5] Lanthanide CPL can

also be used in this context, whereby the chirality in the lanthanide radiation is induced by the environment.^[6]

In the present study, we focus on interaction with the histidine residue, which is believed to exhibit exceptional affinity towards heavy metals. Raman optical activity (ROA) spectroscopy has been used to detect TL and CPL. ROA is normally exploited to measure differences in Raman scattering of right- and left-circularly polarized light caused by vibrational transitions.^[7] Because the luminescence bands of europium are as narrow as the vibrational bands and appear within the operational range of ROA spectrometers, CPL can be measured as well. In addition, the strong laser radiation source makes it possible to observe quite weak signals, which would be undetectable on more common CPL spectrometers.^[8] For example, the strongest Eu^{III} signal that can be measured on our ROA spectrometer is attributable to the ³D₀→⁷F₁ transition^[9, 9] and appears as a (“false”) Raman band shifted by around 1700–2100 cm⁻¹ from the 532 nm laser excitation.

Recently, we showed that CPL spectra of the complex [Eu(dpa)₃]³⁻ offer highly specific insight into the amino acid content of aqueous solutions.^[3c] Similar CPL induction has also been observed for a larger protein.^[3c] Histidine residues gave rise to a particularly strong signal, most probably because of ion pairing, π–π stacking, and electrostatic interactions between the histidine side chain and the dpa ligand. The dpa complex itself exists in two chiral forms (traditionally referred to as “Λ” and “Δ”), which are normally present in equal amounts. Perturbation of the Λ⇌Δ equilibrium in the presence of a chiral component has been suggested as the primary mechanism of chirality induction, although the presence of more than two spectral components indicates other contribu-

[a] E. Brichtová, J. Hudecová, N. Vršková, Dr. J. Šebestík, Prof. P. Bour, Dr. T. Wu
Institute of Organic Chemistry and Biochemistry
Academy of Sciences Flemingovo náměstí 2, 16610 Prague (Czech Republic)
E-mail: wu@uochb.cas.cz

[b] E. Brichtová, Prof. P. Bour
Department of Analytical Chemistry
University of Chemistry and Technology
Technická 5, 16628 Prague (Czech Republic)

[c] J. Hudecová
Faculty of Mathematics and Physics, Institute of Physics
Charles University, Ke Karlovu 5, 12116 Prague (Czech Republic)

Supporting information and the ORCID number(s) for the author(s) of this article can be found under <https://doi.org/10.1002/chem.201800840>.

tions as well. Other mechanisms of chiral CPL discrimination may include selective luminescence quenching or enhancement, especially for weakly bound complexes.^[10]

To better understand the binding mode and the role therein of the main peptide chain, we have synthesized a series of seven histidine-containing model peptides (Figure 1). As a result, we have identified some general trends that provide insight into the interactions between the peptides and the lanthanide probe, which can be at least partially rationalized by molecular dynamics (MD) simulations. In particular, we have correlated the CPL intensity with the binding strength, and have investigated factors affecting the chirality recognition and induction.

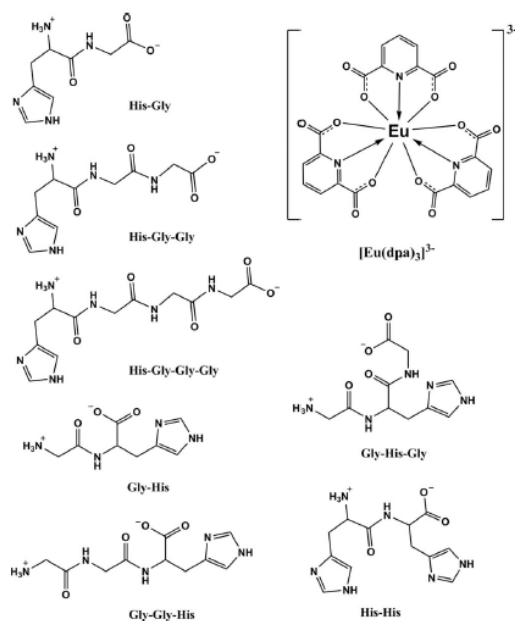


Figure 1. Structures of the $[\text{Eu}(\text{dpa})_3]^{3-}$ complex and the investigated model peptides.

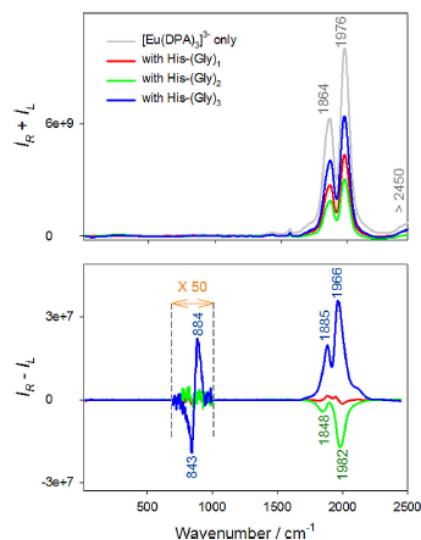


Figure 2. TL and CPL spectra of $[\text{Eu}(\text{dpa})_3]^{3-}$ (4 mM) chelated with $\text{His}-(\text{Gly})_n$ ($n = 1, 2,$ and $3, 20 \text{ mM}, \text{pH } 4$).

Table 1. Assignment of observed europium luminescence bands in solutions of $[\text{Eu}(\text{dpa})_3]^{3-}$ and $\text{His}-(\text{Gly})_n$, Raman shifts from the 532 nm laser frequency (δ , in cm^{-1}), and corresponding wavelengths (λ , in nm).

Transition	$[\text{Eu}(\text{dpa})_3]^{3-}$		with His-Gly		with His-(Gly) ₂		with His-(Gly) ₃	
	δ	λ	δ	λ	δ	λ	δ	λ
${}^5\text{D}_0 \rightarrow {}^7\text{F}_2$	>2450	615	>2450	615	>2450	615	2400	610
							2263	605
${}^5\text{D}_0 \rightarrow {}^7\text{F}_1$	1976	594	2118	600				
	1864	591	1999	595	1982	595		
			1976	594	1976	594	1976	594
			1950	594			1966	594
			1885	591			1887	591
			1866	591	1866	591	1866	591
${}^5\text{D}_1 \rightarrow {}^7\text{F}_2$			887	558			884	558
			846	557			843	557

Results and Discussion

Effect of peptide length for His-(Gly)_n ($n = 1, 2, 3$)

The TL and CPL spectra for this series of peptides when mixed with $\text{Na}_3[\text{Eu}(\text{dpa})_3]$ solution at pH 4 are plotted in Figure 2. They are dominated by the strong $\text{Eu}^{3+} {}^5\text{D}_0 \rightarrow {}^7\text{F}_1$ luminescence band^[13c,11] at around 1900 cm^{-1} . A weaker signal at around 850 cm^{-1} can be ascribed to the ${}^5\text{D}_1 \rightarrow {}^7\text{F}_2$ transition^[11] and is only visible in the differential (CPL) spectrum. On the other hand, invisible in CPL, a TL signal is apparent at the extremity of the spectrometer operational range, close to 2450 cm^{-1} , attributable to the ${}^5\text{D}_0 \rightarrow {}^7\text{F}_2$ transition. The center band frequencies are summarized in Table 1. Vibrational

Raman and ROA intensities are much weaker than the luminescence and almost undetectable under these conditions.

Addition of the peptides leads to a decrease of around 30–70% in the total luminescence compared to that of the pure $\text{Na}_3[\text{Eu}(\text{dpa})_3]$ complex. For CPL, the differences are even more dramatic. Only the His-Gly CPL is rather weak at around 1900 cm^{-1} and hidden in noise at 850 cm^{-1} . Note that this may mean that the interaction with the complex is weak and/or does not lead to chiral discrimination. His-(Gly)₂ provides a much stronger negative CPL band at 1982 cm^{-1} , a weaker one at 1848 cm^{-1} , and a very weak signal at around 850 cm^{-1} . Judging from the CPL intensities, the interaction with the complex is strongest for the longest His-(Gly)₃ peptide, providing

the strongest signal in both the ${}^5D_0 \rightarrow {}^7F_1$ and ${}^5D_1 \rightarrow {}^7F_2$ regions. However, the ${}^5D_0 \rightarrow {}^7F_1$ bands have nearly opposite sign compared to those of His-(Gly)₂. Although the CPL shapes for His-(Gly)₂ and His-(Gly)₃ are not exact "mirror images", as a first approximation we may interpret the results in terms of perturbation of the $\Lambda \rightleftharpoons \Delta$ complex enantiomeric equilibrium by the chiral peptide matrices.^[12] For His-(Gly)₃, the absolute CPL intensity is greater than that for His-(Gly)₂, as is the ratio of the polarized and total luminescences ($CID = 5.0 \times 10^{-3}$ at 1976 cm^{-1}). CID values for other systems at selected wavenumbers are listed in Table 2.

Peptide	1976 cm^{-1}	CID	1864 cm^{-1}
His-Gly	-9.1×10^{-5}		2.3×10^{-4}
His-(Gly) ₂	-4.1×10^{-3}		-1.2×10^{-3}
His-(Gly) ₃	5.0×10^{-3}		3.2×10^{-3}
Gly-His	1.6×10^{-3}		7.6×10^{-4}
Gly-His-Gly	2.7×10^{-3}		1.3×10^{-3}
Gly-Gly-His	2.2×10^{-3}		8.8×10^{-4}
His-His	6.3×10^{-3}		3.8×10^{-3}

Note that, using the ROA terminology, we measure the ratio as the circular intensity difference, $CID = (I_R - I_L)/(I_R + I_L)$, where I_R and I_L are the intensities of the right and left circularly polarized light, respectively. In CPL spectroscopy, the dissymmetry factor is often used instead, $g = 2(I_L - I_R)/(I_L + I_R)$, that is, $CID = -g/2$.

To summarize, the longer peptide binds the europium complex much better than the shorter ones, that is, parts other than the histidine residues are also important for the binding, and the chirality discrimination and induction is determined by the peptide as a whole, not only by the L-histidine moiety.

Position of the histidine in the peptide chain: Gly-His, Gly-His-Gly, Gly-Gly-His, and His-His

Interestingly, few prominent spectral differences are apparent within this series of peptides (Figure 3). As before, the total luminescence of the complex is partially quenched, but only one-sign CPL in the region $1700\text{--}2000 \text{ cm}^{-1}$ appears upon mixing with the peptides. Nevertheless, the spectra do exhibit significant differences, allowing discrimination between different peptide species. His-His clearly provides the strongest CPL signal and a large CID (6.3×10^{-3} , Table 2), which confirms the importance of the histidine residue for binding. The other three peptides of this series provide rather weak CPL, although with comparable CID ratios (CID s as functions of the wavenumber over a broader range are plotted in Figure S1).

Compared to His-(Gly)₂ from the previous series, placing the histidine residue in the middle (Gly-His-Gly) or at the C-terminus (Gly-Gly-His) induces the opposite CPL sign for the ${}^5D_0 \rightarrow {}^7F_1$ signal. The latter two peptides most probably stabilize the

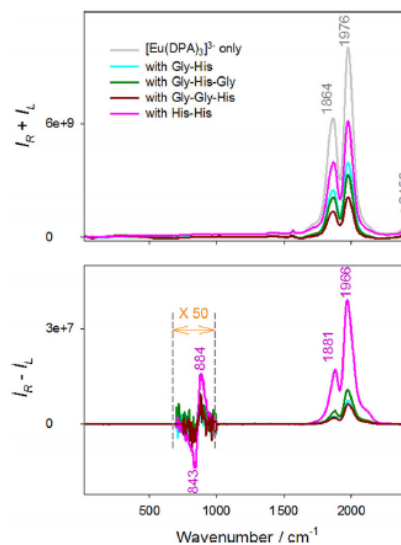


Figure 3. TL and CPL spectra of $[\text{Eu}(\text{dpa})_3]^{3-}$ (4 mM) chelated with Gly-His, Gly-His-Gly, Gly-Gly-His, and His-His (each 20 mM, pH 4).

opposite enantiomer of the complex, but the binding strengths, as judged from the absolute CID ratios, are weaker. As for the CPL, in the sequence His-Gly-Gly, Gly-His-Gly, and Gly-Gly-His, the total luminescence intensity gradually decreases. We can speculate that in His-(Gly)₂ the NH_3^+ charge strengthens the binding potency of histidine, whereas in Gly-His-Gly and Gly-Gly-His the C-terminal COO^- group weakens it. This concept is seemingly not applicable for the His-Gly and Gly-His pairs, both providing weak CPL, although this may be caused by a strong, but not chirality-sensitive interaction. Other factors, such as dissociation equilibria and van der Waals interactions, are also likely to contribute to the electrostatic effects. One also has to realize that "binding" is in all cases very weak and the resultant assembly may not have a rigid geometry.^[3b] Strong complexation of europium with a product of fixed geometry would have led to much larger CID values than those observed in the present study, up to the order of one.^[8a]

CPL of the ${}^5D_1 \rightarrow {}^7F_2$ transition (around 850 cm^{-1}) is consistent with the results for the main ${}^5D_0 \rightarrow {}^7F_1$ bands in that the sign pattern does not change in the second series of peptides, and the $-/+$ couplet shape (if viewed from lower to higher wavenumbers) always accompanies the positive ${}^5D_0 \rightarrow {}^7F_1$ signal.

pH dependence of the spectra

As has been previously shown for individual amino acids, the predominantly positive charge of the peptides at pH 4 favors the interaction with the complex.^[3c] Indeed, the TL and CPL spectra induced by His-Gly, His-(Gly)₂, and His-(Gly)₃ at three pH values (4, 7, and 10), as plotted in Figure S2, document that the interaction is significantly weakened at higher pH.

More detailed inspection reveals further differences, which may allow better understanding of the interaction with the complex. The CPL intensity of His-Gly, which is already weak at pH 4, further decreases to about 20% (at 1885 cm⁻¹) at pH 7, and changes sign at pH 10. This confirms that the electrostatic interaction itself is not solely responsible for the chirality induction. For the (relatively) strong binders His-(Gly)₂ and His-(Gly)₃, the situation is simpler in that the CPL more or less vanishes at higher pH. Moreover, at the two higher pH values, no CPL is observed for the ³D₀→⁷F₂ (>2200 cm⁻¹) and ³D₁→⁷F₂ (≈850 cm⁻¹) transitions. The total luminescence remaining about constant at pH 7 and 10, but decreasing by about 30–60% at pH 4, is more consistently observed within the three peptides than the CPL.

We verified that, under the experimental conditions employed (pH > 4), the luminescence of the pure [Eu(dpa)₃]³⁻ complex does not change. However, slight dissociation may still occur at around pH 4,¹³ which could also contribute to the observed changes, such as the decrease in TL at low pH (Figure S2).

Titration curves

So far, spectra obtained at 5:1 peptide/complex ratios have been reported, around which signals are maximized. TL and CPL intensities obtained for different ratios of the complex and His-(Gly)₂ and His-His peptides, as plotted in Figure S3, confirm that the interaction is rather weak, because the titrations cause only gradual changes in the spectra. As an alternative view, maximum Raman, ROA, and CID intensities at 1976 cm⁻¹ are plotted in Figure 4. It can be seen that the spectral intensities do not stabilize at higher peptide concentrations, that is to say, the dependences differ from “classical” two-system titration curves. Instead, the Raman intensities almost exponentially vanish with increasing peptide concentrations, while the ROA/CID values exhibit maxima at optimal peptide–complex

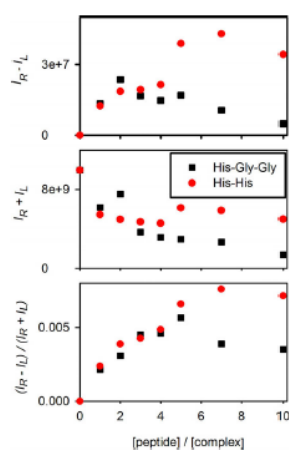


Figure 4. Dependences of the maximal Raman, ROA, and CID signals (at 1976 cm⁻¹) on the peptide/complex molar ratio.

ratios of around 4–7. One may speculate that more peptide molecules become bonded to the complex; however, the actual cause of the concentration dependence will likely be quite complicated, including luminescence quenching by the peptide^{2b1} and possible binding and decomposition of the complex by peptide impurities (mostly trifluoroacetic acid from the synthesis) at very high peptide concentrations.

Theoretical analysis

In spite of the complexity of the lanthanide complex–peptide interactions, molecular dynamics simulation can provide at least a qualitative understanding of the observed data. Calculated dependences of the free energy on the [Eu(dpa)₃]³⁻–His(Gly)_n distance (between Eu and ⁴C of His) are plotted in Figure 5. Free-energy profiles for the other peptides at other

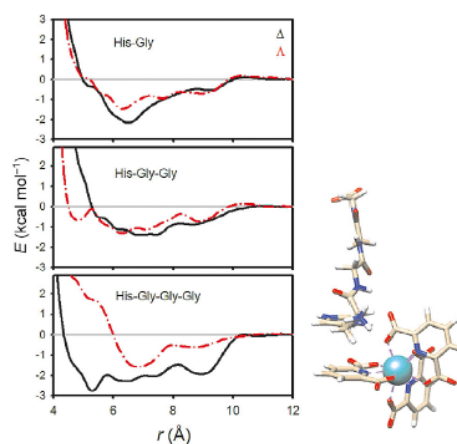


Figure 5. Dependence of the calculated free energy on the Eu–His(Gly)_n peptide distance corresponding to pH ≈ 4, and example of an energy-minimized structure for His-(Gly)₃.

pH values were fairly similar (Figures S4 and S5). The stabilization energies are rather low (ca. 2 kcal mol⁻¹), corresponding to the experimental observations, in particular the nonspecific titration curves discussed above. For His-Gly and His-(Gly)₂, no favoring of the Δ or Λ enantiomer within computational accuracy is apparent. For His-(Gly)₃, however, the Δ binding seems to be more energetically favorable than that of the Λ form. Thus, the simulation does not readily reproduce the chirality inversion observed for His-(Gly)₂ and His-(Gly)₃, but does corroborate the stronger binding observed for His-(Gly)₃.

In all cases, however, the energy “well” is quite broad and shallow. Inspection of geometries obtained close to the energy minima (such as the structure in Figure 5) suggests a significant role of the histidine charge and perhaps a π–π interaction of the histidine ring with the ligand of the complex. In some MD snapshots, interaction of the glycine residues with the complex is also apparent, which is consistent with the relatively high CPL observed for the longest His-(Gly)₃ peptide.

Binding strengths, as defined on the basis of the MD simulations, are compared for more peptides and pH values in Figure 6. The environmental pH (2, 4, 7, and 10) was simulated by different charges on the peptides (+2, +1, 0, and -1, re-

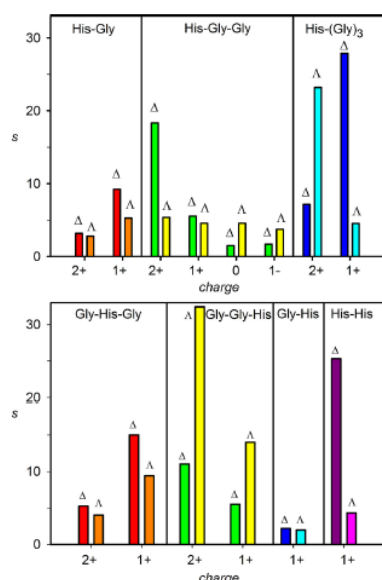


Figure 6. Calculated binding strengths of the peptides s , obtained as the ratio (N_b/N_f) of bonded and free complex molecules in the simulation box.

spectively). At around pH 4 (charge +1), for example, the computation predicts strong binding for His-(Gly)₃ and His-His, nicely corroborating the data in Figures 2 and 3. In addition, the Δ form of the complex is most stabilized, which again is most probably reflected in the same CPL sign.

As noted above, the CPL chirality inversion observed for His-(Gly)₂ and His-(Gly)₃ is not unambiguously supported theoretically; nevertheless, it can be seen that at pH 4 the Δ and Λ forms of His-(Gly)₂ are predicted to be adopted with about the same probability, whereas at higher pH the Λ form is preferred. The inversion can thus be at least partially explained by a residual presence of the neutral species in the sample. However, the theoretical preference for the Λ enantiomer of Gly-Gly-His is inconsistent with the observations. Thus, the simulations at the present level do not seem to be sufficiently reliable to be applied for chirality determination. Nevertheless, they adequately explain many aspects of the binding, including some general trends, and at least suggest that the quite attractive idea of determination of the absolute configuration of a complex through a combination of theory and experiment is possible.

Conclusions

We have synthesized a series of histidine-containing peptides and have monitored their interactions with a racemic Eu^{III} complex through circularly polarized luminescence measurements. The results show that both the length of the peptides and the histidine position therein profoundly affect the binding modes. The acquired data could be very well rationalized by molecular dynamics simulations, although these were not sufficiently accurate to unambiguously provide the absolute configurations of the preferred complex forms. The data and simulation indicate that the interaction of the complex with the peptides is rather weak and non-site-specific in terms of interaction energies and product geometries, although the resultant luminescence and CPL patterns are still quite characteristic for individual peptides. This is promising for future design of similar "smart" probes of peptide, protein, and other biomolecular structures.

Experimental Section

Synthesis: Na₃[Eu(dpa)₃] (dpa = dipicolinate = 2,6-pyridinedicarboxylate; Figure 1) was obtained by the reaction of europium(III) carbonate and pyridine-2,6-dicarboxylic acid (1:3 molar ratio) in water; pH 7 was adjusted with 1 M sodium carbonate solution.^[34] The peptides were synthesized by the Fmoc/tBu strategy on 2-chlorotrityl resin. The volume to mass ratio of the agent solution to the 2-chlorotrityl resin was 10 mL g⁻¹. The synthesized peptides were then deprotected with a 20% solution of 2,2,2-trifluoroethanol in CH₂Cl₂; the trityl group protecting the histidine side chain was cleaved with a mixture of TFA, triisopropylsilane (TIS), and water (9.5:2.5:2.5, v/v). The volatiles were then removed by evaporation, and the residual solid was dissolved in water. Insoluble by-products were removed by filtration. Water was evaporated and the peptide products were recovered by a combination of vacuum evaporation and lyophilization. The products were characterized by TLC on silica-gel-coated aluminum plates, whereby the compounds were visualized by ninhydrin spraying. ¹H and ¹³C NMR spectra were measured at ambient temperature from solutions in 5 mm diameter NMR tubes (see the Supporting Information for further details).

CPL measurement: Back-scattering Raman and scattered circular polarization (SCP) ROA spectra (dominated by Eu TL and CPL) were acquired on a BioTools ROA spectrometer operating with laser excitation at 532 nm and a resolution of 7 cm⁻¹. For the lanthanide CPL measurement, the laser power at the sample was 150–400 mW, and accumulation times were 1 h (for solutions at pH 4), 8 h (pH 7), or 12 h (pH 10). pH was adjusted with 0.1 M HCl or NaOH. Concentrations were 20 mM for peptides and 4 mM for the [Eu(dpa)₃]³⁻ complex. In the presented spectra, the intensities were normalized to the 1650 cm⁻¹ band, and a broad luminescence background attributable to sample impurities was subtracted from the Raman signal.

Computations: The initial geometry of the [Eu(dpa)₃]³⁻ complex was obtained using the Gaussian 09 program,^[44] adopting the B3LYP functional and the 6-31G(d,p) basis set (MWB28 pseudopotential and basis set for Eu). By titration, we found that the Na₃[Eu(dpa)₃] CPL spectra do not change within the interval pH 4–12. We therefore suppose that the charge (-3) of the complex is not changed in our experiments. The solvent was modeled by the conductor-like polarizable continuum solvent model (CPCM).^[15]

The interactions of all seven peptides (Figure 1) with the Λ and Δ forms of the complex in aqueous solution were investigated using Amber 14¹⁶ MD software. To model mild acidic conditions (pH \approx 4, corresponding to most experiments), the histidine aromatic ring and the amine group were protonated ($-\text{NH}_3^+$) and the carboxyl group was deprotonated ($-\text{COO}^-$). For lower pH (< 2), the carboxyl group ($-\text{COOH}$) was also protonated, and for His-(Gly)₂ the neutral and basic forms were considered as zwitterionic and deprotonated peptides. For the other peptides, only structures corresponding to acidic conditions (pH < 2 and pH \approx 4, with peptide charges of +2 and +1, respectively) were investigated. The peptides were inserted into a cubic (30 Å)³ box containing 880 water molecules and one [Eu(dpa)₃]³⁻ ion, initially separated from the peptide by about 12 Å. Separate simulations were performed for the Λ and Δ forms of the complex. MD simulations were run for NVT ensembles using a 1 fs integration step, a temperature of 300 K, and GAFF¹⁷ (dpa ligands), Amber 14SB¹⁸ (His and Gly), or TIP3P⁶¹⁹ (water) force fields.

After an equilibration (1 ns), constrained MD simulations were run for 8 ns. A harmonic penalty function (restraint constant of 4 kcal Å⁻² mol⁻¹) was applied to the distance (r) between the europium atom of the complex and C^α of histidine; the distance was changed from 12 to 9 Å in 1 Å increments and from 9 and 4 Å in 0.5 Å increments. From individual distance distributions, the potential of the mean force $F(r)$ was calculated by the weighted histogram analysis method (WHAM)²⁰ using the Amber 14 scripts.

The simulations indicated rather weak peptide–complex associates with flexible geometries. Therefore, to better evaluate effective relative binding strengths (s), equilibrium ratios of the numbers of bonded (N_b , $r < 10$ Å) and free (N_f , $r > 10$ Å) europium complexes for each box were calculated as $s = N_b/N_f = \int_0^{10} \exp(-F/kT) r^2 dr / \int_{10}^{\infty} \exp(-F/kT) r^2 dr$.

Acknowledgements

This work was supported by the Czech Science Foundation (16-08764Y and 18-05770S), the Ministry of Education (LTC17012/CA15214), and CESNET (LM2015042) and CERIT (LM2015085) computational resources.

Conflict of interest

The authors declare no conflict of interest.

Keywords: biomolecular probe · chemical imaging · circularly polarized luminescence · histidine · lanthanide-binding peptide · molecular dynamics · Raman optical activity · rare earths

- [1] a) J. C. G. Bünzli, *J. Lumin.* **2016**, *170*, 866–878; b) S. M. J. van Duijnhoven, M. S. Robillard, S. Langereis, H. Grul, *Contrast Media Mol. Imaging* **2015**, *10*, 282–308; c) A. S. Klymchenko, *Acc. Chem. Res.* **2017**, *50*, 366–375; d) G. Kramer-Marek, M. R. Longmire, P. L. Choyke, H. Kobayashi, *Curr. Med. Chem.* **2012**, *19*, 4759–4766; e) J. C. G. Bünzli, *Chem. Rev.* **2010**, *110*, 2729–2755; f) U. Resch-Genger, M. Grabolle, S. Cavaliere-Jaricot, R. Nitschke, T. Nann, *Nat. Methods* **2008**, *5*, 763–775; g) M. C. Hefern, L. M. Matosziuk, T. J. Meade, *Chem. Rev.* **2014**, *114*, 4496–4539.
- [2] a) M. Sy, A. Nonat, N. Hildebrandt, L. J. Charbonniere, *Chem. Commun.* **2016**, *52*, 5080–5095; b) S. Shuvaev, M. Starck, D. Parker, *Chem. Eur. J.* **2017**, *23*, 9974–9989.

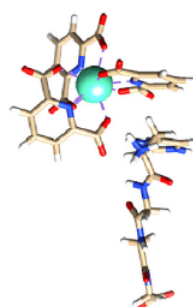
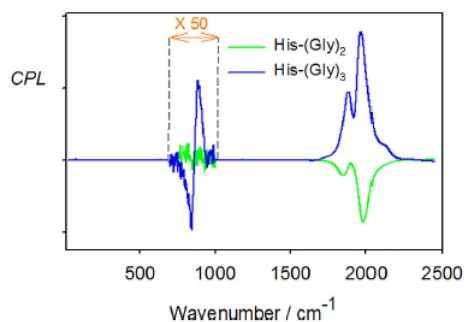
- [3] a) T. Wu, J. Kapitán, V. Andrushchenko, P. Bouř, *Anal. Chem.* **2017**, *89*, 5043–5049; b) T. Wu, J. Průša, J. Kessler, D. Dražinský, J. Valenta, P. Bouř, *Anal. Chem.* **2016**, *88*, 8878–8885; c) T. Wu, J. Kessler, P. Bouř, *Phys. Chem. Chem. Phys.* **2016**, *18*, 23803–23811; d) E. R. Neil, D. Parker, *RSC Adv.* **2017**, *7*, 4531–4540; e) F. Zinna, L. Di Bari, *Chirality* **2015**, *27*, 1–13; f) E. M. Sánchez-Carnerero, A. R. Agarrabertía, F. Moreno, B. L. Maroto, G. Muller, M. J. Ortiz, S. de la Moya, *Chem. Eur. J.* **2015**, *21*, 13488–13500; g) J. Kumar, T. Nakashima, T. Kawai, *J. Phys. Chem. Lett.* **2015**, *6*, 3445–3452; h) J. P. Riehl, G. Muller, *Circularly Polarized Luminescence Spectroscopy and Emission-Detected Circular Dichroism*, Wiley, Hoboken, **2012**.
- [4] a) J. Velisek-Carolan, T. L. Hanley, K. A. Jolliffe, *RSC Adv.* **2016**, *6*, 75336–75346; b) L. Ancel, A. Niedzwiecka, C. Lebrun, C. Gateau, P. Delangle, *C. R. Chim.* **2013**, *16*, 515–523; c) J. A. González-Vera, *Chem. Soc. Rev.* **2012**, *41*, 1652–1664.
- [5] a) K. Barthelmes, A. M. Reynolds, E. Peisach, H. R. A. Jonker, N. J. DeNunzio, K. N. Allen, B. Imperiali, H. Schwalbe, *J. Am. Chem. Soc.* **2011**, *133*, 808–819; b) K. N. Allen, B. Imperiali, *Curr. Opin. Chem. Biol.* **2010**, *14*, 247–254.
- [6] a) G. Muller, *Dalton Trans.* **2009**, 9692–9707; b) R. Carr, N. H. Evans, D. Parker, *Chem. Soc. Rev.* **2012**, *41*, 7673–7686.
- [7] a) T. Wu, X. Z. You, P. Bouř, *Coord. Chem. Rev.* **2015**, *284*, 1–18; b) L. D. Barron, *Biomed. Spectrosc. Imaging* **2015**, *4*, 223–253.
- [8] a) T. Wu, J. Kapitán, V. Mašek, P. Bouř, *Angew. Chem. Int. Ed.* **2015**, *54*, 14933–14936; *Angew. Chem.* **2015**, *127*, 15146–15149; b) T. Wu, P. Bouř, *Chem. Commun.* **2018**, *54*, 1790–1792.
- [9] F. S. Richardson, *Inorg. Chem.* **1980**, *19*, 2806–2812.
- [10] a) J. Yuasa, T. Ohno, H. Tsumatori, R. Shiba, H. Kamikubo, M. Kataoka, Y. Hasegawa, T. Kawai, *Chem. Commun.* **2013**, *49*, 4604–4606; b) M. Leonzio, A. Melchior, G. Faura, M. Tolazzi, M. Bettinelli, F. Zinna, L. Arrico, L. Di Bari, F. Piccinelli, *New. J. Chem.* DOI: <https://doi.org/10.1039/c7nj04640e>.
- [11] K. Binnemans, *Coord. Chem. Rev.* **2015**, *295*, 1–45.
- [12] a) A. Moussa, C. Pham, S. Bommireddy, G. Muller, *Chirality* **2009**, *21*, 497–506; b) J. C. G. Bünzli, C. Piguet, *Chem. Soc. Rev.* **2005**, *34*, 1048–1077; c) G. Muller, F. C. Muller, C. L. Maupin, J. P. Riehl, *Chem. Commun.* **2005**, 3615–3617.
- [13] G. Jones, V. I. Vullev, *J. Phys. Chem. A* **2002**, *106*, 8213–8222.
- [14] Gaussian 09 (Revision D.01), M. J. Frisch, G. W. Trucks, H. B. Schlegel, G. E. Scuseria, M. A. Robb, J. R. Cheeseman, G. Scalmani, V. Barone, B. Mennucci, G. A. Petersson, H. Nakatsuji, M. Caricato, X. Li, H. P. Hratchian, A. F. Izmaylov, J. Bloino, G. Zheng, J. L. Sonnenberg, M. Hada, M. Ehara, K. Toyota, R. Fukuda, J. Hasegawa, M. Ishida, T. Nakajima, Y. Honda, O. Kitao, H. Nakai, T. Vreven, J. A. Montgomery, Jr., J. E. Peralta, F. Ogliaro, M. Bearpark, J. J. Heyd, E. Brothers, K. N. Kudin, V. N. Staroverov, R. Kobayashi, J. Normand, K. Raghavachari, A. Rendell, J. C. Burant, S. S. Iyengar, J. Tomasi, M. Cossi, N. Rega, J. M. Millam, M. Klene, J. E. Knox, J. B. Cross, V. Bakken, C. Adamo, J. Jaramillo, R. Gomperts, R. E. Stratmann, O. Yazyev, A. J. Austin, R. Cammi, C. Pomelli, J. W. Ochterski, R. L. Martin, K. Morokuma, V. G. Zakrzewski, G. A. Voth, P. Salvador, J. J. Dannenberg, S. Dapprich, A. D. Daniels, O. Farkas, J. B. Foresman, J. V. Ortiz, J. Cioslowski, D. J. Fox, Gaussian Inc., Wallingford CT, **2013**.
- [15] A. Klamt, *J. Phys. Chem.* **1995**, *99*, 2224–2235.
- [16] D. A. Pearlman, D. A. Case, J. W. Caldwell, W. S. Ross, T. E. Cheatham, S. DeBolt, D. Ferguson, G. Seibel, P. Kollman, *Comput. Phys. Commun.* **1995**, *91*, 1–41.
- [17] J. Wang, R. M. Wolf, J. W. Caldwell, P. A. Kollman, D. A. Case, *J. Comput. Chem.* **2005**, *25*, 1157–1174.
- [18] J. A. Maier, C. Martinez, K. Kasavajhala, L. Wickstrom, K. E. Hauser, C. Simmerling, *J. Chem. Theory Comput.* **2015**, *11*, 3696–3713.
- [19] W. L. Jorgensen, J. Chandrasekhar, J. D. Madura, *J. Chem. Phys.* **1983**, *79*, 926–935.
- [20] a) S. Kumar, D. Bouzida, R. H. Swendsen, P. A. Kollman, J. M. Rosenberg, *J. Comput. Chem.* **1992**, *13*, 1011–1021; b) B. Roux, *Comput. Phys. Commun.* **1995**, *91*, 275–282.

Manuscript received: February 18, 2018

Accepted manuscript online: April 14, 2018

Version of record online: ■■■ 0000

FULL PAPER



Lanthanide Probe

*E. Brichtová, J. Hudecová, N. Vršková,
J. Šebestík, P. Bouř, T. Wu**



Binding of Lanthanide Complexes to
Histidine-Containing Peptides Probed
by Raman Optical Activity
Spectroscopy



Discerning Eu complex-peptide interactions: Circularly polarized luminescence of an achiral europium complex, as induced by seven model histidine-containing peptides, has been detected by Raman optical activity spectrometry (see graphic) and rationalized by molec-

ular dynamics simulations. The sensitivity and specificity of the signal for each peptide promises future usage in optical probes of peptide and protein structure in chemical imaging and medical diagnosis.

CHEMISTRY

A European Journal

Supporting Information

Binding of Lanthanide Complexes to Histidine-Containing Peptides Probed by Raman Optical Activity Spectroscopy

Eva Brichtová,^[a, b] Jana Hudecová,^[a, c] Nikola Vršková,^[a] Jaroslav Šebestík,^[a] Petr Bouř,^[a, b] and Tao Wu^{*[a]}

chem_201800840_sm_miscellaneous_information.pdf

Contents

Figure S1. The CID ratios in a broader wavenumber range.

Figure S2. pH dependence of the spectra.

Figure S3. TL and CPL $[\text{Eu}(\text{DPA})_3]^{3-}$ spectra, titration by His-(Gly)₂ and His-His.

Figure S4. Calculated free energy profiles of His-(Gly)₂.

Figure S5. Calculated free energy profiles for four peptides.

Structural characterization of peptides

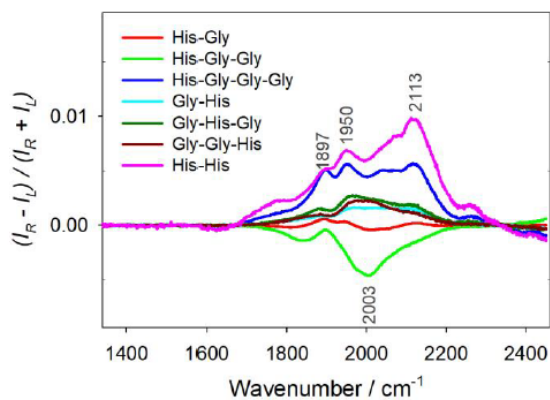


Figure S1. $[\text{Eu}(\text{DPA})_3]^{3-}$ (4 mM) CID (CPL/TL ratio) spectra when chelating with seven peptides (20 mM, pH = 4).

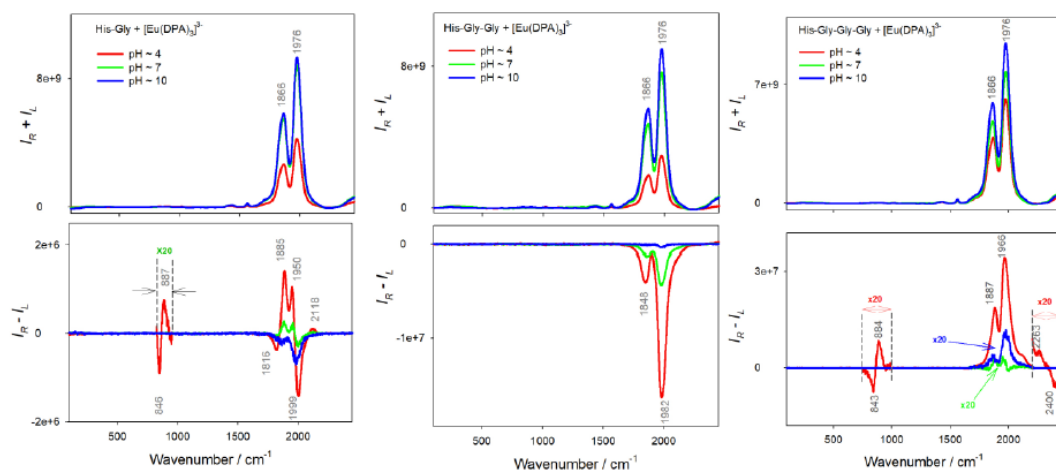


Figure S2. $[\text{Eu}(\text{DPA})_3]^{3-}$ (4 mM) TL and CPL spectra, mixtures with His-Gly, His-Gly-Gly, and His-Gly-Gly-Gly (20 mM) at three different pH values.

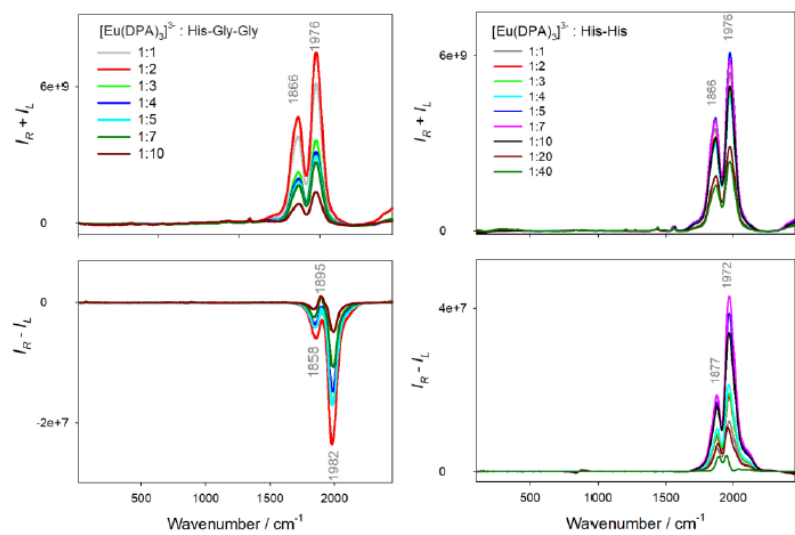


Figure S3. [Eu(DPA)₃]³⁻ (4 mM) TL and CPL spectra in mixtures with His-Gly-Gly and His-His, at pH 4.

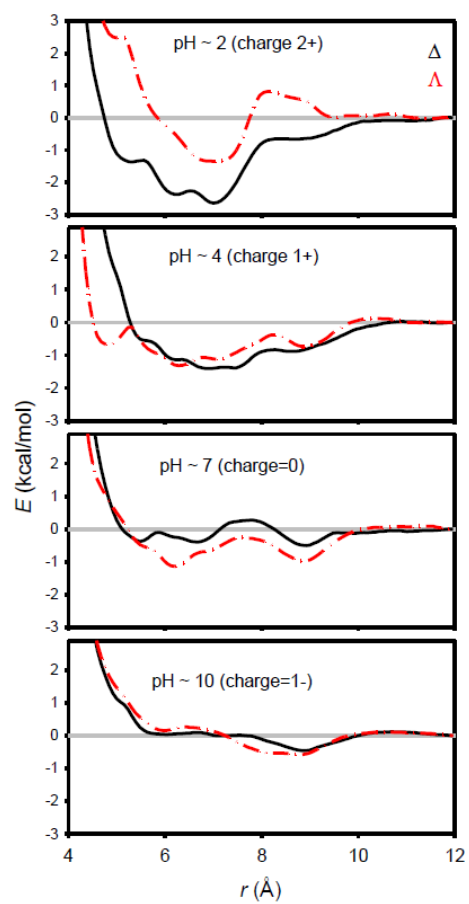


Figure S4. Calculated free energy profiles of His-Gly-Gly in complex with Δ and Λ $[\text{Eu}(\text{DPA})_3]^{3-}$ at different pH.

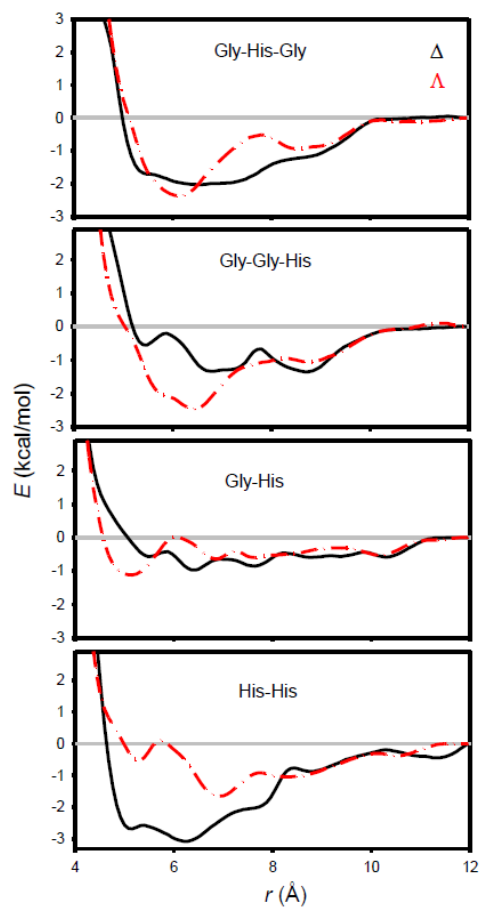


Figure S5. Calculated free energy as dependent on the Eu-peptide distance for four selected peptides.

Structural characterization of prepared peptides

Chemical shifts (δ /ppm) relative to residual HDO in the D₂O solvent are reported. The structure elucidation was aided by various 2D spectra (1H,1H-COSY; 1H,13C-HSQC; 1H,13C-HMBC). High resolution MS spectra (HRMS) recorded on an LTQ Orbitrap XL using electrospray ionization (ESI). Individual peptides were analyzed by HPLC system Agilent 1200 with Poroshell 120 SB-C18 2.7 μ m, 3.0 x 50 mm column, flow rate 1 mL/min, and diode array detection using gradient 5–5–100% of ACN in 0.05% aqueous TFA within 0-1-21 min.; however, the peptides were not retained due to very high positive charge and high polarity. Nevertheless, no hydrophobic impurity was detected. Thus, the peptide purity was assessed using TLC with ninhydrin staining.

H-His-Gly-OH ¹H NMR (400 MHz, D₂O) δ 8.70 (s, 1H, H2_{imidazole}), 7.47 (s, 1H, H4_{imidazole}), 4.37 (t, 1H, CH α _{His}), 4.09 (d, 1H, CH β _{His}), 3.97 (d, 1H, CH' β _{His}), 3.44 (m, 2H, -CH₂_{Gly}). **HRMS (ESI)** (m/z) [M+H]⁺ calculated for C₈H₁₃O₃N₄: 213.09822; found: 213.09827. **Rf** (CHCl₃: MeOH: NH₃ (aq) 2:2:1, v/v) 0.54. **Rf** (EtOH: H₂O: NH₃ (aq) 90:8:2, v/v) 0.38. Amino acid analysis: Gly 0.98 (1), His 1.00 (1).

H-His-Gly-Gly-OH ¹H NMR (400 MHz, D₂O) δ 8.71 (s, 1H, H2_{imidazole}), 7.47 (s, 1H, H4_{imidazole}), 4.39 (t, 1H, CH α _{His}), 4.13 (d, 1H, CH β _{His}), 4.03 (m, 1H, CH' β _{His}), 3.93 (m, 2H, -CH₂_{Gly}), 3.44 (m, 2H, -CH₂_{Gly2}). **HRMS (ESI)** (m/z) [M+H]⁺ calculated for C₁₀H₁₆O₄N₅: 270.11968; found: 270.11976. **Rf** (CHCl₃: MeOH: NH₃ (aq) 2:2:1, v/v) 0.47. **Rf** (EtOH: H₂O: NH₃ (aq) 90:8:2, v/v) 0.22. Amino acid analysis: Gly 1.78 (2), His 1.00 (1).

H-His-Gly-Gly-Gly-OH ¹H NMR (400 MHz, D₂O) δ 8.71 (s, 1H, H2_{imidazole}), 7.47 (s, 1H, H4_{imidazole}), 4.39 (t, 1H, CH α _{His}), 4.04 (m, 6H, CH β _{His}+ CH' β _{His}+ -CH₂_{Gly}+ -CH₂_{Gly2}), 3.45 (d, 2H, -CH₂_{Gly3}). **HRMS (ESI)** (m/z) [M+H]⁺ calculated for C₁₂H₁₉O₅N₆: 327.14114; found: 327.14121. **Rf** (CHCl₃: MeOH: NH₃ (aq) 2:2:1, v/v) 0.40. **Rf** (EtOH: H₂O: NH₃ (aq) 90:8:2, v/v) 0.18. Amino acid analysis: Gly 2.63 (3), His 1.00 (1).

H-Gly-His-Gly-OH ¹H NMR (400 MHz, D₂O) δ 8.63 (s, 1H, H2_{imidazole}), 7.34 (s, 1H, H4_{imidazole}), 4.00 (m, 2H, -CH₂_{Gly}), 3.85 (m, 2H, -CH₂_{Gly2}), 3.31 (dd, 1H, CH β _{His}), 3.22 (dd, 1H, CH' β _{His}), 3.01 (s, 1H, NH), 2.85 (s, 1H, NH), CH α _{His} hidden by solvent. **HRMS (ESI)** (m/z) [M+H]⁺ calculated for C₁₀H₁₄O₃N₅: 252.10912; found: 252.10903. **Rf** (CHCl₃: MeOH: NH₃ (aq) 2:2:1, v/v) 0.55. **Rf** (EtOH: H₂O: NH₃ (aq) 90:8:2, v/v) 0.35. Amino acid analysis: Gly 2.34 (2), His 1.00 (1).

H-Gly-Gly-His-OH ¹H NMR (400 MHz, D₂O) δ 8.59 (s, 1H, H2_{imidazole}), 7.29 (s, 1H, H4_{imidazole}), 3.97 (s, 1H, NH), 3.85 (m, 2H, -CH₂_{Gly}), 3.33 (dd, 1H, CH β _{His}), 3.20 (dd, 1H, CH' β _{His}). **HRMS (ESI)** (m/z) [M+H]⁺ calculated for C₁₀H₁₄O₃N₅: 252.10912; found: 252.10898. **Rf** (CHCl₃: MeOH: NH₃ (aq) 2:2:1, v/v) 0.51. **Rf** (EtOH: H₂O: NH₃ (aq) 90:8:2, v/v) 0.24. Amino acid analysis: Gly 2.15 (2), His 1.00 (1).

H-Gly-His-OH $^1\text{H NMR}$ (400 MHz, D_2O) δ 8.58 (s, 1H, $\text{H}2_{\text{imidazole}}$), 7.28 (s, 1H, $\text{H}4_{\text{imidazole}}$), 3.82 (q, 2H, $-\text{CH}_2_{\text{Gly}}$), 3.31 (dd, 1H, $\text{CH}\beta_{\text{His}}$), 3.20 (dd, 1H, $\text{CH}'\beta_{\text{His}}$), $\text{CH}\alpha_{\text{His}}$ hidden by solvent. **HRMS (ESI)** (m/z) $[\text{M}+\text{H}]^+$ calculated for $\text{C}_8\text{H}_{11}\text{O}_2\text{N}_4$: 195.08765; found: 195.08774. **Rf** (CHCl_3 : MeOH: NH_3 (aq) 2:2:1, v/v) 0.53. **Rf** (EtOH: H_2O : NH_3 (aq) 90:8:2, v/v) 0.37. Amino acid analysis: Gly 0.85 (1), His 1.00 (1).

H-His-His-OH $^1\text{H NMR}$ (400 MHz, D_2O) δ 8.60 (s, 1H, $\text{H}2_{\text{imidazole}}$), 8.53 (s, 1H, $\text{H}'2_{\text{imidazole}}$), 7.34 (s, 1H, $\text{H}4_{\text{imidazole}}$), 7.23 (s, 1H, $\text{H}'4_{\text{imidazole}}$), 4.25 (t, 1H, $\text{CH}\alpha_{\text{His}}$), 3.25 (m, 4H, $\text{CH}\beta_{\text{His}} + \text{CH}'\beta_{\text{His}}$), $\text{CH}'\alpha_{\text{His}}$ hidden by solvent. **HRMS (ESI)** (m/z) $[\text{M}+\text{H}]^+$ calculated for $\text{C}_{12}\text{H}_{15}\text{O}_2\text{N}_6$: 275.12510; found: 275.12513. **Rf** (CHCl_3 : MeOH: NH_3 (aq) 2:2:1, v/v) 0.56. **Rf** (EtOH: H_2O : NH_3 (aq) 90:8:2, v/v) 0.23.